



universität
wien

**EXPLORING THE POTENTIAL OF
TWO-DIMENSIONAL ELECTRONIC SPECTROSCOPY**

Mag. Alexandra Nemeth

DISSERTATION

eingereicht zur Erlangung des akademischen Grades

Doktorin der Naturwissenschaften (Dr. rer. nat.)

Wien, 2010

Studienkennzahl lt. Studienblatt: A091 419
Dissertationsgebiet lt. Studienblatt: Chemie
Betreuer: Prof. Harald F. Kauffmann

Contents

1	Introduction	1
1.1	How it all began	1
1.2	Basic Principles	3
1.3	What 2D-ES can do	6
1.4	Outline	11
2	Theory	13
2.1	Density Matrix Evolution	13
2.2	System-Field Interaction	14
2.3	Line-shape Function	16
2.4	From Time- to Frequency-Domain	18
2.5	Heterodyne Detection	19
3	Experimental Design	21
3.1	Ultrashort Pulse Generation	21
3.2	Setup of the First Generation	24
3.3	Setup of the Second Generation	26
3.4	Sample Handling	28
3.5	Calibration Procedures	29
3.6	Data Acquisition and Evaluation	31
4	PERY	35
4.1	Introduction	36
4.2	Quantum-Chemical Calculations	38
4.3	Experimental Details	39
4.4	Results and Discussion	40
4.4.1	Two-Dimensional Electronic Spectra	40
4.4.2	Rephasing and Non-Rephasing Signal Parts	43
4.4.3	Frequency-Frequency Correlation Function	45
4.4.4	Comparison to Related Four-Wave Mixing Signals	48
4.5	Simulations	49
4.6	Conclusions	55
5	Pinacyanol	57
5.1	Introduction	58
5.2	Experimental Details	60
5.3	Computational Details	60
5.4	Results and Discussion	62
5.4.1	Experimental Two-Dimensional Electronic Spectra	62

CONTENTS

5.4.2	Quantum Chemistry Calculations	66
5.4.3	Numerical Simulations of 2D Spectra	69
5.5	Conclusions	72
6	C8O3	73
6.1	Introduction	74
6.2	Experimental Details	76
6.3	Linear Absorption	76
6.4	Results and Discussion	77
6.4.1	Correlation Spectra	77
6.4.2	Relaxation Spectra	79
6.4.3	Rephasing and Non-Rephasing Spectra	81
6.5	Numerical Simulations	83
6.6	Conclusions	92
7	Rhodamine 6G	95
7.1	Introduction	96
7.2	Experimental Details	97
7.3	Experimental Results	98
7.4	Theory	100
7.4.1	Double-Quantum Two-Dimensional Signals in the Homogeneous Limit . . .	100
7.4.2	Double-Quantum Two-Dimensional Signals within the Cumulant Expansion	103
7.5	Simulations	105
7.6	Discussion	108
7.7	Conclusion	110
8	C8S3	113
8.1	Introduction	114
8.2	Experimental Details	116
8.3	Computational Details	117
8.3.1	Construction of a Microscopic Model	117
8.3.2	Modeling Spectral Properties in the Homogenous Limit	118
8.4	Results and Discussion	122
8.4.1	1Q2D Correlation and Relaxation Patterns	122
8.4.2	2Q2D Correlation Spectra	124
8.5	Conclusions	127
9	Summary and Outlook	129
	Bibliography	131
	List of Figures	150

Acknowledgments

No thesis is ever the product of one person's efforts alone, and certainly this one has been no different. It would never have become reality without the help and support of many people and for this I want to thank all of them.

This thesis has been accomplished in the *Ultrafast Dynamics* group of Prof. Harald F. Kauffmann at the Department of Physical Chemistry at the University of Vienna and at the Technical University of Vienna. Naturally, the first one to thank is my supervisor *Harald F. Kauffmann* whose enthusiasm, support, encouragement, and advice accompanied me from the initial to the final level of this project. It is a pleasure to thank my colleagues *Franz Milota* and *Jaroslav Sperling* for their constant willingness to answer all my questions and for the pleasant working atmosphere they created. Franz Milota deserves my special thanks for sharing his amazing knowledge on optics, experiments, and technical issues with me. I am indebted to Jaroslav Sperling for his support in all fields starting from basic theory questions, over advanced simulations, all the way to scientific publishing. I really learned a lot from you two! In a later stage of my studies *Jürgen Hauer* and *Niklas Christensson* joined the group and took part in the exciting advances in the field of two-dimensional electronic spectroscopy. I specially thank them for many helpful comments on how to improve this dissertation.

People can't live on love and air alone, and I am certainly no exception. This thesis would not have been possible without financial support and I was blessed to receive it from the *Austrian Science Foundation* (FWF) within the projects P18233 and F016/18 and the *Austrian Academy of Sciences* within a DOC-fFORTE scholarship.

Most of the studies that are described in this thesis have been performed in close collaboration with research groups around the world. I owe my deepest gratitude to *Tomáš Mančal* from Charles University in Prague for contributing the theoretical part to many of our publications. Special thanks also go to *Vladimír Lukeš* from Slovak Technical University in Bratislava who performed the quantum-chemical calculations that are presented in this thesis. I am indebted to *Shaul Mukamel* from the University of California in Irvine for his support and expertise before, during, and after my sojourn in his group. Furthermore, I would like to thank *Darius Abramavicius* for helping me with the simulations I performed using the Spectron code.

I would like to express my gratitude to the dean of the Faculty of Physics at the Technical University of Vienna *Gerald Badurek* for providing us with laboratory space at the Technical University.

Last but not least I wish to thank *Renate* and *Magdalena* for sharing all the ups and downs one undergoes from enrollment till graduation and *Christian* for his endless love.

The basic principles which have been exploited are very general and can be applied to other coherent spectroscopies as well. Applications are conceivable in electron spin resonance, nuclear quadrupole resonance, in microwave rotational spectroscopy, and possibly in laser infrared spectroscopy.

W. P. Aue, E. Bartholdi, R. R. Ernst



INTRODUCTION

1.1 How it all began

Spectroscopic methods are one of the most widely applied tools for studying the nuclear and electronic structure and dynamics of atomic and molecular systems. The desired information is obtained by the interaction of matter with electromagnetic waves of all possible wavelengths, covering the range from radiowaves on the low frequency side to γ -rays on the high frequency side. Owing to the multiple ways in which electromagnetic fields can be manipulated (e.g. duration, frequency, polarization, shape, sequence, etc.) these methods have reached a high degree of complexity. To account for these developments, a number of Nobel prizes in physics and chemistry have been awarded [1], e.g. in 1952 to Felix Bloch and Edward Mills Purcell "for their development of new methods for nuclear magnetic precision measurements and discoveries in connection therewith", in 1981 to Nicolaas Bloembergen and Arthur Leonard Schawlow "for their contribution to the development of laser spectroscopy", in 1991 to Richard Ernst "for his contributions to the development of the methodology of high resolution nuclear magnetic resonance (NMR) spectroscopy", and in 1999 to Ahmed Zewail "for his studies of the transition states of chemical reactions using femtosecond spectroscopy", to name only a few examples.

Depending on the characteristics of the excitation field, spectroscopic methods can be classified as time- or frequency domain experiments. In frequency domain measurements, such as resonance light scattering or high resolution absorption/emission spectroscopy, a narrowband light source is typically used to excite a specific spectroscopic transition. For the investigation of dynamics in atomic and molecular physics, time-resolved spectroscopies with a time resolution that is higher than the time scale of the process under investigation are required [2]. Many important physical and chemical processes, such as vibrational and electronic dephasing, rotational and vibrational motion, solvent relaxation, intramolecular energy randomization, energy and electron transfer in photosynthesis, and bond cleavage and formation occur on a femto- to picosecond timescale [3]. The progress in the field of ultrashort laser pulse generation enables to nowadays follow these processes in real time. For measuring dynamics with a time resolution below $\approx 10^{-11}$ s, most

detection electronics (except for streak cameras) are not fast enough. To overcome this problem, many ultrafast spectroscopic techniques use multiple pulses and vary their delays to gate and interrogate the system under investigation. In this case, the time resolution is limited only by the duration of the excitation pulses, but not by the temporal resolution of the detecting device.

Besides providing the required time resolution, the high peak power of ultrashort laser pulses has opened the door to the field of nonlinear spectroscopies. In some instances, especially for few-atom molecules and simple polyatomics with their eigenstates well separated, linear molecular spectroscopies, such as linear absorption and Raman scattering, give direct information on static energy levels, absorption cross-sections, and line broadening mechanisms. However, in complex molecules in the condensed phase with strongly congested electronic levels and various types of transition broadening mechanisms, the microscopic information becomes highly averaged and totally concealed by structure- and featureless line-shapes. These limitations can be overcome by nonlinear spectroscopic methods. The ultimate goal of these techniques is to relate the experimentally observed temporal and spectral response of the system to the microscopic nature of intra- and intermolecular interactions and to reveal static and dynamic effects of the environment (e.g. the solvent) on the system. Solvation effects influence chemical dynamics by providing sources and sinks for energy, influencing molecular motion, inducing transport and relaxation dynamics, and determining the potential energy surfaces on which reactions take place [3]. Since second-order nonlinear signals are symmetry forbidden in isotropic media such as bulk liquids, the third-order nonlinearity is the lowest nonlinear order at which system-bath interactions and solute dynamics in liquids can be probed. The central quantity in third-order nonlinear spectroscopy is the third-order nonlinear polarization $P^{(3)}$, which is induced in the sample by three interactions with pulsed electromagnetic fields [4]. Including the radiated signal field $E_s^{(3)}$, four fields are involved in the experiments, leading to the term four-wave mixing (FWM) spectroscopies.

A milestone in the development of nonlinear techniques in NMR spectroscopy has been the first observation of a spin echo by Hahn in 1950 [5]. Fourteen years later the first photon echo, the optical analogue to the spin echo, has been demonstrated by using short light pulses instead of radio pulses [6]. To observe a photon echo three pulses interact with the sample. The first interaction at $t = 0$ creates an electronic coherence where definite phase relations are established between the excited atoms or molecules. However, if the individual atoms or molecules have slightly different absorption frequencies, their phases evolve differently. The second interaction at time $t = \tau$ stops this evolution by converting the electronic coherence into a population. A third laser pulse at $t = T$ restores the coherence but reverses the phase evolution for each atomic or molecular dipole. After a time $t = T + \tau$ all atoms or molecules are in phase again and form what is called the photon echo (i.e. a macroscopic polarization that can be detected as a pulse). Photon echo spectroscopy can be used to measure population decay and homogeneous phase relaxation, two processes that decrease the intensity of the echo signal. Inhomogeneous phase relaxation on the other hand impedes the rephasing process only if the absorption frequency and thus the phase evolution of the atoms or molecules changes in between the second and third interaction. Thus, photon echo spectroscopy allows to measure homogeneous relaxation processes even in the presence of inhomogeneous line

broadening mechanisms.

Starting from (one-dimensional) echo spectroscopy, a remarkable progress that took its origin in NMR spectroscopy has been the implementation of multi-dimensional techniques. The term multi-dimensional in this context refers to the spectroscopic observable being monitored as a function of two or more independently variable time-intervals or frequencies. As already contemplated in a very early stage in the development of two-dimensional NMR spectroscopy [7] (see quotation above), these techniques found application at increasingly shorter wavelengths. By the end of the last century the first two-dimensional (2D) experiments were demonstrated at approximately the same time in the mid- [8] and near-infrared [9] spectral region, probing vibrational and electronic transitions, respectively. Even though conceptually similar, these two seminal papers featured significant differences in the experimental realization of 2D spectroscopy. While a two-dimensional pump-probe approach (with a narrowband pump pulse scanned in frequency-domain and a broadband probe pulse) was implemented in the former work, the approach adopted in the latter work is the direct analog of 2D NMR experiments with a pulse delay scanned in time-domain and a Fourier transform step from time- to frequency-domain at the heart of the experiment. This latter approach was also pursued in 2D experiments at visible frequencies that were demonstrated for the first time in 2004 [10, 11]. In the meantime, two-dimensional spectroscopies are well established at infrared and visible frequencies (see e.g. Ref. [12] and references therein), and extensions to the ultraviolet and X-ray region have been pondered [13, 14].

Although many basic ideas that are realized in two-dimensional electronic spectroscopy (2D-ES) have been borrowed from its NMR counterpart, there exist nevertheless lots of technical and conceptual differences [15, 16]. The most obvious difference is a consequence of the different frequency ranges used in the excitation source - the radiowaves employed in NMR spectroscopy induce spin transitions, whereas the visible frequencies in 2D-ES induce electronic transitions. The shortest timescales that can be probed in NMR spectroscopy lie in the range of milliseconds, whereas time resolutions of femtoseconds (fs) can be reached in the visible spectral range. Rather than being a drawback, however, these differences enable complementary perceptions on the molecular structure and dynamics of matter.

1.2 Basic Principles of Two-Dimensional Electronic Spectroscopy

Pump-probe (PP) spectroscopy is the most widely applied type of FWM spectroscopy. It relies on exciting the system under investigation with a short, intense pump pulse and interrogating the dynamical evolution with a weak probe pulse after a variable delay. The classification into the category of FWM spectroscopies arises from the fact that the measured signal is generated by two interactions with the pump and one interaction with the probe pulse. Despite its broad use, PP spectroscopy bears a fundamental disadvantage that can be related to Heisenberg's uncertainty principle. In conjunction with ultrashort laser pulses the uncertainty principle states that the product of the temporal and spectral bandwidths must exceed a certain value. This implies that short pulses have a broad frequency spectrum and vice versa. Applied to PP spectroscopy, there

is always a tradeoff between temporal and spectral resolution - selective excitation results in loss of temporal resolution and a high temporal resolution can only be achieved by broadband (i.e. unselective) excitation. By temporally separating the first two interactions in a PP experiment, which is equivalent to spectrally resolving the excitation frequency, two-dimensional electronic spectroscopy allows to overcome this limitation.

2D-ES is based on the correlation of two electronic coherences evolving during two time intervals [17]. To this end a sequence of three laser pulses with wave vectors \mathbf{k}_1 , \mathbf{k}_2 , and \mathbf{k}_3 and time delays t_1 and t_2 interact with the sample and stimulate the generation of a third-order nonlinear polarization $P^{(3)}(\mathbf{k}_s, t_1, t_2, t_3)$ that emits the signal field $E_s^{(3)}(\mathbf{k}_s, t_1, t_2, t_3)$ for a time t_3 . Since the wavelength is much smaller than the sample size, phase-matching conditions yield directional responses and signals only emerge in directions that are linear combinations of the wave vectors of the excitation pulses, i.e. $\mathbf{k}_s = \pm\mathbf{k}_1 \pm \mathbf{k}_2 \pm \mathbf{k}_3$. A negative sign in the wave vector thereby indicates interaction with a complex conjugated field (cf. Eq. (2.6)). Out of the 2^3 possible linear combinations of wave vectors only four ($\mathbf{k}_I = -\mathbf{k}_1 + \mathbf{k}_2 + \mathbf{k}_3$, $\mathbf{k}_{II} = +\mathbf{k}_1 - \mathbf{k}_2 + \mathbf{k}_3$, $\mathbf{k}_{III} = +\mathbf{k}_1 + \mathbf{k}_2 - \mathbf{k}_3$, and $\mathbf{k}_{IV} = +\mathbf{k}_1 + \mathbf{k}_2 + \mathbf{k}_3$) are independent. The remainder of this thesis will focus on the former three, since detecting a signal in the phase-matching direction \mathbf{k}_{IV} would require the presence of at least four electronic levels with energy spacings corresponding to the frequency of the excitation pulses. The following nomenclature will be adopted in this work: signals detected along \mathbf{k}_I (\mathbf{k}_{II}) will be denoted S_I (S_{II}) or rephasing (non-rephasing) single-quantum two-dimensional (1Q2D) spectra; for signals detected along \mathbf{k}_{III} the terms S_{III} or double-quantum two-dimensional (2Q2D) spectra will be used. Most often, the sum of S_I and S_{II} spectra is measured, since this combination yields purely absorptive real parts and purely dispersive imaginary parts [18, 19]. This type of spectrum will be denoted 1Q2D spectrum. Fig. 1.1 illustrates the three different experimental techniques, a representative spectrum calculated for a three-level system in the homogenous limit, and energy ladder diagrams illustrating the contributions to the signals [20].

- In **rephasing 1Q2D spectroscopy** (S_I) (Fig. 1.1a) the interaction of the system with the first pulse ($-\mathbf{k}_1$) induces a single-quantum coherence between the ground- (g) and first-excited state (e) that oscillates for a time t_1 . Interaction with the second pulse ($+\mathbf{k}_2$) converts this coherence into a population or a vibrational wave packet in the ground or excited state. After a time t_2 interaction with the third pulse ($+\mathbf{k}_3$) restores a single-quantum coherence between the ground- and the first-excited state or the first- and second-excited state. This single-quantum coherence radiates the signal field for a time t_3 in the phase matching direction $\mathbf{k}_I = -\mathbf{k}_1 + \mathbf{k}_2 + \mathbf{k}_3$. The two-dimensional spectrum is depicted in frequency-frequency domain by Fourier transforming $t_1 \rightarrow \omega_1$ and $t_3 \rightarrow \omega_3$ while keeping t_2 fixed. Three Liouville space pathways that can be represented graphically by the three energy ladder diagrams in Fig. 1.1a contribute to S_I spectra. In these diagrams time evolves from left to right. Black arrows denote interactions with the electromagnetic field and red (blue) arrows indicate positive (negative) signal fields. The three contributions to S_I spectra can be classified into ground state bleaching (GSB), stimulated emission (SE), and excited state absorption (ESA) and yield positive (GSB, SE) and negative (ESA) absorptive signals. In these Liouville space

pathways the system evolves in conjugate frequencies during t_1 (ω_{eg}) and t_3 (ω_{ge}). This allows for rephasing in an inhomogeneously broadened ensemble, resulting in the formation of an "echo" in case the system has kept some memory of its transition frequency over t_2 . This rephasing effect manifests itself in the characteristic orientation parallel to the diagonal in S_I spectra.

- The pulse sequence for **non-rephasing 1Q2D spectra** (S_{II}) (Fig. 1.1b) differs from the one discussed above by an interchange in the sign of the first two interactions. As a consequence the system evolves with the same frequency during t_1 and t_3 (ω_{eg}) in the three Liouville space pathways contributing to S_{II} signals. Therefore, there is no rephasing effect and the system's

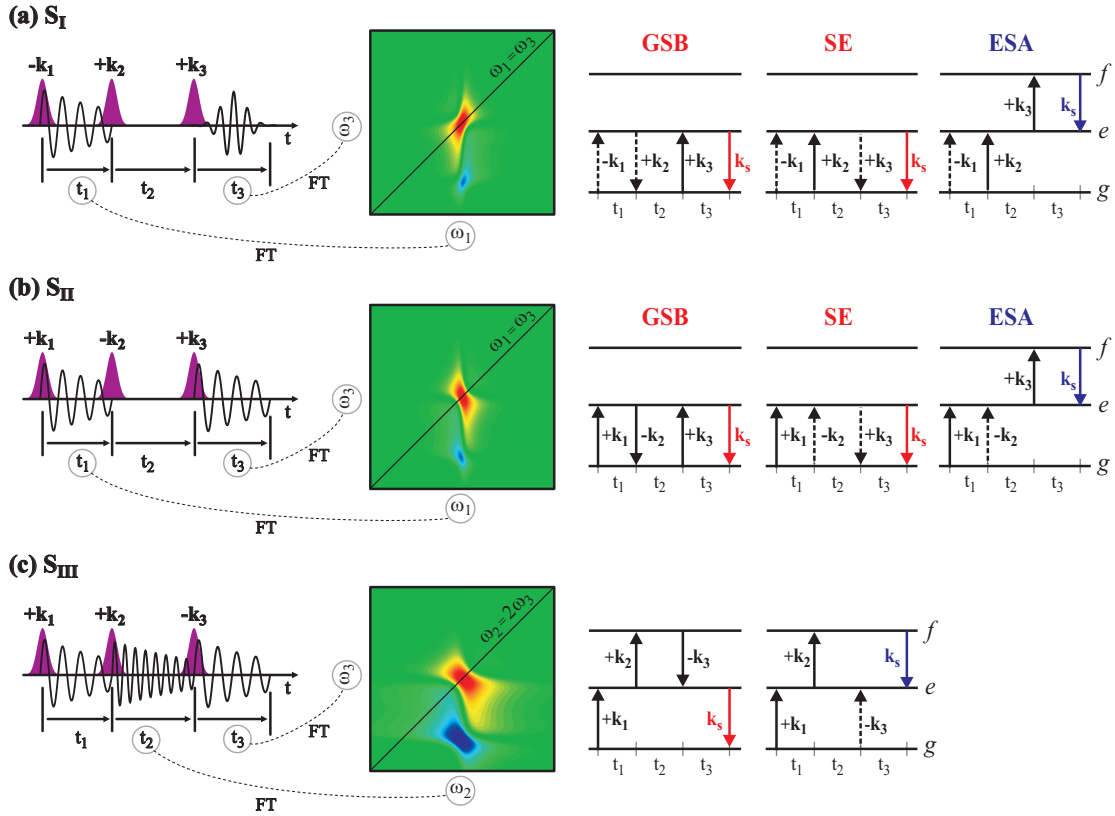


Figure 1.1: Schematic of the three two-dimensional methods S_I (a), S_{II} (b), and S_{III} (c). An illustration of the coherence evolutions and the Fourier transforms used to construct the correlation spectra is shown in the leftmost column. In the central column model calculations of the real part of the S_I , S_{II} , and S_{III} signals based on the homogenous limit of a three-level system with equal transition dipole moments and a red-shifted second excited state are shown. Energy ladder diagrams contributing to each signal are depicted in the rightmost column. Here, g , e , and f denote ground, first excited, and second excited state, respectively. Time runs from left to right. Solid (dashed) arrows indicate interaction with the *ket* (*bra*) side of the density matrix. Red (blue) signal arrows indicate positive (negative) signal contributions.

response is close to a free induction decay. The peaks in non-rephasing 1Q2D spectra feature a characteristic orientation perpendicular to the diagonal.

- In **2Q2D spectroscopy** (S_{III}) (Fig. 1.1c) only two Liouville space pathways contribute to the signal. These two contributions share the same evolution (single-quantum eg -coherence during t_1 , double-quantum fg -coherence during t_2) up to the interaction with the third pulse. This last interaction determines the sign of the contribution, which is positive in case the third pulse acts on the *bra*-side of the density matrix creating a eg -coherence, or negative in case it acts on the *ket*-side and creates a fe -coherence. These two system-field interaction schemes already indicate that the system under investigation must possess at least three electronic levels with an energetic separation that lies within the spectral bandwidth of the excitation pulses. The two-dimensional spectrum is obtained by Fourier transforming $t_2 \rightarrow \omega_2$ and $t_3 \rightarrow \omega_3$ while keeping t_1 fixed. Due to the non-rephasing character of 2Q2D spectroscopy, the orientation of the S_{III} spectrum shows strong similarities with the non-rephasing 1Q2D signal (S_{II}). However, since the system evolves in a double-quantum coherence (fg) during t_2 , that oscillates at approximately twice the frequency of a single-quantum coherence, the peaks appear at approximately twice the frequency along ω_2 in S_{III} than they do along ω_1 in S_{II} .

Compared with related third-order nonlinear techniques, the procedure to obtain a two-dimensional electronic spectrum might sound rather tedious and complicated. However, it bears a number of unique advantages that justify its application. 2D-ES gathers the maximum amount of information that can be inferred by any third-order nonlinear technique. Typical one-dimensional FWM signals such as photon echo, transient grating, and pump-probe spectra can be recovered from a 2D spectrum by projections or cuts. Two-dimensional electronic spectroscopy overcomes the trade-off between time and frequency resolution that is imposed by the time-bandwidth product of the excitation pulses to other techniques. This is due to the fact that the spectral resolution of a 2D experiment is only limited by the maximal delay between the pulses, whereas the temporal resolution is given by the pulse duration. Therefore, selective excitation, competing with high temporal resolution in one-dimensional experiments, is not an issue in 2D spectroscopy. Finally, spreading the information content into two frequency dimensions facilitates the interpretation of congested spectra. The merits of two-dimensional electronic spectroscopy are described more extensively in the following section.

1.3 What Two-Dimensional Electronic Spectroscopy can do

Without claim for completeness, this section aims at highlighting some of the unique capabilities of two-dimensional electronic spectroscopy. The examples are illustrated by model calculations or examples from this thesis and related to the available literature.

Dissect homogeneous and inhomogeneous line-shapes. In time domain, solvation dynamics are characterized by the dephasing time of molecular transitions. In frequency domain the spectral broadening of electronic transitions yields information about intra- and intermolecular interactions. In traditional theories of spectral line-shapes a distinction is made between homogeneous and inhomogeneous contributions. The term homogeneous broadening is used to describe the statistical loss of coherence that all molecules or atoms in the sample experience [21]. The natural line broadening due to the finite lifetime of excited states and collisions of the system with the surrounding bath contribute to the homogeneous spectral profile. In linear absorption a Lorentzian line-shape is indicative of homogeneous broadening. Inhomogeneous broadening on the other hand is the spectroscopic manifestation of the fact that every molecule or atom in the sample may have a slightly different local environment, so that the probability for absorption or emission of light at the frequency ω is not the same for all molecules or atoms. This static distribution of transition frequencies manifests itself in a Gaussian line-shape in linear absorption [4].

Even though homogeneous and inhomogeneous contributions may not always be easily distinguishable in their linear absorption spectra, the 1Q2D spectra ($S_I + S_{II}$) show clear differences in their shapes for homogeneously and inhomogeneously broadened systems (Fig. 1.2) [22, 23]. The 1Q2D spectrum of a two-level system with homogeneous broadening only features a 2D Lorentzian star shape (Fig. 1.2a). Cuts taken along the diagonal and the anti-diagonal both yield Lorentzian line-shapes of the same width. As the inhomogeneous width increases, the peak broadens along the diagonal axis, while the antidiagonal remains unchanged. For large inhomogeneous broadening, a pronounced elliptical peak shape is observed in the 1Q2D spectrum (Fig. 1.2b). Taking a cut along the diagonal reveals a Gaussian line-shape whose width is determined by the inhomogeneous width, whereas the antidiagonal axis preserves the homogeneous line-shape [24]. Thus, the degree of ellipticity of the peak in the 1Q2D spectrum can be taken as an indicator for the amount of inhomogeneity present in the system under investigation [25]. 2D spectroscopy is the only method that allows to simultaneously measure homogeneous and inhomogeneous line-shapes directly.

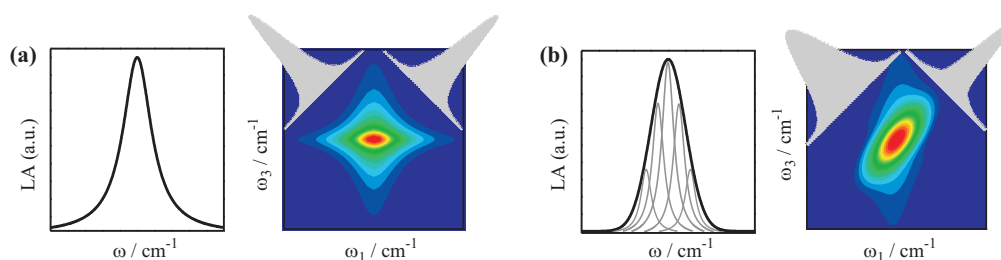


Figure 1.2: Calculated linear absorption spectrum (left) and 1Q2D absolute value spectrum (right) of a homogeneously broadened (a) and an inhomogeneously broadened (b) two-level system. Cuts along the diagonal and anti-diagonal are shown in the upper left and right corner of the 2D spectrum, respectively.

Probe spectral diffusion. With increasing waiting time t_2 each initially excited subpopulation in a dynamically inhomogeneous system will stochastically sample all available local environments and therefore lose its initial correlation of transition frequencies [23]. This spectral diffusion process manifests itself by a change in the line-shapes of a 1Q2D spectrum from elliptical to symmetrical [19, 26] as shown in Fig. 1.3. The decay of asymmetry thereby provides a direct measure of spectral diffusion.

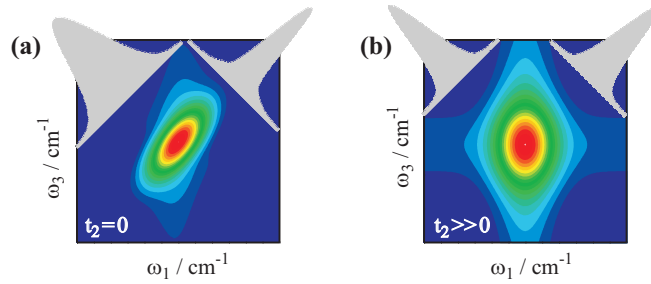


Figure 1.3: Calculated 1Q2D spectra of an inhomogeneously broadened two-level system for $t_2 = 0$ (a) and $t_2 \gg 0$ (b) revealing the effect of spectral diffusion. Cuts along the diagonal and anti-diagonal are shown in the upper left and right corner, respectively.

Identify electronic couplings. Electronic couplings reshape the excited state manifolds of many important systems such as molecular aggregates, polymers, semiconductor quantum wells, and photosynthetic complexes. One of the most prominent advantages of 2D spectroscopy over linear and 1D nonlinear techniques is its capability to directly reveal these couplings by the presence or absence of cross peaks. Fig. 1.4a shows the absolute value 1Q2D spectrum of two uncoupled two-level systems (TLS). Each of the two TLS gives rise to a single peak along the diagonal in the 1Q2D spectrum. The absence of signals at $\omega_1 \neq \omega_3$ indicates that the two TLS do not sense each others presence. The linear absorption spectrum of two uncoupled TLS may not be distinguishable from the linear absorption spectrum of a coupled three-level system. In the 1Q2D spectrum, however, cross peaks at $t_2 = 0$ provide an unbiased proof of electronic coupling as can be seen in Fig. 1.4b, which shows the 1Q2D spectrum of a "V"-type three-level system. The two diagonal peaks stem from transitions from the ground state to each individual single-excited state, whereas the two cross peaks indicate their coupling via the common ground state [27]. The intensity of a cross peak is proportional to the square of the transition dipole moment of the two states involved (i.e. $\propto |\mu_i|^2 |\mu_j|^2$), whereas diagonal peaks scale as $|\mu_i|^4$. Cross peaks indicative of electronic couplings have been measured in semiconductor quantum wells [28], cylindrical J-aggregates [29], potassium vapor [30], and photosynthetic complexes [31].

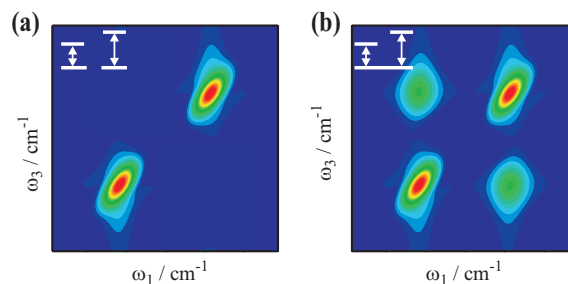


Figure 1.4: Calculated 1Q2D spectra of two uncoupled two-level systems (a) and two coupled two-level systems (b) for $t_2 = 0$. The coupling manifests itself in the appearance of cross peaks in two-dimensional spectra.

Follow the pathways of energy transfer. A second source for cross peaks in 2D spectra, which requires only weakly coupled electronic levels, is energy transfer in the excited state manifold. By recording a series of 1Q2D spectra for increasing waiting times t_2 , the evolution of cross peaks allows to directly reveal the pathways and timescales of energy transfer processes in real time. Cross peaks evolving in the lower half triangle ($\omega_1 > \omega_3$) thereby monitor downhill transfer steps, whereas uphill energy transfer can be followed by the evolution of cross peaks in the upper half triangle ($\omega_1 < \omega_3$). The intensity ratio of a cross peak in the lower half triangle compared to the corresponding peak in the upper half triangle is determined by the detailed balance condition ($\propto \exp\frac{-\Delta E}{kT}$). By means of 1Q2D electronic spectroscopy energy transfer processes have been monitored in a number of natural [31, 32] and artificial [29, 33] light harvesting complexes. An example for the latter is shown in Fig. 1.5 and discussed in more detail in Chapter 6.

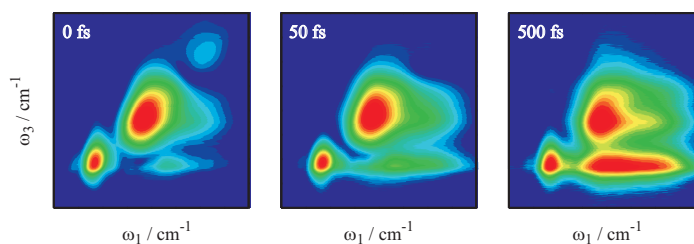


Figure 1.5: Absolute value 1Q2D spectra of C8O3 (cf. Chapter 6) for waiting times $t_2 = 0, 50,$ and 500 fs reveal the pathways of energy flow in these cylindrical aggregates.

Characterize vibronic coherences. The femtosecond laser pulses employed in 2D-ES are usually very broad in the spectral domain and therefore allow to coherently excite a number of vibrational levels. The induced vibrational wave packet manifests itself in oscillating signal intensities and line-shapes in the 1Q2D spectra. Distinct diagonal and cross peaks can be observed in case of

high frequency vibrations [34, 35, 36], whereas only the evolution of a single peak can be followed in case of low frequency vibrations [36, 37, 38]. An example for the latter case is shown in Fig. 1.6 and discussed in more detail in Chapter 4.

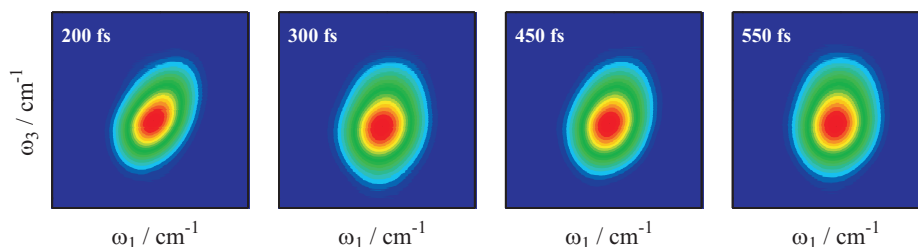


Figure 1.6: Absolute value 1Q2D spectra of PERY (cf. Chapter 4) for waiting times t_2 of 200, 300, 450, and 500 fs. The single peak oscillates with a period of 240 fs induced by coupling of the electronic transition to a vibrational mode with a frequency of 140 cm^{-1} .

Reveal electronic coherences. Recently, signatures of electronic coherences in 1Q2D spectra have received considerable theoretical and experimental attention [39, 40, 41, 42, 43, 44]. Quantum coherence during energy transport in natural photosynthetic complexes has been demonstrated and suggested to increase the efficiency of the transfer process. Fig. 1.7 illustrates the effect of electronic wave packet evolution for a model system of two coupled oscillators. During t_2 the system evolves in an electronic coherence that oscillates at a period determined by the energetic separation of the two excited states involved (38 fs for the example shown in Fig. 1.7). The two cross peaks thereby oscillate out of phase, i.e. the lower energy cross peak has its maxima at t_2 -times at which the higher energy cross peak passes through its minima.

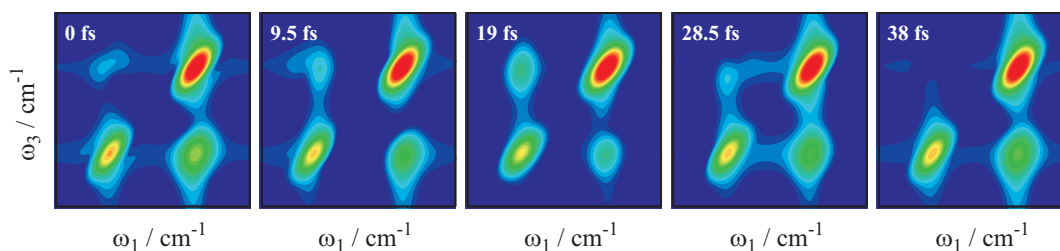


Figure 1.7: Temporal evolution of the 1Q2D spectra of two coupled oscillators. The two excited states are separated in energy by 875 cm^{-1} corresponding to a beating period of 38 fs.

Characterize higher excited states. To accurately describe structural, spectroscopic, and reaction parameters, information on double-excited states is required in addition to the one obtained for single-excited states. In 1Q2D spectroscopy the signals arising from double-excited states are buried under the intense contributions of ground- to single-excited state transitions. 2Q2D-ES allows to characterize higher excited states by singling out excitation pathways that involve a double-quantum coherence between the ground- and a double-excited state. Fig. 1.8 compares the 1Q2D spectrum with the 2Q2D spectrum of C8S3 (cf. Chapter 8). By combining these two methods detailed information on the single- and double-excited state manifolds can be obtained.

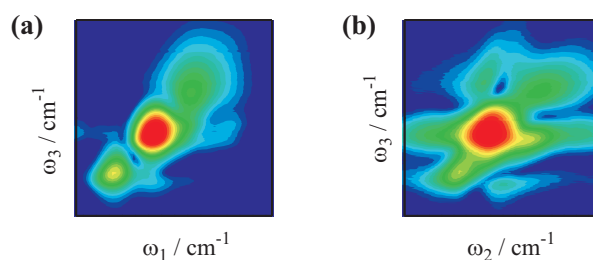


Figure 1.8: Representative absolute value 1Q2D (a) and 2Q2D (b) spectra of C8S3 (cf. Chapter 8). Double-excited state information which is hidden in 1Q2D spectra can be extracted from 2Q2D spectra.

1.4 Outline of the Thesis

This thesis is organized as follows:

- **Chapter 2** provides the basic equations necessary for understanding the principles of two-dimensional electronic spectroscopy.
- The experimental spectra presented in this thesis have been recorded with two different experimental design. Both of them are discussed in detail in **Chapter 3**.
- Presentation of the results obtained during my PhD studies together with a detailed discussion starts in **Chapter 4** with a monomeric dye (PERY) whose FWM signals are strongly modulated by coupling to a low-frequency vibrational mode. The coupling of the electronic transition to the vibrational mode induces a propagating vibrational wave packet that manifests itself in oscillating signal intensities and line-shapes. In the 1Q2D electronic spectra the wave packet motion induces a pronounced beating of the anti-diagonal absorptive peak width, accompanied by orientational changes of the nodal line in the dispersive signal part. The effects can be assigned to periodic alternations in the relative amplitudes of rephasing and non-rephasing contributions to the spectrum. A theory of the time-dependent two-dimensional spectral line-shapes is presented and shown to reproduce the observed effects.

- In **Chapter 5** we simultaneously monitor monomers and van-der-Waals bound dimers of Pinacyanol in a single experiment and illustrate how 2D line-shapes are affected by exciton delocalization induced by electronic intermolecular couplings. A quantitative line-shape analysis of a sequence of 1Q2D spectra up to 10 ps reveals that the similarity of the two peaks at $t_2 = 0$ vanishes on a sub-100 fs time scale.
- Identifying the pathways and timescales of excitation energy transfer is a central goal in the design of artificial light harvesting systems and energy transporting wires. In **Chapter 6** we provide this information for molecular nanotubes formed by the dye C8O3 by correlating excitonic absorption and emission frequencies at various delay periods. In combination with simulations based on a coupled electronic oscillator model the experiments reveal the electronic coupling pattern and show the cascading-type energy transfer pathways.
- By detecting the signal in the phase-matching direction $+\mathbf{k}_1 + \mathbf{k}_2 - \mathbf{k}_3$, the recently developed method of double-quantum two-dimensional electronic spectroscopy (2Q2D-ES) singles out excitation pathways that involve a double-quantum coherence between the ground state (g) and a double-excited state (f). Based on experimental results on the dye Rhodamine 6G, a detailed discussion about the interpretation of 2Q2D spectra and the theory underlying this method is presented in **Chapter 7**.
- In **Chapter 8** we present 1Q2D and 2Q2D spectra of the double-wall cylindrical aggregates formed by the carbocyanine dye C8S3. The narrow line-shapes of molecular aggregates favor the interpretation of 2Q2D spectra of these systems in comparison to monomers which typically exhibit strong system-bath interactions and thus broad spectral shapes. The experimental spectra are reconstructed by employing a microscopic model and simulating the third-order nonlinear response within the quasi-particle scattering approach. Our combined experimental-theoretical study reveals detailed information on the single- and double-exciton manifold.
- A summary of the results presented in this thesis together with some ideas for future research directions are outlined in **Chapter 9**.

Do not worry about your difficulties in Mathematics. I can assure you mine are still greater.

Albert Einstein (1879 - 1955)



THEORY

2.1 Density Matrix Evolution

In Liouville space the system is described by a density matrix ρ instead of a wave function Ψ . The density matrix of a pure state is defined as [4]

$$\rho(t) = |\Psi(t)\rangle\langle\Psi(t)| \quad (2.1)$$

and has the advantage of keeping track of the time-evolution of $|ket\rangle$ and $\langle bra|$ simultaneously. Moreover, it allows to write the density matrix of a statistical average as [45]

$$\rho(t) = \sum_k p_k(t) |\Psi_k(t)\rangle\langle\Psi_k(t)|, \quad (2.2)$$

where $p_k(t)$ is the probability of a system to be in a pure state $|\Psi_k\rangle$. Such a description of statistical ensembles is very important in condensed phase systems, since there are in general no pure states. The time-evolution of the density matrix obeys the quantum Liouville equation

$$\frac{\partial\rho(t)}{\partial t} = -\frac{i}{\hbar}[H(t), \rho(t)] = -\frac{i}{\hbar}L(t)\rho(t) \quad (2.3)$$

where L is the Liouville operator. Since we are interested only in the time-dependent behavior of the system, we can work in the reduced density matrix picture by eliminating the bath variables via taking the trace over the bath [46]. The Hamilton operator $H(t)$ then can be written as the sum of three contributions [47]

$$H(t) = H_S + H_{SB}(t) + H_{SF}(t) = H_0 + H_{SF}(t), \quad (2.4)$$

where H_S denotes the Hamiltonian of the unperturbed system, $H_{SB}(t)$ describes the interaction between the system and the bath, and $H_{SF}(t)$ the coupling of the system with the electromagnetic field.

2.2 System-Field Interaction

For the interaction of the system with the electromagnetic field the semiclassical approximation is usually invoked, whereby the field is treated classically and the system (atom, molecule, semiconductor, etc.) is treated quantum-mechanically. Furthermore, the dipole approximation, where the system is represented as a point dipole as far as the field is concerned, is adopted [4]. With these approximations, the system-field interaction term is written as [48]

$$H_{SF}(t) = -E(\mathbf{r}, t) \cdot V, \quad (2.5)$$

where $E(\mathbf{r}, t)$ denotes the (time-dependent) electric field and V the dipole operator. The electric field is represented as a sum over all incoming fields

$$E(\mathbf{r}, t) = \sum_j (E_j(t)e^{-i\omega_j t + i\mathbf{k}_j \mathbf{r}} + E_j^*(t)e^{i\omega_j t - i\mathbf{k}_j \mathbf{r}}), \quad (2.6)$$

where $E_j(t)$ denotes the temporal field envelope, and * indicates complex conjugation. Depending on the number, timing, frequencies, and directions of the electric fields, different nonlinear optical spectroscopies can be differentiated. If the interaction with the electromagnetic field is assumed to be weak, the system-field interaction can be considered as a perturbation to an equilibrium density matrix $\rho^{(0)}$. The density matrix can then be expanded in a series as [49]

$$\rho(t) = \rho^{(0)}(t) + \rho^{(1)}(t) + \rho^{(2)}(t) + \rho^{(3)}(t) + \dots, \quad (2.7)$$

where the superscript n denotes the order in the field. The n th-order term is given by

$$\begin{aligned} \rho^{(n)}(t) = & \left(\frac{i}{\hbar}\right)^n \int_0^\infty dt_n \int_0^\infty dt_{n-1} \dots \int_0^\infty dt_1 E(\mathbf{r}, t - t_n) E(\mathbf{r}, t - t_n - t_{n-1}) \dots \\ & \times E(\mathbf{r}, t - t_n - t_{n-1} - \dots - t_1) G(t_n) \mathcal{V} G(t_{n-1}) \mathcal{V} \dots G(t_1) \rho(-\infty). \end{aligned} \quad (2.8)$$

In this equation, t_n indicate time-intervals between interactions. $G(t)$ are Liouville space Green functions defined as

$$G(t) = \theta(t) e^{-\frac{i}{\hbar} L_0 t}, \quad (2.9)$$

where $\theta(t)$ denotes the Heaviside step-function. \mathcal{V} is the Liouville space transition dipole moment superoperator given by

$$\mathcal{V}\rho = [V, \rho] \quad (2.10)$$

where $[\dots]$ denotes the commutator.

The dipole operator V is connected to the macroscopic polarization $P(t)$ by its expectation value, i.e.

$$P(t) = \langle\langle V|\rho(t)\rangle\rangle = \text{Tr}[V\rho(t)], \quad (2.11)$$

where $\langle\langle\dots\rangle\rangle$ denotes the expectation value and Tr the trace of the matrix. By combining Eqs. (2.11) and (2.7), also the polarization can be expanded in a power series as

$$P(t) = P^{(0)}(t) + P^{(1)}(t) + P^{(2)}(t) + P^{(3)}(t) + \dots \quad (2.12)$$

The third-order nonlinear polarization $P^{(3)}(t)$, which is the central quantity in third-order nonlinear spectroscopy, can be written as

$$P^{(3)}(\mathbf{r}, t_1, t_2, t_3) = \int_0^\infty dt_3 \int_0^\infty dt_2 \int_0^\infty dt_1 E(\mathbf{r}, t - t_3) \\ \times E(\mathbf{r}, t - t_3 - t_2) E(\mathbf{r}, t - t_3 - t_2 - t_1) R^{(3)}(t_1, t_2, t_3). \quad (2.13)$$

The so-called response functions $R^{(3)}(t_1, t_2, t_3)$ are given by [50]

$$R^{(3)}(t_1, t_2, t_3) = \left(\frac{i}{\hbar}\right)^3 \langle\langle V|G(t_3)\mathcal{V}G(t_2)\mathcal{V}G(t_1)\mathcal{V}|\rho(-\infty)\rangle\rangle. \quad (2.14)$$

The third-order response functions carry the complete microscopic information necessary for the calculation of the optical signal. Basically, they constitute a sequence of interactions (indicated by \mathcal{V}) that are separated by periods in which the system evolves freely according to the Green function G . Graphically, these response functions can be illustrated by double-sided Feynman diagrams. Fig. 2.1 shows the contributions to S_I , S_{II} , and S_{III} spectra illustrated in this way. In

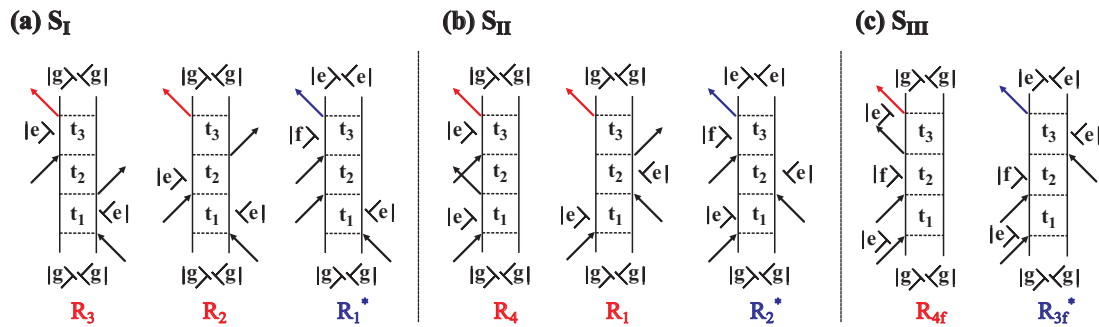


Figure 2.1: Feynman diagrams contributing to S_I (a), S_{II} (b), and S_{III} (c) spectra. $|g\rangle$, $|e\rangle$, and $|f\rangle$ denote ground, first excited, and second excited state, respectively. Time runs from bottom to top. Red (blue) signal arrows indicate positive (negative) signal contributions.

these diagrams the left and right vertical lines indicate the evolution of the $|ket\rangle$ and $\langle bra|$ of the density matrix, respectively. Black arrows denote interactions with the electromagnetic field and red (blue) arrows indicate positive (negative) signal fields. Arrows pointing towards (away from) the vertical lines indicate excitation (deexcitation) and arrows pointing to the left (right) indicate interaction with $-\mathbf{k}_i$ ($+\mathbf{k}_i$). Time evolves from bottom to top. These Feynman diagrams carry the same information as the energy ladder diagrams in Fig. 1.1 and are very useful tools to follow the coherence and population evolution of the system.

2.3 Line-shape Function

Due to interactions of the system with the bath the energy gap between two levels a and b is subject to a stochastic force. Expressed as a frequency, this time-dependent instantaneous energy gap can be written as

$$\omega_{ab}(t) = \langle \omega_{ab} \rangle + \delta\omega_{ab}(t), \quad (2.15)$$

where $\langle \omega_{ab} \rangle$ denotes the (time- or ensemble-) averaged frequency and $\delta\omega_{ab}(t)$ the fluctuating part. The time-evolution of an off-diagonal element of the density matrix is given by

$$\frac{\partial \rho_{ab}(t)}{\partial t} = -i\omega_{ab}(t)\rho_{ab} \quad (2.16)$$

which can be formally solved as

$$\rho_{ab}(t) = e^{-i \int_0^t d\tau \omega_{ab}(\tau)} \rho_{ab}(0) = e^{-i \langle \omega_{ab} \rangle t} \langle e^{-i \int_0^t d\tau \delta\omega_{ab}(\tau)} \rangle \rho_{ab}(0). \quad (2.17)$$

The exponential prefactor in Eq. (2.17) describes a phase that is related to the fluctuating frequency. Assuming that the frequency fluctuations $\delta\omega_{ab}(t)$ are small, the average of the exponential function can be evaluated by a cumulant expansion [51]. By truncating at second order we obtain the so-called line-shape function $g(t)$

$$g(t) = \int_0^t d\tau_2 \int_0^{\tau_2} d\tau_1 \langle \delta\omega(\tau_2) \delta\omega(\tau_1) \rangle. \quad (2.18)$$

Since the frequency-frequency correlation function $\langle \delta\omega(\tau_2) \delta\omega(\tau_1) \rangle$ in equilibrium depends only on the time interval $\tau_2 - \tau_1$, it can be replaced by

$$C(t) = \langle \delta\omega(t) \delta\omega(0) \rangle. \quad (2.19)$$

$C(t)$ describes the fluctuations of the electronic transition due to its interaction with the degrees of freedom of the surrounding. Often the normalized ensemble averaged product of transition

frequency fluctuations $\delta\omega$ is used to discuss the influence of the bath degrees of freedom onto the spectrum. This function is defined as

$$M(t) = \frac{\langle \delta\omega(t)\delta\omega(0) \rangle}{\langle \delta\omega^2 \rangle}, \quad (2.20)$$

and (for high temperatures) equals the real part of the correlation function $C(t)$ normalized to 1 at $t = 0$ [36]. All linear and nonlinear response functions $R^{(n)}$ can now be expressed in terms of the line-shape function $g(t)$.

To model the line-shape function several approaches of different sophistication have been developed [52, 53]. In the simplest case of the **optical Bloch model** the dynamics are either infinitely fast (homogeneous limit) or stationary (inhomogeneous limit). In the former case the correlation function is a delta function ($M(t) = \delta(t)$), in the latter case $M(t) = 1$ [52]. In this model the line-shape function $g(t)$ is always real implying that the center transition frequency does not change in time.

In **Kubo's stochastic model** the electronic transition is considered to be a stochastically perturbed oscillator, making its transition frequency a stochastic function of time. The correlation function is modeled as an exponentially decaying function [25, 54]

$$M(t) = \Delta^2 e^{-\frac{t}{\tau_c}}, \quad (2.21)$$

where τ_c is a correlation time over which the system retains transition frequency information and Δ is the modulation strength of the fluctuating electronic transition frequency [52]. The line-shape function can then be written as

$$g(t) = \Delta^2 \tau_c^2 \left[e^{-\frac{t}{\tau_c}} + \frac{t}{\tau_c} - 1 \right], \quad (2.22)$$

and it is always real, i.e. there is no Stokes shift. There exist two limiting cases in this model [25]

- In the fast modulation (homogeneous) limit $\Delta\tau_c \ll 1$. In this limit the line-shape function can be written simply as $g(t) = \frac{t}{T_2}$ with $T_2 = (\Delta^2\tau_c)^{-1}$. In linear absorption this limiting case gives a Lorentzian line-shape with a width of T_2^{-1} .
- In the slow modulation (inhomogeneous) limit $\Delta\tau_c \gg 1$. In this limit the line-shape function can be written as $g(t) = \frac{1}{2}\Delta^2 t^2$. In linear absorption this gives a Gaussian line-shape with a width of Δ .

One of the most common models for the line-shape function is the so called **multimode Brownian oscillator model**, which enables to describe both solvent modes (by strongly overdamped oscillators) as well as intramolecular vibrational modes (by underdamped oscillators). In this model, the electronic states of the dissolved molecule are coupled to a set of Brownian oscillators, which may be interpreted as the optically active intramolecular vibrations as well as some selected

collective solvent modes [55]. Due to the displacement of the equilibrium positions of the oscillators in the various electronic states, a nonequilibrium distribution of oscillator energy is created upon optical excitation of a molecule. The subsequent relaxation toward the new equilibrium situation can be directly interpreted in terms of solvation dynamics [53]. The line-shape function consists of the sum of contributions from different Brownian oscillators (labeled j) [53]

$$g(t) = \sum_j g_j(t) = \sum_j i\lambda_j \int_0^t d\tau M_j(\tau) + \Delta_j^2 \int_0^t d\tau_1 \int_0^{\tau_1} d\tau_2 M_j(\tau_2), \quad (2.23)$$

where $M(\tau)$ is the normalized transition frequency correlation function. The real part of $g(t)$ describes spectral broadening, whereas the imaginary part of $g(t)$ determines the time-dependent spectral diffusion, e.g. the fluorescence Stokes shift [56]. The reorganisation energy λ_j is a measure for the relative displacement d_j of the potential energy curves of the Brownian oscillator j in both electronic states

$$\lambda_j = \frac{\omega_j d_j^2}{2}, \quad (2.24)$$

with ω_j being the vibrational frequency in both electronic surfaces. The magnitude of the Stokes shift is obtained directly by two times the reorganization energy. The coupling strength Δ_j is a measure of the frequency range over which transition probability between the two electronic states is allowed according to the Franck-Condon principle

$$\Delta_j^2 = \omega_j^2 d_j^2 \left[n(\omega_j) + \frac{1}{2} \right]. \quad (2.25)$$

It controls the width of the spectrum [22]. In the high temperature limit ($k_B T \gg \hbar\omega_j$) Δ_j and λ_j are directly related via

$$\Delta_j^2 = \frac{2k_B T \lambda_j}{\hbar}. \quad (2.26)$$

2.4 From Time- to Frequency-Domain

In nonlinear spectroscopies the nonlinear polarization can not be measured directly. The accessible quantity is the electric signal field $E_s^{(3)}$ that is radiated by the macroscopic polarization $P^{(3)}$ and is related to it via

$$E_s^{(3)}(\mathbf{k}_s, t_1, t_2, t_3) \approx \frac{i2\pi l \omega_3}{n(\omega_3)c} P^{(3)}(\mathbf{k}_s, t_1, t_2, t_3), \quad (2.27)$$

where $n(\omega_3)$ is the sample's refractive index, l is the sample length, and c is the speed of light [57]. The two-dimensional spectrum in frequency-frequency domain is obtained by Fourier transforming two of the three time-delays while keeping the third one fixed, i.e.

$$S_I(\omega_1, t_2, \omega_3) = \int_0^\infty \int_0^\infty dt_1 dt_3 E_I^{(3)}(\mathbf{k}_I, t_1, t_2, t_3) e^{-i\omega_1 t_1 + i\omega_3 t_3}, \quad (2.28)$$

$$S_{II}(\omega_1, t_2, \omega_3) = \int_0^\infty \int_0^\infty dt_1 dt_3 E_{II}^{(3)}(\mathbf{k}_{II}, t_1, t_2, t_3) e^{+i\omega_1 t_1 + i\omega_3 t_3}, \quad (2.29)$$

$$S_{III}(t_1, \omega_2, \omega_3) = \int_0^\infty \int_0^\infty dt_2 dt_3 E_{III}^{(3)}(\mathbf{k}_{III}, t_1, t_2, t_3) e^{+i\omega_2 t_2 + i\omega_3 t_3}. \quad (2.30)$$

E_I , E_{II} , and E_{III} thereby refer to the signal directions $\mathbf{k}_I = -\mathbf{k}_1 + \mathbf{k}_2 + \mathbf{k}_3$, $\mathbf{k}_{II} = +\mathbf{k}_1 - \mathbf{k}_2 + \mathbf{k}_3$, and $\mathbf{k}_{III} = +\mathbf{k}_1 + \mathbf{k}_2 - \mathbf{k}_3$, respectively. Experimentally, the Fourier transform involving t_3 is performed implicitly by the spectrometer if one spectrally resolves the emitted signal field. This procedure directly yields the frequency axis ω_3 . The second frequency axis (ω_1 for S_I and S_{II} and ω_2 for S_{III}) is obtained by scanning t_1 respectively t_2 over a certain range while keeping the remaining delay fixed and performing a Fourier transform from time- to frequency-domain.

2.5 Heterodyne Detection

The third-order nonlinear signal can be homodyne or heterodyne detected. In the former case, one measures the intensity of the signal field with a time- and/or frequency-integrating detector. The measured intensity equals the square of the electric signal field

$$I_{hom} = |E_s^{(3)}|^2. \quad (2.31)$$

A direct proportionality between the measured intensity and the signal field, an improved sensitivity and an improved signal to noise ratio can be achieved by heterodyne detection. In this scheme a new field denoted local oscillator (LO), which propagates in the same direction as the signal field, is overlapped with the latter [58]. The frequency-resolving detector then measures the square of the sum of the signal field and the LO field

$$\begin{aligned} I_{het}(\omega) &= |E_s^{(3)}(\omega) + E_{LO}(\omega)|^2 = |E_s^{(3)}(\omega)|^2 + |E_{LO}(\omega)|^2 + 2\text{Re}[E_{LO}^*(\omega)E_s^{(3)}(\omega)] \\ &= |E_s^{(3)}(\omega)|^2 + |E_{LO}(\omega)|^2 + |E_{LO}(\omega)||E_s^{(3)}(\omega)|\cos(\phi_s - \phi_{LO} + \omega_3\Delta t). \end{aligned} \quad (2.32)$$

Here, ϕ_s and ϕ_{LO} denote the phase of the signal and the local oscillator, respectively, and Δt indicates the time delay between the signal and the local oscillator. By Fourier transforming into time-domain and zeroing the components at zero delay, the two components $|E_s^{(3)}(\omega)|^2 + |E_{LO}(\omega)|^2$ are eliminated. The remaining term is linearly proportional to the signal field and allows for a complete characterization of the field's amplitude and phase.

I am among those who think that science has great beauty. A scientist in his laboratory is not only a technician: he is also a child placed before natural phenomena which impress him like a fairy tale.

Marie Curie (1867 - 1934)



EXPERIMENTAL DESIGN

3.1 Ultrashort Pulse Generation

Fig. 3.1 shows a schematic of the components of our experimental design. Verdi V-18 is a solid-state diode-pumped, frequency-doubled Nd:Vanadate (Nd:YVO₄, neodymium-doped yttrium orthovanadate) laser emitting 16 W of continuous wave light at 532 nm. The output of Verdi V-18 is split at a beamsplitter and used to pump Mira Seed (6 W) and RegA9050 (10 W).

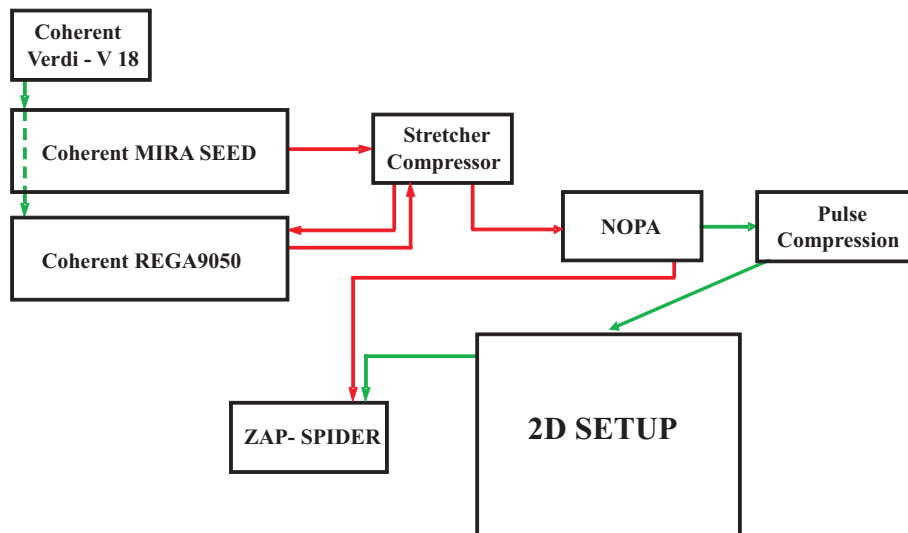


Figure 3.1: Schematic of the components of our experimental design. Pulse generation is accomplished by a regenerative titanium-sapphire amplifier system operating at a repetition rate of 200 kHz. Conversion into the visible spectral region is attained with a noncollinear optical parametric amplifier (NOPA). Second-order dispersion is eliminated with a sequence of fused-silica prisms, while chirped mirrors compensate for third-order dispersion. The pulse duration is determined with zero-additional phase (ZAP) SPIDER.

Mira Seed is a passively modelocked laser that uses Titanium:Sapphire as its gain medium [59]. The technique used to modelock Mira Seed is known as Kerr lens modelocking. The term optical Kerr effect describes the alteration of the index of refraction of a material by the electric field of light at sufficient high intensities. This change of refractive index reduces the beam diameter of short light pulses compared to a continuous wave beam. By placing a slit at an appropriate position within the laser cavity and adjusting its width, the pulse edges are cut and the pulse is shortened in time. Mira Seed is tunable from 780 to 840 nm, in our laboratory it has been optimized for operation at 800 nm. The pulse spectral width is 30 nm, the output power is 420 mW in mode-locked operation mode. With a repetition rate of 76 MHz, this corresponds to a pulse energy of 5.5 nJ. Mira Seed has a built-in prism-compressor, that reduces the pulse length to approx. 30 fs.

Since these pulses would be too intense if they were amplified directly, they are sent to a stretcher-compressor unit, where they are stretched to approximately 10 ps by a grating system [60, 61]. A regenerative amplifier (RegA9050) [62] is then used to amplify the pulses. RegA9050 is also pumped by part of the Verdi-V18 output, however, a Q-switch prevents it from lasing. When saturation in the Ti:Sapphire crystal, constituting the active medium, is reached, a single pulse from Mira Seed is injected by a cavity dumper (an acousto-optic modulator in case of RegA9050). This pulse propagates in the cavity and is amplified at each round trip. When the pulse has reached the maximum possible intensity, it is ejected by the same cavity dumper. Recompression is again achieved in the stretcher-compressor unit. At this stage the output is still centered at 800 nm, but now has a spectral width of 25 nm, a power of 1.05 mW, and a pulse length of 45 fs. The repetition rate is lowered to 200 kHz, and the pulse energy is $\approx 5 \mu\text{J}$.

Tunable pulses in the visible spectral region are attained by a noncollinear optical parametric amplifier (NOPA, Fig. 3.2) [63, 64, 65]. The 800 nm input from the amplifier is split at a 10:90 beamsplitter. 90 % of the energy are focused with a lens ($f = 200 \text{ mm}$) onto a $300 \mu\text{m}$ thick BBO crystal for second harmonic generation. The remaining 10 % are sent to a delay stage and are focused onto a 1 mm thick sapphire crystal to generate white light continuum. The second harmonic and the white light overlap on a 2 mm thick BBO crystal, where part of the white light is amplified in a parametric amplification process. The important advantage of NOPA compared to a collinear optical parametric amplifier (OPA) [66] is the improved compensation of group velocity dispersion that can be achieved due to the noncollinear geometry. Therefore shorter pulses can be obtained. In order to amplify a broader spectral region of the white light, the 400 nm pulses are stretched prior to the parametric amplification step. The NOPA output can be tuned in the region between 490 nm and 720 nm. At 600 nm the spectral width is 40 nm, the power reaches typically 45 mW (pulse energy 225 nJ), and the pulse length can be compressed to less than 20 fs.

Pulse compression in our experimental design is achieved in a two stage process (Fig. 3.3). In a first step dispersion is compensated by a variable number (≈ 24) of reflections off two Brewster-angled chirped mirrors [67, 68, 69]. The mirror coating consists of 58 alternating $\text{SiO}_2/\text{TiO}_2$ layers. TiO_2 has a high refractive index, SiO_2 has a low one, which, when a pulse with higher order chirp is reflected from the mirror, leads to compensation of higher order chirp. The second step is a conventional prism compression [70]. The pulse travels twice through two fused silica prisms.

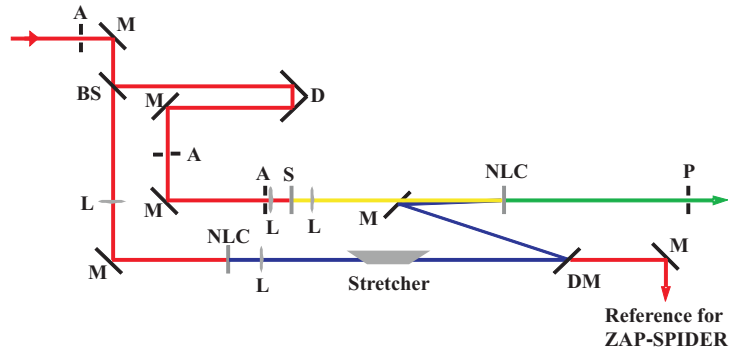


Figure 3.2: Schematic of the noncollinear optical parametric amplifier (NOPA) employed for tuning the pulses in the visible spectral region. A: aperture, M: mirror, BS: beamsplitter, L: lens, D: delay stage, NLC: nonlinear crystal, S: sapphire plate, DM: dichroic mirror, P: pinhole.

Different wavelength components thereby experience different indices of refraction and thus pass through different amounts of glass. By positioning the prisms at an appropriate distance, linear chirp can be eliminated. The distance between the two prisms has to be adjusted when changing the center wavelength of the pulse.

For full characterization of the pulses and to ensure the shortest possible pulse duration at the location of the experiment we apply zero-additional phase spectral phase interferometry for direct electric field reconstruction (ZAP-SPIDER) [71, 72]. To check the validity of our SPIDER traces we further record the frequency-resolved second-harmonic intensity autocorrelation (SHG-FROG) [73] by placing a 50 μm thick β -barium borate (BBO) crystal at the sample position.

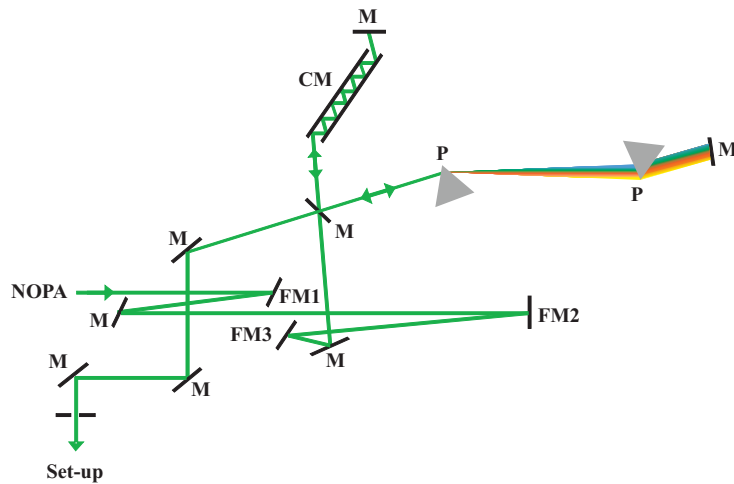


Figure 3.3: Pulse compression is achieved by a combination of chirped mirrors and a prism pair. FM: focusing mirror, M: mirror, CM: chirped mirror, P: prism. FM1 has a ROC of 100 cm, FM2 of 30 cm, and FM3 of 20 cm.

To reduce unwanted higher-order effects and non-resonant signals from the solvent and to prevent the sample from too fast photodegradation the input beam is attenuated by a neutral density filter after the NOPA to yield between 1 and 10 nJ of energy in each of the excitation pulses.

For recording the two-dimensional electronic spectra presented in this thesis two experimental designs have been employed. Our first approach closely followed the one pioneered by the groups of Fleming and Miller [10, 11, 74] (cf. Sec. 3.2). This experimental design is based on a transmission grating for creating two pairs of phase-stabilized pulses. It has a good phase-stability, but is limited to recording S_I and S_{II} spectra since not all time delays can be Fourier transformed without loss of phase information. In order to overcome this limitation we have built a compact setup that is easy to implement and align yet provides passive phase stability between all four pulses involved in the experiment (cf. Sec. 3.3). With this improved design single-quantum (S_I and S_{II}) as well as double-quantum (S_{III}) two-dimensional electronic spectra can be recorded.

3.2 Setup of the First Generation

Our first approach for recording 2D electronic spectra has been based on a diffractive-optics based setup following the experimental configuration reported in Ref. [11, 57, 74] (Fig. 3.4). A 50/50 beam splitter (BS) splits the pre-compressed (to compensate all dispersive elements of the setup) NOPA output into two beams of equal intensity, one of which can be delayed with respect to the other by a computer controlled delay stage to introduce delay t_2 with a resolution of 0.65 fs. Due to the phase stability requirements between pulses 1 and 2, and pulses 3 and LO, a diffractive optical element (DOE, 125 lines/mm), optimized for diffraction into \pm first order, is used to split the two beams focused onto it into four beams [11]. Pulse \mathbf{k}_2 and the local oscillator (LO) are diffracted downwards (dashed lines in Fig. 3.4) and \mathbf{k}_1 and \mathbf{k}_3 are diffracted upwards with respect to the initial beam-height. From this point on, all four beams are reflected from common mirrors to maintain the phase correlations [11, 74]. A spherical mirror (SM) after the transmission grating parallelizes the four beams which are arranged to form the four corners of a square. Pulse \mathbf{k}_2 passes through a pair of glass wedges (WP, thickness 0.9 mm, angle 2° , fused silica) that are oriented in an anti-parallel fashion [74] and mounted on a computer controlled delay stage. By moving one of the wedges the amount of glass in the beam path and therefore the delay of the pulse is changed without introducing lateral beam shifts. This configuration allows for precise delay movements (5.3 as, range ± 250 fs) without influencing the phase stability of the phase locked pulse pair or introducing phase distortions (Fig. 3.5). This arrangement is used to introduce delay t_1 .

Pulses \mathbf{k}_1 and \mathbf{k}_3 pass through equivalent but static wedge pairs to balance the dispersion. The LO does not pass through a wedge pair but is attenuated by a variable neutral density filter (ND) by four to five orders of magnitude and precedes all other pulses by about 550 fs to yield high contrast interferograms. All four beams are focused by a spherical mirror onto the sample to a common spot size of $\approx 200 \mu\text{m}$ to generate the nonlinear signal. Due to the square geometry of the excitation beams and the LO, the signal propagation direction is coincident with the propagation direction

3.2. SETUP OF THE FIRST GENERATION

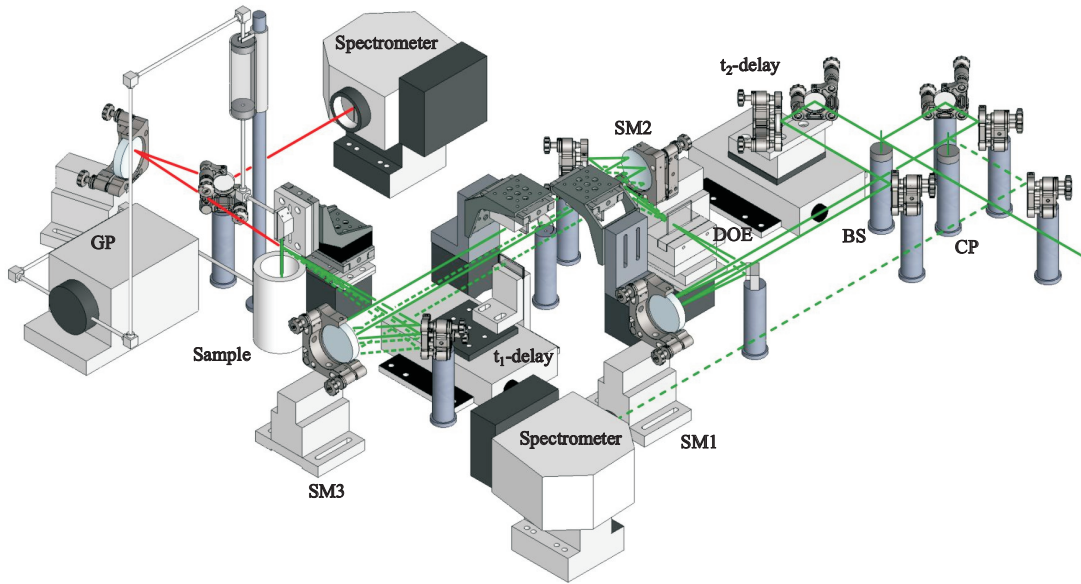


Figure 3.4: Scheme of the experimental setup of the first generation including the pump-probe extension. BS: beam splitter, CP: compensation plate, DOE: diffractive optical element, SM: spherical mirror, GP: gear pump.

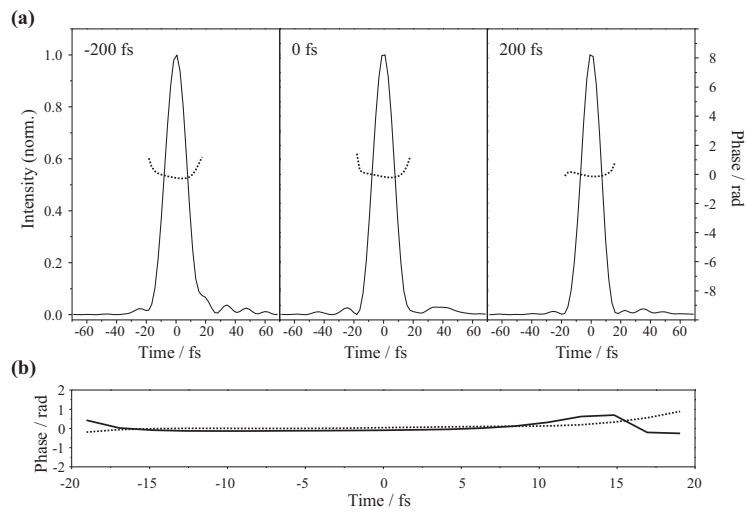


Figure 3.5: (a) ZAP-SPIDER traces for the three wedge positions of -200 fs (left), zero (middle), and +200 fs (right). In all three cases the pulses have a duration of 16 fs and a flat temporal phase. (b) The residuals of the phase differences for zero and -200 fs (dashed line), respectively zero and +200 fs (solid line).

of the LO allowing for heterodyne detection of the signal field with the LO. Data acquisition is accomplished by means of a thermoelectrical cooled spectrometer. A 2400 lines/mm grating in combination with a 1024 pixel photodiode array allows for a spectral resolution of $\approx 3.3 \text{ cm}^{-1}$ in ω_3 .

3.3 Setup of the Second Generation

In order to retain amplitude- and phase-information, the time delay which is Fourier transformed in the data evaluation procedure needs to be precisely set and kept stable. In the first realizations of 2D-ES (including our own work [cf. Sec. 3.2]) only pairs of pulses have been phase stable, imposing limitations to the time-delays that could be Fourier transformed without loss of phase information. With the use of a pulse shaper [75], by implementing active phase-stabilization [76], and uncoupling of time-delays [77] this limitation has been overcome resulting in greater

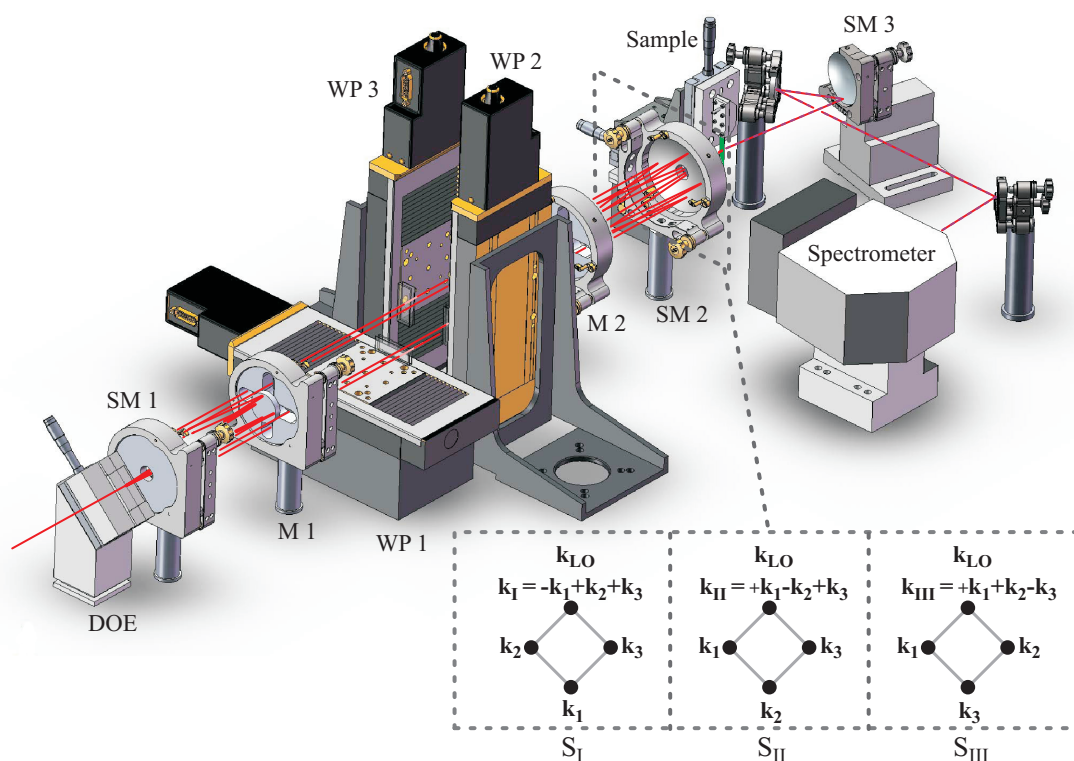


Figure 3.6: Experimental design for recording 1Q2D and 2Q2D electronic spectra. Four phase-stable pulses are generated by a diffractive optical element (DOE). Three of them can be individually delayed by pairs of glass wedges (WP1-3) mounted on computer controlled delay stages. SM: spherical mirror, M: plane mirror. An assignment of the four pulses in the three different methods is shown in the inset. Depending on the method, the labeling of the pulses differs and does not correspond to the labeling of the wedge pairs.

3.3. SETUP OF THE SECOND GENERATION

freedom in the design of experiments. In our laboratory, we have implemented a passively phase-stabilized setup based on a diffractive optical element to achieve the required phase-stability between the three excitation pulses and the local oscillator used for heterodyne detection [20, 78] (Fig. 3.6). With this versatile design pump-probe, homodyne and heterodyne transient grating, two- and three-pulse photon echo, and 1Q2D and 2Q2D electronic spectroscopy experiments can be performed. Since recording 1Q2D spectra and 2Q2D spectra requires different time-delays to be Fourier transformed, the diffractive optical element (DOE) consists of two transmission gratings with a groove spacing of $15\ \mu\text{m}$ that are both optimized for diffraction into \pm first order. By orienting these two gratings perpendicular to each other, four phase-stable pulses in a boxcar geometry are obtained [79]. The DOE is oriented at an angle of 45° with respect to the optical table so that the square formed by the four pulses is also tilted by 45° . The four pulses pass through a hole in the spherical mirror (SM1) and are reflected from a plane mirror (M1) back onto SM1. This arrangement allows to implement the spherical mirror under an angle of 0° which avoids chromatic aberration effects. SM1 parallelizes the four beams which pass by M1 on the top, bottom, right, and left side. Three pairs of glass wedges (WP1-3) mounted on computer controlled delay stages allow to introduce delays with a precision of ≈ 5 attoseconds in all three excitation pulses [74]. Two of these delay stages (WP2, WP3) are mounted on 90° angle brackets, i.e. perpendicular to the optical table, which ensures that no wedge clips another beam during movements. The maximum delay achievable with this configuration without introducing a notable amount of chirp is ± 800 fs as checked by a separate ZAP-SPIDER measurement (Fig. 3.7a). After the delay stages, an identical plane (M2) and spherical mirror (SM2) configuration focuses all four beams to a common spot size of $\approx 200\ \mu\text{m}$ in the sample.

The third-order nonlinear signal induced in the sample by the three excitation pulses propagates collinearly with the local oscillator pulse, which is attenuated by a neutral density filter (not plotted in Fig. 3.6) and passes through the sample ≈ 540 fs before the other pulses. This value is confirmed

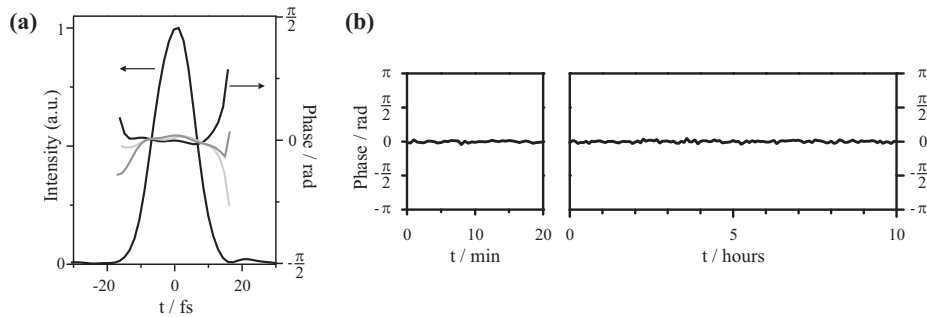


Figure 3.7: (a) Amplitude and temporal phase (black line) of an excitation pulse. The black, dark gray, and light gray lines show the temporal phase at optical path delays of 0 fs, +500 fs, and -500 fs, respectively. (b) Left panel: Short-time (20 min, which corresponds to the duration of a scan) phase stability with a value of $\lambda/90$. Right panel: Long-time phase stability of the setup which corresponds to $\lambda/40$.

by an interferometric measurement involving a $25\ \mu\text{m}$ pinhole (cf. Section 3.6). The signal and the LO are spatially filtered from the excitation pulses and are focused by SM3 onto the entrance slit of a spectrometer consisting of a grating as the dispersive element and a 1024 pixel photodiode array.

The phase-stability of our setup, which amounts to $\lambda/90$ in short term and $\lambda/40$ in long term measurements, is demonstrated in Fig. 3.7b. The measurement of the phase stability was performed as outlined in Ref. [77]. To obtain the phase stability values, the interference fringes, recorded in frequency domain, are analyzed via a complex Fourier transform. The components around zero delay are filtered out and the phase value φ of the remaining fast component and its behavior in time are plotted in Fig. 3.7b.

3.4 Sample Handling

In contrast to other experiments with typical repetition rates of 1 kHz, the high repetition rate of our laser system (200 kHz) strongly facilitates averaging and data acquisition, while the energy of a single pulse is still high enough for nonlinear frequency conversion and well sufficient to induce a third-order nonlinear response in molecular samples. However, the high repetition rate of our laser system also has some drawbacks. While we have not been able to observe any triplet accumulation effects in our samples, we nevertheless observe the formation of a signal in the window material of our flow cell. To eliminate this signal (which can be of the same order of magnitude as the desired third-order nonlinear signals) we have implemented a gravity driven, wire-guided drop jet [80, 81] for the circulation of the sample (Fig. 3.8). In this configuration a stainless steel wire, with a diameter of $300\ \mu\text{m}$, is bent to form an inverse "U" which is clamped between two stainless steel plates. The liquid enters through a hole in one of the plates and leaves

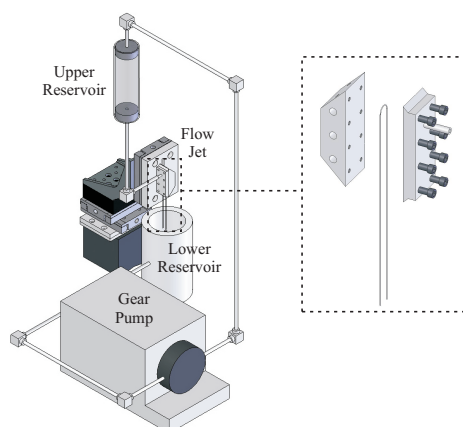


Figure 3.8: Schematic of the flow jet implemented for sample handling. The liquid is pumped by a gear pump from the lower to the upper reservoir, from where it flows between two wires back to the lower reservoir.

at the bottom between the two wires to form a thin film of approx. $200\ \mu\text{m}$ thickness. A gear pump is used to transfer the sample from the lower to the upper reservoir with a flow rate of $\approx 20\ \text{ml/min}$. This configuration has the advantage (i) to avoid signals from cell windows, (ii) obliterating the necessity to compensate the dispersion of the cell material, (iii) to avoid precipitation of the sample on the cell windows, and (iv) to generate a stable and pulsation free sample film. All vessels, tubes, and connectors are made of Teflon[®] to resist organic and corrosive solvents.

Due to the huge disparity in spatial dimensions, some of the samples discussed in this thesis tend to align along the flow direction in thin liquid films even at relatively low flow speeds. This point will be addressed further in the corresponding results chapters. If not indicated otherwise, the three excitation beams are polarized perpendicular to the flow of the jet.

3.5 Calibration Procedures

The points of zero delay between the excitation pulses (i.e. $t_1 = 0$, $t_2 = 0$) are determined by spectral interferometry on a daily basis. To this end a pinhole with a diameter of $25\ \mu\text{m}$ is placed at the sample position where all beams overlap. Two of the beams (1 and 2 for t_1 , 1 and 3 for

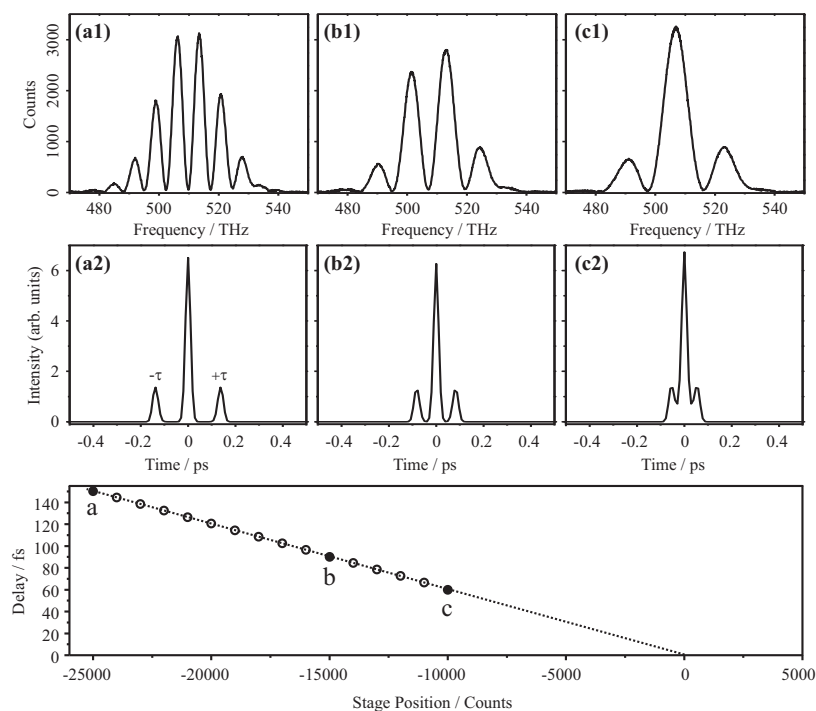


Figure 3.9: Determination of zero-points by spectral interferometry. Panels (a1), (b1), and (c1) show spectral interferograms for stage positions of -25000, -15000, and -10000 counts. Panels (a2), (b2), and (c2) are the corresponding Fourier transforms. The delay τ is plotted in the lowest panel as a function of motor position to extrapolate the zero-point. Values below $\pm 50\ \text{fs}$ are neglected due to the impossibility to resolve the three peaks at $t = 0, \pm\tau$.

t_2 -delay) pass the pinhole while the other two are blocked. Since the diameter of the pinhole is smaller than the focus of the beams (approx. $150 \mu\text{m}$), diffraction generates two collinear plane waves. By spectrally resolving these waves in a spectrometer, they show an interference pattern in which the number and distance of the fringes is a function of the delay-stage position. Fourier transform of these interferograms yields three peaks centered at $t = 0$ and $t = \pm\tau$, where τ is the temporal separation between the pulses. For pulse separations above/below ± 50 fs we plot the delay versus stage position and extrapolate for $\tau = 0$ to determine $t_1, t_2 = 0$. Fig. 3.9 illustrates this procedure in an exemplary manner, where the solid points in the lowest panel correspond to values of the interferograms and Fourier transforms for stage positions of -25000, -15000, and -10000 counts of the motor position (all other points in the lowest panel are measured points but not depicted explicitly).

Prior to each measurement series a calibration coefficient to convert the movement of the stage (in motor steps) into the actually introduced delay has to be determined for each stage separately. Accurate determination of this conversion factor is crucial in the evaluation procedure, since it influences the position of the peaks along the frequency axis obtained from Fourier transform of the scanned time delay (i.e. ω_1 in 1Q2D and ω_2 in 2Q2D spectroscopy). Determination of this calibration coefficient is achieved by selecting a frequency-cut in the frequency resolved interferograms obtained as described above (Fig. 3.10). The intensity of this cut oscillates in time-domain (respectively as a function of stage position) and subsequent Fourier transform of this waveform yields the inverse number of stage steps necessary for one full period at this frequency. Since the period for a given frequency is well known (e.g. 2 fs at 500 THz), the calibration coefficient is the product of the inverse number of steps times the period in femtoseconds. This procedure is repeated for a number of frequency cuts to calculate an average calibration coefficient. To control the validity of this calibration procedure we align the output of a He-Ne laser (with a precisely known frequency) through our setup and perform the same calibration routine.

The spectrometers are calibrated with Neon lamps which possess a spectrum consisting of several narrow lines with well defined wavelengths.

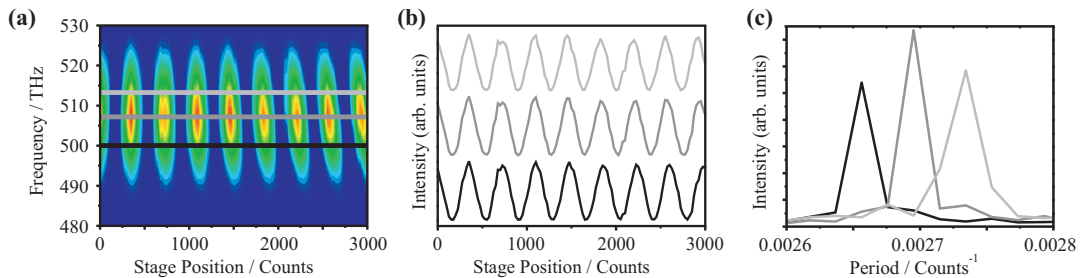


Figure 3.10: Calibration of the stages by spectral interferometry. (a) Frequency resolved scan with 3 frequency cuts at 500 (black), 507 (grey), and 513 THz (light-grey). Panel (b) shows the waveforms of the corresponding frequency cuts and (c) shows the FFT of these, which give the inverse number of counts for one period at the corresponding frequency.

3.6 Data Acquisition and Evaluation

The scanning procedure for recording 2D spectra differs for the two experimental designs. The following description refers to the setup of the second generation, as this design is more universal. Since the signal and the LO have to coincide spatially in all three methods discussed in this thesis, the assignment of the beams differs for S_I , S_{II} , and S_{III} as illustrated in Fig. 3.6 and does not correspond to the labeling of the wedge pairs. The beam interacting with the negative sign is thereby opposite to the LO in all three cases (i.e. \mathbf{k}_1 in S_I , \mathbf{k}_2 in S_{II} , and \mathbf{k}_3 in S_{III} , respectively).

To obtain purely absorptive real parts and purely dispersive imaginary parts in 1Q2D electronic spectra, rephasing (S_I) and non-rephasing (S_{II}) signal parts have to be equally weighted [18, 19]. For collecting S_I -spectra, t_1 (i.e. the delay between the first two excitation pulses) is scanned from 0 to usually 100 or 200 fs in steps of 0.5 fs by moving WP1. S_{II} -spectra are recorded by scanning WP3 and thereby delaying \mathbf{k}_1 from 0 to 100 fs. The delay between the second and third excitation pulse (t_2) is fixed to a certain value before each scan by moving WP2. For recording 2Q2D electronic spectra, pulses 1 and 2 are scanned simultaneously from 0 to -100 fs in steps of 0.25 fs by moving WP2 and WP3 for a fixed value of t_1 . The step-size of 0.5 fs for 1Q2D spectra and 0.25 fs for 2Q2D spectra, respectively, is sufficient for fulfilling the Nyquist sampling criterion. The Nyquist sampling criterion requires that a time-dependent function in which the highest contributing frequency is at x Hz needs to be sampled with a resolution better than $\frac{1}{2x}$ s (in case one is not operating in the rotating frame [79]). For 1Q2D spectra, this implies that the step-size must be no larger than ≈ 0.8 fs, whereas for 2Q2D spectra the step-size should be smaller than 0.4 fs. Decreasing the step-size further does not improve the data quality [82]. This is illustrated in Fig. 3.11 where we plot the phase of the S_{III} -signal of Rhodamine 6G as a function of t_2 for step-sizes of 0.25 fs and 0.1 fs evaluated in the peak maximum (18900 cm^{-1}).

Prior to each scan, the scattering contribution of pulse 3 into the direction of \mathbf{k}_s is recorded

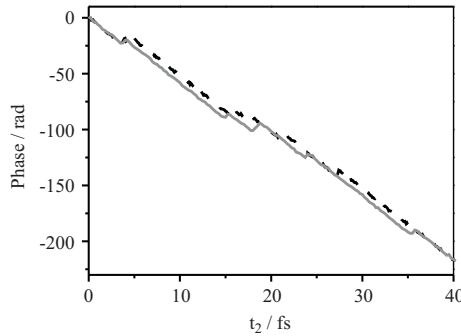


Figure 3.11: Comparison of the phase of the third-order nonlinear signal of Rhodamine 6G detected in the phase-matched direction $+\mathbf{k}_1 + \mathbf{k}_2 - \mathbf{k}_3$ as a function of t_2 for stepsizes of 0.1 fs (dashed line) and 0.25 fs (solid line) evaluated at 18900 cm^{-1} .

by blocking pulses 1 and 2. This contribution has to be recorded and subtracted only once since the delay between pulse 3 and the LO does not change in the course of one scan. The scattering contribution of pulses 1 and 2 on the other hand, is recorded and subtracted from the spectral interferogram for each measuring point by blocking pulse 3 with an automated shutter.

Data evaluation follows the procedure outlined in Ref. [10] and [83]. In a first step, the spectral amplitude and phase of the signal field is extracted from the heterodyned signal by Fourier transform, filtering of the signal components at zero and negative delays, back Fourier transform, and division by the local oscillator spectrum. In a second step, the dataset is Fourier transformed along t_1 to yield the frequency axis ω_1 in case of 1Q2D electronic spectroscopy or along t_2 to yield the frequency axis ω_2 in case of 2Q2D electronic spectroscopy.

Finally, the absolute phase of the complex valued spectrum has to be determined. For 1Q2D spectra this can be done by applying the projection slice theorem, which states that the projection of the 1Q2D signal onto ω_3 equals the spectrally resolved pump-probe spectrum recorded for the same delay t_2 [17]. The pump-probe spectrum is given by

$$S_{PP}(t_2, \omega) = \left(\frac{I_{pr}^{pu}(\omega)}{I_{ref}^{pu}(\omega)} - \frac{I_{pr}^0(\omega)}{I_{ref}^0(\omega)} \right) \frac{I_{ref}^{pu}(\omega) + I_{ref}^0(\omega)}{2\sqrt{I_{pr}^0(\omega)}}, \quad (3.1)$$

where I_{pr}^{pu} and I_{pr}^0 denote the intensities if the probe beam with and without the action of the pump beam, respectively. I_{ref}^{pu} and I_{ref}^0 are the corresponding intensities of the reference beam which is used to eliminate intensity fluctuations of the laser. Since the pump-probe signal is invariant to constant phase shifts of either the pump or the probe beam, the absolute phase can be determined in a procedure termed phasing. In this procedure the phase and delay between the signal and the LO that minimizes the difference between the projection of the 1Q2D spectrum and the spectrally resolved pump-probe signal is searched for.

Determining the absolute phase of 2Q2D spectra requires a different approach since no straightforward connection exists between the 2Q2D signal and an auxiliary measurement such as pump-probe spectroscopy. This is immediately obvious from inspection of the relevant Feynman diagrams (Fig. 2.1) for the different techniques. Bristow *et al.* therefore demonstrated an all-optical method, which is a combination of spatial interference patterns and spectral interferometry, for the retrieval of the absolute phase [84]. Backus *et al.* reported on a spectral interferometry based method in the IR spectral region for obtaining the desired value [85]. Moran *et al.* [86] determine the LO-delay by assuming that the heterodyne transient grating signal from the pure solvent has dispersive properties only. With this method however more than one value can be found that minimizes the contribution from the real part. We adopt a different approach which relies on the high phase stability of our setup [78]. Immediately before or after recording a 2Q2D spectrum we measure a 1Q2D spectrum and determine its absolute phase by phasing with a pump-probe spectrum. This value of the absolute phase and delay between the signal and LO is then applied to phase the 2Q2D spectrum (Fig. 3.12).

When applying this procedure care has to be taken in determining the precise delay between

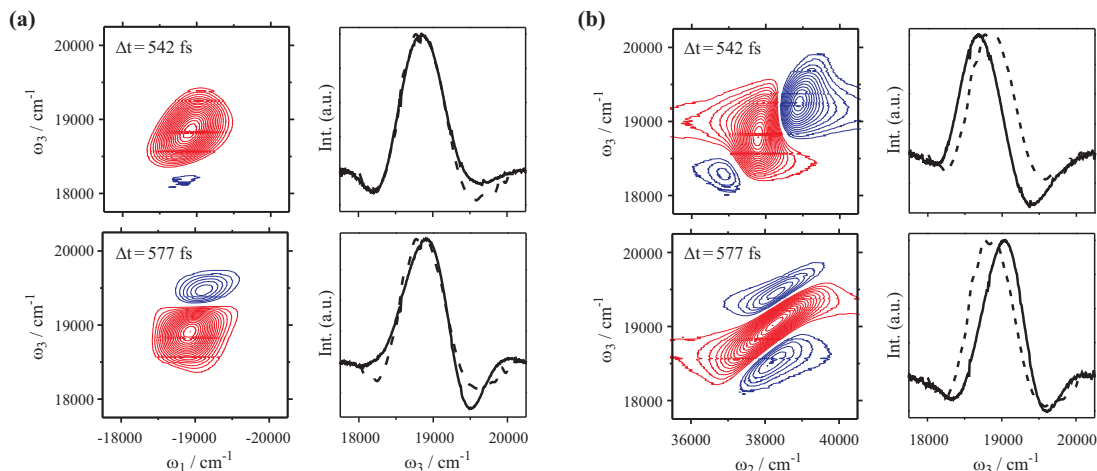


Figure 3.12: Illustration of error sources in the determination of the absolute phase of 1Q2D spectra (a) and 2Q2D spectra (b). The real part of the 1Q2D spectrum (a) and 2Q2D spectrum (b) is shown on the left, their projections onto ω_3 (solid) together with a spectrally resolved pump-probe spectrum (dashed) on the right. The upper panels show the spectra for $\Delta t = 542$ fs, which is the correct value also obtained via spectral interferometry. Phasing with a value of $\Delta t = 577$ fs is depicted in the lower panel.

the signal and the local oscillator. Two values can be found that yield a reasonable agreement between the projection of the 1Q2D spectrum and the pump-probe signal (Fig 3.12a). In case it is not obvious immediately from the inspection of the 1Q2D spectrum which value is the correct one, the delay can be determined with femtosecond precision by Fourier transforming a spectral interferogram and then fine-tuning this value by the phasing procedure outlined above. Taking the incorrect value for the delay between the signal and the LO for phasing the 2Q2D dataset has a huge impact on the spectrum (see Fig. 3.12b, bottom). The real part of the 2Q2D spectrum retains its three-peak structure, however, the nodal line changes its orientation from parallel to the anti-diagonal (as expected from a non-rephasing technique) to parallel to the diagonal line. The latter spectrum would be tempting for interpretation for two reasons: first, all peaks appear at the same frequency along ω_2 as ideally expected from the two Feynman diagrams contributing to the response (the system evolves in the same $|f\rangle\langle g|$ -coherence in both pathways). Second, one could think of extracting the shift of the double-excited state energy from twice the energy of the single-excited state directly from the frequency difference of the positive and negative peaks along ω_3 . However, the delay between the signal and the LO deviates from the one determined by spectral interferometry by ≈ 35 fs in this case, which is well outside experimental errors. Furthermore, theory supports the notion of the anti-diagonal orientation of the 2Q2D spectrum as depicted in the top panel of Fig. 3.12b (cf. Chapter 7).

*In science one tries to tell people, in such
a way as to be understood by everyone,
something that no one ever knew before.
But in poetry, it's the exact opposite.*

Paul Dirac (1902 - 1984)



In this chapter the effect of electron-phonon coupling in two-dimensional Fourier transformed electronic spectroscopy is investigated. We present a series of one- and two-dimensional nonlinear spectroscopic techniques for studying a dye molecule in solution. Ultrafast laser pulse excitation of an electronic transition coupled to vibrational modes induces a propagating vibrational wave packet that manifests itself in oscillating signal intensities and line-shapes. For the two-dimensional electronic spectra we can attribute the observed modulations to periodic enhancement and decrement of the relative amplitudes of rephasing and non-rephasing contributions to the total response. Different metrics of the two-dimensional signals are shown to relate to the frequency-frequency correlation function which provides the connection between experimentally accessible observations and the underlying microscopic molecular dynamics. The effects are reproduced well by simulations based on a Brownian oscillator model.

This chapter is based on

- A. NEMETH, F. MILOTA, T. MANČAL, V. LUKEŠ, H. F. KAUFFMANN, AND J. SPERLING. Vibronic modulation of lineshapes in two-dimensional electronic spectra. *Chem. Phys. Lett.* **459**, 94 (2008)
- A. NEMETH, F. MILOTA, T. MANČAL, V. LUKEŠ, J. HAUER, H. F. KAUFFMANN, AND J. SPERLING. Vibrational wave packet induced oscillations in two-dimensional electronic spectra. I. Experiments. *J. Chem. Phys.* **132**, 184514 (2010)
- T. MANČAL, A. NEMETH, F. MILOTA, V. LUKEŠ, H. F. KAUFFMANN, AND J. SPERLING. Vibrational wave packet induced oscillations in two-dimensional electronic spectra. II. Theory. *J. Chem. Phys.* **132**, 184515 (2010)

4.1 Introduction

Coherent wave packet generation in the manifolds of molecular excited states takes place if the excitation pulses are spectrally broad enough to coherently excite a number of vibrational or electronic levels. Femtosecond (fs) laser pulses meet this criterion in a number of molecular systems and experiments employing such pulses often show signatures of wave packet motion. Modulations of signal intensities induced by vibrational wave packet motion have been observed in a number of nonlinear spectroscopic experiments, including pump-probe [87, 88, 89], transient grating [90], and a variety of photon-echo spectroscopies [90, 91, 92, 93, 94]. A number of theoretical investigations supported the conclusions drawn in these experiments [95, 96, 97, 98, 99]. The influence of intramolecular vibrations should be expected consequently also in two-dimensional electronic spectroscopy which is based on the correlation of electronic coherences evolving during two time periods.

Recent theoretical works on model dimer [41, 44] and trimer [100] systems, and experimental investigations on excitonic complexes [42, 101] and conjugated polymers [102] reported on signatures of electronic wave packets in 1Q2D electronic spectra resulting from coherent excitation of several electronic levels. Possible enhancement of the energy transfer efficiency in photosynthetic light harvesting complexes, due to the presence of excitonic wave packets, was suggested by Engel *et al.* [42]. An assignment of the observed spectral modulations to an excitonic wave packet motion was made, based on a good agreement of the experiment with the predictions of an excitonic model [42, 44]. In the general case, however, contributions of vibrational wave packet motion cannot be excluded and it is therefore of high importance to study the vibrational case separately.

To study the effect of vibrational coherence without perturbations from additional electronic levels, a two-level system is preferential. Quantum-chemistry calculations (cf. Section 4.2) indicate that N,N'-bis(2,6-dimethylphenyl)perylene-3,4,9,10-tetracarboxylicdiimide (PERY), when excited at 20000 cm^{-1} , can be approximated as a two-level electronic system with a number of vibrational modes coupled to the electronic transition [103]. In the linear absorption spectrum of PERY in solution four well resolved vibrational peaks with a frequency separation of $\approx 1400\text{ cm}^{-1}$ can be discerned (Fig. 4.1a). In contrast to a recent work by Tekavec *et al.* [34], in which white light pulses were used to probe the vibronic dynamics, this progression can not be covered with the bandwidth of our laser pulses (900 cm^{-1}). However, by tuning the central excitation energy approximately to the center of the lowest energy peak, nonlinear spectroscopic signals such as transient grating (TG) and three-pulse photon echo peak shift (3PEPS) have been shown to be modulated by a low frequency (140 cm^{-1}) vibrational mode [103]. The associated beating period of 240 fs allows to compare 2D spectra at well-separated maxima, minima, rising and trailing edges of the oscillating nonlinear signal, which minimizes obstructions due to the finite temporal resolution in the experiment.

In this chapter we investigate experimentally and theoretically how coherent excitation of several vibrational levels influences 1Q2D electronic correlation and relaxation spectra. To this end 1Q2D electronic spectra of PERY have been recorded for 20 waiting times t_2 ranging from 0 to

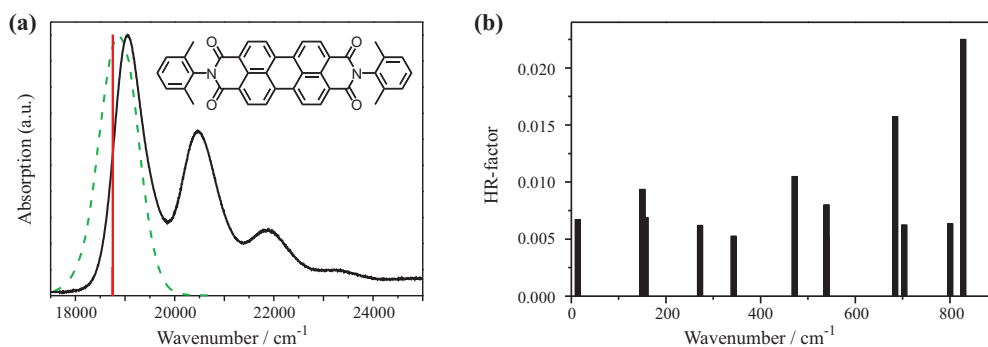


Figure 4.1: (a) Linear absorption spectrum of PERY in toluene (black solid line) and spectrum of the excitation pulses (green dashed line). The red line indicates the position of the lowest energy transition obtained from ZINDO/S calculations. The inset shows the chemical structure of PERY. (b) Huang-Rhys factors determined from semiempirical AM1 calculations. Only modes that possess Huang-Rhys factors larger than 0.005 are plotted.

800 fs covering several periods of pronounced vibrational modulations of the spectra. We show that this low frequency mode induces a periodic change in the ellipticity of the real (absorptive) part and in the slope of the nodal line separating the positive and negative contribution of the imaginary (dispersive) part [38]. Building up on these qualitative observations, we assign these modulations to periodic enhancement and decrement of the rephasing (S_I) and non-rephasing (S_{II}) signal parts and establish connections to the frequency-frequency correlation function $M(t)$.

For the theoretical description of nonlinear spectroscopic signals of simple few electronic level systems with negligible relaxation between the levels, the nonlinear response functions derived in the second order cumulant approximation (see e.g. [4]) provide a framework of unprecedented utility. The nonlinear optical response of such a system can be expressed in terms of line-broadening functions, which are related to the electronic energy gap correlation function (cf. Section 2.3) [4]. Few electronic level systems provide models which enable to disentangle the content of experimental data otherwise difficult to interpret. For example, three pulse photon echo peakshift was identified by Cho *et al.* [104] to reveal the energy gap correlation function. Two-color photon echo peakshift has been found to measure excitonic coupling in a dimer [105] or differences between energy gap correlation functions of two chromophores [106]. Basic 2D spectral line-shapes were classified by Tokmakoff [24] based on a two-level system, and finally, the relation between the nonlinear spectroscopic signals and the normalized energy gap correlation function was studied by de Boeij *et al.* [94] and for 1Q2D spectra by Lazonder *et al.* [107], to name but a few examples.

In some of these works, insightful information was obtained by expanding the line-shape functions (or energy gap correlation functions) in terms of a suitable parameter, e.g. the time delay between two interactions. In this study, we follow the same general approach and expand the line-shape correlation functions (describing the interaction of an electronic transition with an intra-

molecular vibrational mode) in terms of another suitable parameter, the Huang-Rhys factor λ/ω . Here, λ is the reorganization energy and ω the frequency of the mode. The applicability of a low order expansion of the response functions in terms of the Huang-Rhys factor to the description of the 2D experiment is obviously system-dependent but for the dye molecule studied here the results of the theory presented are confirmed by a full response function simulation of the 1Q2D spectra [38].

4.2 Quantum-Chemical Calculations

This section characterizes PERY theoretically and spectroscopically with respect to its two-dimensional π -conjugation by means of quantum-chemical calculations. The electronic ground state geometry of PERY has been optimized using Density Functional Theory (DFT) [108] based on the Becke's three parameter hybrid functional using the Lee, Yang and Parr correlation functional (B3LYP) [109]. The polarized split-valence SV(P) basis set [110] has been used. The obtained optimal structures have been checked by normal mode analysis (no imaginary frequencies for all optimal geometries). Based on the optimized geometry, the vertical transition energies and oscillator strengths between the initial and final states have been calculated using the Configuration Interaction Singles (CIS) method [111] based on the semiempirical ZINDO/S (Zerner's Intermediate Neglect of Differential Overlap) Hamiltonian [112]. For the ZINDO/S calculations, the single excitations from the 10 highest occupied to the 10 lowest unoccupied molecular orbitals have been considered. The DFT calculations have been done using the Turbomole 5.7 package [113] and the optical transitions have been computed using the Argus Lab software [114]. The evaluated theoretical values are used for the interpretation of experimental spectroscopic measurements.

The optimal geometry of D_2 symmetry exhibits a planar central part (Fig. 4.2a). The orientation of the lateral aromatic rings and the core skeleton is nearly perpendicular (dihedral angles of 81.2°) causing a negligible π -conjugation between these molecular fragments. The lateral rings are sterically hindered due to the presence of methyl groups in ortho-position. The opposite mutual arrangement of the neighboring lateral rings is not parallel as can be perceived from the right part of Fig. 4.2a.

The photophysical properties of PERY are primarily determined by the planar geometry of the central part and the related size of the π -conjugation. The experimental absorption spectrum of PERY in toluene (Fig. 4.1a) can be characterized by an intense absorption band with four peaks which are detected in the spectral range of 18000 to 24000 cm^{-1} . The equidistant energy difference (1400 cm^{-1}) between the four peaks indicates a harmonic character of the vibrational progression. The calculated vertical ZINDO/S excitation energies and the oscillator strengths are in good agreement with the experimental absorption spectrum. The ZINDO/S method was parametrized for spectroscopic properties of the π -conjugated aromatic systems and gives transition energies of 18725 cm^{-1} with an oscillator strength $f=1.7814$, 28631 cm^{-1} ($f=0.0001$), 31929 cm^{-1} ($f=0.0002$), and 34536 cm^{-1} ($f=0.8228$). The lowest energy transition is depicted as red line in Fig. 4.1a. The absence of other intensive electronic transitions in the region between 18000 and

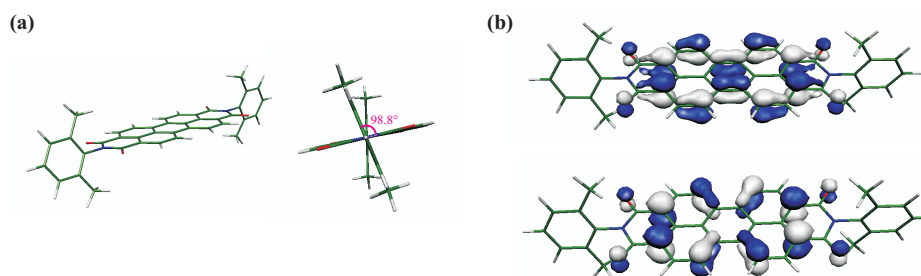


Figure 4.2: (a) Side and front views on the B3LYP/SV(P) optimal structure of PERY in the electronic ground state. (b) Visualization of the HOMO (bottom) and LUMO (top) obtained from ZINDO/S//B3LYP/SV(P) calculations.

24000 cm^{-1} indicates the vibronic origin of the progression observed in the experimental absorption spectrum. Therefore, the first and most intensive peak in the experimental record can be attributed to the $0 \rightarrow 0$ vibronic transition. In this context it is useful to examine the ZINDO/S HOMO and LUMO of the molecule. The HOMO-LUMO excitation plays a dominant role in this energetically lowest optical transition according to the frontier molecular orbital theory, with its contribution being more than 30%. These selected ZINDO/S orbitals are visualized in Fig. 4.2b, demonstrating that both orbitals are delocalized over the center of the core part only. The lobes of the LUMO are oriented more or less perpendicular to the lobes of the HOMO. The shape of the LUMO compared to those of the HOMO indicates that the optical excitation is spread from the central atoms of the core towards the nitrogen atoms.

In order to determine the origin of the vibronic motion reflected in the linear and nonlinear spectroscopic experiments, vibrational line spectra have been calculated. For determining the Huang-Rhys factors semiempirical AM1 calculations were performed using the Mopac program package 2002 [115]. The calculated vibrational spectrum possesses 210 fundamentals between 13 and 3243 cm^{-1} . With the limited bandwidth of our excitation pulses we can only cover modes up to frequencies of approximately 900 cm^{-1} . From Fig. 4.1b, in which modes with a Huang-Rhys factor larger than 0.005 are plotted, it becomes obvious that only a few modes contribute significantly to the observed spectroscopic response.

4.3 Experimental Details

PERY has been purchased from Sigma-Aldrich and used without further purification. Solutions with a concentration of $3 \cdot 10^{-4}$ M have been prepared by dissolving PERY in toluene (spectrophotometric grade, Merck), sonication for ≈ 10 minutes, and filtration to remove undissolved residues. The central excitation energy of our pulses was set to 18800 cm^{-1} (FWHM 920 cm^{-1} , pulse duration 16 fs) and the pulses were attenuated to 10 nJ per pulse at the sample position. For recording 1Q2D electronic spectra, t_2 has been fixed at a certain value and t_1 has been scanned over ± 100 fs with a step size of 0.65 fs to fulfill the Nyquist sampling criterion for this frequency regime. The

experimental 1Q2D spectra have a frequency resolution of 26 cm^{-1} for ω_1 , respectively 3.3 cm^{-1} for ω_3 .

4.4 Results and Discussion

4.4.1 Two-Dimensional Electronic Spectra

Complex signals can be represented either by their real and imaginary parts or by their amplitude and phase. These two representation schemes are displayed for PERY in Figs. 4.3 and 4.4 for t_2 -times of 100, 200, 300, 450, 550, 650, and 800 fs. The real part of a 1Q2D spectrum (first column in Fig. 4.3a) is the product of absorptive line-shapes in ω_1 and in ω_3 . In agreement with approximating PERY as a two-level electronic system, where ground state bleaching and stimulated emission are the only two contributions, it shows a single positive feature. The maximum of the peak is centered slightly below the diagonal ($|\omega_1| > \omega_3$), indicative of a small Stokes shift. The peak experiences periodic modulations in its shape with a period of 240 fs (a detailed analysis is presented in Fig. 4.5). For t_2 -times of 200, 450, and 650 fs, the shape of the absorptive peak is strongly elliptical with the major axis of the ellipse oriented along the diagonal. Contrarily, for $t_2 = 100, 300, 550$, and 800 fs the absorptive peak adopts a more circular shape and the major axis is oriented nearly parallel to the ω_3 -axis. The changes in the ellipticity of the real part can be quantified by determining the diagonal and anti-diagonal widths at a $1/e$ peak-height [42]. As seen by comparing Fig. 4.5a and b, the diagonal widths generally exceed the anti-diagonal ones, and show only a weak dependence on the t_2 -delay. In contrast, the anti-diagonal peak widths are sharply decreased at t_2 -delays of 200, 450, and 650 fs. This counter-evolution is mainly responsible for the strong modulation of the peak shape in the real part of the 1Q2D signal.

The imaginary part of a 1Q2D spectrum is the product of an absorptive line-shape in ω_1 and a dispersive line-shape in ω_3 . In case of a two-level system the imaginary part features two contributions of opposite sign (first column in Fig. 4.3b). Similar to the real part, the imaginary part too exhibits oscillations with a period of 240 fs. The most obvious oscillation is seen in the nodal line separating the positive and negative feature. The angle of this nodal line with respect to the ω_1 -axis changes from being positive for $t_2 = 200, 450$, and 650 fs, to zero or even negative values for $t_2 = 100, 300, 550$, and 800 fs (cf. Fig. 4.5 for a detailed evaluation). In addition to this oscillation of the nodal line, the width of both contributions periodically changes from being narrow for $t_2 = 200, 450$, and 650 fs, to being broad for $t_2 = 100, 300, 550$, and 800 fs.

In Fig. 4.4 we show amplitude and phase representations of the 1Q2D spectra of PERY for t_2 -delays of 100, 200, 300, 450, 550, 650, and 800 fs. The amplitude spectra (first column in Fig. 4.4a) resemble the real part spectra shown in Fig. 4.3a, with a single feature centered slightly below the diagonal. Similar to the real part spectra this positive peak features oscillations in its orientation and shape. For $t_2 = 200, 450$, and 650 fs the peak shape is highly elliptical and its major axis is oriented along the diagonal. For $t_2 = 100, 300, 550$, and 800 fs the peak acquires a more circular shape and is oriented nearly parallel to the ω_3 -axis.

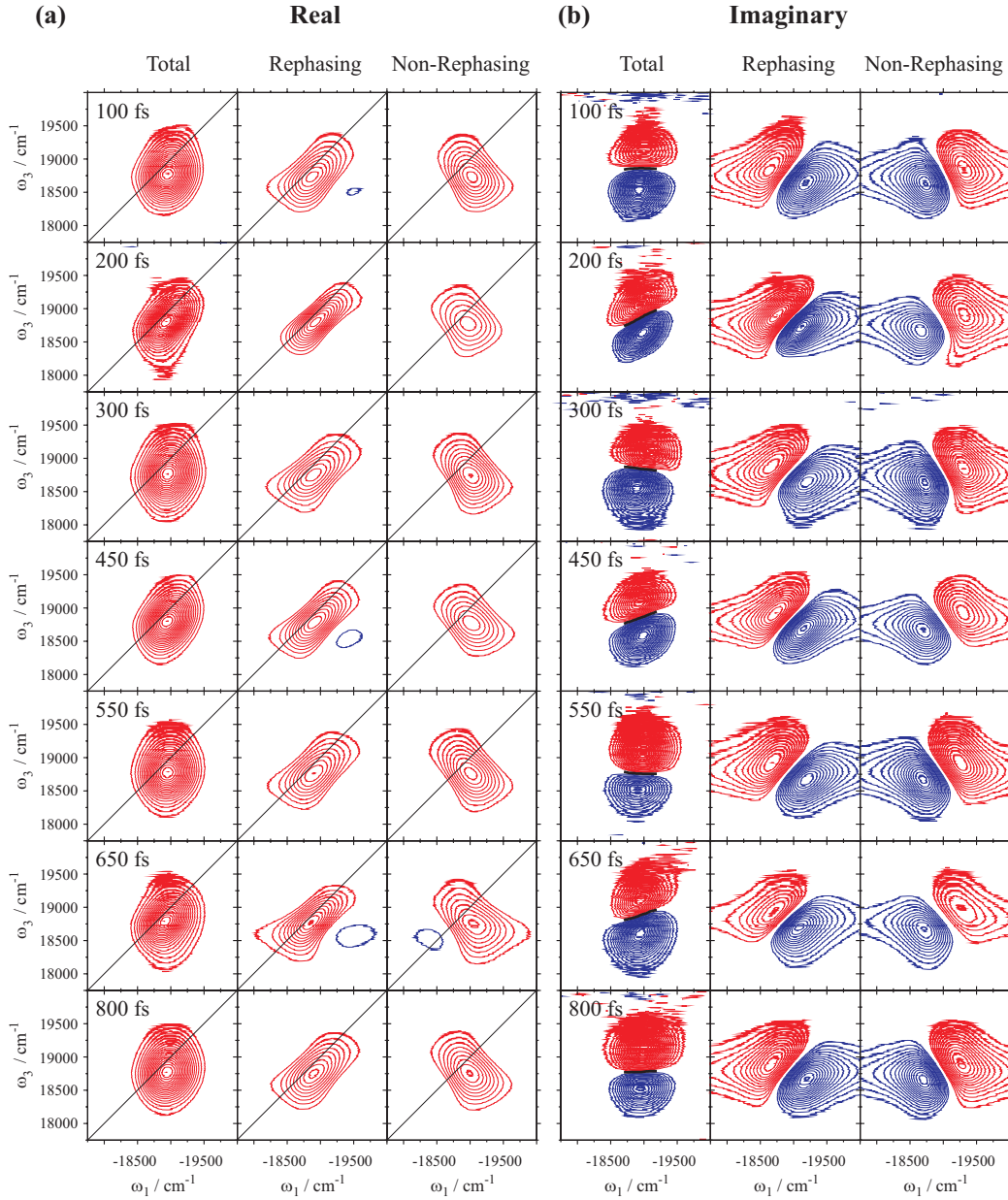


Figure 4.3: (a) Real and (b) imaginary part of the 1Q2D spectra of PERY in toluene for t_2 -delays of 100, 200, 300, 450, 550, 650, and 800 fs. The first, second, and third column of each panel display the corresponding total signal ($S_I + S_{II}$), the rephasing (S_I), and the non-rephasing (S_{II}) part, respectively. All total spectra are normalized to their absolute maximum value, whereas the rephasing and non-rephasing parts are plotted with their respective contribution to the total signal. Contour lines are drawn at 5% intervals starting at $\pm 10\%$. Red lines indicate positive signals, blue lines negative ones. The solid line in the real part indicates the diagonal, whereas the black lines in the imaginary part are drawn at the zero crossings between the positive and negative features.

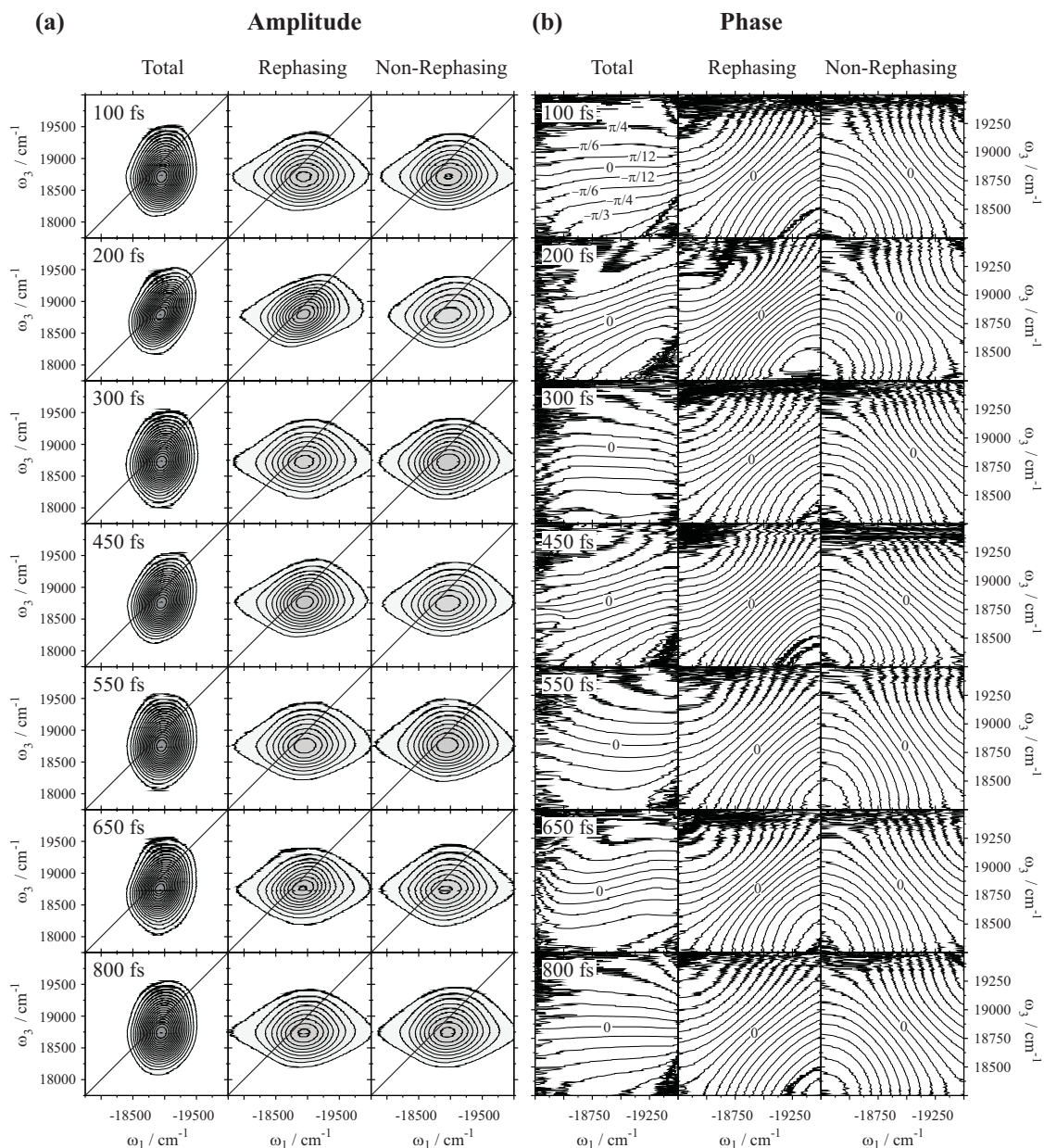


Figure 4.4: (a) Amplitude and (b) phase representation of the 1Q2D spectra of PERY in toluene recorded at t_2 -delays of 100, 200, 300, 450, 550, 650, and 800 fs. The first, second, and third column of each panel display the corresponding total signal ($S_I + S_{II}$), the rephasing (S_I) and the non-rephasing (S_{II}) part, respectively. The amplitude part total spectra are normalized to their absolute maximum value, whereas the rephasing and non-rephasing parts are plotted with their respective contribution to the total signal. Contour lines are drawn at 5% intervals starting at $\pm 10\%$ in the amplitude part spectra and at $\pm \frac{\pi}{12}$ intervals in the phase spectra. The zero-phase line is indicated in each phase spectrum. Note the different spectral range in the representation of the phase spectra.

In the phase spectra (first column in Fig. 4.4b) the lines of constant phase exhibit oscillations in their orientation. For $t_2 = 200, 450,$ and 650 fs the lines of constant phase are oriented along the diagonal, whereas they turn to become horizontal at $t_2 = 100, 300, 550,$ and 800 fs. Note that the phase spectra are shown for a narrower range than the real, imaginary, and amplitude part spectra. All the observed line-shape modulations will be assigned below to periodic modulations in the strength of the rephasing (S_I) and non-rephasing (S_{II}) contributions to the total ($S_I + S_{II}$) signal.

4.4.2 Rephasing and Non-Rephasing Signal Parts

The third-order nonlinear polarization $P^{(3)}(t_1, t_2, t_3)$, which underlies all FWM signals, can be expressed as a convolution of the appropriate response functions $R_i(t_1, t_2, t_3)$ with the electric fields of the excitation pulses (cf. Eq. (2.13)) [4]. Since PERY can be approximated as a two-level system when excited at $20\,000\text{ cm}^{-1}$, only four Feynman diagrams graphically illustrating four response functions within the rotating wave approximation contribute to the signal (cf. Fig. 2.1). The four Feynman-diagrams can be classified as ground state bleaching (GSB) and stimulated emission (SE), depending on whether the system evolves in the ground state (R_3, R_4) or in the excited state (R_1, R_2) during t_2 , respectively. A different classification of the four diagrams arises from the ordering of the first two interactions. In diagrams R_2 and R_3 the first interaction takes place with pulse $-\mathbf{k}_1$, whereas in diagrams R_1 and R_4 the first interaction takes place with positive sign ($+\mathbf{k}_1$). As a consequence the system evolves in conjugate frequencies during t_1 (ω_{ge}) and t_3 (ω_{eg}) in diagrams R_2 and R_3 . This allows for rephasing in an inhomogeneously broadened ensemble, resulting in the formation of an "echo" in case the system has kept some memory of its transition frequency over t_2 . These diagrams therefore contribute to the rephasing signal part. In contrast, the system evolves with the same frequency during t_1 and t_3 (ω_{eg}) in diagrams R_1 and R_4 . These two diagrams are denoted non-rephasing and the systems's response is close to a free induction decay. In addition to these four diagrams there are diagrams that contribute to the signal only if the pulse separation is shorter than the pulse duration, i.e. when the excitation pulses overlap. These diagrams will not be taken into account in this discussion.

Scanning t_1 over positive and negative values equally weights rephasing and non-rephasing 1Q2D pathways. This scanning procedure has been shown to produce purely absorptive real parts and purely dispersive imaginary parts, that are linked via the Kramers-Kronig relation [18, 19]. The rephasing and non-rephasing 1Q2D spectra on their own exhibit phase-twisted line-shapes resulting from mixing of dispersive and absorptive features. The dissection of the total 1Q2D spectrum into its corresponding rephasing and non-rephasing parts is shown in the second and third row of Figs. 4.3 and 4.4 for the real part, imaginary part, amplitude, and phase, respectively. The decomposition was performed by recording the full scan and evaluating only positive t_1 -values for the rephasing part and only negative t_1 -values for the non-rephasing part [116]. Strictly speaking, rephasing signals show up at $\{-\omega_1, +\omega_3\}$ according to the conjugate frequency evolution during t_1 and t_3 . Non-rephasing signals on the other hand appear at $\{+\omega_1, +\omega_3\}$, since the system evolves with the same frequency during t_1 and t_3 . However, to facilitate comparison of the rephasing,

non-rephasing, and total 1Q2D spectra, we plot all signals along $\{-\omega_1, +\omega_3\}$ [117, 118].

From the inspection of Fig. 4.3a, one can immediately see that both rephasing and non-rephasing parts of the real part 1Q2D spectra are of a pronounced elliptical shape. However, the major axis of the ellipse in case of the rephasing part is oriented along the diagonal, whereas it is oriented along the anti-diagonal in case of the non-rephasing part. Each part on its own exhibits oscillations of its amplitude without significant line-shape modulations. The amplitude oscillations, however, are out of phase by π , i.e. the rephasing part has its maxima at t_2 -times of 200, 450 and 650 fs, whereas the non-rephasing part has its maximal amplitude at $t_2 = 100, 300, 550, \text{ and } 800$ fs. Therefore, for t_2 -times of 200, 450, and 650 fs the major contribution to the total signal stems from the rephasing part, whereas for t_2 -times of 100, 300, 550, and 800 fs the non-rephasing part contributes more strongly to the total spectrum. In Fig. 4.5 we present a quantitative evaluation of the respective contributions.

An analogous situation is encountered in the imaginary part as shown in Fig. 4.3b. The nodal line of the rephasing part is oriented along the diagonal, whereas the one of the non-rephasing part is oriented along the anti-diagonal. As a consequence of the out-of-phase oscillations of the amplitudes of the two contributions, the nodal line of the total signal experiences a periodic modulation of its orientation. Similar to the real part, the rephasing and non-rephasing imaginary peak shapes do not change significantly with increasing t_2 -time, it is only their relative contribution to the total signal that varies with t_2 . From inspection of the dispersive part it becomes most obvious how the phase-twisted line-shapes in the rephasing and non-rephasing signal parts cancel upon summation to yield a purely dispersive imaginary part. In Ref. [36] the oscillations of the rephasing, non-rephasing, and sum spectra are explained based on an expansion of the frequency-frequency correlation function in terms of Huang-Rhys factors.

The dissection into rephasing and non-rephasing parts was also performed for the amplitude and phase spectra (Fig. 4.4). For these representations, however, simple addition of the two contributions to yield the total spectrum is not possible. Nevertheless, the oscillations in the total spectra can be assigned to oscillating features in the rephasing and non-rephasing signal parts. In the amplitude part 1Q2D spectra (Fig. 4.4a), we observe a stronger contribution of the rephasing part for t_2 -delays of 200, 450, and 650 fs, and a reverse situation (i.e. an intensity gain of the non-rephasing contribution) for t_2 -delays of 100, 300, 550, and 800 fs. Therefore, the total signal is elliptical and line-narrowed along the anti-diagonal in the former case, and more circular in the latter. In the phase spectra (Fig. 4.4b), the lines of constant phase are oriented along the diagonal in the rephasing part and along the anti-diagonal in the non-rephasing part. This behavior reflects the different sign of the phase accumulated during the two time-intervals t_1 and t_3 according to the different coherence evolution in the rephasing and non-rephasing Feynman diagrams [119]. Depending on the relative strength of the rephasing and non-rephasing contributions, lines of constant phase in the total phase spectrum are either oriented along the diagonal ($t_2=200, 450, \text{ and } 650$ fs), or they rotate down to become approximately parallel to the ω_1 -axis ($t_2=100, 300, 550, \text{ and } 800$ fs). In the next section we discuss relations of the line-shape evolutions in 1Q2D electronic spectra to the frequency-frequency correlation function.

4.4.3 Frequency-Frequency Correlation Function

For electronic spectra in the condensed phase, where transition energy fluctuations are non-Markovian in nature, homogeneous and inhomogeneous timescales are not readily separable. Therefore, such systems are usually described by a frequency-frequency correlation function (FFCF) $M(t)$, defined as

$$M(t) = \frac{\langle \delta\omega_{eg}(t)\delta\omega_{eg}(0) \rangle}{\langle \delta\omega_{eg}^2 \rangle}. \quad (4.1)$$

$M(t)$ is a normalized ensemble averaged product of transition frequency fluctuations ($\delta\omega_{eg}$) separated by time t . For high temperatures it is equal to the real part of the correlation function $C(t)$ (Eq. (2.19)) normalized to 1 at $t = 0$. Since the correlation function in principle carries all relevant information on intramolecular and system-bath dynamics, considerable attention has been drawn over the last decade on how to sample the FFCF by experimentally feasible methods [52, 55, 93]. Once $M(t)$ is known, all linear and nonlinear spectroscopic signals can be calculated via the line-shape function $g(t)$ with knowledge of the reorganization energy λ and the temperature dependent coupling parameter Δ^2 , which reduces to $\frac{2\lambda k_B T}{\hbar}$ at high temperatures (cf. Section 2.3). Such complete information about the transition frequency fluctuations due to intramolecular and system bath coupling is used in Ref. [36] to derive a detailed line-shape theory. Here, we concentrate on the intramolecular part of the $M(t)$ -function which is responsible for the oscillatory dynamics of the line-shapes.

Correlations between line-shape evolutions and the frequency-frequency correlation function have been revealed in 1Q2D spectroscopy by model calculations and experiments in the IR and VIS spectral region [22, 107, 118, 119, 120, 121, 122]. Two quantities extracted from the real part of 1Q2D electronic spectra were shown to be directly proportional to the FFCF: the ellipticity of the peak shape [107] and the center line slope [123, 124]. The ellipticity of the peak as a function of t_2 is defined as [107, 122]

$$E(t_2) = \frac{D^2 - A^2}{D^2 + A^2}, \quad (4.2)$$

where D and A denote the diagonal and anti-diagonal peak widths, respectively. In Fig. 4.5c we plot this ratio for $0 < t_2 < 800$ fs, with the diagonal and anti-diagonal peak widths evaluated at $\frac{1}{e}$ -height. Oscillations with a period of 240 fs are clearly recovered. In Fig. 4.5a and b it is shown that these oscillations arise mainly from modulations of the anti-diagonal width, whereas the diagonal width stays nearly constant over the time-range explored in our experiments [38]. The center line slope (CLS) is extracted by taking cuts parallel to the ω_3 -axis and finding the maximum of the peak. The resulting data points as a function of ω_1 are fit to a first order polynomial. The slope of this line is the center line slope (Fig. 4.5d). Note that in the work by Kwak *et al.* [123] cuts are taken parallel to the ω_1 -axis and the CLS is defined as the inverse of the slope of the line connecting the maxima of the slices. Both the ellipticity and the CLS can vary between 1 and 0 and directly reflect the t_2 -dependent part of the FFCF [107, 123]. The limiting value of 1 can be reached for $t_2 = 0$ and in the absence of a homogeneous component. The deviation from the initial

value of 1 can thereby be related to the magnitude of the homogeneous component, as was shown in Ref. [123]. Relaxation and spectral diffusion processes during t_2 lead to a decrease of the ellipticity and the CLS, until in the long time limit both quantities approach the value of zero, indicative of equal widths along the diagonal and anti-diagonal directions and a slope of the center line that is parallel to the ω_1 -axis. In a previous work it was argued that the CLS has the advantage over the ellipticity of being independent of factors influencing the line-shape (e.g. finite pulse duration, apodization, etc.) [123]. As can be seen in Figs. 4.5c and d we do not observe significant differences between these two quantities. Closely related to the ellipticity of the peak shape is the eccentricity, which is defined as $Ec = \sqrt{1 - \frac{A^2}{D^2}}$ and which has been proposed in earlier works as a measure for the FFCF [125]. Even though the eccentricity takes the same limiting values as the ellipticity, i.e. 1 if $D \gg A$ and 0 if $D=A$ (which is the case for a circle), the two quantities differ for intermediate cases and therefore cannot be compared directly.

As discussed above, a periodic modulation of the rephasing and non-rephasing contribution to the total 1Q2D spectrum induces the observed changes in the real and imaginary parts. In Fig. 4.5e we plot the relative amplitudes of the rephasing (S_I) and non-rephasing (S_{II}) part of the real part 1Q2D spectra. We clearly observe out-of-phase oscillations of these two contributions, with the rephasing part exhibiting its maxima at t_2 -times of 200, 450, and 650 fs and its minima at $t_2 = 100, 300, 550,$ and 800 fs, and the non-rephasing part showing the opposite behavior, i.e. having its maxima at t_2 -times corresponding to minima in the rephasing part and vice versa. Tokmakoff *et al.* [119, 122] defined an inhomogeneity index $I(t_2)$ as

$$I(t_2) = \frac{A_R - A_{NR}}{A_R + A_{NR}}, \quad (4.3)$$

with A_R being the relative amplitude of the rephasing, and A_{NR} the relative amplitude of the non-rephasing part. This quantity was shown to directly relate to $M(t)$ via $M(t_2) = \sin(\frac{\pi I}{2})$. From the inspection of the inhomogeneity index (Fig. 4.5f) one can notice, that the non-rephasing part exceeds the rephasing part in signal strength around t_2 -delays of 300 and 550 fs. For these delays the inhomogeneity index adopts negative values, which is consistent with negative peak shift values observed in Fig. 4.6a.

In the imaginary part of 1Q2D spectra it is the slope of the nodal line separating the positive and negative contribution that is related to $M(t)$ [121]. We extract this slope from our 1Q2D spectra by finding the zero crossing between the positive and negative contribution in the range $-18700 \text{ cm}^{-1} < \omega_1 < -19200 \text{ cm}^{-1}$ and fitting of the resulting data points with a first order polynomial. The slope of the nodal line oscillates with a period of 240 fs (Fig. 4.5g). Note that also the slope takes negative values around $t_2 = 300$ and 550 fs. This agrees well with the observation of negative values of the inhomogeneity index (Fig. 4.5f) and the peak shift (Fig. 4.6a). In case of a three-level system it is the real part that features two peaks of opposite sign, with the positive one stemming from ground state bleaching and stimulated emission and the negative feature arising from excited state absorption. In this case the slope of the nodal line is extracted from the real part spectra [22, 119, 126].

Extracting the frequency-frequency correlation function from the phase spectra (Fig. 4.4h) is

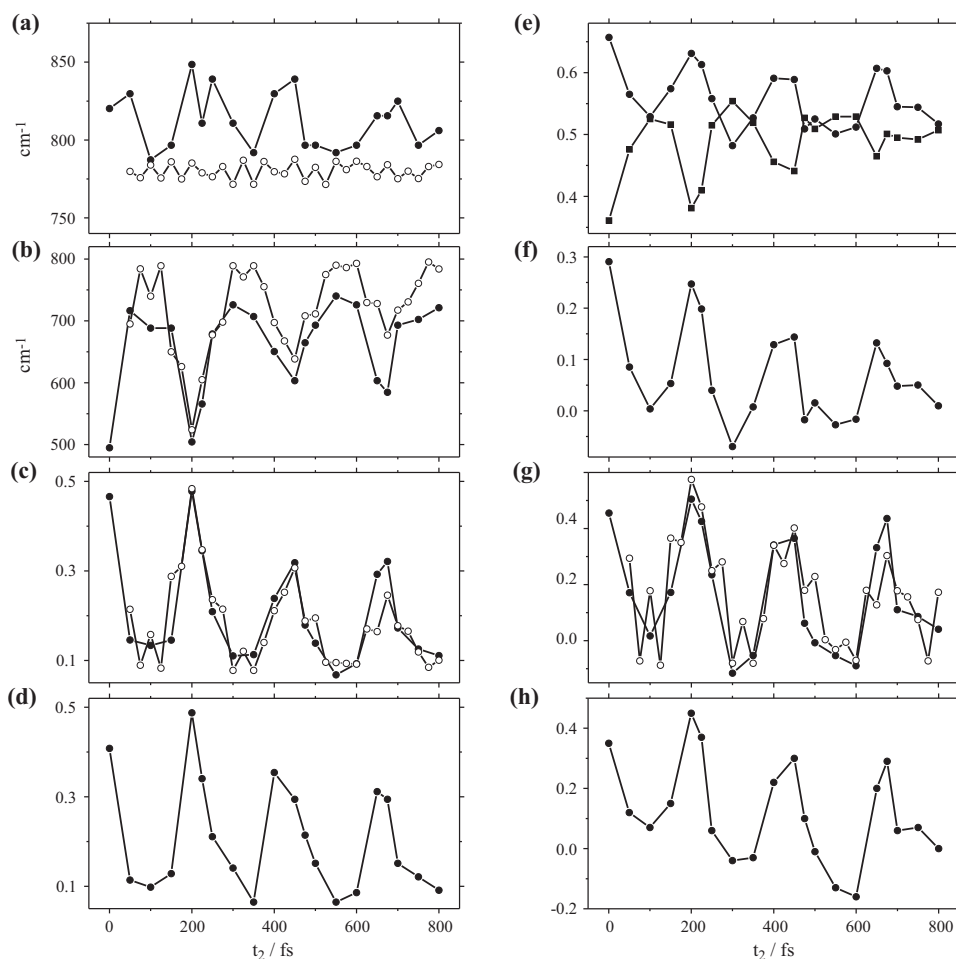


Figure 4.5: Oscillating features extracted from the 1Q2D spectra of PERY in toluene solution. Full symbols refer to experimental data, open symbols to simulations. t_2 -dependence of the (a) diagonal and (b) anti-diagonal width of the real part 1Q2D spectra. (c) Ellipticity of the peak in the real part 1Q2D spectra. (d) Center line slope of the peak in the real part 1Q2D spectra. (e) Relative amplitudes of the rephasing (circles) and the non-rephasing (squares) part of the real part 1Q2D spectra. (f) Inhomogeneity index extracted from the real part 1Q2D spectra. (g) Slope of the nodal line separating the positive and negative feature in the imaginary part 1Q2D spectra. (h) Slope of the $\phi = 0$ phase line in the phase of the 1Q2D spectra.

done by evaluating the slope of lines of constant phase [119, 122]. In Fig. 4.5h we plot this slope for $\phi = 0$ evaluated in the frequency range $-18500\text{cm}^{-1} < \omega_1 < -19250\text{cm}^{-1}$. Again, the oscillating pattern exhibits a period of 240 fs with maxima at t_2 -delays of 200, 450, and 650 fs and minima around $t_2 = 100, 300, 550,$ and 800 fs. Around 300 and 550 fs the slope of lines of constant phase adopts negative values indicative of a tilt towards the anti-diagonal axis.

4.4.4 Comparison to Related Four-Wave Mixing Signals

Heterodyned two-dimensional electronic spectroscopy gathers the maximum amount of information that can be inferred by any third-order nonlinear technique. Nevertheless it is instructive to cross-check our findings against results that are obtained with alternative detection schemes, shown in Fig. 4.6. From the experimental point of view, these signals may be differentiated by the required measuring (scanning) time and setup complexity, while, on the other hand, all of them are related to the functional form of $M(t)$ [52, 93, 94].

The three-pulse photon echo peak-shift (3PEPS) method is a variant of homodyned photon echo spectroscopy, in which the time-integrated nonlinear signal

$$S_{3PE}(t_1, t_2) = \int_0^\infty |P^{(3)}(t_1, t_2, t_3)|^2 dt_3 \quad (4.4)$$

is recorded in a wavevector architecture equivalent to 1Q2D-ES. In each step of a 3PEPS sequence, the delay t_1 is scanned at a fixed delay t_2 , and the position of the (time- and frequency-integrated) signal maximum evaluated along the t_1 -axis. The magnitude of this peak-shift (deviation from $t_1 = 0$) is recorded for a range of t_2 -delays, to give the peak-shift decay. In essence, a finite photon echo peak-shift value indicates the system's ability to rephase a macroscopic coherence (i.e. to cause an echo) after having spent a certain time t_2 in an intermediate state. Fig. 4.6a shows the photon echo peak-shift decay for PERY in toluene, along with a two-dimensional plot of $S_{3PE}(t_1, t_2)$. Both data representations clearly reveal how the photon echo signal maximum oscillates (along t_1) as a function of t_2 , the oscillation being observable for t_2 -delays well beyond one picosecond. In the context of our analysis of the 1Q2D electronic spectra of PERY, it is interesting to note that the peak-shift acquires negative values around the minima of the peak-shift trace (located at t_2 -delays around 100, 350, and 600 fs). In other words, the integrated photon echo (recorded as a function of t_1) may peak at negative t_1 -delays, if non-rephasing signal contributions dominate over rephasing contributions to the total signal. We point out that this finding is consistent with the negative value for the inhomogeneity index and a negative slope of the nodal line in the dispersive 1Q2D signal part, observed at the corresponding t_2 -delays.

For the sake of completeness, Fig. 4.6b and c show the transient grating (TG) and the pump-probe (PP) signals of PERY, in both frequency integrated and frequency resolved representation. The former method records S_{3PE} as a function of t_2 for delay t_1 set to zero (descriptively, the first two excitation pulses form a spatial transmission grating from which the third pulse is scattered off). Note that unlike 3PEPS, TG measurements are sensitive to population decay during t_2 . Time delays are scanned in a similar way in PP measurements (i.e. scanning t_2 for $t_1 = 0$), however, only two pulses are involved in the experiment, the signal being recorded along the direction of the second pulse. Since the PP signal is generated by two interactions with the first pulse (pump), followed by one interaction with the second pulse (probe), t_1 is intrinsically zero. Overall, also our TG and PP data-sets do well align with previously published data [90, 103] and our 1Q2D electronic spectra. In both types of signals, strong intensity oscillations with a period of 240 fs (140 cm^{-1}) can be discerned. The slow decay of the TG signal confirms the absence of any fast

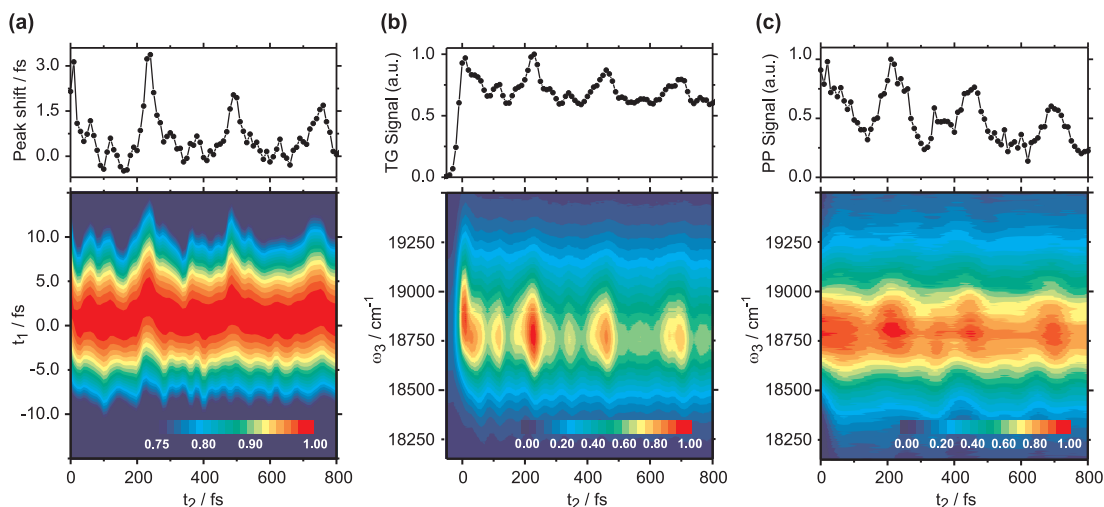


Figure 4.6: One-dimensional four-wave mixing signals of PERY in toluene. Top and bottom panels share the same abscissa, color scales are shown as insets in the bottom panels. (a) Three-pulse photon echo peak-shift trace (top) and the corresponding frequency integrated three-pulse photon echo signal as a function of delay t_1 and t_2 . (b) Frequency integrated (top) and frequency resolved (bottom) transient grating signal. (c) Frequency integrated (top) and frequency resolved (bottom) pump-probe signal.

population decay channels. In line with the discussion above, the PP signal is dominated by (positive) stimulated emission and ground state bleaching contributions, indicating excited state absorption effects to be negligible on the picosecond timescale investigated here.

4.5 Simulations

Overall, the oscillation of the 2D line-shape is qualitatively similar to the one observed for the coherent evolution of electronic states [35, 44], but follows the low-frequency vibrational beats in our case. To substantiate our interpretation of the data, theoretical simulations of the 1Q2D spectra of PERY were performed in the impulsive limit, applying standard semi-classical second order cumulant expansion treatment of the electron-phonon interaction. PERY is treated as an electronic two-level system interacting with intramolecular as well as solvent vibrational modes. Both the overdamped solvent modes and the underdamped oscillatory modes of PERY were treated within the Brownian oscillator model [4]. Expressions for the third order response functions that we use to calculate nonlinear signals can be found in a standard textbook [4]. The total response function of the two-level electronic system is composed of four different response functions, usually denoted as R_1 , R_2 , R_3 , and R_4 , that are functions of the delays between three successive interactions of the system with an incident electric field. This incident field enters the total nonlinear signal via triple convolution with the response functions. Full expressions for the third order nonlinear signal can be found, e.g., in Ref. [10].

In the impulsive limit the 1Q2D spectrum is formally composed of two parts: one contribution where the first interaction takes place with negative sign ($-\mathbf{k}_1$), and another contribution where the first interaction occurs with positive sign ($+\mathbf{k}_1$). In the first case, the signal electric field is proportional to the sum of the response functions $E_I(t_1, t_2, t_3) \propto R_2(t_1, t_2, t_3) + R_3(t_1, t_2, t_3)$, while in the second case, the signal field reads $E_{II}(t_1, t_2, t_3) \propto R_1(t_1, t_2, t_3) + R_4(t_1, t_2, t_3)$. The signal $E_I(t_1, t_2, t_3)$ has the well-known rephasing capability of the photon echo, i.e. its phase evolves with mutually opposite signs during delays t_1 and t_3 . This part of the signal is denoted as rephasing part. In $E_{II}(t_1, t_2, t_3)$, on the other hand, the phase evolves with the same sign during both delays and the signal has consequently no rephasing capability. Based on the rephasing and non-rephasing part of the signal, reconstructed in the experiment by heterodyne detection, the 1Q2D spectrum is defined as

$$S(\omega_1, t_2, \omega_3) = S_I(\omega_1, t_2, \omega_3) + S_{II}(\omega_1, t_2, \omega_3), \quad (4.5)$$

where

$$S_I(\omega_1, t_2, \omega_3) = \int_0^\infty \int_0^\infty dt_1 dt_3 E_I(t_1, t_2, t_3) e^{-i\omega_1 t_1 + i\omega_3 t_3}, \quad (4.6)$$

and

$$S_{II}(\omega_1, t_2, \omega_3) = \int_0^\infty \int_0^\infty dt_1 dt_3 E_{II}(t_1, t_2, t_3) e^{+i\omega_1 t_1 + i\omega_3 t_3}. \quad (4.7)$$

Since the spectral and temporal width are Fourier related quantities, the observable spectral window in a 2D-ES experiment is inversely proportional to the pulse duration. To account for this effect, one can use the fact that the 2D spectrum is a double Fourier transform of the third order signal, which in turn is a triple convolution of the response function with the electric fields of the pulse sequence. Utilizing the fact that the Fourier transform of a convolution of two functions results in a product of their respective Fourier transforms, the effect of the finite bandwidth can be incorporated. Assuming the response functions vary only slowly with t_2 , a correcting factor

$$f(\omega_1, \omega_3) = [A(\omega_1 - \Omega)]^2 A(\omega_3 - \Omega), \quad (4.8)$$

which multiplies the impulsive spectrum can be introduced. $A(\omega)$ is the Fourier transform of the slowly varying temporal envelope of the laser pulse, and Ω is the central frequency of the pulses. The apparent asymmetry of Eq. (4.8) in frequencies ω_1 and ω_3 mirrors the fact that two interactions of the system with the electric field are needed to reach the population period of the experiment, whereas the photon echo signal is stimulated by a single interaction. In our simulations, we assume Gaussian pulses with durations of 21 fs, corresponding to the experimental pulse lengths.

The parameters used for the simulations are obtained by fitting the diagonal and the anti-diagonal width of the absorptive, and the tilt of the nodal line of the dispersive parts of the 1Q2D spectrum for times $t_2 = 200, 300, 450,$ and 550 fs. Although we fit only these four points (using

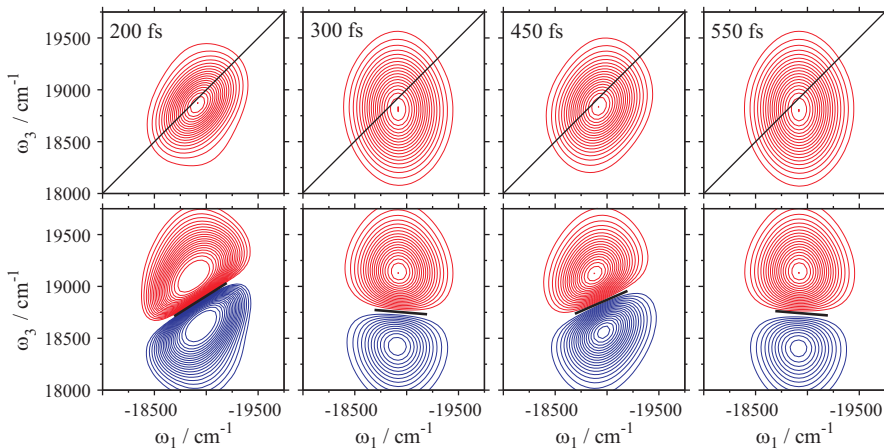


Figure 4.7: Simulated 1Q2D electronic spectra of PERY. The upper (lower) panels show the absorptive (dispersive) signal part at t_2 -delays of 200, 300, 450, and 550 fs. All spectra are normalized to the respective maximum absolute value, contour lines are drawn at 5% intervals, starting at $\pm 10\%$ of the signal intensity. Diagonal lines are shown in the real part spectra; black lines in the imaginary part spectra indicate the zero-crossings between positive and negative contributions.

the least square nonlinear minimization algorithm from the Matlab[®] optimization toolbox), a good qualitative agreement at all waiting times t_2 is achieved. In order to restrict the number of minimization parameters, only reorganization energies of two overdamped solvent modes with correlation times of $\tau_c^{(1)} = 150$ fs and $\tau_c^{(2)} = 650$ fs, and the two slowest modes of underdamped oscillations with frequencies of $\omega_{osc}^{(1)} = 143$ cm^{-1} and $\omega_{osc}^{(2)} = 575$ cm^{-1} are varied. All other modes are neglected in this calculation. In particular, the fast oscillatory modes of PERY do not contribute to the 1Q2D spectrum, because their spectral features lie outside the observation window set by the laser pulse spectrum. The correlation times $\tau_c^{(1)}$, and $\tau_c^{(2)}$ are taken from Ref. [99], while the oscillator frequencies $\omega_{osc}^{(1)}$, and $\omega_{osc}^{(2)}$ are extracted from our TG measurement. Within these limitations, we obtain best results with solvent reorganization energies of $\lambda_{sol}^{(1)} = 39$ cm^{-1} and $\lambda_{sol}^{(2)} = 106$ cm^{-1} , and reorganization energies of the intramolecular modes of $\lambda_{osc}^{(1)} = 110$ cm^{-1} and $\lambda_{osc}^{(2)} = 84$ cm^{-1} . In Fig. 4.7 we present the results of the numerical simulations of the 1Q2D spectra. Close inspection of the figures reveals very good congruity with the experimental spectra. A detailed comparison of experimental and simulated values is presented in Fig. 4.5. We reproduce the positions of the beating maxima and minima, the magnitude of both the diagonal (Fig. 4.5a) and anti-diagonal (Fig. 4.5b) widths, the relative amplitudes of their oscillations, and the trend of the tilt angle (Fig. 4.5g), including the negative sign of the angle at certain waiting times t_2 . The good correspondence of theoretical and experimental results strongly suggests that the observed modulation of the 1Q2D spectra is dominated by the slowest vibrational mode only.

Having obtained good qualitative agreement between experiment and theory on the basis of numerical simulations, we proceed to an analytical analysis that yields further understanding of

the nature of the vibrational effects in 1Q2D electronic spectra. To this end, we study a two-level electronic system interacting with a single underdamped oscillatory mode with frequency $\omega_{osc} = 140 \text{ cm}^{-1}$ and reorganization energy $\lambda_{osc} = 80 \text{ cm}^{-1}$ and a single solvent mode with correlation time $\tau_c = 150 \text{ fs}$ and reorganization energy $\lambda_{solv} = 100 \text{ cm}^{-1}$. These values are of the same characteristic magnitude as in the calculations above. Starting from the same theoretical point as in the numerical calculations (the third order response functions) we perform a separation of the vibrational part of the response from the one of the overdamped solvent mode. Because the response functions R_n have the form of an exponential function of a sum of $g(t)$ functions of different time arguments (see e.g. [4]), the separation can be performed considering the line broadening function $g(t)$ as the sum of vibrational and solvent contributions

$$g(t) = g_{solv}(t) + g_{vib}(t). \quad (4.9)$$

Each response function R_n ($n = 1, \dots, 4$) then can be written as a product of two contributions $R_n(t_1, t_2, t_3) = R_n^{solv}(t_1, t_2, t_3)R_n^{vib}(t_1, t_2, t_3)e^{-i\omega_{eg}(t_1 \pm t_3) - i\lambda_{vib}(t_1 \pm t_3)}$, where the plus sign in the exponent corresponds to the non-rephasing and the minus sign to the rephasing part of the 1Q2D spectrum. If the time t_2 is longer than the solvent correlation time τ_c , the solvent response becomes t_2 -independent and can be written as $R_n^{solv}(t_1, t_2, t_3) = R_n^{(0)}(t_1, t_3)$. We further assume that $g_{vib}(t)$ of the underdamped vibrational mode can be approximated as

$$g_{vib}(t) = i\lambda t + i\frac{\lambda}{\omega} \sin \omega t + \frac{\lambda}{\omega} \Xi(T)[1 - \cos \omega t], \quad (4.10)$$

where $\Xi(T) = \coth(\hbar\omega_{vib}/2k_B T)$, and T is the temperature [4]. In Eq. (4.10) we assume that the damping of the vibrational mode is negligible. Using again the properties of the response functions R_n , we can expand R_n in terms of the Huang–Rhys factors $\frac{\lambda}{\omega}$. This leads to

$$R_n^{vib}(t_1, t_2, t_3) \approx 1 + \frac{\lambda}{\omega} F_n(t_1, t_2, t_3), \quad (4.11)$$

where F is a function containing only sines and cosines of the arguments $t_1, t_2, t_3, t_1 + t_2, t_2 + t_3, t_1 + t_3$, and $t_1 + t_2 + t_3$. Using trigonometric transformations F can be written as

$$F_n(t_1, t_2, t_3) = K_n(t_1, t_3) + H_n(t_1, t_3) \cos(t_2) + G_n(t_1, t_3) \sin(t_2), \quad (4.12)$$

where the complete t_2 -dependence is condensed into the sine and cosine functions. The first, t_2 -independent part, $K_n(t_1, t_3)$, is given by

$$K_1(t_1, t_3) = -i[\sin \omega t_1 - \sin \omega t_3] - \Xi(T)[2 - \cos \omega t_1 - \cos \omega t_3] \quad (4.13)$$

$$K_2(t_1, t_3) = i[\sin \omega t_1 + \sin \omega t_3] - \Xi(T)[2 - \cos \omega t_1 - \cos \omega t_3] \quad (4.14)$$

$$K_3(t_1, t_3) = i[\sin \omega t_1 - \sin \omega t_3] - \Xi(T)[2 - \cos \omega t_1 - \cos \omega t_3] \quad (4.15)$$

$$K_4(t_1, t_3) = -i[\sin \omega t_1 + \sin \omega t_3] - \Xi(T)[2 - \cos \omega t_1 - \cos \omega t_3]. \quad (4.16)$$

The second, cosine-oscillating part, $H_n(t_1, t_3) \cos \omega t_2$, reads

$$\begin{aligned}
H_1(t_1, t_3) &= \Xi(T)[1 - \cos \omega t_3 - \cos \omega t_1 + \cos \omega(t_1 + t_3)] \\
&\quad + i[\sin \omega t_1 - \sin \omega t_3 - \sin \omega(t_1 + t_3)]
\end{aligned} \tag{4.17}$$

$$\begin{aligned}
H_2(t_1, t_3) &= -\Xi(T)[1 - \cos \omega t_3 - \cos \omega t_1 + \cos \omega(t_1 + t_3)] \\
&\quad + i[\sin \omega t_1 - \sin \omega t_3 - \sin \omega(t_1 + t_3)]
\end{aligned} \tag{4.18}$$

$$\begin{aligned}
H_3(t_1, t_3) &= -\Xi(T)[1 - \cos \omega t_3 - \cos \omega t_1 + \cos \omega(t_1 + t_3)] \\
&\quad + i[\sin \omega t_1 + \sin \omega t_3 - \sin \omega(t_1 + t_3)]
\end{aligned} \tag{4.19}$$

$$\begin{aligned}
H_4(t_1, t_3) &= \Xi(T)[1 - \cos \omega t_3 - \cos \omega t_1 + \cos \omega(t_1 + t_3)] \\
&\quad + i[\sin \omega t_1 + \sin \omega t_3 - \sin \omega(t_1 + t_3)] .
\end{aligned} \tag{4.20}$$

The third, sine-oscillating part, $G_n(t_1, t_3) \sin \omega t_2$, is given by

$$\begin{aligned}
G_1(t_1, t_3) &= \Xi(T)[\sin \omega t_3 + \sin \omega t_1 - \sin \omega(t_1 + t_3)] \\
&\quad + i[1 - \cos \omega t_3 + \cos \omega t_1 - \cos \omega(t_1 + t_3)]
\end{aligned} \tag{4.21}$$

$$\begin{aligned}
G_2(t_1, t_3) &= -\Xi(T)[\sin \omega t_3 + \sin \omega t_1 - \sin \omega(t_1 + t_3)] \\
&\quad + i[1 - \cos \omega t_3 + \cos \omega t_1 - \cos \omega(t_1 + t_3)]
\end{aligned} \tag{4.22}$$

$$\begin{aligned}
G_3(t_1, t_3) &= -\Xi(T)[\sin \omega t_3 + \sin \omega t_1 - \sin \omega(t_1 + t_3)] \\
&\quad - i[1 - \cos \omega t_3 - \cos \omega t_1 + \cos \omega(t_1 + t_3)]
\end{aligned} \tag{4.23}$$

$$\begin{aligned}
G_4(t_1, t_3) &= \Xi(T)[\sin \omega t_3 + \sin \omega t_1 - \sin \omega(t_1 + t_3)] \\
&\quad - i[1 - \cos \omega t_3 - \cos \omega t_1 + \cos \omega(t_1 + t_3)] .
\end{aligned} \tag{4.24}$$

The total response can therefore be separated into stationary, cosine-oscillating, and sine-oscillating contributions. The derivation of the functions $K_n(t_1, t_3)$, $H_n(t_1, t_3)$, and $G_n(t_1, t_3)$ is straightforward, and results in expressions which are sums of sine and cosine terms of the arguments ωt_1 , ωt_3 , and $\omega(t_1 + t_3)$. Thus, the total response function R_n can be written as

$$\begin{aligned}
R_n(t_1, t_2, t_3) &= R_n^{(0)}(t_1, t_3) + R_n^{(0)}(t_1, t_3)K_n(t_1, t_3) \\
&\quad + R_n^{(0)}(t_1, t_3)H_n(t_1, t_3) \cos(t_2) + R_n^{(0)}(t_1, t_3)G_n(t_1, t_3) \sin(t_2).
\end{aligned} \tag{4.25}$$

Combining Eqs. (4.25), (4.5), (4.6), and (4.7) we can write for the 1Q2D spectrum

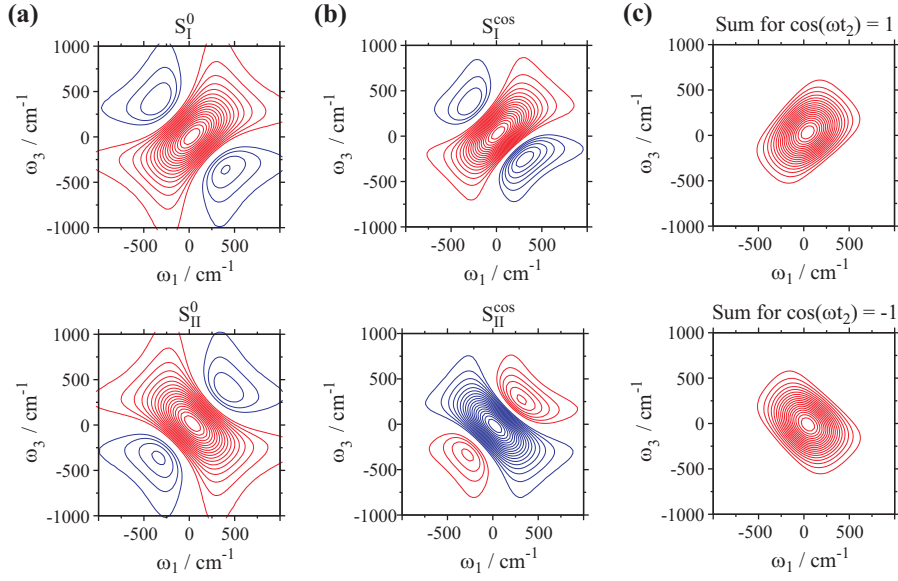


Figure 4.8: Components of the two-dimensional spectrum of an electronic two-level system interacting with a single overdamped and a single underdamped Brownian mode at room temperature. The parameters for the simulation are given in the text. The first column (a) shows the stationary rephasing and non-rephasing components, the second column (b) illustrates the rephasing and non-rephasing prefactors of $\cos \omega t_2$ (see Eq. (4.26)). The last column (c) presents the sum of the stationary and cosine contributions for $\cos \omega t_2 = 1$ (upper), respectively -1 (lower). Every figure is normalized to the maximum of the absolute value (0.5 for stationary, 0.19 for cosine, and 1.0 for the sum).

$$\begin{aligned}
 S(\omega_1, t_2, \omega_3) = & S_I^0(\omega_1, \omega_3) + S_{II}^0(\omega_1, \omega_3) \\
 & + [S_I^{\cos}(\omega_1, \omega_3) + S_{II}^{\cos}(\omega_1, \omega_3)] \cos \omega t_2 + [S_I^{\sin}(\omega_1, \omega_3) + S_{II}^{\sin}(\omega_1, \omega_3)] \sin \omega t_2. \quad (4.26)
 \end{aligned}$$

Fig. 4.8 illustrates the characteristic shapes for $t_2 = \frac{n\pi}{\omega}$ of the contributions of Eq. (4.26) to the absorptive part of the 1Q2D spectra, i.e. where $\sin \omega t_2 = 0$. The first column (Fig. 4.8a) presents the stationary contributions, S_I^0 and S_{II}^0 , the second column (Fig. 4.8b) shows the prefactors of the cosine term in Eq. (4.26), and the third column (Fig. 4.8c) presents the sum of the two for times t_2 when $\cos \omega t_2 = 1$ (upper) and $\cos \omega t_2 = -1$ (lower), respectively. One can immediately notice that all rephasing contributions are elongated along the diagonal of the 2D spectrum, whereas the non-rephasing features are elongated along the anti-diagonal. One striking feature of these partial 1Q2D spectra is the complete sign inversion of the non-rephasing cosine contribution S_{II}^{\cos} with respect to the corresponding stationary non-rephasing contribution S_{II}^0 . For $\cos \omega t_2 = 1$ the summation results in an enhancement of the rephasing part and a decrease of the non-rephasing part of the spectrum, causing an overall elongation along the diagonal. For the $\cos \omega t_2 = -1$ case we observe enhancement of the non-rephasing part and thus elongation along the anti-diagonal. For parameters relevant for our system, the amplitude of the contributions oscillating with a cosine

function are found to be approximately two times larger than the sine functions, and they both are significantly smaller than the stationary contributions. We can therefore expect the most significant changes in the 2D line-shape to oscillate with the cosine of the waiting time t_2 . Evaluation of the rephasing and non-rephasing parts of the absorptive part of our experimental 1Q2D spectra confirms our analysis [37]. The relative amplitudes of the rephasing and non-rephasing parts at waiting times $t_2 = n\pi/\omega$ vary without significant changes of their line-shape. Rather, the oscillation of the diagonal and anti-diagonal width is a result of the periodic enhancement and suppression of rephasing and non-rephasing parts with respect to each other.

4.6 Conclusions

Intramolecular and system-bath (solvation) dynamics can be studied either in time-domain by the frequency-frequency correlation function $M(t)$, or, equivalently, in frequency-domain by the spectral density $\rho(\omega)$. In this chapter we have concentrated on time-domain measures, by presenting different metrics that can be extracted from two-dimensional electronic spectra and that follow the functional form of the frequency-frequency correlation function. These metrics are the ellipticity, the center line slope, and the inhomogeneity index extracted from the real part spectra, the slope of the nodal line in the imaginary part spectra, and the slope of lines of constant phase in the phase spectra. Peak shift curves of PERY measured in solvents of different polarity (nonpolar, polar, and weakly polar) featured similar timescales [103], thus pointing to weak solute-solvent interactions. The observed oscillations in the frequency-frequency correlation function can thus be assumed to be dominated by intramolecular dynamics. The observed beating pattern stems from the fact that during t_2 the density matrix does not only evolve in a population state (ground or excited state), but vibrational coherences can be excited as well. These coherences evolve with a frequency that is given by the difference in frequency of the two states involved. In theoretical works on vibrational effects in 1Q2D-ES, the vibrational sub-levels could be resolved as a consequence of the customized input parameters [35, 127]. Under experimentally feasible conditions effects such as finite pulse durations and finite temperature erode the multipeak structure. In such a situation, vibrational dynamics can not be followed by the evolution of diagonal and cross peaks, but by the evolution of line-shapes and signal intensities, as has been done in the present study. The experimental two-dimensional spectra can be fitted by including two overdamped solvent modes and two underdamped intramolecular modes. Expansion of the vibrational part of the third-order response in terms of the Huang-Rhys factor $\frac{\lambda}{\omega}$ shows that these enhancements and suppressions are caused by the coherent motion of the vibrational degrees of freedom of the molecule.

*Not only is the universe stranger than we
imagine, it is stranger than we can imag-
ine.*

Sir Arthur Eddington (1882 - 1944)



PINACYANOL

In this chapter we present a sequence of two-dimensional electronic spectra of a prototypical cyanine dye, whose spectral properties in aqueous solution are determined by the formation of a monomer-dimer equilibrium. Quantum-chemical methods are utilized to calculate the structure and absorption properties of the two species involved. Our spectroscopic results simultaneously characterize the spectral line-shapes of the two species in terms of underlying dynamic and static disorder, and demonstrate how the two-dimensional technique allows to exploit high spectral and temporal resolution in one and the same experiment. The distinctly different spectral relaxation dynamics are quantified in a two-dimensional line-shape analysis, by extracting the time dependent ratios of the diagonal and anti-diagonal peak-widths. Our findings are in line with theoretical considerations, that predict the fluctuational dynamics of an excitonic dimer state to be exchange-narrowed by excitation delocalization.

This chapter is based on

- A. NEMETH, V. LUKEŠ, J. SPERLING, F. MILOTA, H. F. KAUFFMANN, AND T. MANČAL. Two-dimensional electronic spectra of an aggregating dye: simultaneous measurement of monomeric and dimeric line-shapes. *Phys. Chem. Chem. Phys.* **11**, 5986 (2009)

5.1 Introduction

Several nonlinear spectroscopic techniques have been designed to selectively probe only homogeneous dynamics by eliminating inhomogeneous contributions [4, 128, 129]. These methods can be classified into frequency- and time-domain techniques. The most prominent method operating in frequency domain is spectral hole burning [130, 131], where an intense narrow-band laser is used to selectively excite a small group of molecules from an inhomogeneously broadened ensemble. These excited molecules subsequently undergo a photochemical transformation with the photoproduct absorbing at a different frequency. The homogeneous linewidth can be extracted from the width of the hole, remaining in the absorption spectrum and being probed by a low intensity, narrow-band laser.

A completely different approach is adopted in photon echo spectroscopy, a time domain technique, in which the elimination of inhomogeneous broadening is based upon the rephasing of the coherence decay caused by the diverse transition frequencies of different molecules in two time intervals [93]. For that purpose an ultrashort and thus broad-band laser pulse excites all molecules within its bandwidth into a coherence between the ground and excited state. Differences in the transition frequencies of the excited chromophores causes this coherence to rapidly dephase. Application of a second laser pulse after a certain time delay $t = \tau$ acts as a time reversal, provoking the dephasing coherence to rephase and emit a photon echo signal after $t = 2\tau$. The decay of the photon echo signal is thus solely due to irreversible dephasing brought about by the limited excited state lifetime and phonon-induced pure dephasing.

Two-dimensional electronic spectroscopy allows for the simultaneous observation of homogeneous and inhomogeneous dynamics by spreading the information content into two frequency dimensions. Thereby, line-broadening mechanisms that are static on the timescale of t_2 (time separating the second and third excitation pulse) are projected into the diagonal part of the spectrum, whereas dynamic line-broadening mechanisms can be followed by the evolution of the anti-diagonal width. A sequence of 1Q2D plots therefore gives an intuitive picture on which kind of disorder dominates the electronic transition. In this chapter we will demonstrate the capability of 2D-ES to simultaneously follow the evolution of two distinct species (monomers and dimers of a cyanine dye) that show completely different temporal evolutions of their line-shapes.

For this purpose we have chosen the dye Pinacyanol chloride (1,1'-diethyl-2,2'-carbocyanine chloride) that belongs to the class of cyanine dyes. Due to strong dispersion forces associated with the high polarizability of the chromophore, cyanine dyes tend to form aggregates in aqueous solution at higher concentrations [133], a phenomenon that has first been reported in 1936 by Scheibe and Jelley [134, 135]. Aggregation manifests itself by a new band appearing in the linear absorption spectrum that, depending on the angle α between the transition dipoles of the monomers forming the aggregate and the centers-of-masses joint, is either red- ($0^\circ \leq \alpha < 54.7^\circ$) or blue-shifted ($54.7^\circ < \alpha \leq 90^\circ$) with respect to the monomer absorption. The former case is termed J- or Scheibe-aggregate, whereas the latter type of aggregate is named H-aggregate. Fig. 5.1a schematically depicts the dependence of the interaction energy V on the angle α for the case of a

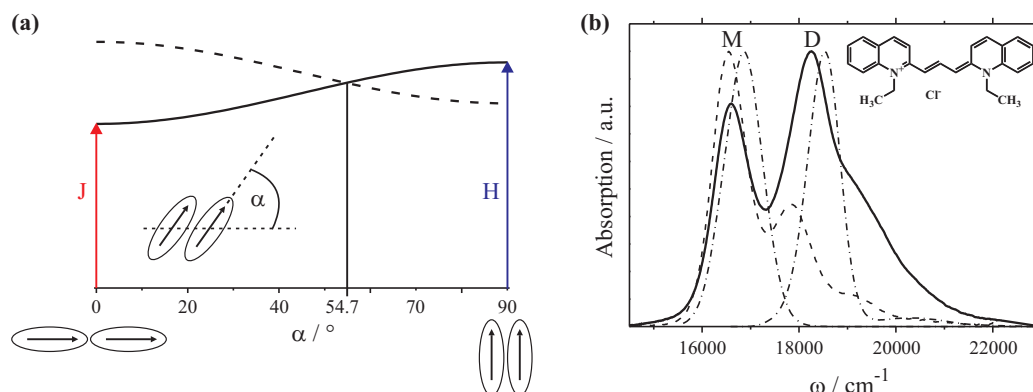


Figure 5.1: (a) Schematic illustration of the dependence of the interaction energy V between two monomers on the angle α between their transition dipoles and the line connecting their centers of mass (Figure adapted from [132]). The solid and dashed line represent the two one-exciton states, with the solid line indicating the allowed and the dashed line the forbidden transition. For the magic angle of 54.7° there is no splitting of the one-exciton states. For angles below this value ($\alpha < 54.7^\circ$) the transition to the lower one-exciton state is allowed (red-shifted J-band), whereas for $\alpha > 54.7^\circ$ a blue-shift of the dimer peak (H-band) is observed. (b) Linear absorption spectrum of Pinacyanol ($c = 1.5 \cdot 10^{-4}$ M) in water/methanol solution (37.5% v/v) (solid line). The low energy peak (M) stems from monomers, dimers (D) absorb at higher frequencies. From concentration-dependent linear absorption spectra, the blue shoulder can be attributed to absorption from trimers and higher aggregates [133]. The absorption spectrum of monomers in methanol is shown for comparison as dashed line. The dashed-dotted lines indicate the simulated absorption bands of Pinacyanol monomer and dimer based on the MD ZINDO/DFTB+ geometries depicted in Fig. 5.4. The chemical structure of Pinacyanol chloride is shown in the inset.

dimer, these two quantities being related by $V \propto 1 - 3 \cos^2 \alpha$ [132].

The degree of aggregation can be controlled by both solute concentration and addition of less polar solvents, thus monomer-dimer equilibria are adjusted as done in the present contribution. This permits effects of excitation delocalization to be studied at the lowest level of aggregation, by direct comparison of monomeric and dimeric line-shapes in 1Q2D-ES spectra. The linear absorption spectrum of Pinacyanol in water/methanol (37.5% v/v) solution at room temperature is shown in Fig. 5.1b. The linear absorption spectrum of Pinacyanol monomers is dominated by a vibrational progression of a 1300 cm^{-1} mode. As expected from the geometry of the dimer discussed in Sec. 5.4, the dimer absorption maximum is blue-shifted with respect to that of the monomer. Upon further increase of the concentration, additional peaks grow in on the blue side of the dimer peak. These peaks can be attributed to trimers and higher aggregates [133]. In the linear absorption spectrum homogeneous and inhomogeneous line-broadening mechanisms both contribute to the resulting line-shape, making it impossible to quantify either the former or the latter. The present contribution

intends to demonstrate how 1Q2D-ES can be used to distinguish and simultaneously characterize spectral line-shapes of distinct physical origin, thereby fully exploiting the broad bandwidth and ultrashort duration of femtosecond laser pulses.

5.2 Experimental Details

1Q2D spectra have been obtained by scanning t_1 for a fixed value of t_2 from -100 to $+100$ fs in steps of 0.65 fs (thus fulfilling the Nyquist sampling theorem). Pinacyanol chloride has been purchased from Sigma Aldrich and used as received. Solutions with $c = 1.5 \cdot 10^{-4}$ M have been prepared in a mixture of water and methanol (37.5 % v/v) giving a maximum absorption of 0.3. The excitation frequency of our laser pulses has been tuned to 17500 cm^{-1} , covering both the monomer and dimer absorption bands. The excitation intensity in these experiments was 10 nJ per pulse. Comparison to spectra recorded with excitation intensities of 4 nJ per pulse revealed no changes in the spectral features, which lead us to the conclusion that higher order and saturation effects do not affect the dynamics under investigation.

5.3 Computational Details

The ground state geometries of the possible conformations of Pinacyanol monomers have been optimized using the DFT and the semiempirical DFTB+ method [136]. For the DFT calculations the SV(P) basis set [137] and the B3LYP [109] and PBE [138] functionals have been employed. Due to numerical problems connected with the geometry optimization of Pinacyanol dimers, the possible van-der-Waals structures have been calculated only using the DFTB+ method, where dispersion interactions have been included. On the basis of the optimized geometries, the vertical electronic absorption and fluorescence transitions have been calculated at the ZINDO level of theory. DFT calculations have been performed using the Turbomol program [113], for the semiempirical DFTB+ calculations the procedure outlined by Aradi *et al.* [136] was followed, whereas the Gaussian03 package was used for ZINDO calculations [139].

Classical on-the-fly MD calculations have been performed with molecular energies and energy gradients computed by the DFTB+ method. In the on-the-fly techniques any precomputation of energy surfaces is avoided and only those data, which are needed at each given point of the trajectory, are computed. The Velocity-Verlet integration scheme [140, 141] has been used to integrate Newton's equations of motion with a 1 fs time step. The dynamics has been equilibrated for 10 ps and has then been continued for 30 ps. Temperature has been set to 300 K and has been controlled by Andersen thermostat [142].

Electronic absorption spectra for Pinacyanol monomer and dimer have been simulated in the gas phase. These simulations have been performed by first sampling the configuration space with an ensemble of thermally equilibrated nuclear geometries, that have been generated by the dynamics simulations described above. For these samples, 25 vertical transition energies and oscillator strengths from the ground to the excited state have been computed. These quantities have been

used to compute the appropriate Einstein coefficients [143]. A Gaussian broadening function has been attributed to each transition having as its height the respective Einstein coefficient and as its width a phenomenological broadening constant of 403 cm^{-1} . The sum of all Gaussian functions plotted against the transition energy gives a post Franck-Condon semi-classical approximation to the spectrum [144].

For the calculations of the 2D spectra we use the well-known third order response function theory [4]. The Hamiltonian of a monomeric system is assumed in the form of

$$H^{(mon)} = [\epsilon_g + V_g(Q)]|g\rangle\langle g| + [\epsilon_e + V_e(Q)]|e\rangle\langle e|, \quad (5.1)$$

where ϵ_g and ϵ_e are pure electronic excitation energies, and $V_g(Q)$ and $V_e(Q)$ are nuclear potential energy surfaces in the electronic ground- and excited states, respectively. Electron-phonon interaction, which is of utmost importance for the time evolution of the 2D spectrum of the studied system, can be identified by splitting this Hamiltonian into pure bath, pure electronic, and interaction terms as $H^{(mon)} = H_B + H_{el} + H_{el-ph}$. This yields

$$H_{el-ph} = \Delta V(Q)|e\rangle\langle e|, \quad (5.2)$$

where $\Delta V(Q) = V_e(Q) - V_g(Q) - \langle V_e(Q) - V_g(Q) \rangle$. Here, the averaging over reservoir degrees of freedom is denoted by $\langle \dots \rangle$. In the third-order response function theory, the influence of the vibrational and other bath modes on the 2D spectrum is comprised in the so-called line-broadening function

$$g(t) = \frac{1}{\hbar^2} \int_0^t d\tau \int_0^\tau d\tau' \langle \Delta V(Q, \tau') \Delta V(Q) \rangle, \quad (5.3)$$

where the time-dependence of $\Delta V(Q, \tau')$ is due to the interaction picture with respect to the bath Hamiltonian H_B . In this work we use the Brownian oscillator model according to Ref. [4] with three parameters, λ (reorganization energy), ω (vibrational frequency) and τ_c (dephasing time) for the $g(t)$ function. The electronic transition energy obtained from the quantum chemical calculation corresponds to the value $\epsilon_e + \lambda - \epsilon_g$.

The dimer peak of the 2D spectrum is assumed to be the result of excitonic interaction between two Pinacyanol molecules. In comparison to the quantum-chemical calculation, this is a significant simplification, as the excitonic model completely neglects any possible overlap of the electronic wavefunctions. The corresponding Hamiltonian reads

$$H^{(dim)} = H_1^{(mon)} \otimes 1_2 + 1_1 \otimes H_2^{(mon)} + J(|g_1\rangle|e_2\rangle\langle e_1|g_2| + h.c.), \quad (5.4)$$

where J is the excitonic resonance coupling and \otimes denotes the direct product of a monomeric Hamiltonian with the unity operator $1_n = |g_n\rangle\langle g_n| + |e_n\rangle\langle e_n|$ defined on the Hilbert space of the other monomer. Such a Hamiltonian naturally contains doubly excited states that are responsible for excited state absorption. The eigenstates of the Hamiltonian in Eq. (5.4), the so-called excitonic

states $|\alpha\rangle$, are formed as linear combinations of the excited states $|n\rangle$ localized on individual monomers

$$|\alpha\rangle = \sum_{n=1}^2 c_n^\alpha |n\rangle, \quad (5.5)$$

where the coefficients c_n^α are obtained from the diagonalization of the electronic Hamiltonian.

The unitary transformation of the whole problem from the basis of local states to the basis of the electronic eigenstates significantly affects the form of the electron-phonon interaction Hamiltonian. If the fluctuations of different site energies due to electron-phonon interaction are independent, the line-shape of the allowed dimer transition is predicted to be narrowed by the mixing of the original monomeric electronic states. The line-shape function then transforms into the excitonic basis according to [145]

$$g_\alpha(t) = \sum_{n=1}^2 |c_n^\alpha|^4 g_n(t). \quad (5.6)$$

Here, the $g(t)$ -functions are defined according to Eq. (5.3) and indices n and α refer to states localized on individual monomers and excitonic states, respectively, as in Eq. (5.5).

5.4 Results and Discussion

5.4.1 Experimental Two-Dimensional Electronic Spectra

1Q2D amplitude spectra of Pinacyanol are displayed in Fig. 5.2a for t_2 times of 0, 20, 70, 2500, and 10000 fs, where we observe clearly distinct behavior of the two species, monomers and dimers. As expected from the linear absorption spectrum we can distinguish two peaks in the 1Q2D amplitude part spectra, the low energy peak corresponds to the monomer absorption and the high energy peak is attributed to dimers. For $t_2 = 0$ fs both peaks exhibit approximately the same line-shapes, with the diagonal width (D) being nearly twice as large as the anti-diagonal width (A) (Fig. 5.2b). Line-shapes in two-dimensional vibrational and electronic spectra have been thoroughly investigated by the groups of Tokmakoff and Jonas [22, 24, 25, 35] for different model systems. From these and related studies it has been concluded that the width along the diagonal is related to inhomogeneous broadening, whereas the width along the anti-diagonal reflects homogeneous dynamics. Finite pulse lengths (implying a limited spectral excitation width) influence more strongly the diagonal width by acting as a spectral filter. The anti-diagonal width, related to the width of the homogenous absorption line, is less disturbed [35] and its time evolution in the 2D spectrum is therefore an interesting source of information about electron-phonon interactions. Our excitation pulses are not broad enough to cover the whole absorption spectrum, therefore the 1Q2D spectra presented in Fig. 5.2a have to be understood as the linear absorption spectrum dressed by the pulse excitation spectrum. In this respect the diagonal widths shown in Fig. 5.2b can only be taken as relative values, limited by the finite spectral bandwidth, which becomes evident by comparison to the 1Q2D spectra simulated in the impulsive limit (Fig. 5.3b). Nevertheless

we can draw conclusions concerning the different behavior of monomers and dimers. While both species feature similar characteristics for $t_2 = 0$ fs, i.e. a ratio of diagonal to anti-diagonal width (D/A) that starts from the same initial value of 1.7 (Fig. 5.2c), their temporal evolution strongly differs. For the monomer the diagonal width stays nearly constant over the timescale explored in our experiments. On the other hand, the anti-diagonal width quickly increases and after 70 fs reaches a plateau with a maximum value that is now approximately as large as the diagonal width. Accordingly, the ratio of the diagonal to anti-diagonal width decreases from 1.7 to 1.1 within 70 fs, resulting in a circular peak shape and indicating no residual inhomogeneity. After 70 fs the shape of the monomer peak can be considered to be invariant and the signal only decreases in intensity.

On the other hand, the dimer peak exhibits a completely different behavior. Within the first 20 fs the dimer peak, that has been slightly twisted off the diagonal at zero delay, rotates clockwise so that its long axis becomes parallel to the diagonal. This, as will be shown below, is due to interferences between positive and negative signals in the absorptive part. In accordance with this clockwise rotation, the diagonal width of the dimer peak increases, whereas the anti-diagonal width slightly decreases. At 70 fs the anti-diagonal width of the dimer peak has reached its minimum.

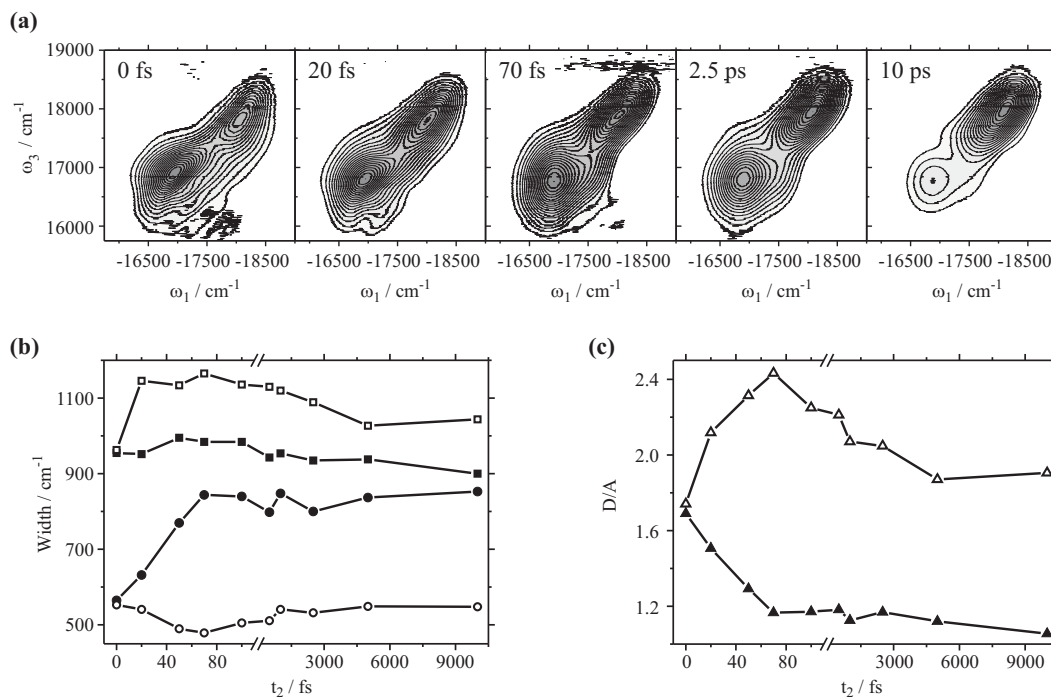


Figure 5.2: (a) 1Q2D amplitude spectra of Pinacyanol for t_2 -times of 0, 20, 70, 2500, and 10000 fs. Contour lines are drawn in 5 % intervals, starting at 10 % signal intensity. All spectra are normalized to the respective signal maximum. (b) 2D line-shape analysis of the amplitude part of Pinacyanol 1Q2D spectra, showing the diagonal (squares) and anti-diagonal (circles) widths of the monomer (filled symbols) and dimer (open symbols) peak. The ratio of the diagonal to anti-diagonal width is depicted in panel (c).

Accordingly the ratio of the diagonal to anti-diagonal width increases from 1.7 to 2.4 within 70 fs. For increasing t_2 -delays the width along the diagonal slightly decreases, leveling off at a value that is approximately twice as large as the anti-diagonal width, as indicated by a diagonal to anti-diagonal width ratio of 1.9. This high value for the ratio D/A , corresponding to a strongly elliptical peak shape, indicates a high degree of inhomogeneity present in the dimers. One possible reason for this inhomogeneity is a broad distribution of monomer distances in the dimers, that leads to a broad distribution of coupling strengths, which in turn implies a broad distribution of transition energies. In contrast, as predicted by exciton theory, fluctuational dynamics that contribute to homogeneous broadening and therefore act on the anti-diagonal width, are reduced in excitonic dimers and higher aggregates as a consequence of excitation delocalization. This is the well-known effect of exchange narrowing [146].

Additionally to the differences in line-shapes, the lifetimes of the two species greatly differ from each other. For zero delay t_2 , due to the stronger overlap of the excitation pulses with the monomer absorption peak, the monomer peak in the 1Q2D spectrum is stronger than the dimer peak. However, in contrast to the dimer that only slowly decays on the timescale of our experiment, the monomer signal quickly decays due to strong non-radiative decay channels [147]. After 10 ps the monomer signal has vanished nearly completely, which is in good agreement with previously determined fluorescence lifetimes from picosecond time-resolved fluorescence measurements [148, 149]. These fast non-radiative decay channels via torsional motion are not open to dimers, which explains their much slower decay rate. The remaining slow decay of the dimer is not apparent from the 1Q2D spectra, as all presented spectra are normalized to their maximum absolute value. It is, however, included in the numerical simulations of the 2D spectra discussed in Sec. 5.4.3.

Turning now to the absorptive (real) part of the 1Q2D spectra (left column in Fig. 5.3a), we find a behavior similar to the amplitude part, except for very short t_2 -delays. In this pulse overlap region additional Liouville space pathways, that do not maintain the correct pulse ordering, contribute to the signal and can produce negative features even for a two-level system where theory predicts only positive signals in the absorptive part [35]. These negative contributions, observed in the absorptive part for both monomer and dimer, are responsible for the distorted peak shapes in the amplitude part at $t_2 = 0$ fs. Except for these differences, the line-shapes and peak amplitudes evolve similar to the amplitude spectra, with the dimer peak keeping its diagonal elongation and signal strength up to at least 10 ps, and the monomer peak quickly acquiring a circular shape within 70 fs and decaying on the timescale of 10 ps.

In the dispersive (imaginary) part of the 1Q2D spectra shown in Fig. 5.3a (right column) we observe a positive and a negative feature for the monomer and the dimer. In analogy to the ratio D/A in the absorptive spectra, the slope of the nodal line, separating the positive and negative contributions, reflects the different behavior of the monomer and dimer in the dispersive spectra. Fig. 5.3a displays this different evolution of the nodal line for the monomer/dimer peaks. For the monomer the angle of the nodal line with respect to ω_1 has a value of 30° for $t_2 = 0$ fs and becomes parallel to the ω_1 -axis within the first 20 fs. For longer t_2 -delays this angle assumes negative values until the monomer signal completely vanishes for $t_2 = 10$ ps. Contrarily, the nodal

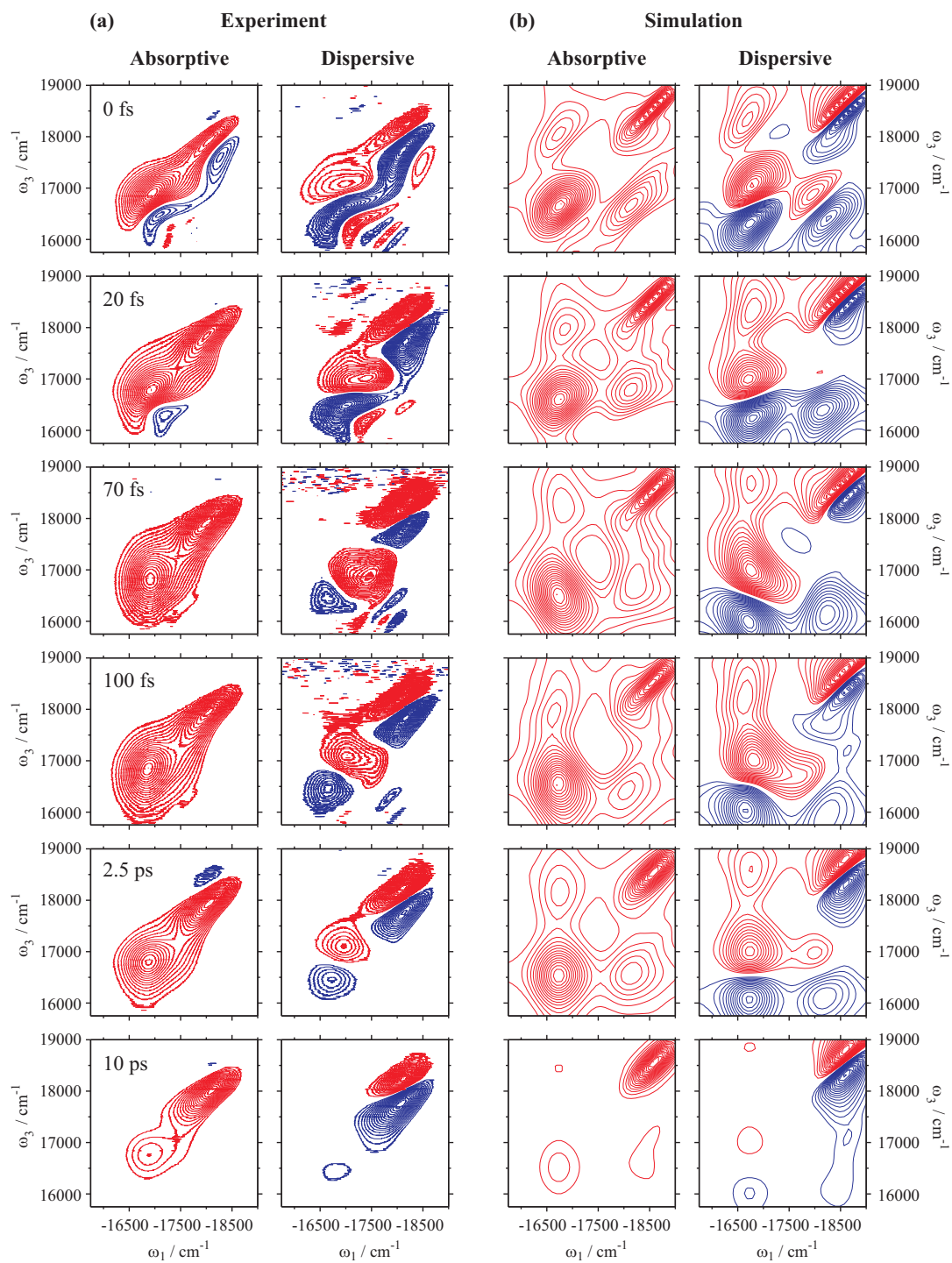


Figure 5.3: Experimental (a) and simulated (b) 1Q2D spectra of Pinacyanol for t_2 -times of 0, 20, 70, 100, 2500, and 10000 fs dissected into absorptive (left column) and dispersive part (right column). Red (blue) lines indicate positive (negative) features. Contour lines are drawn in $\pm 5\%$ intervals, starting at 10% signal intensity. All spectra are normalized to the respective maximum absolute value. Simulations have been performed in the impulsive limit.

line separating the positive and negative contribution of the dimer peak and the ω_1 -axis draw an angle of approximately 30° for all t_2 -times covered in our experiments.

5.4.2 Quantum Chemistry Calculations

To support our experimental findings and provide a basis for the simulation of the 2D spectra, we have performed quantum-chemical calculations on the structure and absorption properties of Pinacyanol monomers and dimers. The computational method most frequently used is Density Functional Theory (DFT), that has been successfully applied to interpret the structure and optical spectra of various π -conjugated systems. However, the application of this approach is limited by the number of atoms. Semiempirical methods offer a reasonable compromise between the reliability of results and hardware requirements.

The optimized DFTB+ geometries of the monomer reveal the existence of eight possible conformations, two of them (M_{cis} , M_{trans}) are depicted in Fig. 5.4. The two most stable conformations have *cis*-orientation of the two nitrogen atoms carrying the ethyl chains and the molecule is almost planar. These two conformations differ only in the mutual orientation of the alkyl groups and they are twisted by approx. $8\text{--}11^\circ$ with respect to the central bridge which is nearly planar. The energy difference of 11 cm^{-1} between the two structures is practically negligible. The two *trans*-conformations are about 1539 cm^{-1} higher in energy with respect to the most stable *cis*-conformation. Similar results are obtained also by DFT calculations employing B3LYP and PBE functionals.

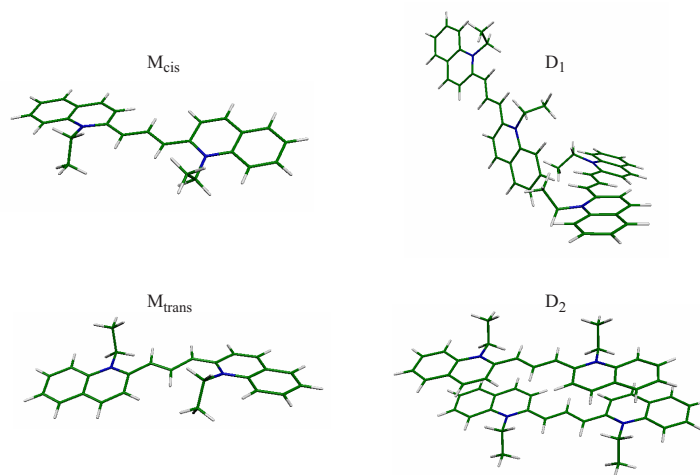


Figure 5.4: Optimal DFTB+ structures of two out of eight possible monomer structures with *cis*- and *trans*-conformation of the two nitrogen atoms, M_{cis} and M_{trans} , respectively, and two out of four possible van-der-Waals dimer structures D_1 and D_2 .

In order to characterize the optical transitions, which have predominantly $\pi - \pi^*$ character, it is useful to examine the occupied and unoccupied molecular orbitals contributing to the lowest energy electronic transition. The lowest theoretical ZINDO vertical electronic transition for the

M_{cis} conformation is located at 17123 cm^{-1} and carries an oscillator strength of $f = 1.692$. 92% of this oscillator strength is associated with the HOMO to LUMO transition depicted in Fig. 5.5. The HOMO orbital is localized predominantly on the molecular bridge with its lobes being oriented perpendicular to the aromatic chain. The LUMO nicely shows the inter-ring bonding character, its orbitals are spread over the atoms connecting the pyrazine units with the molecular bridge. This dominant transition, broadened by a Gaussian function with a width of 403 cm^{-1} , is plotted in Fig. 5.1b for comparison with the experimental linear absorption spectrum. The values for the other stable monomer conformations do not deviate substantially from these results.

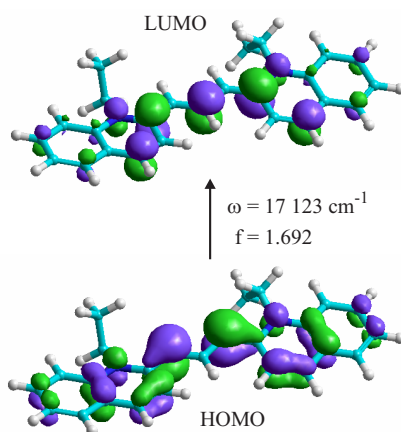


Figure 5.5: ZINDO orbitals based on the optimal DFTB+ geometry M_{cis} depicting the dominating HOMO to LUMO transition.

Due to the large variability of possible orientations of two interacting monomers, the set of starting geometries for dimer geometry calculations have been generated only for the *cis*-conformations. On the basis of DFTB+ calculations we have found four stable van-der-Waals structures, two of them are depicted in Fig. 5.4. Structure D_1 has a T-shape orientation, where the shortest distance between the nitrogen atoms of the two interacting molecules is 6.2 \AA . The sandwich structure D_2 exhibits the highest π -stacking. The interacting molecules in this conformation are practically co-planar and their distance is ca. 3.5 \AA . The remaining two conformations have half-slip sandwich structures with similar parallel orientations of the interacting systems. It seems that the mutual orientation of the alkyl groups plays a significant role in the space separation of the van-der-Waals structures and they determine the equilibrium distance between the interacting monomers.

As expected for a sandwich-type dimer, where the angle between the transition dipole moments of the monomers and the line connecting their centers of mass is 90° , the allowed electronic transition to the first exciton state is blue-shifted with respect to the respective monomer absorption. For the dimer structure D_2 in Fig. 5.4, this allowed transition is located at 18727 cm^{-1} . As predicted from theoretical considerations, the oscillator strength of this transition is about twice the oscillator strength of the corresponding monomer transition and amounts to $f = 3.395$. Fig. 5.6 depicts the HOMO and LUMO making the dominant contribution to this electronic transition, with

HOMO-1→LUMO accounting for 48 % and HOMO→LUMO+1 for 42 % of the oscillator strength. This transition is also plotted in Fig. 5.1b for comparison with the experimentally observed absorption spectrum. In accordance with exciton theory, that predicts an additional red-shifted, forbidden transition for sandwich-type dimers, our quantum-chemical calculations reveal a transition at 14115 cm^{-1} carrying zero oscillator strength. In the three other stable dimer conformations the electronic excitation is localized on one of the two monomers only. Therefore, the excitation energy coincides with the one of the monomer, and we observe no shift of the absorption peak.

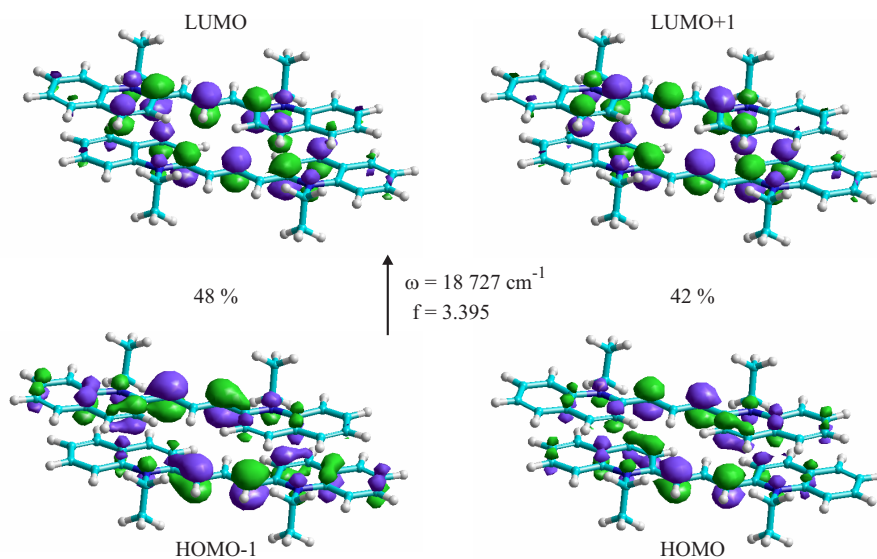


Figure 5.6: ZINDO orbitals based on the optimal DFTB+ geometry D_2 depicting the main contributions to the observed transition at $18\,727\text{ cm}^{-1}$.

Extracting the dimer absorption spectrum from a solution containing both monomers and dimers so far has been accomplished mostly following the iterative procedure outlined by West and Pearce [133]. Essentially, it relies on the additivity of monomer and dimer spectra in case both species are in equilibrium. Applying this procedure to Pinacyanol and its lower vinylogue Pseudoisocyanine leads to a dimer spectrum featuring two main peaks, one coinciding with the monomer absorption maximum and the other being blue-shifted by approx. 1650 cm^{-1} [150, 151, 152, 153]. The former usually is attributed to transitions to the lower one-exciton state, whereas the latter is claimed to stem from transitions to the higher one-exciton state. This picture neither holds with our 2D spectroscopy observations nor with our quantum-chemical calculations. From geometrical considerations it is correct to assign these two peaks to dimers. However, from the spectroscopic point of view, only the higher energy peak can be attributed to dimer absorption, since our calculations suggest that only this peak corresponds to dimeric conformations in which the excitation energy is delocalized over both monomers. According to our calculations the dimer peak detected in literature that coincides with the monomer absorption peak can be associated with dimeric conformations where the electronic excitation energy is still localized on only one

monomer. These two situations can not be distinguished by the procedure described in [133]. The second point substantiating our interpretation is the fact that in case the lower one-exciton state would coincide with the monomer absorption peak, one would expect to see a cross-peak in the 1Q2D spectrum, indicative of coupling between the two one-exciton states due to the common ground state and of relaxation from the higher to the lower one-exciton state. Rather, the absence of such a cross-peak (cf. Figs. 5.2 and 5.3) points towards the fact, that the lower one-exciton transition lies outside the spectral window of our excitation pulses.

5.4.3 Numerical Simulations of 2D Spectra

In order to assign the features of the experimental 1Q2D spectra, we perform a qualitative simulation of the 2D spectra of Pinacyanol in the impulsive limit. To this end we apply third-order response function theory [4] in conjunction with essential ideas of excitonic theory [154] and results of quantum-chemical calculations as discussed in the previous section.

The quantum-chemical calculations have confirmed that in the spectral window of our experiment, the Pinacyanol monomers can be represented by a two-level electronic system. It was argued above that this transition is modulated by nuclear vibrational modes. In our model we therefore introduce a fast vibrational mode of about 1300 cm^{-1} that is clearly distinguishable in the linear absorption spectrum of Pinacyanol monomers (cf. Fig. 5.1b). The frequency of this fast mode corresponds to a period of approx. 25 fs, which is clearly in competition with the temporal width of the laser pulses in our experiment. In the impulsive limit simulations we expect vibrational cross-peaks to be present in the 1Q2D spectrum. These cross-peaks change their magnitude and phase with the oscillator frequency, and consequently, due to the finite pulse-width in the experiments, they are nearly averaged out in the course of integration over the laser pulse envelope. However, one can still expect some weak remnants of these features and certain influences of the fast mode on the time-dependent line-shapes of the 1Q2D peaks to be present. Additional slow underdamped and overdamped vibrational modes are postulated in our model in order to explain the pronounced time evolution of the 1Q2D spectra on a sub-hundred-femtosecond time scale. This spectroscopic model of a monomer is also valid for the dimer configurations, in which the electronic transitions are localized on their component molecules, as discussed in the previous section.

In Ref. [38] we have corrected the impulsive 2D spectra by applying to it the spectrum of the excitation laser pulse. The validity of this procedure relies on a weak dependence of the nonlinear response on the delay t_2 . In Ref. [38] this dependence was sufficiently weak in the spectral region we were investigating, and we could ignore the fast mode completely. In the present situation, however, the cross-peak originating from the 1300 cm^{-1} mode is not well spectrally separated from the rest of the spectrum and its fast oscillations lead to a strong t_2 dependence of the response function. We therefore decided to present only a qualitative theory in the impulsive limit.

Quantum-chemical calculations suggest that one of the four stable structures of such an aggregate is a parallel dimer. Both exciton theory and our quantum-chemical calculations then predict that the upper excitonic level will be optically allowed. Previous studies [150, 151, 152, 153] suggested the presence of an allowed lower exciton transition in the spectral region of the monomer

transition, resulting from a different than parallel geometry of the dimer. In case the dimer had an allowed transition overlapping with the monomer peak, one would expect a cross-peak resulting from the common ground state and from upper to lower exciton level relaxation, and/or excited state absorption, all within our experimental spectral window. Such a relaxation cross-peak does not oscillate with the transition frequency and should therefore, if present, be visible in the measured 1Q2D spectrum (see e.g. the case in Ref. [155]). As such a cross-peak does not appear in our experimental 2D spectra, we assume that the lower excitonic transition is out of our spectral window. The quantum-chemical calculations put the forbidden lower excitonic level much lower than the monomeric transitions and we can therefore, for our purposes, treat the dimer as a two level system, too.

The experimental 1Q2D spectrum confirms the line narrowing predicted in Eq. (5.6) by exhibiting a distinctly narrower anti-diagonal line-shape of the dimeric peak than can be seen in the monomeric peak. Also the fact that changes of the 2D line-shape with delay time t_2 in both the absorptive and dispersive parts of the dimer peak are very weak, suggests that the dimer transition interacts much less with the vibrational modes than the corresponding transition of the monomer.

As the linear absorption analysis suggests (cf. Fig. 5.1b), the dimer peak also exhibits a spectral structure that goes beyond a single electronic transition. It is likely that this structure results from an excitonic interaction between vibrational levels on different monomers. Such a case goes beyond the applicability of a simple linear semiclassical description of the system-bath coupling that we apply in this study. The excitonic interaction between vibrational levels will have an impact on the quantitative aspects of the studied 2D spectrum. Nevertheless, impulsive limit calculations that we present below still agree rather well with the qualitative features of the experimental spectra, suggesting that this type of excitonic effects does not play a significant role in the spectral region covered by our laser pulse.

Fig. 5.3b presents a simulation of 1Q2D spectra at $t_2 = 0, 20, 70, 100, 2500,$ and 10000 fs, all within the impulsive limit. The model was limited to one fast (1350 cm^{-1}) vibrational mode already identified above and one slow (200 cm^{-1}) vibrational mode that is responsible for the short time evolution of the 2D spectra. One overdamped Brownian oscillator mode representing the solvent contribution is added to adjust the line-shapes. After extensive search in the parameter space we have arrived at a set of parameters that qualitatively explains the observed temporal evolution of the 1Q2D spectra in both the short (≤ 100 fs) and long time regime. The fastest mode was assigned a reorganization energy of 500 cm^{-1} and a dephasing time of 1 ps. These parameters lead to a characteristic vibrational progression in the monomeric absorption spectrum, and to a vibrational cross-peaks in the impulsive 2D spectrum. The slow mode with a frequency of 200 cm^{-1} has been assigned a reorganization energy of 100 cm^{-1} and a dephasing time of 1 ps. This mode is responsible for the very fast initial dynamics of the 1Q2D spectrum, characterized by oscillations of its amplitude, and diagonal and anti-diagonal widths of the monomer peak. Finally, the overdamped mode was assigned a reorganization energy of 150 cm^{-1} and a dephasing time of 1 ps. In addition, the monomer signal was damped by a relaxation factor e^{-Kt_2} , where $K = 0.2\text{ ps}^{-1}$ to describe the finite lifetime of the monomer excited state and to qualitatively

reproduce the disappearance of the lower energy peak. In order to describe the dimer peak and its lack of evolution during t_2 we included one overdamped Brownian mode with a reorganization energy of 50 cm^{-1} and an inhomogeneous broadening of the excitonic line with FWHM Δ of 600 cm^{-1} . This accounts for the rather small anti-diagonal and high inhomogeneous widths and for an increase of the homogeneous width at longer t_2 -times. The inhomogeneous broadening was simulated by adding a term αt^2 , where $\alpha = \Delta^2/(16 \ln 2)$, to the line broadening function.

The linear absorption spectrum has been calculated (not shown here) and the concentration of the dimers (i.e. the ratio of the monomer and dimer contributions in the spectrum) has been adjusted to correspond to the experimental absorption maxima. Using these parameters and the impulsive limit, the 1Q2D spectrum is completely dominated by the dimer peak, and we therefore scaled down the dimer peak amplitude by a factor of 0.3 in order to make both peaks distinguishable in the 2D spectrum. In the experiment, similar changes of the magnitude of the peaks naturally occur due to the limited bandwidth of the laser spectrum.

The absorptive part of the simulated 1Q2D spectra (left column in Fig. 5.3b) reproduces the fast change of the monomer peak anti-diagonal width, which is in our simulations a combined effect of the influence of the slow (200 cm^{-1}) vibrational mode, and the change of the shape and magnitude of the vibrational cross-peak. The vibrational cross-peak partially influences the shape of the diagonal peak due to its finite width. The negative features in the short time experimental spectrum appear also in the calculated impulsive 2D spectrum. For the specific parameters used here they persist only for $0 < t_2 < 20 \text{ fs}$ (not shown). In the experimental spectrum an additional negative contribution exists due to the pulse overlap effects. These negative features are not a result of excited state absorption, but are rather an intrinsic feature of a 2D spectrum of an electronic system modulated by electron-phonon interaction. The anti-diagonal width of the monomer peak in the absorptive part increases rapidly between 0 and 70 fs and it is completely round at $t_2 = 2.5 \text{ ps}$ where $t_2 > \tau_c$, with τ_c denoting the dephasing time of the oscillator mode. For t_2 -times of 2.5 ps and 10 ps one can notice the decay of the monomer peak due to relaxation.

For a qualitative comparison, the dispersive part of the 1Q2D spectrum (right column in Fig. 5.3b) is even more interesting. The nodal line of the monomer peak is oriented along the diagonal at $t_2 = 0 \text{ fs}$ in our simulation and it turns rapidly to be parallel to the ω_1 -axis of the spectrum as t_2 increases. At times $t_2 = 70$ and 100 fs , the nodal line is tilted more along the anti-diagonal and the vibrational cross-peak contributes with another nodal line oriented along the diagonal. This feature is visible also in the experimental 1Q2D spectrum at $t_2 = 70$ and 100 fs , and it is therefore possible to conclude that the experimental dispersive part exhibits traces of the vibrational cross-peak.

Comparing the simulated and measured 1Q2D spectra, the following conclusions can be drawn. The short time dynamics of the monomer 2D line-shapes is dictated by the combined effect of a slow vibrational mode with vibrational energy around 200 cm^{-1} and a fast vibrational mode with vibrational energy around 1300 cm^{-1} . In the lower right corner of the dispersive part of the 1Q2D spectrum ($|\omega_1| > \omega_3$) we can distinguish contributions of a vibrational cross-peak. In contrast to the monomeric peak, the dimer contribution to the 1Q2D spectrum exhibits a remarkable absence

of dynamics, lacking all the characteristic traces of electron-phonon interaction. This can be a result of exciton exchange narrowing, or/and a more significant change of the vibrational mode spectrum due to the formation of the dimer. The latter hypothesis is also supported by the increased life time of the dimer with respect to the monomer, which is clearly observed in the 1Q2D spectrum.

In summary, the calculations in the impulsive limit allow for a qualitative analysis of the 2D spectra and are in good agreement with the experimental data. Although we observe a strong vibrational cross peak due to the unlimited spectral bandwidth of the laser pulse in the impulsive limit calculations, which can be perceived only very weakly in the experimental spectra, we are confident that our qualitative conclusions are valid.

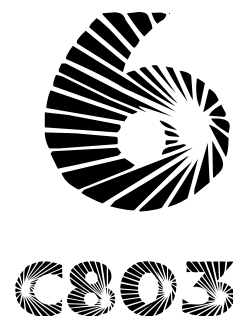
5.5 Conclusions

The present study combines quantum-chemical calculations on the structure, geometry, and transition energies of Pinacyanol monomers and dimers, with experimental and simulated 1Q2D spectra revealing dynamical information on the line-broadening mechanisms of these two species. Our quantum-chemical calculations reproduce the peak positions of monomers and dimers in linear absorption spectra, revealing the existence of a blue-shifted absorption band for sandwich-type dimer conformations, which is in accordance with exciton theory [154]. The temporal evolution of monomeric and dimeric peak shapes is tracked by 2D electronic spectroscopy. The monomer peak exhibits a very fast loss of inhomogeneity that can be followed by the evolution of the ratio D/A in the absorptive part and the slope of the nodal line in the dispersive part. On the other hand, the dimer peak lacks nearly all evolution of its line-shape on the timescales explored in our experiments. These findings are in contrast to transient grating and photon echo studies on a polyphenylenevinylene-based oligomer and its paracyclophane-linked dimer, where the authors find that the homogeneous and inhomogeneous line-broadening processes of these two species are indistinguishable within experimental errors [57].

Since 2D spectroscopy overcomes the boundaries of limited simultaneously high spectral and temporal resolution inherent to one-dimensional techniques, by exploiting the mathematical properties of Fourier transforms, i.e. the frequency resolution being determined by the scanned time range and vice versa, it is the ideal method for simultaneously studying several species in real time. In contrast to the popularity of simple dimer systems in theoretical studies of 2D electronic spectroscopy [41, 43, 44, 156], most experimental studies on molecular systems so far focused on either dilute solutions of non-interacting dye molecules [9, 11, 28, 38, 157] or large complexes, like natural or artificial light harvesters [29, 31]. This discrepancy is somewhat surprising and we regard the present contribution as a first step towards closing this gap.

There is something fascinating about science. One gets such wholesale returns of conjecture out of such a trifling investment of fact.

Mark Twain (1835 - 1910)



In this chapter we investigate the first steps of exciton dynamics in the course of band-to-band energy transfer in the bi-tubular J-aggregate C8O3 by employing two-dimensional coherent electronic spectroscopy. The sub-20 fs measurements provide a direct look into the details of elementary electronic couplings by spreading spectroscopic transition information into two frequency axes. Coupled exciton states are mapped as typical off-diagonal signals in 2D frequency-frequency correlation spectra. Spectral streaking of cross peaks directly reveals inter-band dephasing and exciton population relaxation without making recourse to an a-priori model. The experiments enable to look beneath conventional incoherent population transfer by directly probing the early 100 fs regime. Theory and simulations, based on an effective multi-level scheme and a quantum-dissipative model with experimental pulse envelopes, explain the origin of the cross peaks, reveal the underlying sequences of electronic transitions, recover the streaking patterns of relaxing cross peaks along ω_1 , and reconstruct the space-energy pathways of electronic excitation flow.

This chapter is based on

- A. NEMETH, F. MILOTA, J. SPERLING, H. F. KAUFFMANN, D. ABRAMAVICIUS, AND S. MUKAMEL. Tracing exciton dynamics in molecular nanotubes with 2D electronic spectroscopy. *Chem. Phys. Lett.* **469**, 130 (2009)
- F. MILOTA, J. SPERLING, A. NEMETH, D. ABRAMAVICIUS, S. MUKAMEL, AND H. F. KAUFFMANN. Excitonic couplings and interband energy transfer in a double-wall molecular aggregate imaged by coherent two-dimensional electronic spectroscopy. *J. Chem. Phys.* **131**, 054510 (2009)

6.1 Introduction

One of the challenges in supra-molecular chemistry and molecular nano-engineering is the identification of distinct molecular features and functions that derive from naturally occurring bio-macromolecular systems and to use these properties in bio-mimeting, technical applications. An example is the imitation of the optimized energy flow in the biological light harvesting pigment complex by tailor-made, artificial molecular ensembles. Such molecular architectures, devised to mimic migrational energy trapping and charge separation, must comprise photo-antennae, storage rings, and a non-statistical energy gradient, where the photon absorbed is guided without substantial losses as a molecular exciton on a selective, highly directional space-energy pathway to the exit-channel of chemical conversion [158, 159]. One appealing synthetic route is the potential of certain dye molecules to self-assemble to molecular aggregates [134, 135].

In molecular aggregates, the spatial proximity of molecular transition dipole moments leads to site-to-site coupling (V) and the formation of Frenkel excitons that are shared by many molecules and whose spectroscopic properties have been continuously attracting theoretical [160, 161, 162, 163] and experimental interest [164, 165]. The sharp linear absorption (LA) band of one-dimensional structures, e.g. the J-band of pseudoisocyanine dye aggregates [166, 167], is well-known to be dominated by a few one-exciton states only, lying close in energy, and is spectrally narrowed by excitation delocalization. J-aggregates are the closest molecular analogue of inorganic semiconductors, their unique excitonic structure and high energy transfer efficiency are relevant to many applications such as artificial photosynthesis, polariton science, and sensitized chemical dynamics [168].

J-aggregate-forming dyes usually self-assemble into linear chains, however, recent progress in fabrication enabled the synthesis of cylindrical structures out of carbocyanine dyes [169]. Tubular shapes are commonly encountered structural motifs for naturally occurring and synthetically prepared nanomaterials. Examples range from chlorosomes of green bacteria [170], over viral capsid proteins [171], to carbon nanotubes [172]. The bottom-up approach for double-wall cylindrical aggregates is based on a delicate balance between intermolecular forces, including dispersion forces of the cyanine backbone, and hydrophobic and hydrophilic interactions of the substituents. Essentially, the simultaneous linking of both hydrophobic and hydrophilic substituents to a single chromophore induces self-assembly into double-walled tubules in aqueous solutions. Their architecture is similar to the rod elements in light-harvesting chlorosomes of green photosynthetic bacteria and plants where thousands of bacteriochlorophyll (BChl) molecules self-assemble to a rod-shaped supra-molecular antenna system [173, 174].

A scheme for the self-assembling mechanism of the carbocyanine dye C8O3 is shown in Fig. 6.1a. In aqueous solution, hydrophobic interactions of the octyl-sidechains facilitate the formation of bilayer sheets, which self-assemble into several μm long cylindrical double-wall structures with typical diameters of approx. 10 nm [175]. The double-walled strands further build up helices in which up to five tubules twist around each other forming a chiral suprastructure. Possible application of these chiral systems as building blocks for artificial light harvesting devices [176] or nanometer-scale wires for energy transport [177] renders the characterization of energy flow

pathways and timescales a topic of high interest.

Femtosecond four-wave mixing (FWM) techniques, such as three-pulse photon-echo spectroscopy in conjunction with theoretical treatments [105, 162, 178, 179] have led to progressively deeper understanding of the microscopic dynamics of aggregates for some time past [166, 180, 181, 182]. These excitation-probing configurations, however, measure time-integrated and phase-averaged signal-intensities ($\propto |P^{(3)}(t_1, t_2, t_3)|^2$), and thus interrogate the loss of the squared polarization by one-dimensional projections on distinct delay-times t_i . While exciton dynamics and relaxation in population space can be verified with little difficulty almost routinely, it is hard to extract information about the nature of electronic and nuclear couplings which are the underpinnings of spatial optical femtosecond dynamics from conventional four-wave-mixing experiments.

Coherent two-dimensional electronic spectroscopy is the only technique that directly reveals electronic couplings and energy transfer pathways in real time. This method overcomes the trade-off between spectral and temporal resolution inherent to nonlinear one-dimensional techniques by mapping coupled exciton states onto off-diagonal signals. The cross peak pattern and its variation with t_2 shows the detailed energy transfer pathways, as was first experimentally demonstrated by Brixner *et al.* for the photosynthetic FMO complex in the near-infrared spectral region [31]. For a single J-band aggregate 1Q2D-ES has been demonstrated to visualize the intra-band, heterogeneous dephasing dynamics of closely spaced, delocalized exciton states [183]. In the course of our studies, we have expanded the applicability of the method on the family of cyanine-based multi-band aggregates, with the objective to experimentally trace inter-band excitonic coupling, exciton population relaxation, and energy-transfer, without the necessity to infer a biased model to our experimental data.

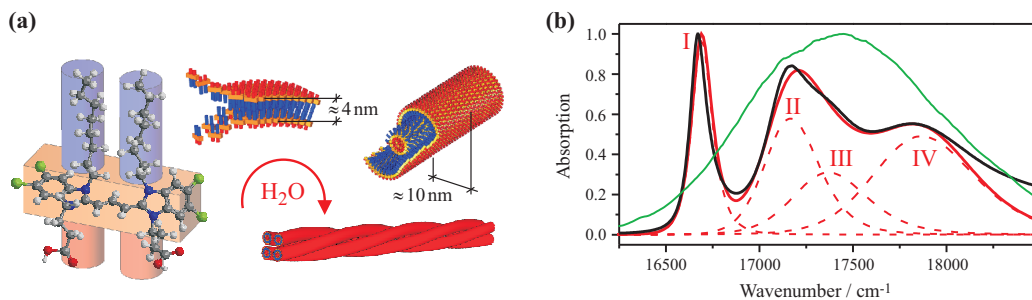


Figure 6.1: (a) Schematic of the self-assembling mechanism for building-up the double-wall tubular system C8O3 and its chiral suprastructure. The chromophore is depicted in orange, hydrophilic (hydrophobic) sidechains are colored red (blue). (b) The experimental linear absorption spectrum (black line) can be satisfactorily described by four electronic oscillators (dashed red lines indicate their individual contributions, solid red line shows their sum). The laser pulse spectrum is shown as the green envelope.

6.2 Experimental Details

The bandwidth of our 16 fs pulses (approx. 1000 cm^{-1}) is broad enough (solid green line in Fig. 6.1b) to entirely cover the absorption spectrum of C8O3 when tuned by the NOPA to a center frequency of 17500 cm^{-1} . To avoid undesired higher-order effects, excitation beams are attenuated to yield less than 3 nJ of energy in each of the excitation pulses. This excitation density has been shown to be low enough to exclude annihilation effects from contributing to the detected signal [184]. t_1 -delays (recorded over positive and negative delays (± 200 fs) for capturing both rephasing and non-rephasing contributions) are sampled above the Nyquist-frequency dictated by the electronic resonances. The carbocyanine dye C8O3 was purchased from FEW Chemicals (Wolfen, Germany) and has been used as received. The aggregate solution has been prepared according to literature [185] with a dye concentration in aqueous solution of $1 \cdot 10^{-4}$ mol/l. With a beam diameter of 5 mm at the focusing mirror (SM3 in Fig. 3.4), this corresponds to a fluence of $3.6 \cdot 10^{14}$ photons/cm², leading to the excitation of 1.7% of the molecules in the focal volume.

6.3 Linear Absorption

In the absence of disorder, i.e. assuming lattice periodicity, excitons are described by Bloch-type (\mathbf{k} -space) wavefunctions. The cylindrical geometry splits the linear absorption of an isolated tubule into a longitudinal (coinciding with the cylinder axis) and two energy-degenerate transversal transition (perpendicular to the cylinder axis) [186] (Fig. 6.2a). The splitting is inversely proportional to the tube diameter, while the red-shift with respect to the monomer transition is a measure for inter-chromophore coupling strengths (Fig. 6.2b). For a double wall system with typical tube-in-tube architecture (inner tube i , outer tube o), with electronic transitions \parallel_i , \parallel_o parallel to the long cylinder axis and \perp_i , \perp_o perpendicular to them (Fig. 6.2c), the naturally arising question is to which extent the spectrum of the bi-tubule molecular nanosystem can be thought of as a simple superposition of two single-tube contributions. In the absence of ground-state interaction, the longitudinal electronic transition \parallel_o of the outer tubule (with a larger diameter d_o and higher self-energy of its ring-unit) is expected to shift to the blue, whereas the splitting $\Delta\omega$ between transitions \parallel_o and \perp_o (inversely dependent on d_o) will be smaller, such that the spectral positions of the perpendicular bands \perp_i and \perp_o tend to coincide.

The linear absorption spectrum of C8O3 in water (Fig. 6.1b) exhibits four excitonic bands (I-IV). Polarized light measurements identify the transitions I and II as polarized parallel to the long cylinder axes with center positions of 16670 cm^{-1} and 17170 cm^{-1} [184]. Changes in the absorption spectrum through the addition of diverse surfactants led to the conclusion that bands I and II correspond to the longitudinally polarized transitions of the inner and the outer cylinder, respectively [187]. The blue-shift of band II with respect to band I in combination with a larger diameter of the outer tube leads to a merging of the two perpendicular transitions associated with the two cylinders into one band (III), showing up as a weak shoulder at 17380 cm^{-1} . Band IV at 17860 cm^{-1} presumably originates from electronic excitations sharing several closely lying tubules

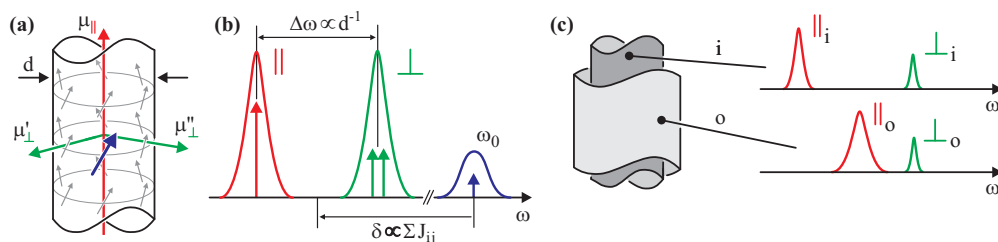


Figure 6.2: (a) Schematic spatial arrangement of monomer transition moments in a homogeneous cylindrical molecular aggregate, resulting in a longitudinal (μ_{\parallel}) and two (energy-degenerate) transversal transitions (μ'_{\perp} , μ''_{\perp}). (b) The corresponding linear absorption spectrum of the single-wall structure. The splitting $\Delta\omega$ between bands \parallel and \perp is inversely proportional to the diameter of the tubule. The spectral red-shift δ with respect to the monomer transition (ω_0) reflects inter-chromophore coupling strengths. (c) Situation for a double walled system with the broadened transition \parallel_o and the coincident transitions \perp_i and \perp_o .

[170] in the helical architecture, similar to the collective excitations in chlorosomal stacks.

The experimental linear absorption and linear dichroism (not shown) spectra can be well reconstructed by a four effective electronic oscillator model, as shown by the red line in Fig. 6.1b. Clearly, information about inter- and intra-band electronic couplings, energy transfer mechanism, or its time-scales cannot be extracted from the linear spectrum. The absence of this kind of information requires the application of nonlinear techniques. So far, the excitonic effects of inter-band coupling have been treated theoretically for closely spaced linear aggregates [188], which have shown that Förster energy transfer mechanism is not valid anymore if the separation of the two chromophores is smaller than the exciton delocalization length. For the case of the similar aggregate C8S3 [189] the microscopic model leads to the conclusion that the inner and outer tube cannot be considered as electronically decoupled but as weakly coupling excitonic manifolds (cf. Chapter 8). Based on recent advances in the field of 2D-ES it is clear that this technique is the instrumentation of choice in the study of molecular fs-couplings. By employing coherent 1Q2D-ES, we demonstrate measurements of off-diagonal peaks in frequency-frequency correlation plots and thus directly probe electronic coupling and electron-phonon scattering. The latter elementary processes are the underpinnings of exciton dynamics allowing the entire state-to-state energy transfer pathways in C8O3 to be imaged in real time.

6.4 Results and Discussion

6.4.1 Correlation Spectra ($t_2 = 0$ fs)

The amplitude of the experimental 1Q2D electronic correlation spectrum ($t_2 = 0$ fs) is depicted in Fig. 6.3a. By comparing the diagonal ($|\omega_1| = \omega_3$) amplitude maxima of the nonlinear signal to the linear absorption (shown along ω_1) we can identify the spectral positions of bands I-IV, as defined in Fig. 6.1b. The relative intensities of the diagonal peaks are different from the absorption

spectrum, since they scale as $|\mu_i|^4$ with the transition dipole, rather than $|\mu_i|^2$ as in LA. In addition, the pulse power spectrum, optimized to cover the entire region of transitions, gives rise to different center-frequency detunings for each of the four transitions and thus affects the relative excitation intensities of the bands. Overall, peak IV is therefore less intense in the 1Q2D spectrum than in 1D LA.

The observation of cross peaks of varying intensities in the off-diagonal $|\omega_1| > \omega_3$ triangular part of the spectrum at $t_2 = 0$ fs indicates coupling between bands. The most prominent cross peak at this delay stems from strong correlations between bands I and III, corresponding to the parallel and perpendicular transitions of the inner cylinder, as well as from couplings between band II and IV. Further, a lower intensity cross peak is indicative of weak coupling between I/IV and I/II. The correlation spectrum is strongly asymmetric and favors cross peaks in the low-energy ($|\omega_1| > \omega_3$) triangle. This is accompanied by the untypical spectral orientations of the off-diagonal peaks which are closely related to the asymmetry of the correlation matrix. They are no longer parallel to the main diagonal as expected for a positive motional correlation at $t_2 = 0$ fs [190], but rather horizontally aligned, i.e. parallel to the ω_1 -axis. This tendency towards early relaxation of cross peaks is mainly caused by the finite width of the excitation pulses. The experimental 1Q2D data are sub-20 fs pulse convolutions and are not corrected by numerical inversion. Fast coherence loss thus breaks the symmetry of the excitation correlation-matrix where the spectral contour of the cross peaks rotates from an alignment originally parallel to the main diagonal into an orientation parallel to the ω_1 -axis. The stretching of the off-diagonal intensities along ω_1 reflects

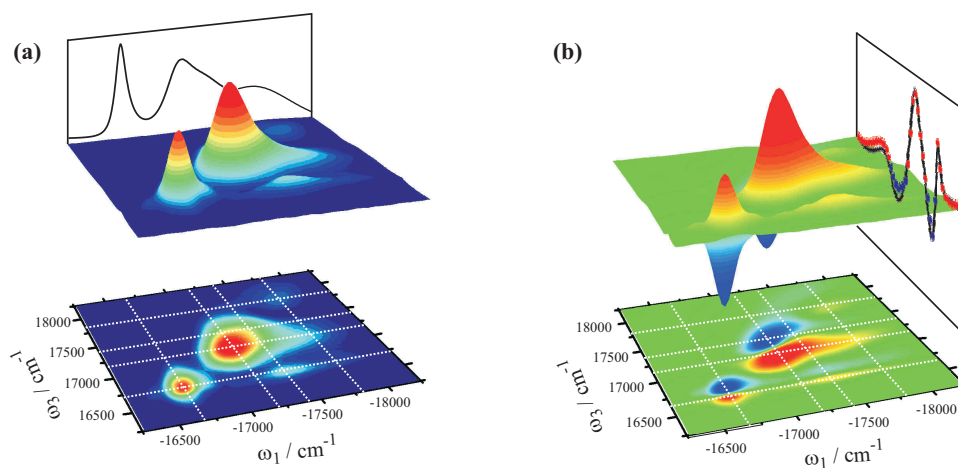


Figure 6.3: Amplitude (a) and absorptive part (b) of the 1Q2D electronic correlation ($t_2 = 0$ fs) spectrum of C8O3. Both spectra are normalized to their respective maximum absolute value. The linear absorption spectrum is plotted along ω_1 in panel (a), whereas the spectrally resolved pump-probe spectrum (red and blue dots) together with the projection of the absorptive part onto ω_3 (black line) is plotted in panel (b). White dotted lines mark the positions of peak maxima in the linear absorption spectrum.

a distribution of inter-band coupling strengths between exciton states that share a common ground state.

Upon examination of the absorptive part of the 1Q2D signal shown in Fig. 6.3b, we can dissect the various pathways which interfere to form the observed 2D pattern. Excitonic intermolecular couplings reshape an aggregate's electronic structure to a manifold of single- and double-excited states, referred to as the one- and the two-exciton manifold, respectively. The two-exciton manifold essentially distinguishes the optical response of an excitonic aggregate from that of an electronic two-level system. As a consequence of the repulsive interactions between excitons, transitions between successively higher excitonic manifolds are blue-shifted with respect to each other. Positive contributions to the absorptive part can thus be assigned to ground state bleaching (GSB) and stimulated emission from one-exciton states (SE), negative contributions arise from excited state absorption (ESA) into the two-exciton manifold [4] (cf. Fig. 1.1). These two contributions are of equal strength for the diagonal peaks of bands I, II, and III, whereas band IV only shows a weak positive feature. The projection of the absorptive part onto the ω_3 -axis agrees very well with the spectrally resolved pump-probe signal as shown on the right side of Fig. 6.3b. Similar to the amplitude spectrum, off-diagonal features are present in the $|\omega_1| > \omega_3$ region of the absorptive part. We observe predominant cross peaks from strongly coupled bands I/III and II/IV, respectively. The observed off-diagonal features are dominated by positive GSB and SE contributions, with ESA signals only having a marginal contribution.

6.4.2 Relaxation Spectra ($t_2 > 0$ fs)

Recording 1Q2D spectra for $t_2 > 0$ fs allows us to directly follow the excitation transfer pathways (Fig. 6.4). The relaxation can be divided thereby into three dynamical regimes. Within the first 50 fs the onset of inter-band dephasing and exciton population relaxation leads to the disappearance of the weak signal of band IV. This loss in intensity is paralleled by (i) a relative increase of the off-diagonal one-exciton signal intensities (positive signals) among all bands in $|\omega_1| > \omega_3$ space, and (ii) the appearance of bi-exciton couplings (negative off-diagonal signals). At t_2 times between 50 and 200 fs, ongoing population relaxation transforms the initial pattern of cross peaks into streak-like shapes, thus mapping out the most efficient relaxation channels. In this regime, the optical dynamics are mainly controlled by the irreversibility of relaxations from doorway-states in the vicinity of band II and III seeded by band IV via IV/III and IV/II off-diagonal traces. After 200 fs the 2D spectrum is mainly governed by relaxation from states in the vicinity of band III. This causes streaking of band II along ω_1 resolving the coupling between band III and II originally hidden under the intense diagonal peak. Furthermore, the cross peak intensities tend to converge to those of the diagonal signals because growing delays t_2 of the analyzing third pulse (\mathbf{k}_3) cause increasing inter-band dephasing. After 500 fs we observe relaxation from band II into band I, a process that completes the cascade of exciton funneling into the lowest accessible state. Thus it is striking that population of I via the II/I coupling pathway between outer and inner cylinder coordinates is strongly delayed compared to the cross peak gain of I via direct III/I coupling. Quite obviously, the initial (delocalized) coherence tries to find the optimum coordinates for the

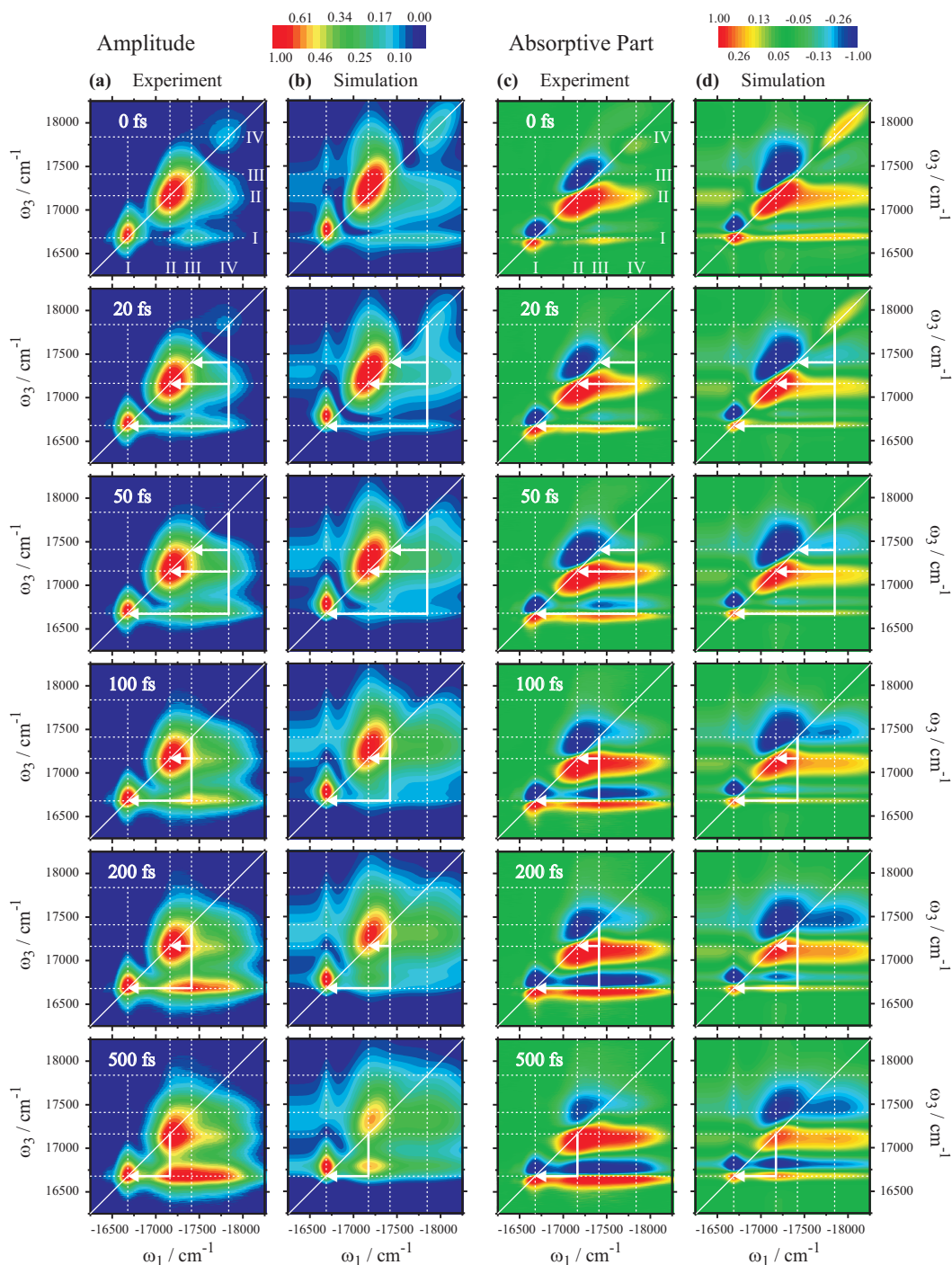


Figure 6.4: (a, b) Amplitude and (c, d) absorptive part representation of 1Q2D spectra of C8O3 for t_2 -delays of 0, 20, 50, 100, 200, and 500 fs (from top to bottom). Panels (a) and (c) show experimental data, panels (b) and (d) display simulated data. All spectra are normalized to their respective maximum absolute value. White dotted lines indicate the peak positions in linear absorption. White arrows mark the main energy transfer pathways.

outer to inner tube population transfer, and this reorganization of excitations must proceed via the migrational, multi-step mechanism which costs time.

The 1Q2D spectra shown in Fig. 6.4 demonstrate that the excitonic energy transfer across the space-energy landscape of bands I-IV is a network of delicately balanced intra-band mixing, single-step energy transfer, and migrational band-to-band processes, that overall determine the distinct signature of excitation energy flow in C8O3 aggregates. The basic steps of exciton pathways and transfer are immediately comprehensible in 2D coherent electronic spectra, without any preconceived bias. White arrows drawn in the 2D spectra (Fig. 6.4) illustrate the predominant band-to-band couplings and population transfer pathways. One fast route to population gain in band I stems from band III and IV via couplings III/I and IV/I in parallel, single-step transfers. The second source term for the population of I proceeding from IV via couplings IV/III, III/II, and II/I is a migrational multi-step process, with the actual tube-to-tube spatial electronic transfer substantially delayed. 2D spectroscopy thus reveals that the dynamics of the downhill energy flow in C8O3 is no trivial irreversible funneling process, but quite obviously complicated by single-step source terms that make the kinetics more complex. Particularly in the proximity of bands II and III, spatio-energetic factors seem to create a kinetic bottle-neck with a significant increase of the exciton dwell-time and population density numbers in bands II/III prior to the final event of II→I outer- to inner-tube transfer.

These particulars and details impressively illustrate why 2D-ES is superior to other third-order techniques. Energy-selective excitation in pump-probe experiments [184] bears a trade-off in time-resolution, whereas the 2D-ES technique allows to exploit broad spectral bandwidths and short temporal widths of ultrafast excitation pulses in one and the same experiment. Moreover, additional insights into the nature of the high-energy, diagonal absorber IV and its unique role as a powerful mediator of optical funneling can be gained in such a study. Quite obviously, its ultrafast deactivation has decisive impact on the early relaxation regime ($t_2 < 50$ fs) which dramatically affects the patterns of initial cross peaks in the subsequent optical dynamics. Despite its short-lived (50 fs) correlation lifetime, the electronic communication of band IV is far-reaching and persistent, and its huge coupling efficiency creates a network of exciton source terms in the fore-front of band II to band I transfer as discussed above. 2D spectra show that the molecular organization of transition IV must differ from those in I, II, and III, i.e. band IV is less compact and more exposed to environmental bath-dynamics which may explain its short correlation survival time.

6.4.3 Rephasing and Non-Rephasing Spectra

The time reversal in the scanning procedure of coherence time t_1 , from negative to positive time-delays, produces both S_I and S_{II} time-domain signals that contribute into the phase-matched directions \mathbf{k}_I and \mathbf{k}_{II} to make up the total signal, i.e. a superposition of the photon echo (S_I) and optical free induction decay (S_{II}) profiles. The absorptive 1Q2D spectrum is the sum of the two signals. Based on the third order response function theory, each of the two contributions is given by the Fourier transform of its corresponding response functions [191]. Following a previous theoretical treatment [122], one expects two limiting cases for the evolution of S_I and S_{II} data. For

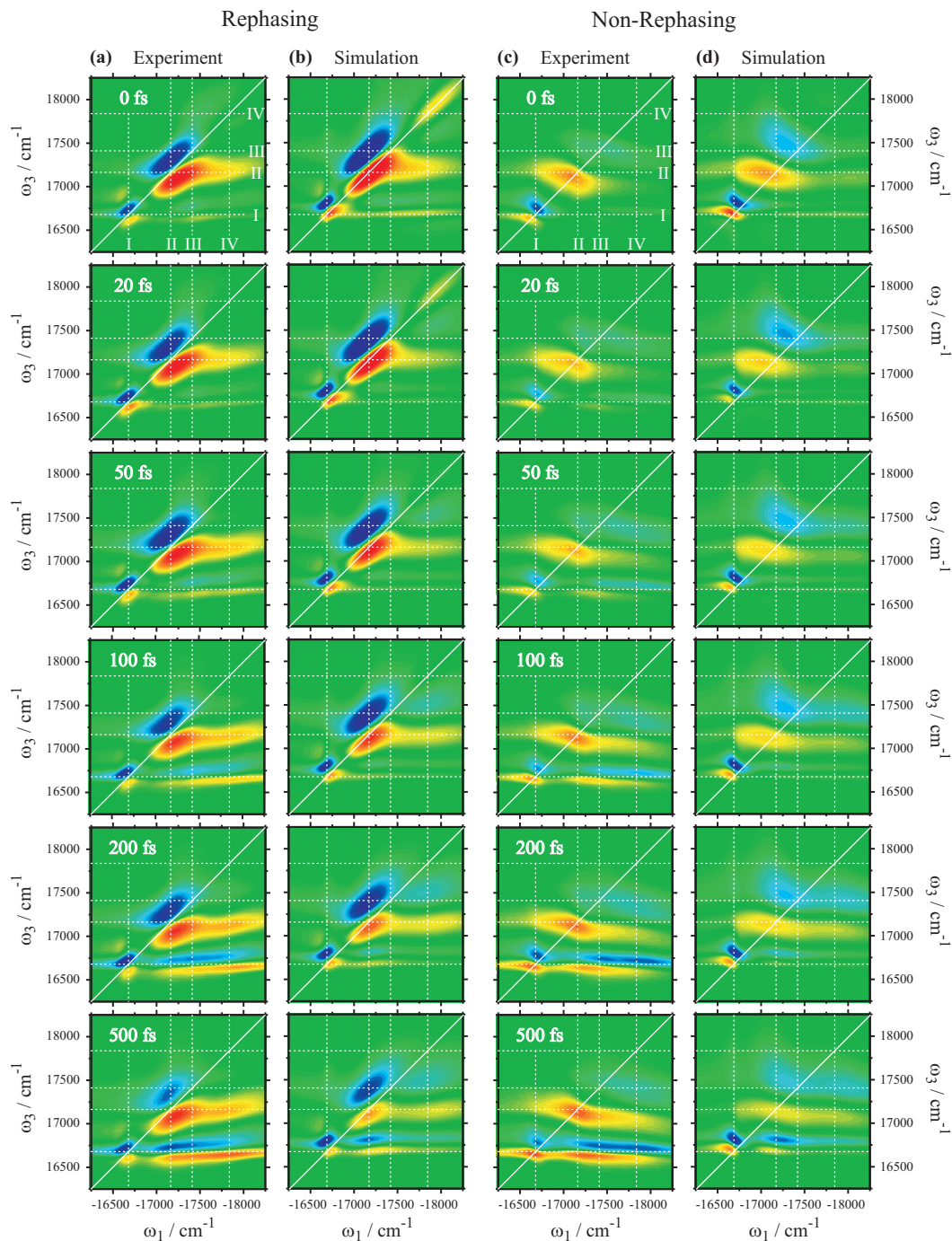


Figure 6.5: (a, b) Rephasing and (c, d) non-rephasing real part representation of 1Q2D spectra of C8O3 for t_2 -delays of 0, 20, 50, 100, 200, and 500 fs (from top to bottom). Panels (a) and (c) show experimental data, panels (b) and (d) display simulated data. All spectra are displayed with their relative contribution to the absorptive spectra shown in Fig. 6.4. White dotted lines indicate the peak positions in linear absorption.

early t_2 -times, shorter than the correlation time τ_c (in this limit the frequency correlation function $C(t)$ has not decayed much), the S_I signal is much more intense than the S_{II} one. For longer t_2 -times the intensity of the S_{II} signal increases. The ratio of the rephasing/non-rephasing signal intensities are controlled then by the loss of correlation memory of the echo signal [192].

Fig. 6.5a and c display the experimental S_I and S_{II} spectra for $t_2 = 0, 20, 50, 100, 200,$ and 500 fs, respectively. Both the S_I and S_{II} signals show their typical line-shapes: while the former are elongated along the diagonal, due to density matrix rephasing, the latter are oriented into the direction of the anti-diagonal axis [18, 117, 118]. Their sum is thus oriented horizontally for uncorrelated exciton states. For waiting times up to 200 fs, the experimental S_I signal is much stronger than the non-rephasing one ($S_I/S_{II} \approx 3$). Conversely, for longer waiting times $t_2 > 200$ fs, the intensity of the S_{II} signal grows and both contributions nearly equalize in intensity in the asymptotic regime.

Comparison of decomposed rephasing and non-rephasing 1Q2D spectra reveals details of inter-band couplings and their different contributions to the absorptive ($S_I + S_{II}$) 1Q2D spectra (Fig. 6.4b). Accordingly, one perceives that the early coupling between IV and II and its powerful streaking is mainly accessible to the rephasing wave-vector architecture. On the other hand, the effect of rephasing and non-rephasing pulse sequences is less pronounced for couplings IV/I and III/I. Each of the IV/I and III/I cross peak streakings from S_I and S_{II} data simply differ by tiny positive/negative slopes of equal size whose orientations (angle) relative to the ω_1 axis average-out in the $S_I + S_{II}$ experimental spectra to yield the horizontal streak spectrum.

The phase-twisted line-shapes may be used to disentangle the spectral convolution of band transitions II and III and thus to characterize the spectroscopic features of these bands. Since diagonal line-widths of individual transitions are narrower in the non-rephasing spectrum, they have the potential to spectrally resolve closely spaced diagonal and off-diagonal peaks usually concealed along the main diagonal trace of photon echo data [193]. Quite obviously, the intense and inhomogeneously broadened peak II overlapping peak III in LA (Fig. 6.1b) becomes spectrally resolved in the S_{II} spectra. For $t_2 \geq 50$ fs a negative feature at the location of the cross peak IV/III, indicative of coupling between IV and III can be observed. Due to oppositely signed contributions (positive SE and GSB from IV/III and negative ESA from III/II) only the weak ESA contributions of IV/III coupling and the positive contributions of SE and GSB of III/II are visible.

6.5 Numerical Simulations

The third-order nonlinear signal $E_s^{(3)}(t_1, t_2, t_3)$ and its double Fourier transform $E_s^{(3)}(\omega_1, t_2, \omega_3)$ analog are reconstructed by theory and computational simulation [191]. The procedures aim at recovering inter-band electronic couplings, exciton relaxation, and population transfer and rely on the calculation of the third-order optical response function, that reflect the system properties relevant for the specific experiment through all possible system Liouville space pathways [4]. A microscopic calculation of the response functions, however, requires explicit information about the precise architecture of C8O3 and the nature of its single- and double-excited eigenstates. The

mesoscopic tubular aggregates dealt with in this contribution contain a huge number of molecules. A microscopic model that incorporates monomeric site-disorder needs to contain at least roughly several thousands of coupled chromophores for a double-wall cylindrical structure with converged spectral properties (i.e. the spectra are independent of the length of the cylinder). For instance, for 1000 two-level molecules we obtain 1000 single-exciton states and ≈ 500000 double-exciton states. The signal calculation would then have to involve three-fold summation over these states. This rough estimate already precludes any atomistic-type approach for calculating nonlinear signals, thus being far beyond the currently available computational resources.

However, the linear absorption spectrum (Fig. 6.1b) suggests that only few optically active single-exciton bands are relevant. In order to represent the observed features and to quantify relaxation pathways and timescales, we therefore create an effective exciton model containing single- and double-excited states. These states represent the whole excitonic bands of the tubule, which show up in the absorption spectrum. The bands can be single- or double-excited, thus each band is represented by an anharmonic oscillator. This allows to implement an iterative fitting procedure of effective model parameters and reveals the physical basis of the underlying processes.

The system is represented by the Hamiltonian

$$\hat{H}_S = \hbar \sum_{e=1}^4 \varepsilon_e \hat{B}_e^\dagger \hat{B}_e + \frac{1}{2} \hbar \sum_{e,e'=1}^4 \Delta_{ee'} \hat{B}_e^\dagger \hat{B}_{e'}^\dagger \hat{B}_e \hat{B}_{e'} \quad (6.1)$$

where \hat{B}_e^\dagger is the Bosonic creation operator of the e th band exciton. The Hamiltonian parameters are: ε_e is the energy of the e th one-exciton band (determined from LA), $2\varepsilon_e + \Delta_{ee}$ its bi-exciton energy and $\varepsilon_e + \varepsilon_{e'} + \Delta_{ee'}$ is the energy of the state if the double-exciton is distributed between the exciton bands e and e' . The quantity Δ gives the binding energies of two-exciton bands and thus is the representation of exciton couplings: if all off-diagonal elements of the matrix $\Delta_{ee'}$ are zero, the Hamiltonian represents uncoupled oscillators and the two-dimensional spectrum at zero delay time t_2 will have no inter-exciton cross peaks. Thus fitting of the 2D spectrum provides a handle to determine the matrix $\Delta_{ee'}$.

This system is coupled to the laser field through the system-field interaction Hamiltonian

$$\hat{H}_{SF}(t) = - \sum_{e=1}^4 \mu_e \cdot \mathbf{E}_t(t) \hat{B}_e^\dagger + \frac{1}{\sqrt{2}} \mu_e^{(2)} \cdot \mathbf{E}_t(t) \hat{B}_e^{\dagger 2} \hat{B}_e + h.c., \quad (6.2)$$

where μ_e is the transition dipole from the ground state to the single-exciton e and $\mu_e^{(2)}$ is its correction for the transition from the single- to the double-exciton state. $\mathbf{E}_t(t)$ represents the total laser field. In the simulations we have assumed the same polarization for all pulses.

The relaxation dynamics originates from the system-bath coupling, represented by

$$\hat{H}_{SB} = \hbar \sum_{e=1}^4 \sum_{\alpha} d_{e\alpha} \hat{B}_e^\dagger \hat{B}_e (\hat{a}_{\alpha}^\dagger + \hat{a}_{\alpha}) \quad (6.3)$$

where \hat{a}_α^\dagger and \hat{a}_α are the harmonic bath excitation creation and annihilation operators for the mode α and $d_{e\alpha}$ is the coupling strength between the mode α and exciton band e . For the infinite number of bath modes, we use the continuous bath spectral density reflecting uncorrelated fluctuations of transition energies

$$C_e''(\omega) = \pi \sum_{\alpha} d_{e\alpha}^2 [\delta(\omega - w_\alpha) - \delta(\omega + w_\alpha)], \quad (6.4)$$

where w_α is the characteristic frequency of the α th harmonic bath mode. The specific choice of the spectral density reflecting the multi-mode overdamped Brownian oscillator bath model uniquely defines the line-shapes of both single- and double-exciton states. We then have

$$C_e''(\omega) \equiv \sum_{\alpha}^M 2\lambda_{e,\alpha} \frac{\omega\Lambda_\alpha}{\omega^2 + \Lambda_\alpha^2}. \quad (6.5)$$

Here the α th Brownian mode is characterized by the relaxation timescale of the bath correlations Λ_α^{-1} and the coupling strength between the e th oscillator and α th bath mode $\lambda_{e,\alpha}$.

To account for correlated spectral line-broadening, each effective oscillator is coupled to an overdamped Brownian oscillator given by Eq. (6.3). This results in fluctuations of system Hamiltonian parameters. Fluctuations of eigenstate energies induce spectral broadenings. For the whole system this results in the matrix of the line-shape functions g_{ab} , which characterize correlated fluctuation of transition energies of a and b global states. The line-shape function is related to the fluctuation correlation function as described in Ref. [4]. For our model of a set of Brownian coordinates (see Eq. (6.5)) the line-shape function is given by

$$g_{ab}(t) = \sum_{\alpha}^M \frac{\lambda_{ab,\alpha}}{\Lambda_\alpha} \left(\frac{2k_B T}{\hbar\Lambda_\alpha} - i \right) (\exp[-\Lambda_\alpha t] + \Lambda_\alpha t - 1). \quad (6.6)$$

In the present model, we have assumed that the bath-induced fluctuations of the single- and double-excited state of each effective oscillator are fully correlated, whereas for different oscillators the fluctuations of levels are uncorrelated. Within these assumptions, the line-shape functions for the double-excited states can be uniquely deduced from the line-shape functions of the single-excited states.

As a starting point, by examining the linear absorption spectrum and identifying the four observed peaks I, II, III, and IV, we postulate four single-exciton bands and represent them by four single-exciton states. Their transition energies and transition dipole moments (transition amplitudes) are deduced by using the decomposition of the experimental absorption spectrum into four Gaussian peaks by a least-square fitting procedure, which provide a starting set of parameters. To cover the spectral line-shapes we couple each single-exciton state to two over-damped Brownian oscillator coordinates ($M = 2$) [47]. The first (fast) will be responsible for the homogeneous line-width (Lorentzian line-shape), while the second (static) will be responsible for the inhomogeneous line-width (Gaussian line-shape).

Table 6.1: One-exciton state energies (ε_e), their transition dipoles [$\mu = (x, y, z)$; $y = 0$ so we give just (x, z)], and system-bath coupling strengths (λ) for the two bath Brownian modes (the corresponding bath timescales $\Lambda_{fast}^{-1} = 50$ fs, $\Lambda_{slow}^{-1} = \infty$). Bi-exciton diagonal binding energies (Δ_{ee}), bi-exciton state energies ($\varepsilon_f = 2\varepsilon_e + \Delta_{ee}$), and their transition dipoles (no combination states) are given as well. Note that here $\mu_{ef} = \sqrt{2}\mu_e + \mu_e^{(2)}$.

Band	I	II	III	IV
$\varepsilon_e/\text{cm}^{-1}$	16705	17170	17400	17890
$\mu_e, (x, z)/\text{a.u.}$	(0, 110)	(0, 136)	(66, 95)	(90, 148)
$\lambda_{fast}/\text{cm}^{-1}$	20	40	40	40
$\lambda_{slow}/\text{cm}^{-1}$	0	30	60	140
$\Delta_{ee}/\text{cm}^{-1}$	150	250	50	0
$\varepsilon_f/\text{cm}^{-1}$	33560	34590	34850	35780
$\mu_e^{(2)}, (x, z)/\text{a.u.}$	(0, 40)	(0, 20)	(0, 10)	(-9, -15)
$\mu_{ef}, (x, z)/\text{a.u.}$	(0, 196)	(0, 212)	(93, 144)	(118, 194)

The linear absorption spectrum is obtained by

$$\kappa_A(\omega) \propto \omega \text{Im} \int_0^\infty dt \exp(i\omega t) R^{(1)}(t) \quad (6.7)$$

where

$$R^{(1)}(t) = \frac{i}{3} \sum_e |\mu_{eg}|^2 \exp(-i\varepsilon_e t - \gamma_{eg} t - g_{ee}(t)) \quad (6.8)$$

is the linear response function. $g(t)$ is the complex line-shape function originating from the system-bath interaction and is computed from the bath spectral densities. Note that system-bath couplings $\lambda_{e\alpha}$ induce the shifts of resonant absorption frequencies through $g(t)$. Additionally, we have tuned the transition dipole directions away from all-parallel alignment using linear dichroism data (not shown). This adjustment improves the fit of the 1Q2D correlation signals described later. The adjusted parameters (transition energies, transition dipole amplitudes, and system-bath coupling constants) are listed in Tab. 6.1. The resulting calculated linear absorption being depicted in Fig. 6.1b gives a quite satisfactory fit to the experimental data.

Expressions of the $R_I^{(3)}$ and $R_{II}^{(3)}$ response functions can be written for an excitonic aggregate model with the ground state g , a single-exciton manifold e , and a double-exciton manifold f of the system eigenstates. We then have for the \mathbf{k}_I response function [191]:

$$R_{I,SE}^{(3)}(t_1, t_2, t_3) = \sum_{e_4 e_3 e_2 e_1} \langle (\mu_{ge_4} \cdot \mathbf{E}_4(\bar{\omega}_4 + \omega_{ge_4})) (\mu_{e_3g} \cdot \mathbf{E}_3(\bar{\omega}_3 - \omega_{e_3g})) (\mu_{e_2g} \cdot \mathbf{E}_2(\bar{\omega}_2 - \omega_{e_2g})) \rangle \\ \times (\mu_{ge_1} \cdot \mathbf{E}_1(\bar{\omega}_1 + \omega_{ge_1})) \exp(-i\xi_{e_4g} t_3 - i\xi_{ge_1} t_1 - \varphi_E^{(I)}(t_3, t_2, t_1)) \mathcal{G}_{e_4 e_3, e_2 e_1}(t_2), \quad (6.9)$$

$$\begin{aligned}
 R_{\text{I},GSB}^{(3)}(t_1, t_2, t_3) &= \sum_{e_4, e_1} \langle (\mu_{ge_4} \cdot \mathbf{E}_4(\bar{\omega}_4 + \omega_{ge_4})) (\mu_{e_4g} \cdot \mathbf{E}_3(\bar{\omega}_3 - \omega_{e_4g})) (\mu_{e_1g} \cdot \mathbf{E}_2(\bar{\omega}_2 - \omega_{e_1g})) \\
 &\quad \times (\mu_{ge_1} \cdot \mathbf{E}_1(\bar{\omega}_1 + \omega_{ge_1})) \rangle \exp(-i\xi_{e_4g}t_3 - i\xi_{ge_1}t_1 - \varphi_B^{(I)}(t_3, t_2, t_1)), \quad (6.10)
 \end{aligned}$$

$$\begin{aligned}
 R_{\text{I},ESA}^{(3)}(t_1, t_2, t_3) &= - \sum_{fe_4e_3e_2e_1} \langle (\mu_{e_3f} \cdot \mathbf{E}_4(\bar{\omega}_4 + \omega_{e_3f})) (\mu_{fe_4} \cdot \mathbf{E}_3(\bar{\omega}_3 - \omega_{fe_4})) (\mu_{e_2g} \cdot \mathbf{E}_2(\bar{\omega}_2 - \omega_{e_2g})) \\
 &\quad \times (\mu_{ge_1} \cdot \mathbf{E}_1(\bar{\omega}_1 + \omega_{ge_1})) \rangle \exp(-i\xi_{fe_3}t_3 - i\xi_{ge_1}t_1 - \varphi_A^{(I)}(t_3, t_2, t_1)) \mathcal{G}_{e_4e_3, e_2e_1}(t_2), \quad (6.11)
 \end{aligned}$$

where we have introduced the complex frequencies $\xi_{ab} \equiv \varepsilon_a - \varepsilon_b - i\gamma_{ab}$, (ab) density matrix coherence damping γ_{ab} , transition dipoles μ_{ab} between exciton states a and b , zero-centered laser pulse spectral envelopes $\mathbf{E}_j(\omega)$ of pulses $j = 1, 2, 3, 4$, the pulse carrier frequencies $\bar{\omega}_j$, orientational averaging of scalar products $\langle \dots \rangle$, time dependent correlation-damping phase functions φ as well as single-exciton propagation Green's functions \mathcal{G} .

For the \mathbf{k}_{II} response functions we similarly get

$$\begin{aligned}
 R_{\text{II},SE}^{(3)}(t_1, t_2, t_3) &= \sum_{e_4e_3e_2e_1} \langle (\mu_{ge_4} \cdot \mathbf{E}_4(\bar{\omega}_4 + \omega_{ge_4})) (\mu_{e_3g} \cdot \mathbf{E}_3(\bar{\omega}_3 - \omega_{e_3g})) (\mu_{ge_1} \cdot \mathbf{E}_2(\bar{\omega}_2 + \omega_{ge_1})) \\
 &\quad \times (\mu_{e_2g} \cdot \mathbf{E}_1(\bar{\omega}_1 - \omega_{e_2g})) \rangle \exp(-i\xi_{e_4g}t_3 - i\xi_{e_2g}t_1 - \varphi_E^{(II)}(t_3, t_2, t_1)) \mathcal{G}_{e_4e_3, e_2e_1}(t_2), \quad (6.12)
 \end{aligned}$$

$$\begin{aligned}
 R_{\text{II},GSB}^{(3)}(t_1, t_2, t_3) &= \sum_{e_4e_2} \langle (\mu_{ge_4} \cdot \mathbf{E}_4(\bar{\omega}_4 + \omega_{ge_4})) (\mu_{e_4g} \cdot \mathbf{E}_3(\bar{\omega}_3 - \omega_{e_4g})) (\mu_{ge_2} \cdot \mathbf{E}_2(\bar{\omega}_2 + \omega_{ge_2})) \\
 &\quad \times (\mu_{e_2g} \cdot \mathbf{E}_1(\bar{\omega}_1 - \omega_{e_2g})) \rangle \exp(-i\xi_{e_4g}t_3 - i\xi_{e_2g}t_1 - \varphi_B^{(II)}(t_3, t_2, t_1)), \quad (6.13)
 \end{aligned}$$

$$\begin{aligned}
 R_{\text{II},ESA}^{(3)}(t_1, t_2, t_3) &= - \sum_{fe_4e_3e_2e_1} \langle (\mu_{e_3f} \cdot \mathbf{E}_4(\bar{\omega}_4 + \omega_{e_3f})) (\mu_{fe_4} \cdot \mathbf{E}_3(\bar{\omega}_3 - \omega_{fe_4})) (\mu_{ge_1} \cdot \mathbf{E}_2(\bar{\omega}_2 + \omega_{ge_1})) \\
 &\quad \times (\mu_{e_2g} \cdot \mathbf{E}_1(\bar{\omega}_1 - \omega_{e_2g})) \rangle \exp(-i\xi_{fe_3}t_3 - i\xi_{e_2g}t_1 - \varphi_A^{(II)}(t_3, t_2, t_1)) \mathcal{G}_{e_4e_3, e_2e_1}(t_2). \quad (6.14)
 \end{aligned}$$

The fluctuation-induced line-shape functions φ for each pathway in Eqs. (6.9-6.14) account for their correlated dephasing and relaxation. Based upon the results of previous work [191, 194] we use cumulant expansion techniques, where we properly account for coherent and population dynamics and take care of correlated bath fluctuations between various time intervals. Thus we obtain the

respective fluctuation induced line-shapes. The spectral broadening correlation functions for the third order response in Eqs. (6.9-6.14) are given in terms of the line broadening functions $g(t)$.

A single-exciton propagation Green's functions \mathcal{G} describes free-field density matrix dynamics in the singly-excited manifold due to fluctuations of inter-band couplings. Various levels of theory have been developed to describe system excited state dynamics with fluctuations. Using the second order perturbation theory within the Markovian approximation, the Green's function satisfies the Redfield equation

$$\frac{d}{dt}\mathcal{G}_{e_4e_3,e_2e_1} = -i\delta_{e_4e_2}\delta_{e_3e_1}\omega_{e_2e_1}\mathcal{G}_{e_2e_1,e_2e_1} + \sum_{e''e'}K_{e_4e_3,e''e'}^{(R)}\mathcal{G}_{e''e',e_2e_1}. \quad (6.15)$$

Here $K^{(R)}$ is the Redfield relaxation superoperator. This type of equation may lead to non-physical, negative or larger than 1 exciton probabilities for specific choices of $K^{(R)}$. We therefore use the secular approximation which decouples the density matrix populations and coherences. In the secular approximation we have

$$K_{e_4e_3,e_2e_1}^{(R)} = (1 - \delta_{e_4e_3})\delta_{e_4e_2}\delta_{e_3e_1}\gamma_{e_4e_3} + \delta_{e_4e_3}\delta_{e_2e_1}K_{e_4e_2}. \quad (6.16)$$

The Green's function is then given by

$$\mathcal{G}_{e_4e_3,e_2e_1}(t) = (1 - \delta_{e_4e_3})\delta_{e_4e_2}\delta_{e_3e_1}e^{-i\xi_{e_4e_3}t} + \delta_{e_4e_3}\delta_{e_2e_1}[e^{-Kt}]_{e_4e_2}, \quad (6.17)$$

where K is the population transport rate matrix: its element $K_{e_4e_2}$ denotes the exciton transfer rate from state e_2 to e_4 , while the diagonal elements satisfy $K_{ee} = -\sum_{e'}K_{e'e}$. Population relaxation has been incorporated by specifying the transport rates between the single-excited states of the effective electronic oscillators, thus giving rise to lifetime broadening.

In our simulations we use the Markovian approximation for the off-diagonal fluctuations. All diagonal fluctuations are included into the spectral broadening functions. Only life-time-broadenings are then included in the dephasing parameters γ which gives $\gamma_{ab} = \frac{(K_{aa}+K_{bb})}{2}$. While the relaxation parameters can be calculated using a microscopic bath model of the off-diagonal Hamiltonian fluctuations [191], we have fitted the rate matrix directly for our phenomenological model.

The nonlinear signals are then calculated using Eqs. (6.9-6.14) [194], which allows to properly treat bath correlations and exciton transport, respectively. The fast mode of the Brownian oscillator is the main source of exciton transport. The static mode induces spectral diffusion and is thus responsible for Gaussian spectral line-shapes. The dephasing rates γ have been used to include only finite lifetime contributions to the dephasings. All other dephasing-correlation contributions enter through the line-shape functions φ and $g(t)$.

The calculation of the third order nonlinear response functions requires knowledge of bi-exciton states f , and population transport rates. These are unavailable from the linear spectrum and there is no straightforward procedure to deduce bi-exciton states. However, the bi-exciton bands

participate in shaping the two-dimensional spectrum as their signals contribute as convolutions of single-exciton bands. Thus, we proceed with the model of coupled oscillators which is equivalent to our primary estimate of four single-exciton states. The doubly-excited states can be separated into two groups. (i) Double-excitations of the e^{th} oscillator, $f \equiv (ee)$, with energy $2\varepsilon_e + \Delta_{ee}$. (ii) Doubly-excited inter-mode state of the whole system, when two oscillators e and e' are single excited (so-called combination state), $f = (ee')$, $e \neq e'$. Such states have energy $\varepsilon_e + \varepsilon_{e'} + \Delta_{ee'}$. Each oscillator can be excited to its own doubly-excited state $f = (ee)$ only from its single-excited state e , with the amplitude of this transition being the dipole $\mu_{e,(ee)} = \sqrt{2}\mu_e + \mu_e^{(2)}$. The transition dipole from the single excited state of the oscillator e into the combination state $f = (e'e')$, $e' \neq e''$ is given by $\mu_{e,(e'e'')} = \delta_{ee'}\mu_{e''} + \delta_{ee''}\mu_{e'}$. These spectroscopic parameters are sufficient for the characterization of nonlinear properties of the coupled oscillator model. The spectral peak positions and amplitudes are now determined by ε , μ (these affect the linear absorption and the 2D spectra), and Δ , $\mu^{(2)}$ (which affect only 2D spectra).

In Fig. 6.6 the complete 14-level scheme (4 one-exciton levels of optically active excitonic bands, 4 bi-exciton levels representing intra-band double-excitations, and 6 additional bi-exciton levels representing inter-band double-excitations) which has been used to model the data is illustrated. This model is fully consistent with the Hamiltonian in Eq. (6.1). The fitting procedure of the bi-exciton manifold was performed using experimental 2D signals as follows: First, we consider $t_2 = 0$ delay so that exciton transport does not enter and keep all off-diagonal $\Delta_{ee'} = 0$ but vary only the diagonal elements Δ_{ee} to account for the intra-band one- to two-band transitions associated with each of the bands I to IV. In this way the corresponding energetic positions and intensities are

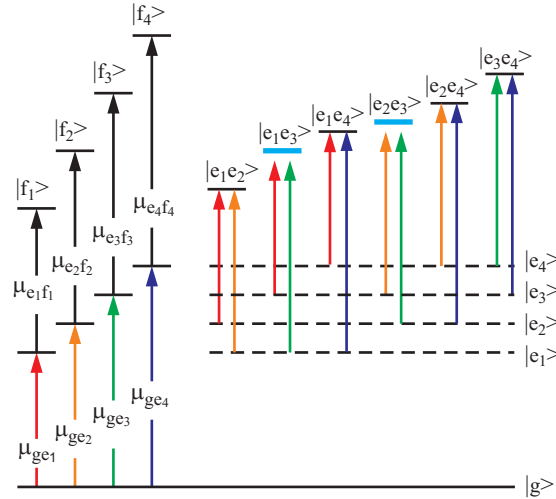


Figure 6.6: Fourteen-level scheme consisting of four one-exciton states (e), four intra-band two-exciton states (f), and six inter-band combination states (ee') to model the experimental data. Blue horizontal lines mark the combination transitions I-III and II-III at which an energy off-set needs to be introduced for satisfactorily recovering the experimentally observed coupling pattern.

Table 6.2: Energies of combination bands ($\epsilon_{ee'}$) and their energetic off-sets ($\Delta_{ee'}$).

Combination-Band	I-II	I-III	I-IV	II-III	II-IV	III-IV
$\epsilon_{ee'}/\text{cm}^{-1}$	33875	34155	34595	34820	35060	35290
$\Delta_{ee'}/\text{cm}^{-1}$	0	50	0	250	0	0

adjusted for best match of positive and negative contributions to the diagonal peaks in the 1Q2D signal (cf. Tab. 6.1). In a second step, to model the off-diagonal signal intensities induced by electronic inter-band couplings, we additionally tune the off-diagonal elements of $\Delta_{ee'}$ (Tab. 6.2). This allows to uniquely determine the inter-band coupling strengths. The simulation procedure is summarized graphically in Fig. 6.7.

Iterative readjustment of population transfer rates among all of the bands I to IV involved in energy transfer is taken into consideration for best numerical agreement with the experimental data at various delay times, i.e. optimum reconstruction of electronic couplings, relaxation rates, population streaking, and energy flow in terms of the various Liouville space pathways of the density matrix trajectory and their corresponding optical response functions. In all calculations the theoretical response functions have been convoluted with the experimental Gaussian pulses to account for the finite width of the sub-20 fs pulse envelope taken from the experiment. Overall, the quality of the computational spectra compared to their experimental counter-parts (Fig. 6.4b and d, Fig. 6.5b and d) is good and comparable with the trends described in literature [18, 117, 118]. The fit recovers the dynamical line-shapes of diagonal and cross peaks quite adequately. The distinct line-shapes of S_I , S_{II} and absorptive $S_I + S_{II}$ signals have been reproduced as well.

A survival probability of an exciton state, given it is prepared in the initial state e is given by $\mathcal{G}_{ee,ee}(t)$. Alternatively the survival time can be estimated using the population transport matrix (Tab. 6.3). Its diagonal elements are the rates at which the exciton population is depleted from these states. Due to detailed balance the diagonal rate corresponding to state e is equal to the sum of all rates (along a column in Tab. 6.3) at which an exciton is transferred to all other states e' . For instance the rate $K_{IV,IV}$ of band IV covers a sum of exciton population loss-times responsible for the population gain of bands III, II, and I. In Tab. 6.3 we present inverse rates which correspond to the exciton survival times. We thus get τ_{IV} of 50 fs, τ_{III} of 174 fs, τ_{II} of 403 fs. The 8.5 ps timescale of band I in our model is related to the thermally activated uphill energy transfer. This is because we do not include exciton relaxation to the ground state. The calculated rates presented in Tab. 6.3 demonstrate the downward energy transport $IV \rightarrow III$, $III \rightarrow II$, and $II \rightarrow I$. The fastest pathway, with a rate of 50 fs, is associated with $IV \rightarrow III$, where energy transfers from the peripheral excitons to the excitonic band of the tube core. This equilibrates in approx. 200 fs through the $III \rightarrow II$ pathway. The final relaxation into band I (≈ 400 fs) is the slowest step. For this reason it is legitimate to state that the balance between bands III and II remains intact even with the $II \rightarrow I$ transfer process.

As shown in Fig. 6.4b and d, and Fig. 6.5b and d the dynamic line-shapes can be captured

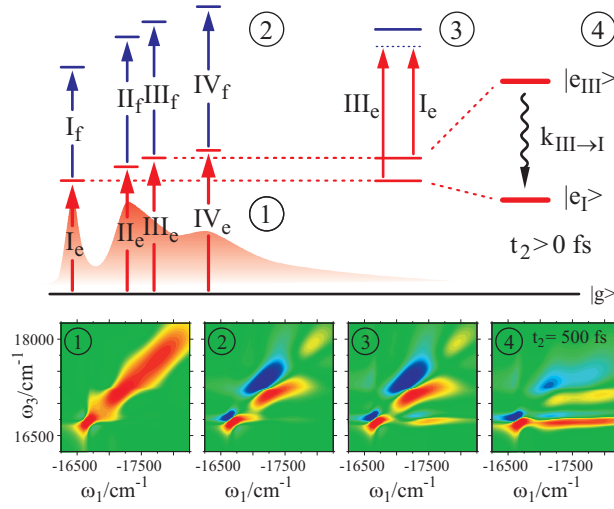


Figure 6.7: Stepwise strategy for iterative fitting of the experimental 2D data. (1) Construction of the linear absorption spectrum by assigning transition energies, transition dipole moments, and line-shapes (system-bath coupling strengths) to four single-excited states individually coupled to overdamped Brownian oscillators. This gives an absorptive part 1Q2D spectrum with positive diagonal peaks (lower panel). (2) Four double-excited states are introduced into the effective level scheme, to account for intra-band one- to two-exciton transitions associated with each of the bands I to IV. (3) Six combination transitions are superimposed on the assembled level structure (schematically depicted for bands I and III in the upper panel) to model off-diagonal signal intensities induced by electronic inter-band couplings. The shift of a particular combination band (blue horizontal solid line) with respect to the sum of the two single-excitation energies involved (blue dotted line), provides a good measure of inter-band coupling strengths. (4) Assignment of inter-band exciton relaxation rates in an iterative fitting procedure. The lower panel shows the calculated 1Q2D spectrum for $t_2 = 500$ fs.

satisfactorily with our simulation procedure. The simulation of the relaxation spectra recovers the off-diagonal peaks and their streaking features. Moreover, the decay of diagonal intensities is adequately reconstructed for longer times t_2 . The effective level scheme (Fig. 6.6) immediately explains band-to-band coupling and its origin due to inter-band combination transitions. From this point-of-view, fields can act on two different single-excited states (say $|e_1\rangle$ and $|e_2\rangle$), which can be seen as a double-excited combination transition $|e_1e_2\rangle$. The contributions of these combination transitions exactly cancel in the case of non-interacting single-excited states, i.e. when (i) the transition moments are kept (i.e. μ_{ge_2} connects $|e_1\rangle \rightarrow |e_1e_2\rangle$ and μ_{ge_1} connects $|e_2\rangle \rightarrow |e_1e_2\rangle$) and (ii) the energy of the double-excited (combination) state matches the sum of the two states involved. By shifting the combination transition energy, one can eliminate this cancelation and induce a cross peak. This corresponds to "exciton-repelling/attracting" interactions [195]. The 1Q2D spectra calculated this way are very sensitive to the shift and thus provide a good test for the coupling pattern between the aggregate bands.

Table 6.3: Inter-band exciton population transfer rates (in ps^{-1}) as derived from a four band model and an iterative fitting procedure of the experimental two-dimensional spectra. To facilitate intuitive comparison, the arrangement of the relaxation rate matrix follows the frequency coordinates of the diagonal and off-diagonal peaks in the experimental spectra. An off-diagonal element of the shown matrix thus corresponds to the population transfer rate from a state indicated by the column into a state indicated by the row. According to the principle of detailed balance, the rates for up-hill and down-hill transfer (forward and backward rates) between two states are related by the Boltzmann condition (room temperature). Inverse lifetimes are given on the diagonal.

	I	II	III	IV
I	0.117	-1.20	0	0
II	-0.117	2.48	-4.03	0
III	0	-1.28	5.76	-20.0
IV	0	0	-1.73	20.0

While the simulation recovers the off-diagonal features and their streak-like shapes quite satisfactorily, their intensities deviate from experimental data for longer t_2 -delays, particularly in the high energy spectral region which will require a moderate re-adjustment of the model. This difference can be explained by considering that the density of exciton states steeply rises with increasing energies as predicted from microscopic models of linear spectral properties of cylindrical J-aggregates [196]. Consequently the assignment of a single effective electronic oscillator to a particular exciton band is only justified in the low energy region where the level density is sparse. At higher energies the average oscillator-strength per state will increasingly differ from the effectively observed transition moment. Furthermore, disorder-induced fluctuations of oscillator-strengths can be expected to lead to an increasing number of weakly absorbing states whose overall contribution to the dynamics cannot be neglected. Finally, this tendency is further enhanced as 2D cross peaks are proportional to the product of the squared transition dipole magnitudes of both of the states involved in energy transfer ($\propto |\mu_i|^2 |\mu_j|^2$). As observed in our experiments, this leads to an increase of cross peak intensity as long as one of the states (in our case band I) is a strong absorber, even if the transition moment of the corresponding diagonal signal of the other state is weak.

6.6 Conclusions

In this work, 1Q2D coherent electronic spectroscopy has been applied to study the excitonic energy transfer in the double-wall cylindrical aggregate C8O3. Correlation measurements of exciton absorption (ω_1) and emission (ω_3) frequencies have experienced a new dimension in the perception of the underpinnings that cause exciton scattering and population transfer. Cross peak signals predominantly emerging in the low-energy off-diagonals ($|\omega_1| > \omega_3$) of the (asymmetric) correlation matrix provide a direct image of electronic coupling and early dissipation dynamics, model-free and

without any preconceived bias. The cross peaks for snap-shots at early waiting times t_2 illustrate the first steps of inter-band exciton dynamics smoothed by finite pulse spectral convolution and very early electron-phonon dephasing. With increasing waiting time t_2 and ongoing population relaxation, the off-diagonal peaks translate into characteristic streaking patterns which become oriented parallel to the ω_1 -axis. Taking into consideration that the excitation energy transfer rates vary over roughly an order of magnitude, it can be concluded that cascading pathways play a substantial role in the downhill energy transfer of high energy excitons into the lowest energy band I with intermediate states in the vicinity of band II.

Our measurements have shown that coherent 2D electronic spectroscopy produces a novel quality of molecular inter-band spectroscopy in the visible optical transition regime. We have demonstrated how 1Q2D-ES can be used to trace electronic coupling, single-step and sequential band-to-band energy transfer and, combined with model simulations, reveal transfer rates for the energy-space excitation flow in a multi-band aggregate. This study is the first rigorous, experimental/theoretical work applied to the puzzle of ultrafast correlations in the tubular aggregate C8O3, in aqueous solution and at room temperature, for cross peaks measured at the shortest wavelength reported so far.

These experiments are superior to spectrally resolved pump-probe (PP) spectroscopy. One advantage is that 2D-ES as a phase-locked and time-resolved heterodyne FWM technique uses three excitation pulses, so that a clear timing axis for the coherence time t_1 exists along which the time ordering of the first two pulses can be interchanged. This leads to rephasing photon-echo spectra S_I and non-rephasing oFID spectra S_{II} . Both spectra yield inter- and intra-band couplings, but the S_I spectra eliminate inhomogeneous broadening. On the other hand, the S_{II} data with their orientation along the anti-diagonal have narrower diagonal line-widths which helps to identify band III (congested in the S_I data) as a (low-intense) disentangled absorber on the main diagonal. Furthermore, spectrally resolved PP spectroscopy interrogates the intensity dynamics of the exciton bands and measures the tube-to-tube transfer via population transfer [197]. Thus the technique reflects the incoherent, downhill population flow from band IV to band I along the main diagonal trace as it was shown by pump-probe simulations for directed energy transfer in a two exciton manifold [198]. 1Q2D-ES, however, spans-up the entirety of diagonal and off-diagonal signals of the correlation matrix and thus measures time-dependent correlations not only along the diagonal ($|\omega_1| = \omega_3$), but also the cross peaks at $|\omega_1| \neq \omega_3$.

In summary, we have demonstrated highly directed exciton transfer mediated by electronic interactions in molecular nanotubes at room temperature. Our study shows how coherent 1Q2D electronic spectroscopy can be used to trace electronic coupling, single-step and sequential band-to-band energy transfer, simultaneously employing high spectral and temporal resolution. The efficient funneling into a single exciton band makes the system an obvious candidate for an artificial light-harvesting device.

The important thing in science is not so much to obtain new facts as to discover new ways of thinking about them.

Sir William Bragg (1862 - 1942)



RHODAMINE 6G

This chapter aims at providing a detailed understanding of double-quantum coherence two-dimensional (2Q2D) electronic spectroscopy. The method is utilized to probe the dynamic fluctuations of electronic states in a solvated molecule at approximately twice the energy of the ground state bleach transition. The 2Q2D spectrum gives insight into the energetic position and spectral fluctuations (system-bath interaction) of the probed excited states. Combining it with single-quantum two-dimensional (1Q2D) electronic spectroscopy enables to determine the strength of the excited state absorption transition, the relative detuning of electronic states, as well as the dynamics of the single-quantum coherence. To investigate the correlation of spectral fluctuations in different electronically excited states we have carried out experiments on a solvated dye (Rhodamine 6G) with 23 fs pulses centered at the maximum of the linear absorption spectrum. The 2Q2D spectrum reveals three peaks of alternating signs with the major negative peak located at higher frequencies along the emission axis compared to the single positive peak. The 1Q2D spectrum on the other hand shows a negative peak stemming from excited state absorption at lower frequencies along the emission axis. Analysis of the signal in the homogenous limit fails to account for this observation as well as the number of peaks in the 2Q2D spectrum. Employing a three-level model in which all time correlations of the third-order response function are accounted for via second-order cumulant expansion gives good agreement with both the 1Q2D and 2Q2D data. The analysis furthermore shows that the fluctuations of the probed electronic states are highly correlated reflecting the modulation by a common nuclear bath and similarities in the nature of the electronic transitions.

This chapter is based on

- A. NEMETH, F. MILOTA T. MANČAL, T. PULLERITS, J. SPERLING, J. HAUER, H. F. KAUFFMANN, AND N. CHRISTENSSON. Double-quantum two-dimensional electronic spectroscopy of a three-level system: Experiments and Simulations. *J. Chem. Phys.* **133**, 094505 (2010)

7.1 Introduction

In contrast to S_I and S_{II} experiments, which have been discussed up to now, signals along \mathbf{k}_{III} can only be observed for systems with at least three electronic levels, thus being predestined for probing electron correlation effects [199]. The three-level system required for the observation of the 2Q2D signal arises naturally in the spectroscopy of vibrational modes in the IR spectral region, where 2Q2D spectroscopy has been employed to measure diagonal and off-diagonal anharmonicities [200]. For electronic transitions one should expect that higher lying electronic states are accessible within the bandwidth of the excitation pulses (i.e. with an energy of $\approx 2\omega_{eg}$ with respect to the ground state). In mean field models of electronic structure, like Hartree-Fock, there is a state at twice the HOMO-LUMO energy with a wave function that is given by a double HOMO-LUMO excitation [199, 201]. We will refer to this type of state as a doubly excited state in this chapter. Neglecting the coupling to a nuclear bath (see Section 7.4.2), the mean field model predicts that the signal vanishes due to destructive interference of the two Feynman pathways contributing to the signal (cf. Fig. 2.1) [199]. Going beyond mean field models, electron correlation and exchange effects will shift the electronic states, thereby lifting the cancelation of the signal [13, 199, 202]. In systems where electron correlation and exchange effects are small, such as semiconductors or molecular aggregates, the shift of the second excited state relative to the first gives information about the bi-exciton binding energy, i.e. the binding energy of the two-electron-hole pair quasiparticle. The binding energy and the dynamics of the non-radiative two-exciton states have been investigated in GaAs quantum wells [75, 203].

Recently, 2Q2D electronic spectroscopy has been applied to molecules in solution [204, 205]. In contrast to semiconductors [206], quantum wells [75, 202, 203, 207], and molecular aggregates [208], molecules often display large electron correlation and exchange effects (of the order of eV) [209, 210]. The changes of the energy levels due to these effects can thus easily shift the doubly excited state out of the bandwidth of the laser pulses used in the experiments [13]. However, in molecules there is usually a large number of electronically excited states in the vicinity of $2\omega_{eg}$ and some of these states may give rise to a 2Q2D signal. Due to the strong electron correlation and exchange effects, the interpretation of the frequency shift of the probed excited state relative to $2\omega_{eg}$ is less clear for molecules than in semiconductors or molecular aggregates. Despite the uncertainty about the origin of the second excited state, 2Q2D spectroscopy supplies valuable information about the properties of these excited state transitions including the relevant correlation functions and state energies. This information is important for the proper interpretation of other nonlinear spectroscopic experiments as these transitions will modulate any four-wave mixing signal due to the presence of excited state absorption (ESA). One particularly interesting question is the correlation of the transition frequency fluctuations of different electronic states.

An area where 2Q2D electronic spectroscopy shows great potential lies in the field of molecular aggregates. For these systems one usually employs the two-level Frenkel exciton model to describe the electronic structure [201]. According to this model, the coupled chromophores give rise to an excited state with a wave function that can be written as a product of single excitations of the

monomer. This model readily explains the strong ESA feature slightly blue-shifted relative to the ground state bleach (GSB) in light harvesting complexes [155, 211], whereas the monomer only shows a broad, weak, and featureless ESA [212, 213]. Theoretical studies in a protein-pigment complex using the two-level Frenkel exciton model have shown that the 2Q2D spectrum is dominated by signals originating from two-exciton states with a large delocalisation length and thus can be used to probe the correlation between excited states [208].

However, describing the monomer by a three-level system, i.e. including an excited state with a transition energy close to twice the GSB, has important consequences for the electronic structure of the aggregate. In the two-level Frenkel exciton model there is no relaxation between the two- and one-exciton manifolds since the two-exciton states are formed as products of single excitations in the site basis [155, 201] (i.e. the two-exciton state will decay with the single exciton lifetime). The presence of a state with twice the energy of the first excited state in the monomer alters the two-exciton wavefunction of the aggregate by mixing in of the doubly excited molecular wave function. This opens up a relaxation pathway via internal conversion from the two-exciton band down to the first exciton manifold [214] and the spectral position and degree of mixing will control the rate of annihilation in these systems. It is thus important to characterize electronic states with approximately twice the energy of the GSB for the constituent pigments, in order to understand the dynamics of molecular aggregates .

Similar to experiments in inorganic semiconductors, 2Q2D spectroscopy is a promising tool for the determination of the two-exciton binding energy and the delocalization of the two-exciton states in molecular aggregates. However, from the discussion above it is clear that detailed information about the electronic structure of the constituent pigments is needed for such studies. Accordingly, it is important to experimentally and theoretically investigate the basic properties of this technique using a simple molecule and study how to extract the energies of the probed excited states from experiments. By further analyzing the line-shape of the 2Q2D spectrum it becomes possible to address the correlation of the transition frequency fluctuation of the participating transitions. It becomes evident from the above considerations that several hitherto unknown problems, including the choice of two- versus three-level monomer excitation schemes, electron-phonon couplings, and the nature of excitation dipole fluctuations dramatically affect electron-electron correlations of molecular double-excitations or two-exciton band structures in molecular aggregates. The special signatures imprinted onto the coherent signal in 2Q2D spectroscopy by the above mentioned effects are puzzling and are the key issue to be studied in this chapter.

7.2 Experimental Details

For collecting S_I and S_{II} spectra, t_1 (i.e. the delay between the first two excitation pulses) is scanned from -100 to 100 fs in steps of 0.5 fs. For recording 2Q2D electronic spectra, pulses 1 and 2 are scanned simultaneously from 0 to -100 fs in steps of 0.25 fs for a fixed value of t_1 . Rhodamine 6G solutions with a concentration of $1.7 \cdot 10^{-4}$ M have been prepared with spectrophotometric grade ethanol (Sigma-Aldrich). No photo-degradation was observed during the course of the measure-

ments for the employed pulse energy of 3 nJ, corresponding to a fluence of $1.44 \cdot 10^{14}$ photons/cm² or an excitation of 2.24% of the molecules in the sample volume.

7.3 Experimental Results

Figs. 7.1a and b displays rephasing (S_I) and non-rephasing (S_{II}) 1Q2D electronic spectra for Rhodamine 6G. The real and imaginary parts show the typical characteristics of rephasing and non-rephasing 1Q2D spectra of a simple chromophore. The peaks and the nodal lines are directed along the diagonal (anti-diagonal) for the rephasing (non-rephasing) spectrum. In the real part of the total 1Q2D spectrum ($S_I + S_{II}$, Fig. 7.1c) we find a strong positive feature stemming from ground state bleaching (GSB) and stimulated emission (SE) and a weak, red-shifted negative feature arising from ESA at $\omega_3 = 18200$ cm⁻¹. The elongation of the total 1Q2D spectrum along the diagonal indicates spectral inhomogeneity on the timescale of the experiment [107, 122]. Extending the measurement to longer t_2 values reveals the presence of spectral diffusion as the spectrum acquires a more circular shape (data not shown).

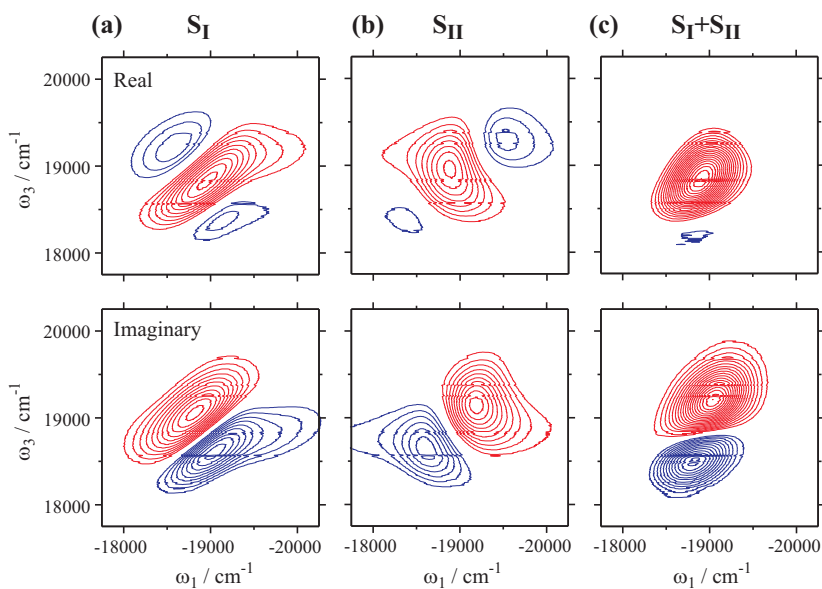


Figure 7.1: 1Q2D spectra of Rhodamine 6G for $t_2 = 0$ separated into real (upper row) and imaginary (lower row) part. (a) S_I -technique (rephasing 1Q2D). (b) S_{II} -technique (non-rephasing 1Q2D). (c) The sum of these two spectra yields an absorptive real part and a dispersive imaginary part. Contour lines are drawn in steps of $\pm 5\%$, starting at 10% signal intensity. Positive (negative) features are drawn in red (blue). The S_I and S_{II} spectra are drawn with their relative contributions to the 1Q2D ($S_I + S_{II}$) spectra, which are normalized to their respective maximum absolute value.

The 2Q2D electronic spectrum of Rhodamine 6G, separated into real and imaginary parts, is plotted in Fig. 7.2. Since the system evolves in a double-quantum coherence during t_2 , the features

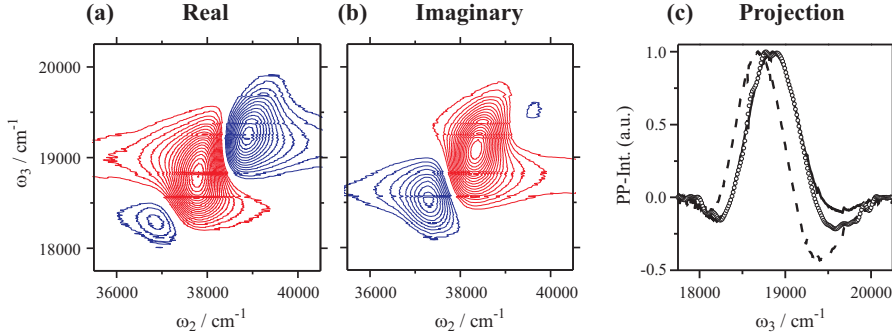


Figure 7.2: (a) Real and (b) imaginary part of the 2Q2D spectrum of Rhodamine 6G for $t_1 = 0$. Contour lines are drawn in steps of $\pm 5\%$, starting at 10% signal intensity. Positive (negative) features are drawn in red (blue). The spectra are normalized to their respective maximum absolute value. (c) Projections of the real part of the 1Q2D spectrum (solid) and the 2Q2D spectrum (dashed) onto the ω_3 -axis as compared to a spectrally resolved pump-probe spectrum (circles).

appear at approximately twice the single-quantum frequency ω_{eg} along ω_2 . The 2Q2D technique probes non-rephasing Feynman pathways (Fig. 2.1c) and the real part of the 2Q2D signal shows similarities to the S_{II} technique with respect to the direction of the spectrum (compare to Fig. 7.1b). For the 2Q2D technique, causality ensures that no signal is generated in the $+\mathbf{k}_1 + \mathbf{k}_2 - \mathbf{k}_3$ direction for $t_2 < 0$ and $t_3 < 0$. This implies that the 2Q2D spectrum only involves a half-sided Fourier transform, which results in phase-twisted line-shapes (cf. Section 7.4.1). Causality also affects the S_I and S_{II} techniques, and it is firmly established that the real parts of S_I and S_{II} spectra display negative components already for a two-level system [18]. These stem from the dispersive parts of the optical response and they cancel when S_I and S_{II} spectra are added together giving absorptive line-shapes for the real part of 1Q2D measurements ($S_I + S_{II}$) [18]. Beyond the homogenous limit, a balancing of S_I and S_{II} spectra is not sufficient to ensure absorptive signals since strong system-bath interactions and a finite Stokes shift also give rise to negative components in 1Q2D spectra [22]. Our experimental results reveal strong negative features in our S_I and S_{II} spectra (Fig. 7.1a and b) that almost disappear in the total 1Q2D spectrum (Fig. 7.1c). This illustrates the danger of techniques involving half-sided Fourier transforms. In these techniques it is not generally possible to use the sign of a specific feature to assign it to a specific Feynman pathway as can be done for 1Q2D spectra [215]. Even in the homogenous limit there is no possibility to construct absorptive line-shapes for 2Q2D spectra within third-order nonlinear spectroscopy, and there is consequently no unique connection between the sign of a feature in the 2Q2D spectrum and the sign of the response function. We argue that the presence of more than two peaks in the 2Q2D spectrum reflects the phase-twisted line-shapes of the signals in this experiment. Neglecting the weaker negative feature for a moment, the main negative peak in the real part 2Q2D spectrum is located at higher frequencies along ω_3 compared to the positive one. Using a simplistic interpretation

based on the Feynman diagrams (Fig. 2.1c) one would interpret this as a blue shift of the ESA relative to GSB. This is in contradiction with the results obtained by the 1Q2D spectra, where the ESA contribution is red-shifted compared to GSB and SE, and additional theoretical investigations are needed to interpret the 2Q2D spectrum.

7.4 Theory

To understand the appearance of 2Q2D spectra, and the relation to 1Q2D spectra, we consider an electronic three-level system coupled to a heat bath. The central quantity in third-order nonlinear spectroscopy is the third-order polarization [4]

$$P^{(3)}(\mathbf{r}, t) = \int_{-\infty}^{\infty} \int_{-\infty}^{\infty} \int_{-\infty}^{\infty} dt_3 dt_2 dt_1 E(\mathbf{r}, t - t_1) E(\mathbf{r}, t - t_1 - t_2) E(\mathbf{r}, t - t_1 - t_2 - t_3) R^{(3)}(t_1, t_2, t_3), \quad (7.1)$$

where the response functions are given by

$$R^{(3)} = \left(\frac{i}{\hbar}\right)^3 \langle\langle \mu | G(t_3) \mathcal{V} G(t_2) \mathcal{V} G(t_1) \mathcal{V} | \rho(-\infty) \rangle\rangle. \quad (7.2)$$

Here, μ is the transition dipole moment operator, \mathcal{V} is the Liouville space transition dipole moment superoperator, and $G(t)$ are Liouville space Green functions. Both, the (time independent) transition dipole moment (super-) operator and the Green functions depend on the particular model and level structure. For the remainder of this paper we will consider a three-level system with energy levels $|g\rangle$, $|e\rangle$, and $|f\rangle$, where the $|g\rangle \rightarrow |e\rangle$ and $|e\rangle \rightarrow |f\rangle$ transitions have comparable energies.

The potential energy surfaces along an effective nuclear coordinate q for this system are shown in Fig. 7.3. For this model there are only two unique pathways that are accessible in the 2Q2D experiment. The corresponding Feynman diagrams are shown in Fig. 2.1c, and the corresponding four point correlation functions read

$$\begin{aligned} R^{(2Q2D)} &= R_{4f} - R_{3f}^* = \langle\langle \mu_{eg} | G_{eg}(t_3) \mathcal{V}_{eg,fg} G_{fg}(t_2) \mathcal{V}_{fg,eg} G_{eg}(t_1) \mathcal{V}_{eg,gg} | \rho_{gg}(-\infty) \rangle\rangle \\ &\quad - \langle\langle \mu_{fe} | G_{fe}(t_3) \mathcal{V}_{fe,fg} G_{fg}(t_2) \mathcal{V}_{fg,eg} G_{eg}(t_1) \mathcal{V}_{eg,gg} | \rho_{gg}(-\infty) \rangle\rangle \\ &= |\mu_{eg}|^2 |\mu_{fg}|^2 \left[\langle\langle G_{eg}(t_3) G_{fg}(t_2) G_{eg}(t_1) | \rho_{gg}(-\infty) \rangle\rangle - \langle\langle G_{fe}(t_3) G_{fg}(t_2) G_{eg}(t_1) | \rho_{gg}(-\infty) \rangle\rangle \right]. \quad (7.3) \end{aligned}$$

7.4.1 Double-Quantum Two-Dimensional Signals in the Homogeneous Limit

To illustrate the spectral line-shapes obtained in the 2Q2D experiment, we derive closed form expressions for the response function $R^{(2Q2D)}$ in Eq. (7.3). If the bath has a short correlation time,

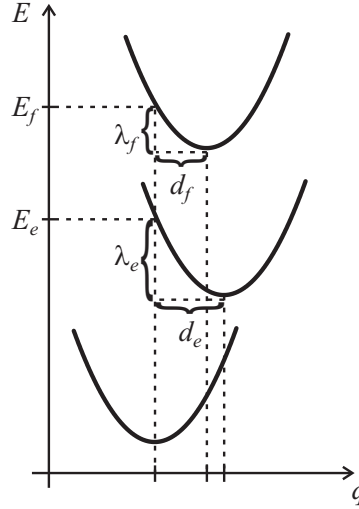


Figure 7.3: Potential energy surfaces for the $|g\rangle$, $|e\rangle$, and $|f\rangle$ states. The dimensionless displacements along the effective nuclear coordinate q are denoted by d_e and d_f . The corresponding reorganisation energies (λ_e and λ_f) are indicated in the figure. The energies of the levels (denoted by E_e and E_f) refer to the vertical transition energies.

we can apply the homogenous (motional narrowing) limit where the average over the four point correlation function factorizes into averages over the individual propagators [4]. For R_{4f} we obtain

$$\langle\langle G_{eg}(t_3)G_{fg}(t_2)G_{eg}(t_1)|\rho(-\infty)\rangle\rangle \approx \langle\langle G_{eg}(t_3)|\rho(-\infty)\rangle\rangle \langle\langle G_{fg}(t_2)|\rho(-\infty)\rangle\rangle \langle\langle G_{eg}(t_1)|\rho(-\infty)\rangle\rangle. \quad (7.4)$$

The averaged Green function in the Bloch approximation reads [4]

$$\langle\langle G_{mn}(t)|\rho(-\infty)\rangle\rangle = \theta(t) \exp(-\Gamma_{mn}t) \exp(-i\omega_{mn}t), \quad (7.5)$$

where $\omega_{mn} = \frac{1}{\hbar}(E_m - E_n)$, Γ_{mn} is a relaxation rate constant, and $\theta(t)$ is the step function reflecting the causality of the response. The propagator and Eq. (7.5) can be Fourier transformed using standard formulas. Applying the homogenous limit to R_{4f} and R_{3f}^* (Eq. (7.4)) and taking the Fourier transform of the propagators in Eq. (7.5) along ω_2 and ω_3 , we obtain the real part of the 2Q2D spectrum in the impulsive limit as

$$S^{(2Q2D)}(\omega_2, \omega_3) = \frac{\mu_{fe}^2 \mu_{eg}^2}{(\omega_2 - \omega_{fg})^2 + \Gamma_{fg}^2} \times \left\{ \frac{\Gamma_{eg}\Gamma_{fg} - (\omega_3 - \omega_{eg})(\omega_2 - \omega_{fg})}{(\omega_3 - \omega_{eg})^2 + \Gamma_{eg}^2} - \frac{\Gamma_{fe}\Gamma_{fg} - (\omega_3 - \omega_{fe})(\omega_2 - \omega_{fg})}{(\omega_3 - \omega_{fe})^2 + \Gamma_{fe}^2} \right\}. \quad (7.6)$$

Eq. (7.6) highlights some of the properties of the 2Q2D spectrum in the homogeneous limit. Assuming that all relaxation rates are identical, the signal in the homogeneous limit vanishes if $\omega_{eg} = \omega_{fe}$.

Furthermore, it is clear from Eq. (7.6) that the term corresponding to R_{4f} (R_{3f}^*) is not strictly positive (negative). This is directly analogous to the phase-twisted line-shapes in rephasing (S_I) and non-rephasing (S_{II}) 1Q2D spectra [18]. From the Feynman diagrams in Fig. 2.1c it is obvious that 2Q2D spectroscopy is a non-rephasing technique, and Eq. (7.6) predicts a spectrum that is elongated along the anti-diagonal [18, 200, 216]. Fig. 1.1 compares the real parts of the S_I , S_{II} , and S_{III} techniques for the model discussed above, highlighting the strong similarities between the S_{II} and S_{III} techniques originating in the non-rephasing character of these experiments. Neither the direction of the spectrum nor the phase-twisted line-shapes are related to our particular choice of Green functions or the application of the homogeneous limit discussed above, but reflect the properties of the four point correlation functions and causality of the optical response.

Fig. 7.4a shows the 2Q2D spectrum calculated via Eq. (7.6) for the case where $|\Delta\omega| > \Gamma$ ($\Delta\omega = \omega_{eg} - \omega_{fe}$). The signal is elongated along the anti-diagonal and shows two peaks of different signs corresponding to the two response functions R_{4f} and R_{3f}^* . The two peaks are centered at the same ω_2 and displaced by $\Delta\omega$ along ω_3 . This case corresponds to the narrow line width limit where the line width of each transition is much smaller than the splitting between them. In this narrow line width limit the 2Q2D spectrum can be interpreted with simple arguments related to the double-sided Feynman diagrams shown in Fig. 2.1c. Turning to the opposite case ($|\Delta\omega| < \Gamma$, cf. Fig. 7.4b) we find that the 2Q2D spectrum changes its appearance substantially. The two main peaks are no longer aligned at the same ω_2 and they move further apart as Γ increases. The same trend holds for the position of the peaks along ω_3 . In case the line width is comparable to or larger than the splitting of the states, the energy difference between the positive and negative peak in the 2Q2D spectrum is no longer a good indicator of $\Delta\omega$.

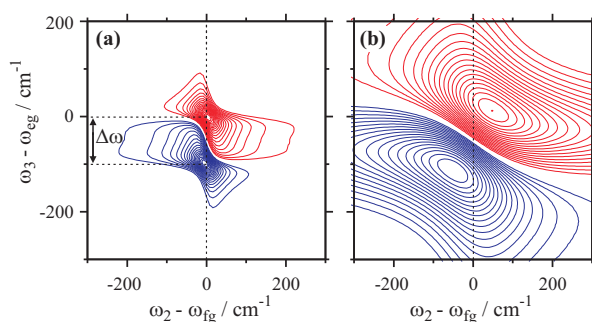


Figure 7.4: 2Q2D spectra in the impulsive limit invoking the homogeneous limit and the Bloch approximation. (a) $\Delta\omega = 100 \text{ cm}^{-1}$, $\Gamma = 25 \text{ cm}^{-1}$. (b) $\Delta\omega = 100 \text{ cm}^{-1}$, $\Gamma = 125 \text{ cm}^{-1}$. Contour lines are drawn on a linear scale with 5% increments. Red (blue) lines refer to positive (negative) contributions.

This example shows that the overlap of the two contributing pathways can drastically change the appearance of the 2Q2D spectrum. Electronic transitions of molecules in solution typically exhibit a strong coupling to the environmental modes and the total reorganization energy is of

the order of 500-1000 cm^{-1} . It is clear that the narrow line width limit is never valid for solvated molecules and we expect that the influence of the overlap of the two response functions is critical for understanding the 2Q2D spectrum. However, comparing the experimental results (Fig. 7.2) with the simulations in Fig. 7.4 it is obvious that the homogeneous limit cannot explain the experimental results even for an arbitrary line-shape function. The simulations in the homogenous limit fail to account for the number of peaks in the 2Q2D spectrum as well as the different appearance of the negative feature in 1Q2D and 2Q2D spectra.

7.4.2 Double-Quantum Two-Dimensional Signals within the Cumulant Expansion

The homogenous limit does not allow for any correlation of bath fluctuations for different time periods. This level of theory can thus not account for the Stokes shift. In order to incorporate correlations of transition frequency fluctuations between different periods and for an arbitrary line-shape as well as finite Stokes shift we use the second-order cumulant expansion [4] to express the four point correlation functions in terms of line shape functions. The relevant response functions have been derived elsewhere [10, 47, 217], so we quote the results important for the double-quantum coherence response functions in our analysis, namely

$$R_{4f} = (|\mu_{eg}||\mu_{fe}|)^2 \exp \{i(\omega_{eg}t_1 + \omega_{fg}t_2 + \omega_{eg}t_3)\} \\ \times \exp \left\{ \begin{array}{l} -g_{ee}(t_1) + g_{ef}(t_1) - g_{ee}(t_2) + 2g_{ef}(t_2) - g_{ff}(t_2) \\ -g_{ee}(t_3) + g_{ef}(t_3) + g_{ee}(t_1 + t_2) - g_{ef}(t_1 + t_2) \\ +g_{ee}(t_2 + t_3) - g_{ef}(t_2 + t_3) - g_{ee}(t_1 + t_2 + t_3) \end{array} \right\} \quad (7.7)$$

and

$$R_{3f}^* = (|\mu_{eg}||\mu_{fe}|)^2 \exp \{i(\omega_{eg}t_1 + \omega_{fg}t_2 + \omega_{fe}t_3)\} \\ \times \exp \left\{ \begin{array}{l} -g_{ee}(t_1) + g_{ef}(t_1) + g_{ee}(t_2) - g_{ef}(t_2) - g_{ee}^*(t_3) \\ +g_{ef}^*(t_3) - g_{ee}(t_1 + t_2) - g_{ee}(t_2 + t_3) + 2g_{ef}(t_2 + t_3) \\ -g_{ff}(t_2 + t_3) + g_{ee}(t_1 + t_2 + t_3) - g_{ef}(t_1 + t_2 + t_3) \end{array} \right\}. \quad (7.8)$$

Here, $g_{ab}(t)$ are complex line-shape functions defined as

$$g_{ab}(t) = \int_0^t d\tau_1 \int_0^{\tau_1} d\tau_2 C_{ab}(\tau_2) \quad (7.9)$$

$$C_{ab}(t) = \frac{1}{\hbar^2} \langle \Delta W_{ag}(t) \Delta W_{bg}(0) \rangle \quad (7.10)$$

where $C_{ab}(t)$ is the energy gap correlation function and $\Delta W_{ag} = W_a(q) - W_g(q) - \langle W_a(q) - W_g(q) \rangle$ is the energy gap operator. The response functions involving the $|f\rangle$ -level depend on three correlation

functions since we have chosen to set the ground state as a reference potential energy surface. Their mutual relations depend on the particular character of the bath. In a single Brownian mode model depicted in Fig. 7.3 rather strict relations apply. The bath interacts with the electronic transition through a single effective coordinate q which couples to both the rest of the bath and the electronic transition. The displacement of the effective mode in the electronic state a ($a = e, f$) is d_a . The time evolution of the energy gap operator is given by [4]

$$\Delta W_{ag}(t) = U_g^*(t)\Delta W_{ag}U_g(t) = \hbar\omega_a d_a U_g^*(t)qU_g(t), \quad (7.11)$$

where $U_g(t)$ is the nuclear time evolution operator corresponding to the electronic ground state. Here we elaborate on the simplest case where the bath can be described by a single Brownian oscillator mode.

For a single harmonic nuclear coordinate the three energy gap correlation functions read

$$C_{ab}(t) = \omega_a\omega_b d_a d_b \langle q(t)q \rangle. \quad (7.12)$$

Here $\langle q(t)q \rangle$ is the autocorrelation function of the generalized coordinate q . The experimentally accessible quantity is the reorganization energy given by

$$\lambda_a = S_a\omega_a = \frac{1}{2}\omega_a d_a^2, \quad (7.13)$$

where S is the Huang-Rhys factor. Assuming that the frequency of the mode is the same in all states, we arrive at

$$C_{ab}(t) = d_a d_b c(t), \quad (7.14)$$

with

$$c(t) = \omega^2 \langle q(t)q \rangle. \quad (7.15)$$

The three correlation functions ($C_{ee}(t), C_{ff}(t), C_{ef}(t)$) are not independent but related to the bath induced fluctuations of the same coordinate. The magnitude of the diagonal correlation functions $C_{ee}(t)$ and $C_{ff}(t)$ depends on the displacement of the involved state (relative to the ground state) in direct analogy with the results for a two-level system. The magnitude of the cross-correlation function $C_{ef}(t)$ depends on the displacement associated with both transitions $|g\rangle \rightarrow |e\rangle$ and $|g\rangle \rightarrow |f\rangle$. Because the displacement can be negative, an anti-correlation is also allowed.

Extending the above relation to a multimode bath of independent Brownian oscillators one finds that

$$C_{ab} = \sum_j d_a^{(j)} d_b^{(j)} \omega_j^2 \langle q_j(t) q_j \rangle = \sum_j d_a^{(j)} d_b^{(j)} c^{(j)}(t). \quad (7.16)$$

In the multimode picture the cross correlation function is determined by the overlap of the displacement vectors $\mathbf{d}_a = (d_a^{(1)}, \dots, d_a^{(N)})$ corresponding to the two excited electronic states. A cross correlation function $C_{ef}(t)$ of a multi-component bath is therefore rather freely related to the self-correlation functions associated with the two transitions.

7.5 Simulations

For our simulations we use a simple parametrization of the different correlation functions. We use a correlation function $C_{ee}(t)$ with vibrational modes obtained from resonance Raman experiments [218] ($\sum_j \lambda_j = 353 \text{ cm}^{-1}$) and three over-damped modes reflecting fast ($\tau_G = 40 \text{ fs}$, $\lambda_G = 150 \text{ cm}^{-1}$ and $\tau_{E_1} = 100 \text{ fs}$, $\lambda_{E_1} = 150 \text{ cm}^{-1}$) and slow ($\tau_{E_2} = 1 \text{ ps}$, $\lambda_{E_2} = 100 \text{ cm}^{-1}$) bath fluctuations, where E and G refer to Gaussian and exponential modes respectively. This correlation function gives good agreement with the linear absorption spectrum of the $|g\rangle \rightarrow |e\rangle$ transition. In the next step we assume that the shape of the normalized correlation function is the same for $C_{ee}(t)$ and $C_{ff}(t)$ and use the displacement of the $|g\rangle \rightarrow |f\rangle$ transition (d_f) as a free parameter. For a multi-component bath, Eq. (7.16) shows that the form of $C_{ef}(t)$ is only loosely related to those of $C_{ee}(t)$ and $C_{ff}(t)$. We thus start with a single component bath model, i.e. with Eq. (7.14), and relax its strict prescription for $C_{ef}(t)$ if it conflicts with experimental evidence. The remaining parameters of the model are the energy of the $|g\rangle \rightarrow |f\rangle$ transition, $\omega_{fg} = \omega_{eg} + \omega_{fe}$, and the relative transition dipole moment μ_{fe}/μ_{eg} . The latter cannot be obtained from the 2Q2D experiment since both pathways depend on the same transition dipole moments (see Eq. (7.6)). To estimate the magnitude of the transition dipole moments we complement the simulations of the 2Q2D spectrum with simulations of the 1Q2D experiment at $t_2 = 0$.

Figs. 7.5 and 7.6 summarize the simulations of the 2Q2D and 1Q2D experiments on Rhodamine 6G in solution. These simulations employ the finite pulse envelopes used in the experiments and the cumulant expansion expression for the response functions. The simulations of the 2Q2D spectra in Fig. 7.5 are in good agreement with the experimental data in Fig. 7.2 and accurately capture the number of peaks, their signs, energetic positions, and relative intensities. As a consequence of the phase-twisted line shapes in 2Q2D spectra we observe three peaks even though there are only two Feynman pathways contributing to the signal. This effect is smaller in the homogenous limit (Fig. 7.4) and we find that the number of peaks and their relative intensities depend sensitively on the bath description as well as the difference between ω_{eg} and ω_{fe} . Fig. 7.6 depicts the simulations of the real and imaginary part of the 1Q2D spectrum in which all pulse overlap effects and the contributions from the double-quantum coherence pathways have been included. The simulations reproduce the negative contribution at low ω_3 in the real part and the two approximately equally strong features of opposite sign in the imaginary part. Finally, the simulations reproduce the

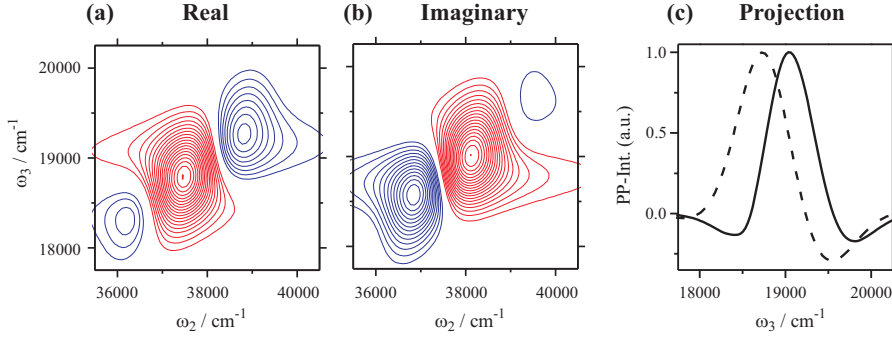


Figure 7.5: (a) Real and (b) imaginary part of the simulated 2Q2D spectrum. Contour lines are drawn on a linear scale with $\pm 5\%$ increments starting from the 10% level. Red (blue) lines refer to positive (negative) contributions. (c) Projection of the 1Q2D spectrum (solid) and 2Q2D spectrum (dashed) onto the ω_3 -axis.

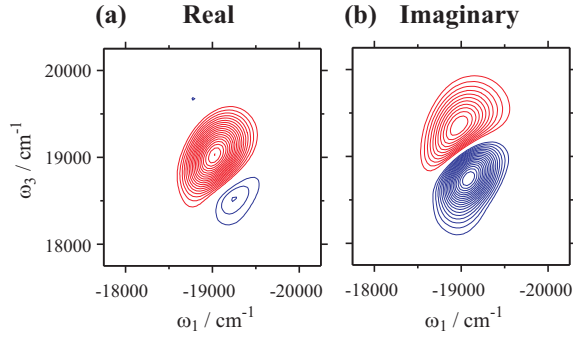


Figure 7.6: (a) Real and (b) imaginary part of the simulated 1Q2D spectrum of Rhodamine 6G for $t_2 = 0$. Contour lines are drawn on a linear scale with $\pm 5\%$ increments starting from the 10% level. Red (blue) lines refer to positive (negative) contributions.

energy difference between the peaks of the projection of the 1Q2D and 2Q2D spectrum onto ω_3 (cf. Fig. 7.5c).

The simulations clearly reveal that the correlation functions $C_{ee}(t)$ and $C_{ff}(t)$ have to be very similar in order to match the width of the 2Q2D spectrum. For a single component bath this corresponds to the case where the displacements in $|e\rangle$ and $|f\rangle$ are almost the same (i.e. $d_f \approx d_e$). For the simulations of the 2Q2D spectrum alone we find a good fit using $C_{ff}(t) = 0.9 \cdot C_{ee}(t)$ if Eq. (7.14) is applied to obtain the cross correlation function i.e. $C_{ef}(t) = \sqrt{0.9} \cdot C_{ee}(t)$. Contradictory to experimental results, this choice of correlation functions gives rise to a very narrow ESA contribution in the 1Q2D spectrum. This is not surprising since the ESA pump-probe spectrum approaches a δ -function as $C_{ff}(t) \rightarrow C_{ee}(t)$ [219]. Relaxing the single bath component prescription, but keeping the overall shape of $C_{ef}(t)$ we find a more realistic line width of the ESA contribution in the 1Q2D experiment with $C_{ef}(t) = C_{ff}(t) = 0.9 \cdot C_{ee}(t)$. The minor change in the magnitude of the cross-correlation function $C_{ef}(t)$ has a limited impact on the line-shapes in

the 2Q2D experiment and illustrates the sensitivity of different experiments to different correlation functions. The simulations thus show that the spectral distribution of the displacements $d_e(\omega)$ and $d_f(\omega)$ are similar but the average displacement is slightly less in state $|f\rangle$.

Besides the different correlation functions and their relations, an important parameter determining the appearance of the 2Q2D spectrum is the energy of the $|g\rangle \rightarrow |f\rangle$ transition. This value has a profound impact on the 2Q2D spectrum with our realistic choice of correlation functions. Using Eq. (7.6) and Fig. 7.5, it is tempting to erroneously conclude that the $|e\rangle \rightarrow |f\rangle$ transition is blue-shifted relative to the GSB contribution since the strongest negative component in the 2Q2D spectrum is at high ω_3 . However, this is in contrast to the 1Q2D spectrum (Fig. 7.6) where the ESA contribution is seen at lower ω_3 . It is difficult to understand this apparent contradiction within the homogeneous limit. The simulations in Fig. 7.4 with a red-shifted $|e\rangle \rightarrow |f\rangle$ transition also display a red-shifted negative component in the 2Q2D spectrum (and a red shift in the absorptive 1Q2D spectrum, data not shown). Comparing to the simulations within the cumulant expansion (Fig. 7.5) it is clear that a red-shifted $|e\rangle \rightarrow |f\rangle$ transition can also give rise to a negative component at high energy in the 2Q2D spectrum and a red-shifted negative component in the 1Q2D spectrum. In our simulations we accommodate these findings by a choice of $\Delta\omega = 500 \text{ cm}^{-1}$, corresponding to a red shift of the $|e\rangle \rightarrow |f\rangle$ transition relative to the GSB contribution. In general it is not possible to extract $\Delta\omega$ directly from the 2Q2D spectrum if the system-bath interaction is strong as in the case of electronic transitions in molecules in solution.

The last parameter of the model is the relative strength of the transition dipole moments μ_{fe} and μ_{eg} . This value is difficult to estimate from experiments due to the finite bandwidth of the pulses, pulse overlap effects, and the overlap of positive and negative contributions in the 2Q2D signal. After determining the correlation functions and $\Delta\omega$ from the 2Q2D experiments we used μ_{fe}/μ_{eg} as a parameter in the simulation of the 1Q2D spectrum. Weak negative features in the 1Q2D spectrum can result from pulse overlap effects, inertial motions, and finite Stokes shift [22]. We find that these effects, accounted for in our model, are too weak to explain the negative feature in the 1Q2D spectrum. Rather, the amplitude of the negative feature is controlled by the $|e\rangle \rightarrow |f\rangle$ transition dipole moment. To account for the relatively weak ESA feature seen in the experiments we conclude that $\mu_{fe}/\mu_{eg} \leq 0.2$. The full analysis of our experiments puts our results in good agreement with the estimation of the ESA cross section made by Hammond [220], showing an excited state with an energy of $36000 - 37000 \text{ cm}^{-1}$. These studies also have shown that the ESA transition has a different polarization compared to the GSB contribution. This could affect our estimation of the strength of the transition dipole moment. The mutual orientation of the transition dipole moments will be important for the interpretation of pump-probe anisotropy experiments [221], but this issue is beyond the scope of the present study.

Fig. 7.5c shows the projection of the simulated 1Q2D and 2Q2D spectra onto the ω_3 axis. The 2Q2D projection shows a clear red-shift relative to the pump-probe signal (which equals the projection of the 1Q2D spectrum) and a stronger negative contribution. This also reflects the difference between the two signals seen in the experiment (Fig. 7.2c). Considering the Liouville pathways underlying these signals (Fig. 2.1) there is no basis for an equivalence of these two

projections. For instance, the 2Q2D projection lacks a GSB contribution and the positive (R_{4f}) and negative (R_{3f}^*) response functions always have the same magnitude in contrast to the SE and ESA contributions in pump-probe spectroscopy. This projection can only match the pump-probe spectrum if one employs the homogenous limit, assumes that all dephasing rates are equal, neglects the Stokes shift, and supposes that the ratio of the transition dipole moments is $\mu_{fe}/\mu_{eg} = \sqrt{2}$. Using pump-probe spectra in order to phase 2Q2D spectra thus lacks theoretical foundation and alternative methods must be used as discussed in Section 3.6.

7.6 Discussion

The presence of a 2Q2D signal is unambiguous experimental evidence for the presence of a state at roughly twice the energy of the optically allowed $|g\rangle \rightarrow |e\rangle$ transition. Analyzing the line-shapes gives information about the coupling of the $|g\rangle \rightarrow |e\rangle$ and $|g\rangle \rightarrow |f\rangle$ transitions to the bath, their energies, and the transition dipole moments. However, this analysis does not give any information about the nature of the electronic excitation. For mean field models, where electron-electron correlation and exchange effects are neglected, there should be a state at twice the HOMO-LUMO energy, which can be written as the product of single excitations [201]. However, it is well known that the exchange and correlation terms can significantly alter the energy of electronic states in molecules. The exchange term raises the first excited state while having little impact on the doubly excited state, which is a closed shell excitation [204, 205]. This term, estimated as the singlet-triplet splitting, is on the order of 2200 cm^{-1} for Rhodamine B [210] and we expect it to be of the same magnitude for Rhodamine 6G. Moreover, the electron-electron correlation term in molecular systems can be substantial [222]. Typically this lowers the energy of the doubly excited state relative to that of the singly excited state. This effect is particularly strong in polyenes and carotenoids where the doubly excited state is lowered below the singly excited state upon inclusion of electron correlations [209]. In our experiment we find that the $|e\rangle \rightarrow |f\rangle$ transition is red shifted compared to the $|g\rangle \rightarrow |e\rangle$ transition by about 500 cm^{-1} . Using a simple estimation of the singlet triplet splitting, $\omega_{S-T} = 2200 \text{ cm}^{-1}$ [210], we find that already this value is large enough to shift the doubly excited state outside the bandwidth of our laser pulses. Additionally, electron-electron correlation should further lower the doubly excited state, shifting the $|e\rangle \rightarrow |f\rangle$ transition even further. Consequently, the state we observe ($|f\rangle$) has little to do with the doubly excited state of the mean field model, and the energy of the $|e\rangle \rightarrow |f\rangle$ transition relative to the $|g\rangle \rightarrow |e\rangle$ transition should not be interpreted as the interaction (i.e. exchange and correlation) energy in this case, as has been done in previous publications [204, 205].

The presence of an excited state at roughly twice the energy of the $|g\rangle \rightarrow |e\rangle$ transition is important for the interpretation of spectroscopic signals. The presence of an ESA contribution in the region of the GSB contribution is known for many important molecules such as chlorophylls [213], bacteriochlorophylls [212], and carotenoids [215, 219] and has also been shown in a large number of dyes [204, 205]. Depending on the strength, spectral position, and dynamics, these states may play a role in the analysis of the experiments of these pigments. Unless this transition

is weak, the analysis of any optical experiment should take into consideration the three-level nature of the pigment when explaining the ultrafast dynamics. Recently it was shown that to accurately account for the fast dynamics of the 1Q2D spectrum in β -carotene it is necessary to include an ESA transition from S_2 [215, 219]. The presence of such a transition also has impact on the analysis of intensity dependence studies involving pump-probe spectroscopy [223, 224].

We have demonstrated in the previous section that it is possible to use the 2Q2D experiment to obtain the displacement of the excited state $|g\rangle \rightarrow |f\rangle$ transition (d_f), and we found that it was very similar to the displacement of the $|g\rangle \rightarrow |e\rangle$ transition (d_e). Even though the 2Q2D pathways are of little relevance to experiments like pump-probe outside the pulse overlap region, the correlation functions and state energies derived from this experiment determine the response functions relevant to the pump-probe ESA contribution too. These pathways generate signals with different appearance depending on d_f . If $d_f = 0$, the ESA pump-probe signal will mirror the SE signal and shift to the blue as t_2 increases. If $d_f = d_e$, the pump-probe signal results in a δ -function ESA spectrum. Beyond the homogenous limit, the dynamics of the bath give rise to different dynamics of SE and ESA for an arbitrary displacement of state $|f\rangle$. This type of information is difficult to extract directly from pump-probe spectra for two reasons. First, the overlap of three pathways contributes to the pump-probe sequence, while only two pathways contribute to the 2Q2D signal (Fig. 2.1). Second, the information about the energy gap correlation functions are contained both in the relaxed spectral line-shape and in the change of the line-shape with waiting time t_2 . Pump-probe spectra are typically analyzed in the homogenous limit where the spectral line-shape is independent of t_2 . As such, the fitting algorithms can only accurately quantify the relaxed line-shape, and this information is not sufficient to unambiguously determine the energy gap correlation functions [225].

Our study indicates that the interpretation of the spectra is greatly simplified if the line-shapes of the individual transitions are featureless, narrow, and display a small Stokes shift. In contrast to molecules, excitons typically interact less strongly with the bath due to their delocalized excitations and therefore they show rather narrow spectral line-shapes [146, 226]. This situation is typically encountered in molecular dimers [227] and aggregates [33, 101, 228]. For molecular aggregates, the presence of an excited state in the monomer at twice the HOMO-LUMO energy has consequences for the electronic structure and relaxation pathways in the aggregates. In the two-level Frenkel exciton model, used to interpret spectroscopy on natural and bacterial light harvesting complexes [155], the two-exciton state wave functions are formed by a product of single excitations in the site basis. At high flux, more than one excitation can be present in the aggregate at once. As the excitons diffuse over the aggregate they may encounter each other and annihilate. Such a process is only possible if a state $|f\rangle$ absorbing the energy of the two excitons exists. Its presence may open a new decay channel between two- and one-exciton bands introduced by the $|f\rangle \rightarrow |e\rangle$ internal conversion, which may be much faster than the one mediated by the $|e\rangle \rightarrow |g\rangle$ transition. The spectral position of the $|e\rangle \rightarrow |f\rangle$ transition in the site basis will thus tune the decay rate of the two-exciton state and thereby the annihilation rate. This effect has been shown to control the temperature dependence of annihilation in the LH2 complex [214] illustrating the importance

of the spectral properties of higher excited states in these biologically relevant pigments. Clearly, 2Q2D spectroscopy could be used to select molecules with an appropriate excited state energy structure to tune the annihilation dynamics in aggregates.

7.7 Conclusion

The ability of multidimensional spectroscopy to select specific excitation pathways by changing the order and direction of the excitation pulses makes it a versatile tool for investigation of dynamics in the condensed phase. Our newly developed setup [78] allows for phase stable experiments for any time ordering of the excitation pulses. As such we have demonstrated three different experimental techniques S_I (rephasing 1Q2D), S_{II} (non-rephasing 1Q2D), and S_{III} (2Q2D) on Rhodamine 6G in solution. Unlike 1Q2D (i.e. $S_I + S_{II}$) spectroscopy, the 2Q2D experiment only involves pathways that propagate in a double-quantum coherence during t_2 and no direct link to auxiliary measurements such as pump-probe spectroscopy exists. To obtain the correct absolute phase of the 2Q2D spectrum we exploit the high phase stability of the setup and use the absolute phase obtained from a 1Q2D measurement carried out directly before or after the measurement of the 2Q2D signal [78].

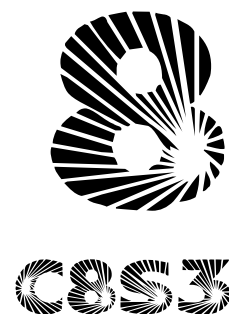
The implementation of the double-quantum coherence technique enables direct probing of excited states at twice the energy of the first optically allowed transition. Detecting a signal in this experiment provides unambiguous experimental proof for the presence of an ESA transition within the bandwidth of the excitation pulses. This property of a 2Q2D signal is highly useful in molecules with congested electronic spectra, where the interpretation of pump-probe results can be cumbersome [215]. The 2Q2D spectrum reveals two main features of opposite sign directed along the anti-diagonal. In addition the spectrum reveals a second weak negative peak at lower energy. The strong positive peak is located at slightly lower frequencies than the GSB contribution (as seen in pump-probe) and the strongest negative feature is located at higher frequencies. This is found to be in contrast to the real part of the total 1Q2D spectrum where we find a weak ESA feature located at lower frequencies than the GSB signal along ω_3 . Analyzing the results in the homogenous limit we are able to correctly predict the direction of the spectrum but not the number of peaks nor the different appearance of the negative feature (ESA) in 1Q- and 2Q2D spectra. To reconcile these observations it is necessary to go beyond the homogenous limit in the analysis of the experiments. Employing the cumulant expansion on a three-level system coupled to a heat bath, we obtain a good fit to both the 1Q2D and 2Q2D spectrum with a model including a red-shifted ESA transition. Our model correctly reproduces the three peaks seen in the 2Q2D spectrum as well as their relative intensities, signs, and spectral positions. Our experiments show that the fluctuations of the two probed states ($|e\rangle$ and $|f\rangle$) relative to the ground state are strongly correlated, reflecting the modulation by a common nuclear bath and a similar nature of the electronic transitions.

Due to the strong electron-interaction (correlation and exchange) effects in this type of dye, we find that it is not possible to interpret the shift of the observed higher excited state in terms of a two-exciton binding energy. Furthermore, our results highlight the complexity of a 2Q2D spectrum

for samples with strong system-bath interaction, where the overlap between the two contributing pathways has a strong impact on the spectra and leads to difficulties in their interpretation. However we show that with proper analysis, 2Q2D spectra provide information about the energies, system-bath interactions, as well as the transition dipole moments of the probed transition. This information is needed to account for ESA contributions in other four-wave mixing experiments. Furthermore, quantifying such states may be important in molecular aggregates where they open up fast relaxation channels between the one- and two-exciton manifolds.

All truths are easy to understand once they are discovered; the point is to discover them.

Galileo Galilei (1564 - 1642)



The efficiency of natural light-harvesting complexes relies on delocalization and directed transfer of excitation energy on spatially well-defined arrangements of molecular absorbers. Coherent excitation delocalization and long-range molecular order are also central prerequisites for engineering energy flows in bio-inspired devices. Double-wall cylindrical aggregates have emerged as excellent candidates that meet these criteria. So far, the experimental signatures of exciton relaxation in these tubular supra-molecules could not be linked to models encompassing their entire spatial structure. Based on the power of two-dimensional electronic spectroscopy, we characterize the motion of excitons in the three-fold band structure of the bi-tubular aggregate C8S3 through temporal, energetic, and spatial attributes. The double-quantum two-dimensional electronic spectra of C8S3 aggregates show well-resolved two-exciton resonances of weakly scattering exciton pairs. The narrow spectral line widths of the two-excitons imply that two excitons scatter elastically and conserve their populations. Accounting for intra- as well as inter-wall electronic interactions in the framework of a Frenkel exciton basis, we employ numerical computations using a homogeneous microscopic model. The combination of 1Q2D and 2Q2D experimental spectra together with simulations in the framework of the nonlinear exciton equations enables us to characterize the exciton and two-exciton band structure. Our results suggest that the investigated molecular nanotubes are an attractive candidate for excitation energy accumulation.

This chapter is based on

- J. SPERLING, A. NEMETH, J. HAUER, D. ABRAMAVICIUS, S. MUKAMEL, H. F. KAUFFMANN, AND F. MILOTA. Excitons and Disorder in Molecular Nanotubes: A 2D Electronic Spectroscopy Study and First Comparison to a Microscopic Model. *J. Phys. Chem. A* **114**, 8179 (2010)

8.1 Introduction

A novel ansatz in the development of artificial light harvesters is the transfer of the self-organization tendency of organic surfactants to molecular dyes [229]. The approach relies on linking hydrophobic and hydrophilic substituents to aggregate forming molecular dyes with efficient excitonic couplings. Among such amphiphilic (hydrophilic *and* hydrophobic) chromophores, the class of cyanine derivatives has the outstanding ability to self-organize into tubular structures that result from the interplay between the hydrophobic effect and the dispersive interactions between π -electrons of the cyanine backbone [230]. As illustrated in Fig. 8.1a for a tubular aggregate formed by the dye 3,3'-bis(3-sulfopropyl)-5,5',6,6'-tetrachloro-1,1'-dioctylbenzimidacarbocyanine (C8S3), the spatial structure of the supramolecules can be well characterized on a mesoscopic scale [189]. In a motif that is typical for molecular nanotubes, the C8S3-chromophores are wrapped into a double-wall cylinder, with an inner diameter of ≈ 10 nm, a wall-to-wall distance of ≈ 4 nm, and lengths approaching the micrometer scale. The complexes thereby strongly resemble the rod elements in light-harvesting chlorosomes of green bacteria, which contain a huge number of bacteriochlorophylls in cylindrical arrangements of comparable diameters and serve to supply the bacterial reaction center with excitation energy [170, 231].

Even though the idea to use self-assembled tubules for building artificial light-harvesting complexes or to combine them as energy transport wires with photochemical reaction partners is tantalizing, up to now, experimental and theoretical studies addressing inter-wall exciton transport have not been clearly linked. As in linear aggregates, the spectroscopic properties (like e.g. narrow linear absorption line-shapes) of cylindrical aggregates are determined by the close spatial proximity of coupled molecular transition dipoles and the consequent formation of Frenkel-excitons [160]. However, in contrast to one-dimensional structures, the linear absorption (LA) of a periodic lattice with cylindrical symmetry splits into a longitudinal (coinciding with the cylinder axis) and two energy-degenerate transversal transitions (perpendicular to the cylinder axis, cf. Fig. 6.1) [186, 189]. The isotropic LA spectrum of C8S3 in aqueous solution (Fig. 8.1b) shows two well-resolved peaks of bands e_1 and e_2 (located at 16530 cm^{-1} and 16860 cm^{-1}) and a broad shoulder at higher energies (band e_3). Bands e_1 and e_2 have been assigned to longitudinal transitions of the inner and outer cylinder, respectively, with their transversal transitions energetically coinciding in a high energy wing (band e_3). The question arises to which extent this spectral shape can be regarded as an additive superposition of two single-wall contributions. In contrast to simple dimer systems, which can be easily classified into weak, intermediate, and strong coupling regimes by looking at the ratio of coupling strength to dephasing constant [102], this categorization is not that straightforward in large systems, where non-nearest neighbor couplings have to be considered as well.

There exist some discrepancies in the available literature dealing with the treatment of band-mixing effects due to inter-wall electronic couplings. In a combined experimental and theoretical analysis of C8S3 the inter-wall interactions have been assumed to be weak and treated perturbatively [189]. Recently, by looking into the slightly different derivative C8O3 and employing

systematic experimental two-dimensional electronic spectroscopy studies, our group [29, 33] and Womick *et al.* [232, 233] identified off-diagonal peaks in 1Q2D correlation spectra ($t_2 = 0$), in favor of a non-perturbative nature of electronic inter-wall interactions. Since these partly controversial results have been claimed for two morphologically slightly different derivatives, the extent of comparability is not clearly defined so far, as detailed experimental work on the bi-tubular system formed by C8S3 that might clarify the conflicting results is missing up-to now. The morphology of C8S3 is less complicated as compared to the supra-molecular structure formed by the dye C8O3 [29]. The supra-molecular helical structure found in C8O3, which manifests itself by an additional electronic transition, is absent in the thio-analog C8S3. Thus, the coupling patterns including diagonal and off-diagonal peaks in 2D correlation and relaxation spectra can be expected to be less congested and more clearly arranged. This makes the simulation of the two-dimensional response feasible on the basis of an atomistic model for the first time.

The information that can be obtained from linear absorption spectra is restricted to line-shapes and energetic positions of single-exciton states. To access higher exciton manifolds, one has to resort to nonlinear methods such as 2D-ES. The spectroscopy of doubly-excited states allows to access specific geometric and dynamic parameters and yields information about correlations and distinct relaxation patterns. The most prominent example in this context are the fast relaxation pathways of doubly-excited DNA optimized to avoid genetic damage even under high levels of sunlight radiation [234]. This phenomenon is also very important for the photoprotection of photosynthetic reaction centers (RC) [235]. In photosynthetic antenna chlorosomes, however, the opposite case is beneficial: two or more excitations must have weak scattering and relaxation in order to accumulate the energy, which is transferred later to the RCs, within the antennae. These antennae would be very inefficient, if only one excitation per ≈ 100000 molecules survived.

The accurate characterization of excitation transport and relaxation is central in the search for

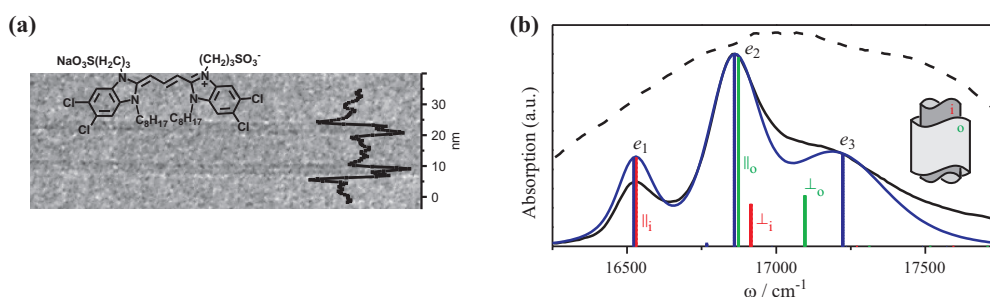


Figure 8.1: (a) Chemical structure of the monomer and a cryogenic transmission microscopy image of the aggregated sample C8S3. The curve on the right side shows the horizontally integrated image gray tone. (b) Experimental (solid black) and simulated (blue) linear absorption spectrum, together with the stick spectrum of the double-wall (blue), the inner (red), and outer (green) cylinder. The experimental excitation spectrum is shown as black dashed line.

efficient synthetic molecular photon energy conversion devices. Tightly bound molecular aggregates are promising candidates for primary photon harvesters. In molecular aggregates, intermolecular interactions create collective excitations termed excitons, that can be grouped in bands according to the number of excitations (i.e. (one-) exciton band e , two-exciton band f , etc.). Strongly bound aggregates feature narrow spectral line shapes as a consequence of excitation delocalization leading to averaging over individual fluctuations [226]. Due to molecular flexibility the phonon degrees of freedom on the other hand are limited to intramolecular vibrations, which are localized on individual molecules. Therefore, the non-radiative exciton decay is inhibited by the weak overlap of exciton and phonon wave functions.

In this chapter, detailed 1Q2D and 2Q2D experiments on the three-fold band structure of C8S3 aggregates are presented in conjunction with a novel theoretical-numerical simulation. A key point of the present work is to explore the nature of excitonic inter-wall couplings and wave-function mixing that determine the particulars and details of the optical exciton dynamics in C8S3. We find evidence for electronic inter-wall interactions and their spectroscopic signatures from an atomistic computational analysis of 1Q2D electronic correlation and relaxation spectra. By applying 2Q2D-ES signatures of exciton correlations in C8S3 aggregates are investigated. The third-order nonlinear signals are reconstructed by a microscopic model employing a double-wall cylindrical structure [189]. The experiments in combination with the microscopic cylindrical model simulations specifically trace spatio-temporal excitonic transfer and are therefore a realistic extension of previous simulations performed on single-wall cylinders and linear spectroscopic properties [186, 196, 197, 236]. In addition, the model is superior to the coupled multi-level energy scheme employed in previous works [29, 33], that used experimental input quantities from 1D and 2D spectroscopy in the absence of structural information and energy-space relations.

8.2 Experimental Details

For all experiments, C8S3 was dissolved in water and gently stirred for one week under exclusion of light. This stock solution ($c = 5 \cdot 10^{-4}$ mol/l) was diluted with water (1:1) before the measurements to yield an absorption of ≈ 0.4 in the maximum. As can be seen by comparison with the spectrum of our excitation pulses (Fig. 8.1b), the spectral bandwidth allows to cover each of the three absorption bands with at least 80 % of the maximal spectral pulse intensity. Due to the huge disparity in spatial dimensions, tubular aggregates tend to align along the flow direction in thin liquid films even at relatively low flow speeds. By switching the light polarization between parallel and vertical to the jet, this allows preferential excitation of either longitudinal or transversal transition moments (for which we use the terminology *parallel* respectively *vertical* excitation in the following).

For the two-dimensional experiments, the output of the NOPA was tuned to 17100 cm^{-1} ($\Delta\omega_{\text{FWHM}} = 1500 \text{ cm}^{-1}$, $\Delta t = 17 \text{ fs}$). To reduce unwanted higher-order effects and non-resonant signals from the solvent and to prevent the sample from too fast photodegradation the input beam is attenuated by a ND filter (after the NOPA) to yield not more than 0.5 nJ of energy in each

of the excitation pulses. This energy corresponds to a fluence of $2.2 \cdot 10^{13}$ photons/cm² for each excitation pulse, which results in excitation of 0.08% of the molecules. 1Q2D spectra have been recorded by scanning the t_1 -delay from -200 fs to +200 fs in 0.5 fs steps, while t_2 is stepped from 0 to 100 fs in steps of 0.25 fs for recording 2Q2D spectra.

8.3 Computational Details

8.3.1 Construction of a Microscopic Model

Essential aspects of the relaxation dynamics in tubular aggregates may be presumed to originate from site disorder and the consequent variation of the spatio-energetic exciton characteristics across the spectrum. In contrast to the assessable number of coupled pigments in most of the natural antennas currently studied in nonlinear experiments [237, 238, 239], molecular nanotubes are huge with respect to their building-blocks. The sheer number of molecules building up the tubular structure is an obstacle in any theoretical approach that aims to account for individual site-properties, like site-orientation or static site-disorder.

In C8S3, roughly one hundred sites fill a tubular volume of one nanometer length [189, 230], so that roughly 10^4 sites would be needed to set up a reasonably converged structure with a length to diameter ratio of approx. 10:1. An atomistic calculation of the nonlinear response of N excitonically coupled sites requires explicit information of the N single- and the $N(N-1)/2$ double-excited eigenstates [47]. Even though we clearly perceive disorder effects from the streaking of the diagonal and off-diagonal peaks in the experimental two-dimensional electronic spectra, a simulation of nonlinear spectra within a microscopic model that includes disorder effects is too expensive. Therefore, in order to keep the computational expenses manageable, we employ an infinite model in the homogeneous limit.

To recover the structural motif of the nanotubes in our simulations we employ a one-dimensional periodic infinite system with a unit cell containing two rings of sites. Each site represents a monomer building up the cylindrical aggregate. The inner (outer) cylinder has a diameter of 10.8 nm (15.6 nm) and contains 2 (4) sites per ring. Subsequent rings are rotated by 9° (18°) and translated along the cylinder axis by 0.0585 nm (0.065 nm) in the inner (outer) cylinder. The monomers are modeled as two-level quantum systems with a transition frequency of 18840 cm^{-1} and are characterized by a dipole moment represented by two charges ($q = \pm 0.34 e$) separated by 0.7 nm [189]. The angle between the cylinder axis and the transition dipole is 46.2° (36.2°) in the inner (outer) cylinder. Each site is coupled to a harmonic bath (an overdamped Brownian oscillator with a timescale of 50 fs) by a strength of 500 cm^{-1} [4]. To simulate the infinite system we apply periodic boundary conditions along the cylinder axis, which gives Bloch-type exciton states with a lattice wave vector κ [240]. Since the optical wavelength is usually much larger than the exciton spatial coherence length, only excitons with near-zero lattice wave vector $\kappa = 0$ carry non-zero transition amplitude.

One unit-cell of the double-wall cylindrical structure in our model contains 112 sites, leading

to 112 exciton sub-bands in the whole exciton band. However, the cylindrical symmetry limits the number of optically relevant excitons. For a single cylinder only three excitons from different sub-bands are optically active. The lowest-energy $\kappa = 0$ exciton is polarized parallel (\parallel) and the two degenerate higher-energy $\kappa = 0$ excitons are polarized perpendicular (\perp) to the cylinder axis (Fig. 8.1b). The splitting between these transitions is inversely proportional to the cylinder diameter. Accordingly, the longitudinal and transversal transitions of the inner cylinder (\parallel_i and \perp_i) are separated further in energy than the respective transitions of the outer cylinder (\parallel_o and \perp_o). Upon combining the two cylinders to a double-wall structure the two parallel sub-bands (\parallel_i and \parallel_o) retain their positions and intensities, whereas the two perpendicular sub-bands (\perp_i and \perp_o) mix and can no longer be attributed to individual cylinders. The optical intensity of the lower energy perpendicular sub-band thereby tends to zero, justifying its neglect for the remainder of this chapter. Overall, only three peaks, corresponding to the longitudinal transitions of the inner and outer cylinder and a transversal transition stemming from both walls can be discerned in the linear absorption spectrum. We will refer to them by excitons e_1 , e_2 , and e_3 , respectively. Inhomogeneous broadening was accounted for in the simulations by convoluting the homogeneous spectrum with a Gaussian function in time domain with a frequency-dependent width of the form $\exp(0.0019(\omega - 14700))$. The simulated linear absorption spectrum agrees well with experiment (Fig. 8.1b).

8.3.2 Modeling Spectral Properties in the Homogenous Limit

To reconstruct the linear as well as nonlinear signals of C8S3 within a microscopic (homogenous) model, we employ a one-dimensional periodic lattice (structural parameters as described above), whose unit cell contains two circular arrangements of transition dipoles. In the following, we label the sites inside a single unit cell by indices m and identify each cell by its position vector \mathbf{R} . Each chromophore is treated as an identical two-level system. Due to translational invariance, the chromophore coupling $J_{mm'}(\mathbf{R} - \mathbf{R}')$ is a function of the distance between the cells \mathbf{R} and \mathbf{R}' . The real-space Hamiltonian is [50]:

$$\hat{H} = \sum_{\mathbf{R}\mathbf{R}'} \sum_{mn} J_{mn}(\mathbf{R} - \mathbf{R}') \hat{B}_{\mathbf{R}m}^\dagger \hat{B}_{\mathbf{R}'n} + \frac{\Delta}{2} \sum_{\mathbf{R}} \sum_m \hat{B}_{\mathbf{R}m}^{\dagger 2} \hat{B}_{\mathbf{R}m}^2, \quad (8.1)$$

where $\hat{B}_{\mathbf{R}m}^\dagger$ is the exciton creation operator on the m^{th} chromophore in the \mathbf{R}^{th} cell, and $\hat{B}_{\mathbf{R}m}$ is the conjugate annihilation operator. We use Boson statistics for the excitons with commutation relations $[\hat{B}_{\mathbf{R}m}, \hat{B}_{\mathbf{R}'n}^\dagger] = \delta_{mn} \delta_{\mathbf{R}\mathbf{R}'}$. This model is called soft-core boson model. The first term in the Hamiltonian represents one-exciton site energies $\epsilon = J_{mm}(0)$ and resonant interactions, while the second term is a double-exciton binding parameter: taking $\Delta \rightarrow \infty$ we recover the two-level chromophore model.

The one-exciton states of this system are the Bloch states with wavefunctions

$$\Psi_{\mathbf{R}m}^{\mathbf{q}\lambda} = \frac{1}{\sqrt{L}} e^{-i\mathbf{q}\mathbf{R}} \phi_{m\lambda}(\mathbf{q}), \quad (8.2)$$

where L is the number of unit cells. Each eigenstate has a pair of quantum numbers $\mathbf{q}\lambda$ where λ denotes different Davydov's subbands in the one-exciton band, and $\mathbf{q} = \frac{\pi}{L}[-1, 1]$, with a step $\delta\mathbf{q} = \frac{2\pi}{L}$, is the momentum. ϕ are the one-exciton states of a unit cell:

$$\sum_n J_{mn}(\mathbf{q})\phi_{n\lambda}(\mathbf{q}) = \epsilon_\lambda(\mathbf{q})\phi_{m\lambda}(\mathbf{q}), \quad (8.3)$$

where

$$J_{mn}(\mathbf{q}) = \sum_{\mathbf{R}} e^{i\mathbf{q}\mathbf{R}} J_{mn}(\mathbf{R}), \quad (8.4)$$

and $\epsilon_\lambda(\mathbf{q})$ is the exciton energy at λ Davydov's subband.

Exciton response to the optical fields is given in terms of many-exciton propagators - the exciton Green's functions. The single-exciton Green's function is $G_{\mathbf{q}\lambda}(t) = \theta(t)e^{-i\epsilon_\lambda(\mathbf{q})t - \gamma_\lambda(\mathbf{q})t}$, where $\gamma_\lambda(\mathbf{q})$ is the exciton dephasing. The linear response function essential for calculating the linear absorption and linear dichroism spectra is given by [4]

$$R^{(1)} = \sum_\lambda |\mu_\lambda|^2 G_\lambda(t), \quad (8.5)$$

where $\mu_\lambda = L \sum_m \mu_m \phi_{m\lambda}$ is the single-exciton transition dipole (the summation is over a single-cell). Note that we assumed $La \ll \bar{\lambda}$, where a is the lattice constant and $\bar{\lambda}$ is the optical wavelength. Thus only zero-momentum exciton states contribute to the response and the $\mathbf{q} = 0$ parameter can be neglected.

The third order response also depends on the double-exciton states. An explicit calculation of the doubly-excited states of an infinite system would require introducing an additional lattice wave vector corresponding to the translational symmetry of an exciton pair. The alternative quasiparticle picture allows to avoid this extension by considering the excitons as interacting particles [50, 191]. This is accomplished by using the Heisenberg representation for the exciton polarization operator and expanding the Heisenberg equation of motion for the polarization in the incoming optical field. The solution of the equation allows to calculate the third order response functions and to express the two-exciton resonances using the exciton scattering matrix Γ via the Dyson equation. Using the quasi-particle representation, the third order response can be calculated from the Green's function solution of the Nonlinear Exciton Equations (NEE) [50, 241]. For the phase-matching direction $\mathbf{k}_I = -\mathbf{k}_1 + \mathbf{k}_2 + \mathbf{k}_3$ we find

$$\begin{aligned} R_I^{(3)}(t_1, t_2, t_3) &= \sum_{\lambda_4 \lambda_3 \lambda_2 \lambda_1} \sum_{\lambda'_2 \lambda'_3 \lambda'_2 \lambda'_1} \mu_{\lambda_4} \mu_{\lambda_3} \mu_{\lambda_2} \mu_{\lambda_1} \\ &\times \int_0^\infty d\tau G_{\lambda_4}(t_3 - \tau) V_{\lambda_4 \lambda'_1 \lambda'_2 \lambda'_3} G_{\lambda'_1}^*(\tau) G_{\lambda'_2 \lambda'_3, \lambda'_2 \lambda'_3}^{(Y)}(\tau) G_{\lambda'_2 \lambda'_1, \lambda_2 \lambda_1}^{(N)}(t_2) G_{\lambda_1}^*(t_1). \end{aligned} \quad (8.6)$$

Here V is the "scattering potential" obtained by transforming the second term in the Hamiltonian to the single-exciton eigenstate basis, $G^{(Y)}$ is the double-exciton Green's function, and $G^{(N)}$ is the

single-exciton density-matrix Green's function; both in the single-exciton basis. This expression reflects the interaction and propagation sequence in third order response, i.e. the first interaction generates one exciton which propagates according to G^* , the second interaction generates a density matrix in single-exciton space that propagates according to $G^{(N)}$. After the third-interaction we have factorized the propagation into $G_{\lambda'_1}^*$ and $G_{\lambda'_2\lambda'_3,\lambda''_2\lambda_3}^{(Y)}$ to account for double-exciton states. These particles finally interact through the scattering potential and generate the signal at λ_4 . Similar to the linear response, we included only the zero-momentum states which do interact with the field.

To avoid the explicit calculation of $G^{(Y)}$, which involves finding all double-exciton states, we describe their resonances using the exciton scattering matrix $\Gamma_{\lambda_4\lambda_3\lambda_2\lambda_1}$. In the frequency domain we have

$$G^{(Y)}(\omega) = G^{(0)}(\omega) + G^{(0)}(\omega)\Gamma(\omega)G^{(0)}(\omega), \quad (8.7)$$

where $G_{\lambda_4\lambda_3,\lambda_2\lambda_1}^{(0)}(\omega) = \delta_{\lambda_4\lambda_2}\delta_{\lambda_3\lambda_1}I_{\lambda_2\lambda_1}(\omega)$ is the free-double-exciton Green's function (when excitons do not interact) with $I_{\lambda_2\lambda_1}(\omega) = (\omega - \epsilon_{\lambda_2} - \epsilon_{\lambda_1} + i\gamma_{\lambda_2} + i\gamma_{\lambda_1})^{-1}$.

The response function using this scattering matrix after applying double Fourier transform is

$$R_I^{(3)}(\omega_1, t_2, \omega_3) = \sum_{\lambda_4\lambda_3\lambda_2\lambda_1} \sum_{\lambda'_2\lambda'_1} \mu_{\lambda_4}\mu_{\lambda_3}\mu_{\lambda_2}\mu_{\lambda_1} G_{\lambda_4}(\omega_3) \\ \times \Gamma_{\lambda_4\lambda'_1\lambda'_2\lambda_3}(\omega_3 + \epsilon_{\lambda'_1} + i\gamma_{\lambda'_1}) I_{\lambda'_2\lambda_3}(\omega_3 + \epsilon_{\lambda'_1} + i\gamma_{\lambda'_1}) G_{\lambda'_2\lambda'_1,\lambda_2\lambda_1}^{(N)}(t_2) G_{\lambda_1}^*(\omega_1). \quad (8.8)$$

The scattering matrix is calculated using the Dyson equation and its final form for two-level molecules is:

$$\Gamma_{\lambda_4\lambda_3\lambda_2\lambda_1}(\omega) = \sum_{mn} \phi_{m\lambda_4}\phi_{m\lambda_3}\phi_{n\lambda_2}\phi_{n\lambda_1} [D^{-1}(\omega)]_{mn} \quad (8.9)$$

and

$$D_{mn}(\omega) = \frac{1}{L} \sum_{\mathbf{q}} \sum_{\lambda_2\lambda_1} \frac{\phi_{m\lambda_2}(\mathbf{q})\phi_{m\lambda_1}(-\mathbf{q})\phi_{n\lambda_2}^*(-\mathbf{q})\phi_{n\lambda_1}^*(\mathbf{q})}{\omega - \epsilon_{\lambda_2}(\mathbf{q}) - \epsilon_{\lambda_1}(-\mathbf{q}) + i\gamma_{\lambda_2}(\mathbf{q}) + i\gamma_{\lambda_1}(-\mathbf{q})}. \quad (8.10)$$

The exciton density matrix Green's function is obtained from the Redfield equation for the density matrix [191]:

$$\frac{d}{dt}\rho_{\lambda\lambda'} = -i(\epsilon_{\lambda} - \epsilon_{\lambda'})\rho_{\lambda\lambda'} - \sum_{\lambda''\lambda'''} K_{\lambda\lambda',\lambda''\lambda'''}\rho_{\lambda''\lambda'''}, \quad (8.11)$$

where K is the Redfield relaxation rate matrix. We use the secular approximation for the density matrix, so that the populations (diagonal elements in the density matrix) and the coherences (off diagonal elements in the scattering matrix) evolve independently. The populations follow the Pauli master equation and the coherences show exponentially damped oscillations. The Redfield rate matrix then attains the form:

$$K_{\lambda\lambda',\lambda''\lambda'''} = \delta_{\lambda\lambda'}\delta_{\lambda''\lambda'''}K_{\lambda\lambda,\lambda''\lambda'''} + \delta_{\lambda\lambda''}\delta_{\lambda'\lambda'''}(1 - \delta_{\lambda\lambda'})\gamma_{\lambda\lambda'}^{(N)}. \quad (8.12)$$

$K_{\lambda\lambda,\lambda''\lambda'''}$ is the population transport rate from exciton state λ'' to λ and $\gamma_{\lambda\lambda'}^{(N)}$ is the dephasing rate for inter-band coherence (i.e., coherence between single exciton states).

The final signal is obtained by convoluting the response function with the envelopes of the optical fields (semi-impulsive limit). The signal expressions become very simple if pulse overlapping regions can be neglected. We then have

$$\begin{aligned} S_I^{(3)}(\omega_1, t_2, \omega_3) = & \sum_{\lambda_4\lambda_3\lambda_2\lambda_1} \sum_{\lambda_2'\lambda_1'} \mu_{\lambda_4}\mu_{\lambda_3}\mu_{\lambda_2}\mu_{\lambda_1} \times E_4^*(\epsilon_{\lambda_4} - \omega_4)E_3(\omega_3 - \epsilon_{\lambda_3})E_2(\omega_2 - \epsilon_{\lambda_2})E_1^*(\epsilon_{\lambda_1} - \omega_1) \\ & \times G_{\lambda_4}(\omega_3)\Gamma_{\lambda_4\lambda_1'\lambda_2'\lambda_3}(\omega_3 + \epsilon_{\lambda_1'} + i\gamma_{\lambda_1'})I_{\lambda_2'\lambda_3}(\omega_3 + \epsilon_{\lambda_1'} + i\gamma_{\lambda_1'})G_{\lambda_2'\lambda_1',\lambda_2\lambda_1}^{(N)}(t_2)G_{\lambda_1}^*(\omega_1). \end{aligned} \quad (8.13)$$

Similar expressions can be derived for S_{II} and S_{III} . Calculation of the signal requires knowledge of the relaxation parameters. These are calculated assuming that each chromophore is coupled to a statistically independent bath represented by a single overdamped Brownian oscillator. It is characterized by a spectral density of transition energy fluctuations, $\tilde{\epsilon}(t)$ [178]:

$$C''(\omega) = \frac{1}{2} \int dt e^{i\omega t} \langle [\tilde{\epsilon}(t), \tilde{\epsilon}(0)] \rangle = 2l \frac{\omega\Lambda}{\omega^2 + \Lambda^2}. \quad (8.14)$$

The relaxation rates in real space then can be calculated using the second-order perturbation theory in fluctuations and taking the Markovian (fast fluctuation) limit. For our system, using the auxiliary function [191]

$$M^{(\pm)}(\omega) = \int_0^\infty dt e^{i\omega t} \int \frac{d\omega'}{2\pi} C''(\omega') \left[\coth\left(\frac{\beta\hbar\omega'}{2}\right) \cos(\omega t) \mp i \sin(\omega t) \right], \quad (8.15)$$

we obtain

$$\gamma_\lambda = \sum_{\lambda'} M^{(+)}(\epsilon_\lambda - \epsilon_{\lambda'})\phi_{\lambda\lambda'}, \quad (8.16)$$

$$K_{\lambda'\lambda',\lambda\lambda} = 2\text{Re}M^{(+)}(\epsilon_\lambda - \epsilon_{\lambda'})\phi_{\lambda\lambda'}, \quad (8.17)$$

where $\phi_{\lambda\lambda'} = \eta \sum_n \phi_{n\lambda}^2 \phi_{n\lambda'}^2$. For the inter-band coherences we neglect the pure dephasing and use $\gamma_{\lambda\lambda'}^{(N)} = \frac{1}{2}(K_{\lambda\lambda,\lambda\lambda} + K_{\lambda'\lambda',\lambda'\lambda'})$. The parameter $\eta = L^{-1}$ vanishes for the limit $L \rightarrow \infty$. This is physically justified since relaxation in infinite systems reflects a coherent act over the whole infinite set of molecules with the probability vanishing for such an event. However, realistic systems with moderate disorder are characterized by some coherence length κ , where the realistic wavefunctions are delocalized. We thus use $\eta = \kappa^{-1}$ and leave this number as a fitting parameter.

The approach presented here bears considerable advances compared to the effective model of coupled oscillators used in the analysis of 1Q2D electronic spectra of C8O3 [29, 33] (cf. Chapter 6). On the one hand, the new treatment uses the Green's function solution of the nonlinear exciton

equations (NEE) and the exciton scattering matrix for the description of the double-exciton resonances. On the other hand, the bi-tubular architecture of C8S3 and its energy-space coordinates are taken into account explicitly in this simulation which yields solutions for 1Q2D and 2Q2D spectra in the limit of periodic boundary conditions.

8.4 Results and Discussion

8.4.1 1Q2D Correlation and Relaxation Patterns

Fig. 8.2 shows the real part of the complex 1Q2D signals recorded for both parallel and vertical excitation. The linear absorption spectrum is reflected for $t_2 = 0$ in the signals along the diagonal ($|\omega_1| = \omega_3$), which divides the plots into two triangular parts ($|\omega_1| > \omega_3$ and $|\omega_1| < \omega_3$). Note however, that signals in 2D spectra scale differently with the transition dipole moment than those in LA spectra ($|\mu_i|^4$ vs. $|\mu_i|^2$). Additionally, the intensities of the 2D signals are reshaped by the finite pulse spectrum. Depending on whether the system evolves in a one-exciton coherence or a coherence between a one- and a two-exciton state during t_3 , absorptive 1Q2D-ES signals of coupled absorbers feature both positive and negative contributions [10, 48, 183]. In the language of pump-probe spectroscopy, 1Q2D peaks with negative sign are related to excited-state absorption (ESA) from the one- into the two-exciton band, whereas positive features can be assigned to ground state bleaching (GSB) and stimulated emission (SE) [48, 191]. Since transitions between successively higher exciton manifolds are blue-shifted with respect to each other, ESA contributions to the 1Q2D signal become shifted off of the diagonal into $|\omega_1| < \omega_3$. The 1Q2D absorptive correlation spectra shown in Fig. 8.2, show this effect for all three bands e_1 , e_2 , and e_3 .

The most striking 1Q2D signals are the off-diagonal peaks being indubitable fingerprints of electronic couplings [29, 31, 33]. Due to these off-diagonal cross-intensities, the correlation spectra ($t_2 = 0$) in Fig. 8.2 are asymmetric with respect to the diagonal. For parallel excitation (Fig. 8.2a), the two strong peaks e_1 and e_2 of the LA are recovered along the diagonal, and we observe around 10% of the maximal intensity at the band e_1 /band e_2 off-diagonal coordinate in $|\omega_1| > \omega_3$. Peak e_3 can not be seen as diagonal peak in 1Q2D-ES under parallel excitation, it is however directly detectable from the cross peak signal between bands e_2 and e_3 whose intensity is proportional to $|\mu_{e_2}|^2|\mu_{e_3}|^2$. Also for vertical excitation (Fig. 8.2b), the cross-intensities for e_1/e_2 and e_2/e_3 in $|\omega_1| > \omega_3$ are non-zero. The diagonal signal of band e_3 is clearly seen in Fig. 8.2b, although its intensity is substantially weaker than one would expect from its corresponding peak intensity in linear absorption. Generally, off-diagonal intensities reveal electronic couplings between the bands in the aggregate, the variation in the coupling patterns reflecting the dominant orientations of transition dipole moments. Vertical excitation increases the relative contribution of band e_3 and highlights its correlation mostly with the longitudinal transition of the outer cylinder (band e_2).

Apart from the differences in the correlation plots ($t_2 = 0$) for parallel and vertical excitation, the temporal evolution of the relaxation spectra ($t_2 = 50, 200$, and 500 fs) is governed by comparable tendencies. A striking feature is the growing-in of an intense cross peak in $|\omega_1| > \omega_3$, that

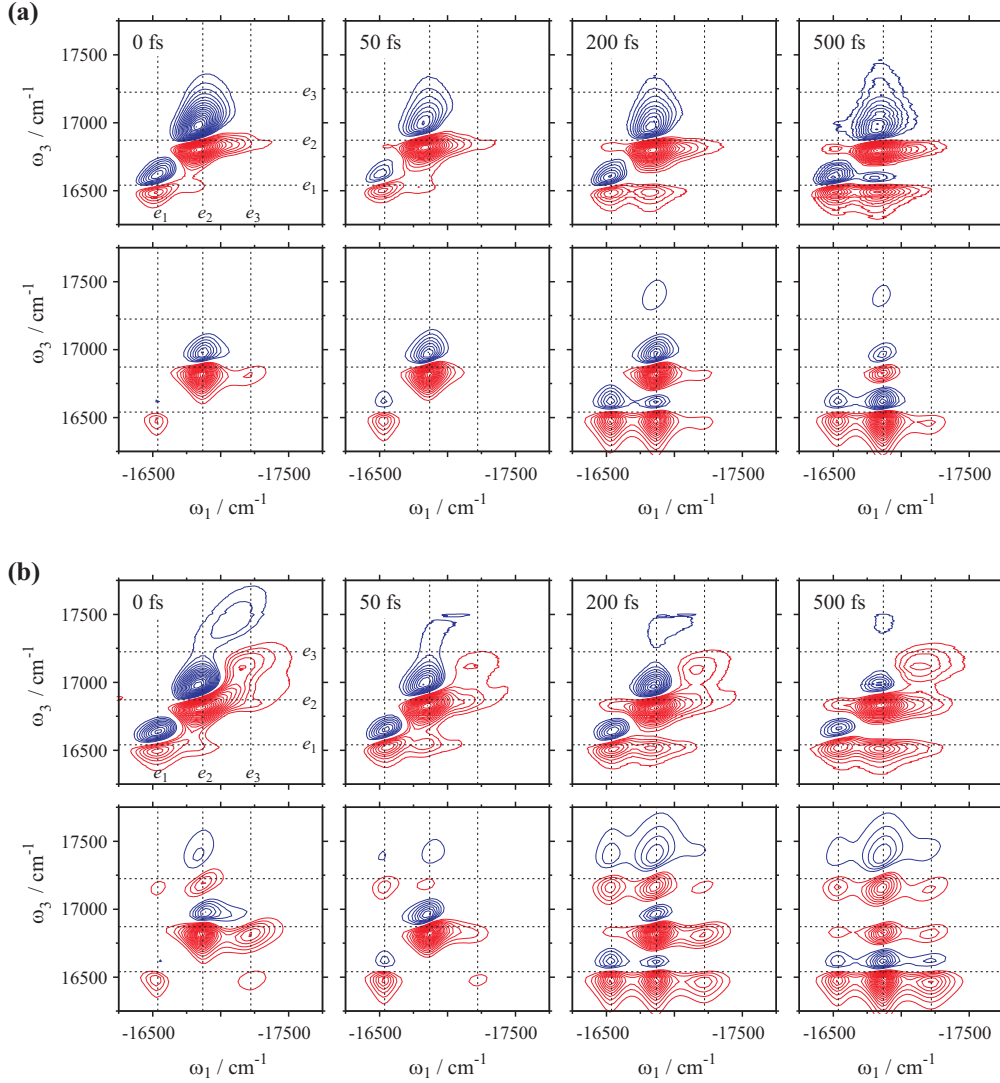


Figure 8.2: Absorptive parts of 1Q2D electronic spectra recorded with excitation pulses polarized (a) parallel and (b) vertical to the flow direction. The upper row displays experimental data, whereas simulations are shown in the lower row of each panel. From left to right each row shows the 1Q2D correlation spectrum ($t_2 = 0$ fs) and relaxation spectra recorded for t_2 -delays of 50, 200, and 500 fs, respectively. Contour lines are drawn in $\pm 5\%$ intervals, starting at 10% signal intensity. Red (blue) contours indicate positive (negative) features. All spectra are normalized to their maximum absolute value.

arises via exciton relaxation from band e_2 into band e_1 (cf. Fig. 8.2). At increasing t_2 -delays, the off-diagonal signals grow in intensity and acquire a more and more elliptic shape with the long axis parallel to the ω_1 -axis, thereby extending from the $|\omega_1|$ -coordinate of bands e_1 and e_2 far into higher frequencies. Because of simultaneous energy uphill transfer from e_1 to e_2 at longer waiting times (i.e. on a slower timescale), a much weaker off-diagonal feature appears at reversed

coordinates ($|\omega_1| < \omega_3$). At the same time, the relative intensity of band e_2 decreases, while the relative diagonal peak intensity of band e_1 steadily increases. Within 500 fs, the motion of relaxing excitons thus reshapes the diagonal signals of band e_1 and band e_2 into peaks of almost equal intensity. This is an unbiased observation and a convincing proof of concurrent inter-tube exciton transfer driven by electronic coupling and relaxation, thereby conveniently illustrating the gain in information content by spreading the system's response into two dimensions.

Our experimental findings prompt us to draw the following conclusions. First, 2D electronic spectra prove that all of the excitonic bands of C8S3 are coupled. Second, intensity growth of cross peaks with increasing waiting time t_2 images ongoing exciton population relaxation. Third, since a cross peak imaging exciton transfer in a 1Q2D relaxation spectrum is proportional to the product of the squared transition dipole magnitudes of both of the states involved ($\propto |\mu_i|^2 |\mu_j|^2$), it permits to observe the process as long as at least one of the states absorbs strong enough. In our case, the formation of streaked profiles, despite the only weak diagonal intensities at high frequencies, reflects the characteristics of excitonic states to substantially change across the spectrum of eigenstates [228].

As illustrated in Fig. 8.2 the key spectral properties of the experimental 1Q2D signals can be reasonably reproduced in the homogeneous limit. We recover the asymmetry of the two triangular 2D signal parts. Though the diagonal signal of band e_3 is missing for parallel excitation conditions, its cross-correlation with band e_2 is readily perceived. Similar is true for the intensity rearrangements in the sequence of 1Q2D relaxation spectra.

8.4.2 2Q2D Correlation Spectra

Double-quantum two-dimensional electronic spectroscopy (2Q2D-ES) has been designed specifically to probe correlated dynamics of double-excitations. The properties of the two-exciton band of molecular aggregates are influenced by exciton-exciton correlations/scattering, which shift them with respect to the sum of the two contributing excitons. 2Q2D-ES is sensitive to these correlations by yielding a signal only in case the parameters of an exciton pair are not additive for a two-exciton state, i.e. $\epsilon_f \neq \epsilon_e + \epsilon_{e'}$ and/or $\mu_{fe} \neq \mu_{e'g}$ and $\mu_{fe'} \neq \mu_{eg}$ [13]. If these conditions are not met, the two system-field interaction configurations describing 2Q2D-ES (Fig. 2.1c) are of equal strength and opposite sign, and they exactly cancel. Three types of two-excitons can be distinguished: (i) Strongly bound biexcitons have non-additive energies resulting in isolated peaks in 2Q2D-ES. (ii) Weakly scattering two-excitons have negligible shifts from the sum of the energies of the two excitons involved showing a peak correlated with the energies of the two excitons in 2Q2D-ES. (iii) Non-interacting two-excitons do not show up in 2Q2D-ES.

In the exciton scattering representation of 2Q2D-ES, the first two pulses (delayed by t_1) create two excitons, which propagate and scatter during the second delay time t_2 . A third pulse then annihilates one exciton and the last exciton is detected after some delay t_3 . The third and fourth excitons are not limited to eigen-excitons due to particle scattering: they may be given by exciton superpositions. The two-dimensional frequency domain signal $S_{\text{III}}(t_1, \omega_2, \omega_3)$ is depicted by Fourier transforming $t_2 \rightarrow \omega_2$ and $t_3 \rightarrow \omega_3$ while keeping t_1 fixed. The spectrum maps doubly-excited

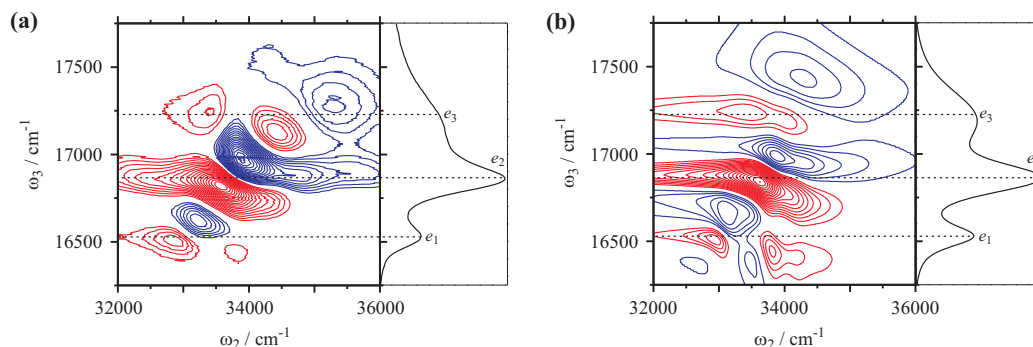


Figure 8.3: (a) Experimental and (b) simulated real part 2Q2D spectra of C8S3 aggregates for vertical excitation. Contour lines are drawn in $\pm 5\%$ intervals, starting at 10% signal intensity. Red (blue) contours indicate positive (negative) features. Both spectra are normalized to their absolute maximum value. The experimental and simulated linear absorption spectra are plotted for comparison on the right side of panel (a) and (b), respectively. Dashed horizontal lines mark the peak maxima in the linear absorption spectra.

resonances along ω_2 and both unperturbed and perturbed exciton resonances along ω_3 .

2Q2D-ES has demonstrated its merits in application to semiconductor quantum wells revealing detailed information about the energetic positions and dynamics of bound biexcitons and unbound two-excitons [203, 207]. Generally, the method is most promising for systems featuring weak system-bath interactions and narrow line-shapes, a situation typically encountered in molecular aggregates and nanostructured semiconductors. As the system-bath interactions grow stronger and the line-shapes become broader, the interpretation of 2Q2D signals complicates as outlined in detail in Chapter 7 [20].

The experimental 2Q2D spectrum of C8S3 aggregates (Fig. 8.3a) reveals exciton resonances and scattering-induced energy shifts (Δ) of exciton pairs from the additive energy values. The direction of the shift (sign of Δ) can be determined from the relative position of the positive and negative contributions. The negative contribution appears at higher (lower) frequencies along ω_3 than the positive contribution if $\Delta > 0$ ($\Delta < 0$), corresponding to exciton-exciton repulsion (attraction). The blue-shift of the negative signals observed in the 2Q2D spectrum is consistent with earlier experiments on linear J-aggregates [166]. A remarkable feature in the 2Q2D spectrum of C8S3 aggregates is the similarity in the peak line widths along ω_2 and ω_3 , which map the dephasings of two-excitons and excitons, respectively. The similar line widths along the two axes imply that the exciton pairs have the same relaxation pathways as the contributing excitons. Thus, putting more excitons into the nanotubes does not raise new relaxation channels.

The simulated 2Q2D spectrum is presented in Fig. 8.3b. Comparison with experiment reveals a good overall agreement of the peak positions, relative intensities, and line shapes. For assigning the observed peak pattern we resort to narrow homogeneous spectra obtained by reducing the system-bath coupling strength by a factor of five (Fig. 8.4). All peaks correlate well with the

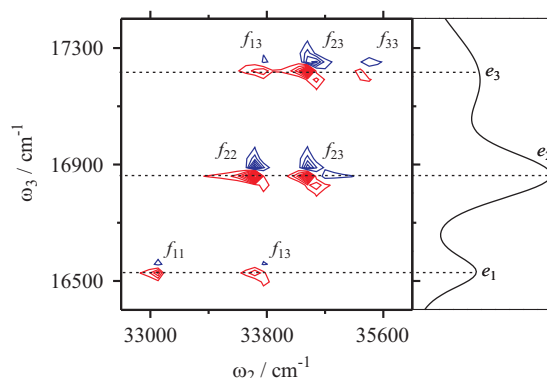


Figure 8.4: Simulated 2Q2D spectra of C8S3 aggregates with system-bath coupling set to 100 cm^{-1} and no Gaussian broadening. Contour lines are drawn in $\pm 5\%$ intervals, starting at 5% signal intensity. Red (blue) contours indicate positive (negative) features. The simulated linear absorption spectrum is plotted for comparison. Dashed horizontal lines mark the peak maxima in the linear absorption spectrum.

energies of exciton pairs along ω_2 , indicating that we do not observe bound biexcitons. Rather, the observed 2Q2D spectrum signifies weakly scattering excitons, which form distinct two-exciton sub-bands. The observed two-excitons are composed of two types of sub-bands: "overtone", where the same exciton is doubly excited, and "combinations", where two different excitons are excited. Having three types of excitons (e_1 , e_2 , e_3), the two-exciton band of these aggregates consists of six two-exciton sub-bands: three overtone sub-bands, $f_{jj} \approx 2e_j$ ($j = 1, 2, 3$), and three combination sub-bands (f_{12} , f_{13} , f_{23}). The three overtone sub-bands appear along the "diagonal" $\omega_2 = 2\omega_3$. The remaining four peaks can be assigned to two combination sub-bands. A combination sub-band yields two peaks that share the same frequency along ω_2 , but appear at the two corresponding frequencies along ω_3 . With this information, we can assign the four peaks to the combination sub-bands f_{13} and f_{23} . From the fact that no signals show up between f_{11} and f_{22} along ω_2 , we can conclude that the combination sub-band f_{12} is not accessible. This is a direct consequence of the spatial delocalization of these excitons on the cylindrical structure. Excitons e_1 and e_2 belong exclusively to the inner and outer cylinder, respectively, whereas exciton e_3 is delocalized between both cylinders. Therefore, the two-exciton sub-bands including e_3 (f_{13} and f_{23}) are accessible from the longitudinal exciton sub-bands of both cylinders (e_1 and e_2). The f_{12} combination sub-band thus behaves as coupled harmonic oscillators - it carries no nonlinear signature.

Our microscopic model demonstrates how exciton and two-exciton sub-bands build-up and how they are mapped in the 2Q2D spectrum. The retrieved properties of the exciton bands allow us to conclude that these molecular nanotubes may be very efficient energy accumulators. All observed exciton peaks are related to weak scattering of excitons; no bound biexciton are observed. The narrow spectral line widths of the peaks in ω_2 indicate weak dephasing and decay of exciton pairs, i.e. their dephasing is of the same order of magnitude as for the constituting excitons. This implies

that the main exciton scattering mechanism is elastic inter-exciton scattering. For efficient light harvesting, it is very important that exciton pairs experience repulsion-like interactions. In this case the decay of interacting exciton pairs into non-interacting excitons of the same energies is energetically preferable. This is achieved via weak exciton-phonon coupling and implies that the system is a weakly anharmonic multimode oscillator with respect to excitons.

The interaction with phonons is the main source of relaxation between exciton sub-bands and exciton decay. In a microscopic description exciton-phonon coupling leads to thermal fluctuations of the molecular parameters on a multitude of timescales. Fast fluctuations, which are described in the Markovian limit, are the driving force for energy dissipation. The rate of dissipation is proportional to the square of the exciton-phonon coupling amplitude. DNA has an efficient photoprotection, since each DNA excitation is only weakly delocalized and may be associated with an independent DNA unit. Each unit possesses a set of vibrational modes which efficiently dissipate excitation energy. In large molecular aggregates like chlorosomes or C8S3 aggregates, excitons are highly delocalized and thus have small overlap with the localized molecular vibrations. Two-exciton bands representing weak exciton scattering are expected to retain all properties of the contributing excitons, including their spatial delocalization and, thus, the weak non-radiative decay. Such scattering does not provide new mechanism for exciton decay and completely differs from photoprotection in DNA. Bound biexcitons on the other hand might be trapping centers for propagating exciton pairs. The photosynthetic complex LHC-II has strong non-radiative decay pathways for exciton pairs, which are associated with the bound carotenoid molecules. Thus the bound biexcitons in LHC-II may be associated with a specific molecule. Due to its distinct nature such a state acquires specific pathways of relaxation and is involved in the photoprotection processes. The absence of bound biexcitons in C8S3 aggregates is preferable for efficient energy accumulation.

Slow (static) fluctuations on the other hand reflect equilibrium inhomogeneities. In small aggregates they can be modeled using statistical sampling of diagonal disorder. In periodic systems it is impossible to include spatially uncorrelated diagonal disorder. Spatially correlated slow fluctuations lead to convolution expressions of spectroscopic signals. This model is reasonable for cylindrical nanotubes, since the molecular geometry is very compact and cylinder squeezing, stretching, or bending results in spatially correlated effects that only weakly perturb exciton transport and decay. Spatially uncorrelated static fluctuations lead to contraction of the exciton delocalization length and contribute to an increase in the effective exciton-phonon coupling. This may lead to formation of deep defects and exciton traps, which in return reduces the energy accumulation efficiency.

8.5 Conclusions

The present sample is only one out of the available tubular supramolecules. Nevertheless, we expect our key conclusions to be general, and to hold also for structures that are either spatially even more complex (like interwoven tubules [29, 101, 233]), or whose detailed microscopic structure

is tuned toward new morphologies by the admixture of surfactants [101, 242]. In particular, a simple translation of spectral (energetic) band positions into spatial properties will generally fail in these huge systems ($\approx 10^4$ chromophores as compared to, e.g., 7 chromophores in the intensively studied Fenna-Matthews-Olson protein [31, 193]), due to the delocalization of excitons induced by both intra- and inter-wall couplings. It is the consideration of all electronic interactions, in the framework of an excitonic Hamiltonian basis, which provides an appropriate description of the experimental data.

Because of intra- and inter-wall electronic interactions, all bands share at least part of their wavefunction on the inner cylindrical assembly [244]. As band e_1 is dominated by (site-) localized transitions located on the inner tubule, the energy downhill motion of relaxing excitons is associated with an overall spatial transfer towards the inner wall and, simultaneously, a localization on a decreasing number of molecular sites. Even for quite large tubular segments, the lower energy parts of the absorption spectrum are determined by a handful of states only. Thus, the essential spectral signatures of exciton motion can be fitted either into phenomenological schemes of effective levels (cf. Chapter 6) [29, 33, 101, 232], or, as demonstrated in this chapter, recovered in the infinite limit of a microscopic model.

The picture we draw can be readily connected to the recently reported correlated fluctuation of excitonic bands in a related tubular aggregate [233]. Since we find all exciton wavefunctions to be at least partly located on one and the same wall, and to consequently overlap in space (i.e. to involve common molecular chromophores), also their fluctuations share a certain degree of correlation. Notably, the effect does not necessarily implicate correlated fluctuations of individual molecular sites. We further note, that even in the presence of disorder, only a relatively small number of states governs the aggregate's spectroscopic properties. Combined with the notion that fluctuation amplitudes become exchange-narrowed for delocalized (excitonic) states, our considerations are thus in line with experimentally observed inter-band coherences [101, 232], as a consequence of a slowly dephasing, small ensemble of excitons. In a broader context, our results indicate that for large excitonic systems, inter-band coherences result from the physics that governs the evolution of highly delocalized electronic states, and do not necessitate a surrounding protein matrix like in small natural photosynthetic complexes [42].

This contribution provides a guideline of how excitons in supramolecular systems can be studied, despite the limits currently set for connecting experimental and theoretical state-of-the-art methodologies. Though we report on an artificial light harvester that self-assembles in aqueous solution, it is inspiring to think about likely functional analogies to tubular complexes occurring in nature [231, 243], which, similarly, do not require any structural templates. Many optical properties of molecular and atomic systems are solely determined by transitions between the ground and single-excited states. An accurate description of geometric, spectroscopic, and reaction parameters, however, requires knowledge on higher excited states as well. Investigating the single- and double-excited state manifold in a synthetic light-harvesting complex as is done in the present study can serve as a first step towards a deeper understanding of exciton dynamics, motion, and relaxation.

*Science may set limits to knowledge, but
should not set limits to imagination.*

Bertrand Russell (1872 - 1970)



SUMMARY AND OUTLOOK

During the last decade multi-dimensional ultrafast spectroscopies have shown great potential by opening an increasingly broad experimental window into the structure and dynamics of atomic and molecular systems on femtosecond and picosecond timescales. The versatility and significance of two-dimensional electronic spectroscopy relies on the gain of additional information obtained by spreading the spectra into two frequency dimensions. Important experimental insights have been obtained by studying line-broadening dynamics in solution [19, 107, 227], revealing electronic couplings and pathways of energy transfer in natural [31, 239] and artificial [29, 33] light harvesting complexes, investigating electronic and vibronic coherences [37, 38, 40, 42], and probing exciton-exciton interactions in semiconductors [27, 28], to name only a few examples. Interpretation to this rich source of information has been partly provided from close connection of these experimental achievements with theoretical efforts [36, 43, 48, 145, 191].

The present work summarizes part of our efforts in the field of 2D-ES. The progress thereby ran parallel on two tracks: on the one hand, improvements in the instrumentation have led to a broader applicability of the method. By implementing a compact, easy to align, and passively phase-stabilized setup for recording 2D electronic spectra in three different phase-matching directions [78], it has become possible to study not only single-quantum but also double-quantum coherences [20]. On the other hand, the existing methods have been applied to study the electronic and vibronic dynamics of molecular systems of varying complexity. An electronic two-level system whose electronic transition is coupled to a low-frequency vibrational mode has served as a starting point in our investigations. The vibrational wave packet that is induced by excitation with a femtosecond laser pulse manifests itself in oscillating line-shapes in the 1Q2D spectra [38]. The observed beating pattern can be attributed to out-of-phase oscillations in the intensities of the rephasing and non-rephasing signal contributions [37]. In a second step, the line-shape dynamics of a monomer-dimer system in equilibrium have been investigated [227]. It was found, that exciton

delocalization effects in the dimer strongly influence the timescale of spectral diffusion. The degree of complexity reached its maximum in the investigation of pathways and timescales of energy transfer in double-wall cylindrical J-aggregates [29, 33, 244]. Exciton dynamics in these molecular nanotubes have been characterized by temporal, energetic, and spatial properties. In addition, the double-exciton manifold of C8S3 aggregates has been studied by 2Q2D-ES with the goal to gain a deeper understanding of the electronic structure and dynamics in this class of systems.

New ideas for future directions of research are provided partly from theory and partly from multi-dimensional techniques in nuclear magnetic resonance and infrared spectroscopies. Due to difficulties in the experimental realization in connection with the short wavelengths applied, the realization of new concepts in 2D-ES lags behind comparable developments at longer wavelengths.

The polarization of the excitation pulses is a degree of freedom that has not been fully exploited yet in the design of 2D experiments. First results have been obtained for light harvesting complexes [193, 245, 246] and semiconductor quantum wells [247, 248, 249]. In a step towards employing shaped excitation pulses in 2D experiments, several groups recently developed experimental designs on the basis of a pulse shaper [77, 250, 251, 252]. Of particular interest will be the combination of polarization pulse shaping with genetic algorithms to amplify or suppress specific diagonal and/or cross peaks in 2D spectra [253, 254].

Additional structural and dynamical information can be gained by performing transient 2D electronic spectroscopy, as has been demonstrated successfully in the infrared spectral region [255, 256]. In these experiments a prepulse induces a non-equilibrium configuration in the system whose evolution is probed with conventional 2D spectroscopy.

The third-order nonlinear polarization which is probed in four-wave mixing experiments is a function of three time delays (t_1 , t_2 , and t_3) or their corresponding frequencies (ω_1 , ω_2 , and ω_3). In this study we have restricted ourselves to two-dimensional measurements in which one of the three variables is held constant while the other two are varied. In principle, however, it is also possible to vary all three parameters and thereby create a three-dimensional contour map. First proof-of-principle experiments and calculations have been performed in the visible and infrared spectral region [257, 258, 259, 260].

Regarding the evolution of multi-dimensional spectroscopies from NMR over infrared to visible wavelengths, it seems only natural that the development will proceed towards even shorter wavelengths in the UV and X-ray range. However, a number of experimental barriers have to be overcome first, so that up to now these considerations exist only in theory [13, 14]. Since many interesting classes of molecules such as nucleic acids, DNA, amino acids, and proteins, however, absorb in this spectral region it is definitely worth the effort.

Bibliography

- [1] <http://nobelprize.org>
- [2] W. DEMTRÖDER. Laser spectroscopy. Springer Verlag, Berlin (1991).
- [3] G. R. FLEMING AND P. G. WOLYNES. Chemical Dynamics in Solution. *Physics Today* **43**, 36 (1990).
- [4] S. MUKAMEL. Principles of Nonlinear Optical Spectroscopy. Oxford University Press, Oxford (1995).
- [5] E. L. HAHN. Spin Echoes. *Phys. Rev.* **80**, 580 (1950).
- [6] N. A. KURNIT, I. D. ABELLA, AND S. R. HARTMANN. Observation of a photon echo. *Phys. Rev. Lett.* **13**, 567 (1964).
- [7] W. P. AUE, E. BARTHOLDI, AND R. R. ERNST. Two-dimensional spectroscopy. Application to nuclear magnetic resonance. *J. Chem. Phys.* **64**, 2229 (1976).
- [8] P. HAMM, M. LIM, AND R. M. HOCHSTRASSER. Structure of the Amide I Band of Peptides Measured by Femtosecond Nonlinear-Infrared Spectroscopy. *J. Phys. Chem. B* **102**, 6123 (1998).
- [9] J. D. HYBL, A. W. ALBRECHT, S. M. GALLAGHER FAEDER, AND D. M. JONAS. Two-Dimensional Electronic Spectroscopy. *Chem. Phys. Lett.* **297**, 307 (1998).
- [10] T. BRIXNER, T. MANČAL, I. V. STIOPKIN, AND G. R. FLEMING. Phase-Stabilized Two-Dimensional Electronic Spectroscopy. *J. Chem. Phys.* **121**, 4221 (2004).
- [11] M. L. COWAN, J. P. OGILVIE, AND R. J. D. MILLER. Two-Dimensional Spectroscopy using Diffractive Optics based Phased-Locked Photon-Echoes. *Chem. Phys. Lett.* **386**, 184 (2004).
- [12] S. MUKAMEL, Y. TANIMUAR, AND P. HAMM. Coherent Multidimensional Optical Spectroscopy. *Acc. Chem. Res.* **42** (2009).
- [13] Z. LI, D. ABRAMAVICIUS, AND S. MUKAMEL. Probing Electron Correlations in Molecules by Two-Dimensional Coherent Optical Spectroscopy. *J. Am. Chem. Soc.* **130**, 3509 (2008).
- [14] S. MUKAMEL, D. ABRAMAVICIUS, L. YANG, W. ZHUANG, I. V. SCHWEIGERT, AND D. V. VORONINE. Coherent Multidimensional Optical Probes for Electron Correlations and Exciton Dynamics; From NMR to X-rays. *Acc. Chem. Res.* **42**, 553 (2009).
- [15] D. KEUSTERS, H.-S. TAN, AND W. S. WARREN. Role of Pulse Phase and Direction in Two-Dimensional Optical Spectroscopy. *J. Phys. Chem. A* **103**, 10369 (1999).
- [16] C. SCHEURER AND S. MUKAMEL. Magnetic Resonance Analogies in Multidimensional Vibrational Spectroscopy. *Bull. Chem. Soc. Jpn.* **75**, 989 (2002).

BIBLIOGRAPHY

- [17] D. M. JONAS. Two-Dimensional Femtosecond Spectroscopy. *Annu. Rev. Phys. Chem.* **54**, 425 (2003).
- [18] M. KHALIL, N. DEMIRDÖVEN, AND A. TOKMAKOFF. Obtaining absorptive lineshapes in two-dimensional infrared vibrational correlation spectra. *Phys. Rev. Lett.* **90**, 47401 (2003).
- [19] J. D. HYBL, A. A. FERRO, AND D. M. JONAS. Two-dimensional Fourier transform electronic spectroscopy. *J. Chem. Phys.* **115**, 6606 (2001).
- [20] A. NEMETH, F. MILOTA, T. MANČAL, T. PULLERITS, J. SPERLING, J. HAUER, H. F. KAUFFMANN, AND N. CHRISTENSSON. Double-quantum two-dimensional electronic spectroscopy of a three-level system: Experiments and Simulations. *J. Chem. Phys.* **133**, 094505 (2010).
- [21] M. DANTUS AND V. V. LOZOVY. Experimental coherent laser control of physicochemical processes. *Chem. Rev.* **104**, 1813 (2004).
- [22] J. D. HYBL, Y. CHRISTOPHE, AND D. M. JONAS. Peak Shapes in Femtosecond 2D Correlation Spectroscopy. *Chem. Phys.* **266**, 295 (2001).
- [23] J. P. OGILVIE AND K. J. KUBARYCH. Multidimensional Electronic and Vibrational Spectroscopy: An Ultrafast Probe of Molecular Relaxation and Reaction Dynamics. *Advances in Atomic, Molecular, and Optical Physics.* **57**, Elsevier (2009).
- [24] A. TOKMAKOFF. Two-Dimensional Line Shapes Derived from Coherent Third-Order Non-linear Spectroscopy. *J. Phys. Chem. A* **104**, 4247 (2000).
- [25] K. OKUMURA, A. TOKMAKOFF, AND Y. TANIMURA. Two-dimensional line-shape analysis of photon-echo signal. *Chem. Phys. Lett.* **314**, 488 (1999).
- [26] J. D. HYBL, A. YU, D. A. FARROW, AND D. M. JONAS. Polar Solvation Dynamics in the Femtosecond Evolution of Two-Dimensional Fourier Transform Spectra. *J. Phys. Chem. A* **106**, 7651 (2002).
- [27] X. LI, T. ZHANG, S. MUKAMEL, R. P. MIRIN, AND S. T. CUNDIFF. Investigation of electronic couplings in semiconductor double quantum wells using coherent optical two-dimensional Fourier transform spectroscopy. *Solid State Commun.* **149**, 361 (2009).
- [28] C. N. BORCA, T. ZHANG, X. LI, AND S. T. CUNDIFF. Optical two-dimensional Fourier transform spectroscopy of semiconductors. *Chem. Phys. Lett.* **416**, 311 (2005).
- [29] A. NEMETH, F. MILOTA, J. SPERLING, D. ABRAMAVICIUS, S. MUKAMEL, AND H. F. KAUFFMANN. Tracing exciton dynamics in molecular nanotubes with 2D electronic spectroscopy. *Chem. Phys. Lett.* **469**, 130 (2009).
- [30] X. DAI, A. D. BRISTOW, D. KARAIKAJ, AND S. T. CUNDIFF. Two-dimensional Fourier transform Spectroscopy of Potassium Vapor. arXiv:1001.1955v1 (2010).

-
- [31] T. BRIXNER, J. STENGER, H. M. VASWANI, M. CHO, R. E. BLANKENSHIP, AND G. R. FLEMING. Two-dimensional spectroscopy of electronic couplings in photosynthesis. *Nature* **434**, 625 (2005).
- [32] G. S. SCHLAU-COHEN, T. R. CALHOUN, N. S. GINSBERG, E. L. READ, M. BALLOTTARI, R. BASSI, R. V. GRONDELLE, AND G. R. FLEMING. Pathways of Energy Flow in LHCII from Two-Dimensional Electronic Spectroscopy. *J. Phys. Chem. B* **113**, 15352 (2009).
- [33] F. MILOTA, J. SPERLING, A. NEMETH, D. ABRAMAVICIUS, S. MUKAMEL, AND H. F. KAUFFMANN. Excitonic couplings and interband energy transfer in a double-wall molecular aggregate imaged by coherent two-dimensional electronic spectroscopy. *J. Chem. Phys.* **131**, 054510 (2009).
- [34] P. F. TEKAVEC, J. A. MYERS, K. L. M. LEWIS, AND J. P. OGILVIE. Two-dimensional electronic spectroscopy with a continuum probe. *Opt. Lett.* **34**, 1390 (2009).
- [35] S. M. GALLAGHER-FAEDER AND D. M. JONAS. Two-dimensional Electronic Correlation and Relaxation Spectra: Theory and Model Calculations. *J. Phys. Chem. A* **103**, 10489 (1999).
- [36] T. MANČAL, A. NEMETH, F. MILOTA, V. LUKEŠ, H. F. KAUFFMANN, AND J. SPERLING. Vibrational wave packet induced oscillations in two-dimensional electronic spectra. II. Theory. *J. Chem. Phys.* **132**, 184515 (2010).
- [37] A. NEMETH, F. MILOTA, T. MANČAL, V. LUKEŠ, J. HAUER, H. F. KAUFFMANN, AND J. SPERLING. Vibrational wave packet induced oscillations in two-dimensional electronic spectra. I. Experiments. *J. Chem. Phys.* **132**, 184514 (2010).
- [38] A. NEMETH, F. MILOTA, T. MANČAL, V. LUKEŠ, H. F. KAUFFMANN, AND J. SPERLING. Vibronic modulation of lineshapes in two-dimensional electronic spectra. *Chem. Phys. Lett.* **459**, 94 (2008).
- [39] A. ISHIZAKI AND G. R. FLEMING. Theoretical examination of quantum coherence in a photosynthetic system at physiological temperature. *Proc. Nat. Acad. Sci.* **106**, 17255 (2009).
- [40] G. PANITCHAYANGKON, D. HAYES, K. A. FRANSTED, J. R. CARAM, E. HAREL, J. WEN, R. E. BLANKENSHIP, AND G. S. ENGEL. Long-lived quantum coherence in photosynthetic complexes at physiological temperature. *Proc. Nat. Acad. Sci.* page doi:10.1073/pnas.1005484107 (2010).
- [41] Y.-C. CHENG AND G. R. FLEMING. Coherence Quantum Beats in Two-Dimensional Electronic Spectroscopy. *J. Phys. Chem. A* **112**, 4254 (2008).
- [42] G. S. ENGEL, T. R. CALHOUN, E. L. READ, T.-K. AHN, T. MANČAL, Y.-C. CHENG, R. E. BLANKENSHIP, AND G. R. FLEMING. Evidence for wavelike energy transfer through quantum coherence in photosynthetic systems. *Nature* **446**, 782 (2007).

BIBLIOGRAPHY

- [43] P. KJELLBERG, B. BRÜGGEMANN, AND T. PULLERITS. Two-dimensional electronic spectroscopy of an excitonically coupled dimer. *Phys. Rev. B* **74**, 024303 (2006).
- [44] A. V. PISLIAKOV, T. MANČAL, AND G. R. FLEMING. Two-dimensional optical three-pulse photon echo spectroscopy. II: Signatures of coherent electronic motion and exciton population transfer in dimer two-dimensional spectra. *J. Chem. Phys.* **124**, 234505 (2006).
- [45] B. I. GRIMBERG, V. V. LOZOVY, M. DANTUS, AND S. MUKAMEL. Ultrafast Nonlinear Spectroscopic Techniques in the Gas Phase and Their Density Matrix Representation. *J. Phys. Chem. A* **106**, 697 (2002).
- [46] S. H. LIN, R. ALDEN, R. ISLAMPOUR, H. MA, AND A. A. VILLAEYS. Density Matrix Method and Femtosecond Processes. World Scientific Publishing Co Pte Ltd, Singapore (1991).
- [47] S. MUKAMEL AND D. ABRAMAVICIUS. Many-body approaches for simulating coherent nonlinear spectroscopies of electronic and vibrational excitons. *Chem. Rev.* **104**, 2073 (2004).
- [48] M. CHO. Coherent Two-Dimensional Optical Spectroscopy. *Chem. Rev.* **108**, 1331 (2008).
- [49] S. MUKAMEL AND R. F. LORING. Nonlinear response function for time-domain and frequency-domain four-wave mixing. *J. Opt. Soc. Am. B* **3**, 595 (1986).
- [50] V. CHERNYAK, W. M. ZHANG, AND S. MUKAMEL. Multidimensional femtosecond spectroscopies of molecular aggregates and semiconductor nanostructures: The nonlinear exciton equations. *J. Chem. Phys.* **109**, 9587 (1998).
- [51] R. KUBO. *Adv. Chem. Phys.* **15**, 101 (1969).
- [52] T. JOO, Y. JIA, J.-Y. YU, M. J. LANG, AND G. R. FLEMING. Third-order nonlinear time domain probes of solvation dynamics. *J. Chem. Phys.* **104**, 6089 (1996).
- [53] E. T. J. NIBBERING, D. A. WIERSMA, AND K. DUPPEN. Ultrafast electronic fluctuation and solvation in liquids. *Chem. Phys.* **183**, 167 (1994).
- [54] J. R. SCHMIDT, N. SUNDLASS, AND J. L. SKINNER. Line shapes and photon echoes within a generalized Kubo model. *Chem. Phys. Lett.* **378**, 559 (2003).
- [55] W. P. DE BOEIJ, M. S. PSHENICHNIKOV, AND D. A. WIERSMA. On the relation between the echo-peak shift and Brownian-oscillator correlation function. *Chem. Phys. Lett.* **253**, 53 (1996).
- [56] G. R. FLEMING AND M. CHO. Chromophore-Solvent Dynamics. *Annu. Rev. Phys. Chem.* **47**, 109 (1996).
- [57] A. MORAN, J. MADDOX, J. HONG, J. KIM, R. NOME, G. BAZAN, S. MUKAMEL, AND N. SCHERER. Optical coherence and theoretical study of the excitation dynamics of a highly

- symmetric cyclophane-linked oligophenylenevinylene dimer. *J. Chem. Phys* **124**, 194904 (2006).
- [58] M. F. EMDE, W. P. DE BOEIJ, M. S. PSHENICHNIKOV, AND D. A. WIERSMA. Spectral interferometry as an alternative to time-domain heterodyning. *Opt. Lett.* **22**, 1338 (1997).
- [59] C. SPIELMANN, P. F. CURLEY, T. BRABEC, AND F. KRAUSZ. Ultrabroadband Femtosecond Lasers. *IEEE J. Quantum Electron.* **30**, 1100 (1994).
- [60] D. STRICKLAND AND G. MOUROU. Compression of Amplified Chirped Optical Pulses. *Opt. Comm.* **56**, 219 (1985).
- [61] F. SALIN, J. SQUIER, G. MOUROU, AND G. VAILLANTCOURT. Multikilohertz Ti:Al₂O₃ amplifier for high-power femtosecond pulses. *Opt. Lett.* **16**, 1964 (1991).
- [62] T. B. NORRIS. Femtosecond pulse amplification at 250 kHz with a Ti:sapphire regenerative amplifier and application to continuum generation. *Opt. Lett.* **17**, 1009 (1992).
- [63] T. WILHELM, J. PIEL, AND E. RIEDLE. Sub-20-fs pulses tunable across the visible from a blue-pumped single-pass noncollinear parametric converter. *Opt. Lett.* **22**, 1494 (1997).
- [64] M. NISOLI, S. STAGIRA, S. DE SILVESTRI, O. SVELTO, G. VALIULIS, AND A. VARANAVICIUS. Parametric generation of high-energy 14.5-fs light pulses at 1.5mm. *Opt. Lett.* **23**, 630 (1998).
- [65] A. SHIRAKAWA, I. SAKANE, AND T. KOBAYASHI. Pulse-front-matched optical parametric amplification for sub-10fs pulse generation tunable in the visible and near infrared. *Opt. Lett.* **23**, 1292 (1998).
- [66] M. K. REED, M. K. STEINER-SHEPARD, AND D. K. NEGUS. Widely tunable femtosecond optical parametric amplifier at 250 kHz with a Ti:sapphire regenerative amplifier. *Opt. Lett.* **19**, 1855 (1994).
- [67] G. STEINMEYER. Brewster-angled chirped mirrors for high-fidelity dispersion compensation and bandwidths exceeding one optical octave. *Opt. Express* **11**, 2385 (2003).
- [68] P. BAUM, M. BREUER, E. RIEDLE, AND G. STEINMEYER. Brewster-angled chirped mirrors for broadband pulse compression without dispersion oscillations. *Opt. Lett.* **31**, 2220 (2006).
- [69] R. SZIPÖCS AND A. KÖHAZI-KIS. Theory and design of chirped dielectric mirrors. *Appl. Phys. B* **65**, 115 (1997).
- [70] R. L. FORK, O. E. MARTINEZ, , AND J. P. GORDON. Negative dispersion using pairs of prisms. *Opt. Lett.* **9**, 150 (1984).
- [71] P. BAUM AND E. RIEDLE. Design and Calibration of zero-additional-phase SPIDER. *J. Opt. Soc. B* **22**, 1875 (2005).

BIBLIOGRAPHY

- [72] P. BAUM, S. LOCHBRUNNER, AND E. RIEDLE. Zero-additional-phase SPIDER: full characterization of visible and sub-20-fs ultraviolet pulses. *Opt. Lett.* **29**, 210 (2004).
- [73] R. TREBINO, K. W. DELONG, D. N. FITTINGHOFF, J. N. SWEETSER, M. A. KRUMBÜGEL, B. A. RICHMAN, AND D. J. KANE. Measuring ultrashort laser pulses in the time-frequency domain using frequency-resolved optical gating. *Rev. Sci. Instrum.* **68**, 3277 (1997).
- [74] T. BRIXNER, I. V. STIOPKIN, AND G. R. FLEMING. Tunable Two-Dimensional Femtosecond Spectroscopy. *Opt. Lett.* **29**, 884 (2004).
- [75] K. STONE, K. GUNDOGDU, D. B. TURNER, X. LI, S. T. CUNDIFF, AND K. A. NELSON. Two-Quantum 2D FT Electronic Spectroscopy of Biexcitons in GaAs Quantum Wells. *Science* **324**, 1169 (2009).
- [76] A. D. BRISTOW, D. KARAIKAJ, X. DAI, T. ZHANG, C. CARLSSON, K. R. HAGEN, R. JIMENEZ, AND S. T. CUNDIFF. A Versatile Ultra-Stable Platform for Optical Multidimensional Fourier-Transform Spectroscopy. *Rev. Sci. Instr.* **80**, 073108 (2009).
- [77] V. I. PROKHORENKO, A. HALPIN, AND R. J. D. MILLER. Coherently-controlled two-dimensional photon echo electronic spectroscopy. *Opt. Exp.* **17**, 9764 (2009).
- [78] A. NEMETH, J. SPERLING, J. HAUER, H. F. KAUFFMANN, AND F. MILOTA. Compact phase-stable design for single- and double-quantum two-dimensional electronic spectroscopy. *Opt. Lett.* **34**, 3301 (2009).
- [79] K. GUNDOGDU, K. W. STONE, D. B. TURNER, AND K. A. NELSON. Multidimensional coherent spectroscopy made easy. *Chem. Phys.* **341**, 89 (2007).
- [80] M. J. TAUBER, R. A. MATHIES, X. CHEN, AND S. E. BRADFORTH. Flowing liquid sample jet for resonant Raman and ultrafast optical spectroscopy. *Rev. Sci. Instrum.* **74**, 4958 (2003).
- [81] S. LAIMGRUBER, H. SCHACHENMAYR, B. SCHMIDT, W. ZINTH, AND P. GILCH. A femtosecond stimulated Raman spectrograph for the near ultraviolet. *Appl. Phys. B* **85**, 557 (2006).
- [82] G. M. ALBER AND A. G. MARSHALL. Effect of sampling Rate on Fourier Transform Spectra: Oversampling is Overrated. *Appl. Spectrosc.* **44**, 1111 (1990).
- [83] S. M. GALLAGHER, A. W. ALBRECHT, J. D. HYBL, B. L. LANDIN, B. RAJARAM, AND D. M. JONAS. Heterodyne detection of the complete electric field of femtosecond four-wave mixing signals. *J. Opt. Soc. Am. B* **15**, 2338 (1998).
- [84] A. D. BRISTOW, D. KARAIKAJ, X. DAI, AND S. T. CUNDIFF. All-optical retrieval of the global phase for two-dimensional Fourier-transform spectroscopy. *Opt. Exp.* **16**, 18017 (2008).

-
- [85] E. H. G. BACKUS, S. GARRETT-ROE, AND P. HAMM. Phasing problem of heterodyne-detected two-dimensional infrared spectroscopy. *Opt. Lett.* **33**, 2665 (2008).
- [86] A. MORAN, S. PARK, AND N. SCHERER. Coherent Electronic and Nuclear Dynamics for Charge Transfer in 1-Ethyl-4-(carbomethoxy)pyridinium Iodide. *J. Phys. Chem. B* **110**, 19771 (2006).
- [87] A. ZEWAİL. Femtochemistry. *J. Phys. Chem.* **97**, 12427 (1993).
- [88] H. L. FRAGNITO, J.-Y. BIGOT, P. C. BECKER, AND C. V. SHANK. Evolution of the vibronic absorption spectrum in a molecule following impulsive excitation with a 6 fs optical pulse. *Chem. Phys. Lett.* **160**, 101 (1989).
- [89] T. KOBAYASHI, T. SALTO, AND H. OHTANI. Real-time spectroscopy of transition states in bacteriorhodopsin during retinal isomerization. *Nature* **414**, 531 (2001).
- [90] D. S. LARSEN, K. OHTA, Q.-H. XU, M. CYRIER, AND G. R. FLEMING. Influence of intramolecular vibrations in third-order, time-domain resonant spectroscopies. I. Experiments. *J. Chem. Phys.* **114**, 8008 (2001).
- [91] P. C. BECKER, H. L. FRAGNITO, J. Y. BIGOT, C. H. BRITO CRUZ, R. L. FORK, AND C. V. SHANK. Femtosecond Photon Echoes from Molecules in Solution. *Phys. Rev. Lett.* **63**, 505 (1989).
- [92] R. W. SCHOENLEIN, D. M. MITTLEMAN, J. J. SHIANG, A. P. ALIVISATOS, AND C. V. SHANK. Investigation of Femtosecond Electronic Dephasing in CdSe Nanocrystals Using Quantum-Beat-Suppressed Photon Echoes. *Phys. Rev. Lett.* **70**, 1014 (1993).
- [93] W. P. DE BOEIJ, M. S. PSHENICHNIKOV, AND D. A. WIERSMA. Ultrafast solvation dynamics explored by femtosecond photon echo spectroscopies. *Annu. Rev. Phys. Chem.* **49**, 99 (1998).
- [94] W. P. DE BOEIJ, M. S. PSHENICHNIKOV, AND D. A. WIERSMA. System-bath correlation function probed by conventional and time-gated stimulated photon echo. *J. Phys. Chem.* **100**, 11806 (1996).
- [95] Y. J. YAN AND S. MUKAMEL. Femtosecond Pump-Probe Spectroscopy of Polyatomic Molecules in Condensed Phases. *Phys. Rev. A* **41**, 6485 (1990).
- [96] W. T. POLLARD, H. L. FRAGNITO, J.-Y. BIGOT, C. V. SHANK, AND R. A. MATHIES. Quantum-mechanical theory for 6 fs dynamic absorption spectroscopy and its application to Nile blue. *Chem. Phys. Lett.* **168**, 239 (1990).
- [97] W. T. POLLARD, S. L. DEXHEIMER, Q. WANG, L. A. PETEANU, C. V. SHANK, AND R. A. MATHIES. Theory of Dynamic Absorption Spectroscopy of Nonstationary States. 4. Application to 12-fs Resonant Impulsive Raman Spectroscopy of Bacteriorhodopsin. *J. Phys. Chem.* **96**, 6147 (1992).
-

BIBLIOGRAPHY

- [98] L. DHAR, J. A. ROGERS, AND K. A. NELSON. Time-Resolved Vibrational Spectroscopy in the Impulsive Limit. *Chem. Rev.* **94**, 157 (1994).
- [99] K. OHTA, D. S. LARSEN, M. YANG, AND G. R. FLEMING. Influence of intramolecular vibrations in third-order, time-domain resonant spectroscopies. II. Numerical calculations. *J. Chem. Phys.* **114**, 8020 (2001).
- [100] Y.-C. CHENG, G. S. ENGEL, AND G. R. FLEMING. Elucidation of population and coherence dynamics using cross-peaks in two-dimensional electronic spectroscopy. *Chem. Phys.* **341**, 285 (2007).
- [101] F. MILOTA, J. SPERLING, A. NEMETH, AND H. F. KAUFFMANN. Two-dimensional electronic photon echoes of a double band J-aggregate: Quantum oscillatory motion versus exciton relaxation. *Chem. Phys.* **357**, 45 (2009).
- [102] E. COLLINI AND G. D. SHOLES. Coherent Intrachain Energy Migration in a Conjugated Polymer at Room Temperature. *Science* **323**, 369 (2009).
- [103] D. S. LARSEN, K. OHTA, AND G. R. FLEMING. Three pulse photon echo studies of nondipolar solvation: Comparison with a viscoelastic model. *J. Chem. Phys.* **111**, 8970 (1999).
- [104] M. CHO, J.-Y. YU, T. JOO, Y. NAGASAWA, S. A. PASSINO, AND G. R. FLEMING. The integrated photon echo and solvation dynamics. *J. Phys. Chem.* **100**, 11944 (1996).
- [105] M. YANG AND G. R. FLEMING. Two-color three-pulse photon echoes as a probe of electronic coupling in molecular complexes. *J. Chem. Phys.* **110**, 2983 (1999).
- [106] T. MANČAL AND G. R. FLEMING. Probing electronic coupling in excitonically coupled heterodimer complexes by two-color three-pulse photon echoes. *J. Chem. Phys.* **121**, 10556 (2004).
- [107] K. LAZONDER, M. S. PSHENICHNIKOV, AND D. A. WIERSMA. Easy interpretation of optical two-dimensional correlation spectra. *Opt. Lett.* **31**, 3354 (2006).
- [108] R. G. PARR AND W. YANG. Density-Functional Theory of Atoms and Molecules in Chemistry. Springer, New York (1991).
- [109] A. D. BECKE. Density-functional thermochemistry. IV. A new dynamical correlation functional and implications for exact-exchange mixing. *J. Chem. Phys.* **104**, 1040 (1996).
- [110] T. H. DUNNING AND P. J. HAY. Methods of electronic structure Theory. Plenum Press, New York (1977).
- [111] J. B. FORESMAN, M. HEAD-GORDON, J. A. POPLE, AND M. J. FRISCH. Toward a systematic molecular orbital theory for excited states. *J. Phys. Chem.* **96**, 135 (1992).

-
- [112] M. C. ZERNER, G. H. LOEW, R. F. KIRCHNER, AND U. T. MÜLLER-WESTERHOFF. An intermediate neglect of differential overlap technique for spectroscopy of transition-metal complexes. *Ferrocene. J. Am. Chem. Soc.* **102**, 589 (1980).
- [113] R. AHLRICHS, M. BÄR, M. HÄSER, H. HORN, AND C. KÖLMEL. Electronic structure calculations on workstation computers: The program system turbomole. *Chem. Phys. Lett.* **162**, 165 (1989).
- [114] M. A. THOMPSON. Arguslab 4.0.1, planaria software llc, seattle, wa. (2004).
- [115] J. J. P. STEWART. <http://mtzweb.stanford.edu/programs/documentation/mopac2002/index.html>. (Fujitsu Ltd. 2001).
- [116] We note that $t_1 = 0$ is included in the evaluation of both rephasing and non-rephasing parts resulting in a negligible deviation only of the sum from the total spectrum.
- [117] N.-H. GE, M. T. ZANNI, AND R. M. HOCHSTRASSER. Effects of Vibrational Frequency Correlations on Two-Dimensional Infrared Spectra. *J. Phys. Chem. A* **106**, 962 (2002).
- [118] M. KHALIL, N. DEMIRDÖVEN, AND A. TOKMAKOFF. Coherent 2D IR spectroscopy; Molecular structure and dynamics in solution. *J. Phys. Chem. A* **107**, 5258 (2003).
- [119] J. L. LOPARO, S. T. ROBERTS, AND A. TOKMAKOFF. Multidimensional infrared spectroscopy of water. I. Vibrational dynamics in two-dimensional IR line shapes. *J. Chem. Phys.* **125**, 194321 (2006).
- [120] S. WOUTERSEN, R. PFISTER, P. HAMM, Y. MU, D. S. KOSOV, AND G. STOCK. Peptide conformational heterogeneity revealed from nonlinear vibrational spectroscopy and molecular-dynamics simulations. *J. Chem. Phys.* **117**, 6833 (2002).
- [121] K. KWAK AND M. CHO. Molecular dynamics simulation study of N-methylacetamide in water. II. Two-dimensional infrared pump-probe spectra. *J. Chem. Phys.* **119**, 2256 (2003).
- [122] S. T. ROBERTS, J. J. LOPARO, AND A. TOKMAKOFF. Characterization of spectral diffusion from two-dimensional line shapes. *J. Chem. Phys.* **125**, 084502 (2006).
- [123] K. KWAK, S. PAR, I. J. FINKELSTEIN, AND M. D. FAYER. Frequency-frequency correlation functions and apodization in two-dimensional infrared vibrational echo spectroscopy: A new approach. *J. Chem. Phys.* **127**, 124503 (2007).
- [124] S. PARK, K. KWAK, AND M. D. FAYER. Ultrafast 2D-IR vibrational echo spectroscopy: a probe of molecular dynamics. *Laser Phys. Lett.* **4**, 704 (2007).
- [125] I. J. FINKELSTEIN, H. ISHIKAWA, S. KIM, A. M. MASSARI, AND M. D. FAYER. Substrate binding and protein conformational dynamics measured by 2D-IR vibrational echo spectroscopy. *Proc. Nat. Acad. Sci.* **104**, 2637 (2007).

BIBLIOGRAPHY

- [126] J. D. EAVES, J. J. LOPARO, C. J. FECKO, S. T. ROBERTS, A. TOKMAKOFF, AND P. L. GEISSLER. Hydrogen bonds in liquid water are broken only fleetingly. *Proc. Nat. Acad. Sci.* **102**, 13019 (2005).
- [127] D. EGOROVA, M. F. GELIN, AND W. DOMCKE. Analysis of cross peaks in two-dimensional electronic photon-echo spectroscopy for simple models with vibrations and dissipation. *J. Chem. Phys.* **126**, 074314 (2007).
- [128] A. B. MYERS. Molecular electronic spectral broadening in liquids and glasses. *Annu. Rev. Phys. Chem.* **49**, 267 (1998).
- [129] J. L. SKINNER AND W. E. MOERNER. Structure and Dynamics in Solids As Probed by Optical Spectroscopy. *J. Phys. Chem.* **100**, 13251 (1996).
- [130] B. M. KHARLAMOV, L. A. BYKOVSKAYA, AND R. I. PERSONOV. "Hole-burning spectra". A new method for obtaining fine structure in absorption spectra of organic molecules. *Chem. Phys. Lett.* **50**, 407 (1977).
- [131] S. VÖLKER. Hole-Burning Spectroscopy. *Annu. Rev. Phys. Chem.* **40**, 499 (1989).
- [132] A. H. HERZ. Aggregation of sensitizing dyes in solution and their adsorption onto silver halides. *Adv. Colloid Interfac.* **8**, 237 (1977).
- [133] W. WEST AND S. PEARCE. The Dimeric State of Cyanine Dyes. *J. Phys. Chem.* **69**, 1894 (1965).
- [134] G. SCHEIBE. Über die Veränderlichkeit des Absorptionsspektrums einiger Sensibilisierungs-farbstoffe und deren Ursache. *Angew. Chemie* **49**, 563 (1936).
- [135] E. E. JELLEY. Spectral Absorption and Fluorescence of Dyes in the Molecular State. *Nature* **12**, 1009 (1936).
- [136] B. ARADI, B. HOURAHINE, AND T. FRAUENHEIM. DFTB+, a Sparse Matrix-Based Implementation of the DFTB Method. *J. Phys. Chem. A* **111**, 5678 (2007).
- [137] J. B. COLLINS, P. R. SCHLEYER, J. S. BINKLEY, AND J. A. POPLE. Self-consistent molecular orbital methods. XVII. Geometries and binding energies of second-row molecules. A comparison of three basis sets. *J. Chem. Phys.* **64**, 5142 (1976).
- [138] J. P. PERDEW, K. BURKE, AND M. ERNZERHOF. Generalized Gradient Approximation Made Simple. *Phys. Rev. Lett.* **77**, 3865 (1996).
- [139] M. J. FRISCH, G. W. TRUCKS, H. B. SCHLEGEL, G. E. SCUSERIA, M. A. ROBB, J. R. CHEESEMAN, J. A. MONTGOMERY JR., T. VREVEN, K. N. KUDIN, J. C. BURANT, J. M. MILLAM, S. S. IYENGAR, J. TOMASI, V. BARONE, B. MENNUCCI, M. COSSI, G. SCALMANI, N. REGA, G. A. PETERSSON, H. NAKATSUJI, M. HADA, M. EHARA, K. TOYOTA, R. FUKUDA, J. HASEGAWA, M. ISHIDA, T. NAKAJIMA, Y. HONDA, O. KITAO,

- H. NAKAI, M. KLENE, X. LI, J. E. KNOX, H. P. HRATCHIAN, J. B. CROSS, C. ADAMO, J. JARAMILLO, R. GOMPERTS, R. E. STRATMANN, O. YAZYEV, A. J. AUSTIN, R. CAMNI, C. POMELLI, J. W. OCHTERSKI, P. Y. AYALA, K. MOROKUMA, G. A. VOTH, P. SALVADOR, J. J. DANNENBERG, V. G. ZAKRZEWSKI, S. DAPPRICH, A. D. DANIELS, M.-C. STRAIN, O. FARKAS, D. K. MALICK, A. D. RABUCK, K. RAGHAVACHARI, J. B. FORESMAN, J. V. ORTIZ, Q. CUI, A. G. BABOUL, S. CLIFFORD, J. CIOSLOWSKI, B. B. STEFANOV, G. LIU, A. LIASHENKO, P. PISKORZ, I. KOMAROMI, R. L. MARTIN, D. J. FOX, T. KEITH, M. A. AL-LAHAM, C. Y. PENG, A. NANAYAKKARA, M. CHALLACOMBE, P. M. W. GILL, B. JOHNSON, W. CHEN, M. W. WONG, C. GONZALEZ, AND J. A. POPLER. Gaussian 03, revision a.1, gaussian, inc., pittsburgh, pa. (2003).
- [140] L. VERLET. Computer "Experiments" on Classical Fluids. II. Equilibrium Correlation Functions. *Phys. Rev.* **165**, 201 (1968).
- [141] F. NEGRI AND G. ORLANDI. Computational Photochemistry. Theoretical and Computational Chemistry, V. 16, Elsevier, Amsterdam (2005).
- [142] H. C. J. ANDERSEN. Molecular dynamics simulations at constant pressure and/or temperature. *J. Chem. Phys.* **72**, 2384 (1980).
- [143] B. H. BRANDSEN AND C. J. JOACHAIN. Physics of Atoms and Molecules. Longman Group Limited, London (1983).
- [144] M. BARBATTI, G. GRANUCCI, M. PERSICO, M. RUCKENBAUER, M. VAZDAR, M. ECKERT-MAKSIC, AND H. LISCHKA. The on-the-fly surface-hopping program system Newton-x: Application to ab initio simulation of the nonadiabatic photodynamics of benchmark systems. *J. Photochem. Photobiol. A* **190**, 228 (2007).
- [145] M. CHO, H. M. VASWANI, T. BRIXNER, J. STENGER, AND G. R. FLEMING. Exciton Analysis in 2D Electronic Spectroscopy. *J. Phys. Chem. B* **109**, 10542 (2005).
- [146] E. W. KNAPP. Lineshapes of Molecular Aggregates. Exchange Narrowing and Intersite Correlation. *Chem. Phys.* **85**, 73 (1984).
- [147] F. HEISEL, J. A. MIEHE, AND J. RACHIDI. The dynamics of the intramolecular and orientational motions of Pinacyanol. *Chem. Phys. Lett.* **134**, 379 (1987).
- [148] C. J. TREDWELL AND C. M. KEARY. Picosecond time resolved fluorescence lifetimes of the polymethine and related dyes. *Chem. Phys.* **43**, 307 (1979).
- [149] P. J. THISTLETHWAITE AND H. J. GRIESSER. The temperature dependence of the fluorescence lifetime of pinacyanol iodide. *Chem. Phys. Lett.* **91**, 58 (1982).
- [150] H. MIN, J. PARK, J. YU, AND D. KIM. The Spectroscopic Studies on the Aggregation Behavior of Cyanine Dyes. *Bull. Korean. Chem. Soc.* **19**, 650 (1998).

BIBLIOGRAPHY

- [151] B. NEUMANN AND P. POLLMANN. Investigation of two cyanine dyes at normal and high pressure by UV/Vis spectroscopy. *Phys. Chem. Chem. Phys.* **2**, 4784 (2000).
- [152] R. SABATE, M. GALLARDO, A. DE LA MANZA, AND J. ESTELRICH. A Spectroscopy Study of the Interaction of Pinacyanol with n-dodecyltrimethylammonium Bromide Micelles. *Langmuir* **17**, 6433 (2001).
- [153] B. KOPAINSKY, J. K. HALLERMEIER, AND W. KAISER. The first step of aggregation of PIC: the dimerization. *Chem. Phys. Lett.* **83**, 498 (1981).
- [154] E. G. McRAE AND M. KASHA. *Physical Processes in Radiation Biology*. Plenum Press, New York (1963).
- [155] D. ZIGMANTAS, E. L. READ, T. MANČAL, T. BRIKNER, A. T. GARDINER, R. J. COGDELL, AND G. R. FLEMING. Two-dimensional electronic spectroscopy of the B800-B820 light-harvesting complex. *Proc. Nat. Acad. Sci.* **103**, 12672 (2006).
- [156] V. SZÖCS, T. PALSZEGI, V. LUKES, J. SPERLING, F. MILOTA, W. JAKUBETZ, AND H. F. KAUFFMANN. Two-dimensional Electronic Spectra of Symmetric Dimers: Intermolecular Coupling and Conformational States. *J. Chem. Phys.* **124**, 124511 (2006).
- [157] P. TIAN, D. KEUSTERS, Y. SUZAKI, AND W. S. WARREN. Femtosecond Phase-Coherent Two-Dimensional Spectroscopy. *Science* **300**, 1553 (2003).
- [158] X. HU AND K. SCHULTEN. How nature harvests sunlight. *Phys. Today* **50**, 28 (1997).
- [159] V. SUNDRÖM. Light in elementary biological reactions. *Prog. Quant. Electron.* **24**, 187 (2000).
- [160] A. S. DAVYDOV. *Theory of Molecular Excitons*. Plenum Press, New York (1971).
- [161] H. FIDDER, J. KNOESTER, AND D. A. WIERSMA. Optical properties of disordered molecular aggregates: A numerical study. *J. Chem. Phys.* **95**, 7880 (1991).
- [162] T. MEIER, V. CHERNYAK, AND S. MUKAMEL. Femtosecond photon echoes in molecular aggregates. *J. Chem. Phys.* **107**, 8759 (1997).
- [163] M. DAHLBOM, T. MINAMI, V. CHERNYAK, T. PULLERITS, V. SUNDRÖM, AND S. MUKAMEL. Exciton-Wave Packet Dynamics in Molecular Aggregates Studied with Pump-Probe Spectroscopy. *J. Phys. Chem. B* **104**, 3976 (2000).
- [164] H. FIDDER, J. TERPSTRA, AND D. A. WIERSMA. Dynamics of Frenkel excitons in disordered molecular aggregates. *J. Chem. Phys.* **94**, 6895 (1991).
- [165] R. VAN GRONDELLE, L. VALKUNAS, AND H. VAN AMERONGEN. *Photosynthetic Excitons*. World Scientific (1997).

- [166] H. FIDDER, J. KNOESTER, AND D. A. WIERSMA. Observation of the one-exciton to two-exciton transition in a J aggregate. *J. Chem. Phys.* **98**, 6564 (1993).
- [167] H. FIDDER. Absorption and emission studies on pure and mixed j-aggregates of pseudoisocyanine. *Chem. Phys.* **341**, 158 (2007).
- [168] T. KOBAYASHI. J-Aggregates. World Scientific, Singapore (1996).
- [169] A. PAWLIK, A. OUART, S. KIRSTEIN, H.-W. ABRAHAM, AND S. DAEHNE. Synthesis and UV/Vis spectra of J-aggregating 5,5',6,6'-tetrachlorobenzimidacyanine dyes for artificial light-harvesting systems and for asymmetrical generation of supramolecular helices. *Eur. J. Org. Chem.*, 3065 (2003).
- [170] V. I. PROKHORENKO, D. B. STEENSGAARD, AND A. R. HOLZWARTH. Exciton Theory for Supramolecular Chlorosomal Aggregates: 1. Aggregate Size Dependence of the Linear Spectra. *Biophys. J.* **85**, 3173 (2003).
- [171] Y. XU, J. YE, H. LIU, E. CHENG, Y. YANG, W. WANG, M. ZHAO, D. ZHOU, D. LIU, AND R. FANG. DNA-templated CMV viral capsid proteins assemble into nanotubes. *Chem. Comm.* **1**, 49 (2008).
- [172] P. M. AJAYAN. Nanotubes from Carbon. *Chem. Rev.* **99**, 1787 (1999).
- [173] L. A. STAEHELIN, J. R. GOLECKI, AND G. DREWSA. Supramolecular organization of chlorosomes (chlorobium vesicles) and of their membrane attachment sites in chlorobium limicola. *Biochim. Biophys. Acta - Bioenerg.* **589**, 30 (1980).
- [174] A. R. HOLZWARTH, K. GRIEBENOW, AND K. SCHAFFNER. Chlorosomes, photosynthetic antennae with novel self-organized pigment structures. *J. Photochem. Photobiol. A* **65**, 61 (1992).
- [175] H. VON BERLEPSCH, C. BÖTTCHER, A. OUART, C. BURGER, S. DHNE, AND S. KIRSTEIN. Supramolecular structures of J-Aggregates of carbocyanine dyes in solution. *J. Phys. Chem. B* **104**, 5255 (2000).
- [176] T. S. BALABAN. Tailoring Porphyrins and Chlorins for Self-Assembly in Biometric Artificial Antenna Systems. *Acc. Chem. Res.* **38**, 612 (2005).
- [177] K. TAKAZAWA, Y. KITAHAMA, Y. KIMURA, AND G. KIDO. Optical Waveguide Self-Assembled from Organic Dye Molecules in Solution. *Nano Lett.* **5**, 1293 (2005).
- [178] V. CHERNYAK AND S. MUKAMEL. Collective coordinates for nuclear spectral densities in energy transfer and femtosecond spectroscopy of molecular aggregates. *J. Chem. Phys.* **105**, 4565 (1996).
- [179] W. M. ZHANG, T. MEIER, V. CHERNYAK, AND S. MUKAMEL. Exciton-migration and three-pulse femtosecond optical spectroscopies of photosynthetic antenna complexes. *J. Chem. Phys.* **108**, 7763 (1998).

BIBLIOGRAPHY

- [180] M. CHACHISVILLIS, T. PULLERITS, M. R. JONES, C. N. HUNTER, AND V. SUNDRÖM. Vibrational dynamics in the light-harvesting complexes of the photosynthetic bacterium *rhodobacter sphaeroides*. *Chem. Phys. Lett.* **224**, 345 (1994).
- [181] T. JOO, Y. JIA, J.-Y. YU, D. M. JONAS, AND G. R. FLEMING. Dynamics in Isolated Bacterial Light Harvesting Antenna (LH2) of *Rhodobacter Sphaeroides* at Room Temperature. *J. Chem. Phys.* **100**, 2399 (1996).
- [182] L. D. BOOK, A. E. OSTAFIN, N. PONOMARENKO, J. R. NORRIS, AND N. F. SCHERER. Exciton Delocalization and Initial Dephasing Dynamics of Purple Bacterial LH2. *J. Phys. Chem. B* **104**, 8295 (2000).
- [183] I. STIOPKIN, T. BRIKNER, M. YANG, AND G. R. FLEMING. Heterogeneous Exciton Dynamics Revealed by Two-Dimensional Optical Spectroscopy. *J. Phys. Chem. B* **110**, 20032 (2006).
- [184] A. PUGZLYS, P. R. HANIA, R. AUGULIS, K. DUPPEN, AND P. H. M. VAN LOOSDRECHT. Cylindrical Aggregates of 5,5',6,6'-Tetrachlorobenzimidacarbocyanine Amphiphilic Derivatives: Structure-Related Optical Properties and Exciton Dynamics. *Int. J. Photoenergy* page 1 (2006).
- [185] H. VON BERLEPSCH, C. BÖTTCHER, A. OUART, M. REGENBRECHT, S. AKARI, U. KEIDERLING, H. SCHNABLEGGER, S. DÄHNE, AND S. KIRSTEIN. Surfactant-induced changes of morphology of J-aggregates: superhelix-to-tubule transformation. *Langmuir* **16**, 5908 (2000).
- [186] C. DIDRAGA, J. A. KLUGKIST, AND J. KNOESTER. Optical Properties of Helical Cylindrical Molecular Aggregates: The homogeneous limit. *J. Phys. Chem. B* **106**, 11474 (2002).
- [187] H. VON BERLEPSCH, S. KIRSTEIN, R. HANIA, C. DIDRAGA, A. PUGZLYS, AND C. BÖTTCHER. Stabilisation of individual tubular J-aggregates by poly(vinyl alcohol). *J. Phys. Chem. B* **107**, 14176 (2003).
- [188] C. DIDRAGA, V. A. MALYSHEV, AND J. KNOESTER. Excitation Energy Transfer between Closely Spaced Multichromophoric Systems: Effects of Band Mixing and Intraband Relaxation. *J. Phys. Chem. B* **110**, 18818 (2006).
- [189] C. DIDRAGA, A. PUGZLYS, P. R. HANIA, H. VON BERLEPSCH, K. DUPPEN, AND J. KNOESTER. Structure, spectroscopy and microscopic model of tubular carbocyanine dye aggregates. *J. Phys. Chem. B* **108**, 14976 (2004).
- [190] M. CHO, T. BRIKNER, I. STIOPKIN, H. VASWANI, AND G. R. FLEMING. Two Dimensional Electronic Spectroscopy of Molecular Complexes. *J. Chin. Chem. Soc.* **53**, 15 (2006).
- [191] D. ABRAMAVICIUS, B. PALMIERI, D. V. VORONINE, F. SÁNDA, AND S. MUKAMEL. Coherent Multidimensional Optical Spectroscopy of Excitons in Molecular Aggregates: Quasi-particle versus Supermolecule Perspectives. *Chem. Rev.* **109**, 2350 (2009).

-
- [192] S. M. GALLAGHER-FAEDER AND D. M. JONAS. Phase-resolved time-domain nonlinear optical signals. *Phys. Rev. A* **62**, 033820 (2000).
- [193] E. L. READ, G. S. SCHLAU-COHEN, G. S. ENGEL, J. WEN, R. E. BLANKENSHIP, AND G. R. FLEMING. Visualization of Excitonic Structure in the Fenna-Matthews-Olson Photosynthetic Complex by Polarization-Dependent Two-Dimensional Electronic Spectroscopy. *Biophys. Journal* **95**, 847 (2008).
- [194] D. ABRAMAVICIUS, L. VALKUNAS, AND S. MUKAMEL. Transport and correlated fluctuations in the nonlinear optical response of excitons. *EPL* **80**, 17005 (2007).
- [195] A. V. MALYSHEV, V. A. MALYSHEV, AND J. KNOESTER. Probing Quantum-Mechanical Level Repulsion in Disordered Systems by Means of Time-Resolved Selectively Excited Resonance Fluorescence. *Phys. Rev. Lett.* **98**, 087401 (2007).
- [196] C. DIDRAGA AND J. KNOESTER. Optical spectra and localization of excitons in inhomogeneous helical cylindrical aggregates. *J. Chem. Phys.* **121**, 10687 (2004).
- [197] A. PUGZLYS, R. AUGULIS, P. H. M. VAN LOOSDRECHT, C. DIDRAGA, V. A. MALYSHEV, AND J. KNOESTER. Temperature-Dependent Relaxation of Excitons in Tubular Molecular Aggregates: Fluorescence Decay and Stokes Shift. *J. Phys. Chem. B* **110**, 20268 (2006).
- [198] A. TORTSCHANOFF AND S. MUKAMEL. Pump-Probe Simulation of the Two-Exciton Manifold of Dendrimers. *J. Phys. Chem. A* **106**, 7521 (2002).
- [199] S. MUKAMEL, R. OSZWALDOWSKI, AND L. YANG. A coherent nonlinear optical signal induced by electron correlations. *J. Chem. Phys.* **127**, 221105 (2007).
- [200] E. C. FULMER, P. MUKHERJEE, A. T. KRUMMEL, AND M. T. ZANNI. A pulse sequence for directly measuring the anharmonicities of coupled vibrations: Two-quantum two-dimensional infrared spectroscopy. *J. Chem. Phys.* **120**, 8067 (2004).
- [201] V. MAY AND O. KÜHN. Charge and Energy Transfer Dynamics in Molecular Systems. Wiley-VCH, Berlin (2000).
- [202] L. YANG AND S. MUKAMEL. Two-dimensional correlation spectroscopy of two-exciton resonances in semiconductor quantum wells. *Phys. Rev. Lett.* **100**, 057402 (2008).
- [203] K. W. STONE, D. TURNER, K. GUNDOGDU, S. T. CUNDIFF, AND K. A. NELSON. Exciton-exciton correlations revealed by two-quantum, two-dimensional Fourier transform optical spectroscopy. *Acc. Chem. Res.* **42**, 1452 (2009).
- [204] J. KIM, V. M. HUXTER, C. CURUTCHET, AND G. D. SCHOLLES. Measurement of Electron-Electron Interactions and Correlations Using Two-Dimensional Electronic Double-Quantum Coherence Spectroscopy. *J. Phys. Chem. A* **113**, 12122 (2009).
-

BIBLIOGRAPHY

- [205] J. KIM, S. MUKAMEL, AND G. D. SCHOLES. Two-Dimensional Electronic Double-Quantum Coherence Spectroscopy. *Acc. Chem. Res.* **42**, 1375 (2009).
- [206] L. J. YANG, T. H. ZHANG, A. D. BRISTOW, S. T. CUNDIFF, AND S. MUKAMEL. Isolating excitonic Raman coherence in semiconductors using two-dimensional correlation spectroscopy. *J. Chem. Phys.* **129**, 234711 (2008).
- [207] D. KARAIKAJ, A. D. BRISTOW, L. YANG, X. DAI, R. P. MIRIN, S. MUKAMEL, AND S. T. CUNDIFF. Two-quantum Many-body coherences in Two-Dimensional Fourier-Transform Spectra of Exciton Resonances in Semiconductor Quantum Wells. *Phys. Rev. Lett.* **104**, 117401 (2010).
- [208] D. ABRAMAVICIUS, D. V. VORONINE, AND S. MUKAMEL. Double-quantum resonances and exciton-scattering in coherent 2D spectroscopy of photosynthetic complexes. *Proc. Nat. Acad. Sci.* **105**, 8525 (2008).
- [209] K. SCHULTEN, I. OHMINE, AND M. KARPLUS. Correlation effects in spectra of polyenes. *J. Chem. Phys.* **64**, 4422 (1976).
- [210] R. W. CHAMBERS AND D. R. KEARNS. Triplet states of some common photosensitizing dyes. *Photochem. Photobiol.* **10**, 215 (1969).
- [211] M. CHACHISVILIS, O. KUHN, T. PULLERITS, AND V. SUNDSTRÖM. Excitons in photosynthetic purple bacteria: Wavelike motion or incoherent hopping? *J. Phys. Chem. B* **101**, 7275 (1997).
- [212] M. BECKER, V. NAGARAJAN, AND W. W. PARSON. Properties of the excited-singlet states of Bacteriochlorophyll-A and Bacteriopheophytin-A in polar solvents. *J. Am. Chem. Soc.* **113**, 6840 (1991).
- [213] P. MALY, R. DANIELIUS, AND R. GADONAS. Picosecond absorption-spectroscopy of chlorophyll-a dihydrate. *Photochem. Photobiol.* **45**, 7 (1987).
- [214] B. BRUGGEMANN, N. CHRISTENSSON, AND T. PULLERITS. Temperature dependent exciton-exciton annihilation in the LH2 antenna complex. *Chem. Phys.* **357**, 140 (2009).
- [215] N. CHRISTENSSON, F. MILOTA, A. NEMETH, J. SPERLING, H. F. KAUFFMANN, T. PULLERITS, AND J. HAUER. Two-Dimensional Electronic Spectroscopy of beta-Caroten. *J. Phys. Chem. B* **113**, 16409 (2009).
- [216] E. C. FULMER, F. DING, AND M. T. ZANNI. Heterodyned fifth-order 2D-IR spectroscopy of the azide ion in an ionic glass. *J. Chem. Phys.* **122**, 034302 (2005).
- [217] J. SUNG AND R. J. SILBEY. Four wave mixing spectroscopy for a multilevel system. *J. Chem. Phys.* **115**, 9266 (2001).

- [218] S. SHIM, C. M. STUART, AND R. A. MATHIES. Resonance Raman cross-sections and vibronic analysis of rhodamine 6G from broadband stimulated Raman spectroscopy. *ChemPhysChem* **9**, 697 (2008).
- [219] N. CHRISTENSSON, T. POLIVKA, A. YARTSEV, AND T. PULLERITS. Photon echo spectroscopy reveals structure-dynamics relationships in carotenoids. *Phys. Rev. B* **79**, 245118 (2009).
- [220] P. R. HAMMOND. Comparison of experimental and theoretical excited-state spectra for Rhodamine-6G. *IEEE J. Quant. Electronics* **16**, 1157 (1980).
- [221] E. R. SMITH, D. A. FARROW, AND D. M. JONAS. Response functions for dimers and square-symmetric molecules in four-wave-mixing experiments with polarized light. *J. Chem. Phys.* **123**, 12 (2005).
- [222] K. RAGHAVACHARI AND J. B. ANDERSON. Electron correlation effects in molecules. *J. Phys. Chem.* **100**, 12960 (1996).
- [223] E. PAPAGIANNAKIS, I. H. M. VAN STOKKUM, M. VENGRIS, R. J. COGDELL, R. VAN GRONDELLE, AND D. S. LARSEN. Excited-state dynamics of carotenoids in light-harvesting complexes. I. Exploring the relationship between the S-1 and S* states. *J. Phys. Chem. B* **110**, 527 (2006).
- [224] J. SAVOLAINEN, T. BUCKUP, J. HAUER, A. JAFARPOUR, C. SERRAT, M. MOTZKUS, AND J. L. HEREK. Carotenoid deactivation in an artificial light-harvesting complex via a vibrationally hot ground state. *Chem. Phys.* **357**, 181 (2009).
- [225] P. HAMM, M. LIM, AND R. M. HOCHSTRASSER. Non-markovian dynamics of the vibrations of ions in water from femtosecond infrared three-pulse photon echoes. *Phys. Rev. Lett.* **81**, 5326 (1998).
- [226] J. P. LEMAISTRE. Localization length and intraband scattering of excitons in linear aggregates. *Chem. Phys.* **246**, 283 (1999).
- [227] A. NEMETH, V. LUKEŠ, J. SPERLING, F. MILOTA, H. F. KAUFFMANN, AND T. MANČAL. Two-Dimensional Electronic Spectra of an Aggregating Dye: Simultaneous Measurement of Monomeric and Dimeric Line-shapes. *Phys. Chem. Chem. Phys.* **11**, 5986 (2009).
- [228] F. MILOTA, J. SPERLING, A. NEMETH, T. MANČAL, AND H. F. KAUFFMANN. Two-dimensional Electronic Spectroscopy of Molecular Excitons. *Acc. Chem. Res.* **42**, 1364 (2009).
- [229] J. KNOESTER. Light-harvesting J-Aggregates. Special Issue of the Int. J. Photoenergy (2006).
- [230] S. KIRSTEIN AND S. DÄHNE. J-aggregates of Amphiphilic Cyanine Dyes: Self-Organization of Artificial Light Harvesting Complexes. *Int. J. Photoenergy* **2006**, 1 (2006).

BIBLIOGRAPHY

- [231] S. GANAPATHY, G. T. OOSTERGETEL, P. K. WAWRZYNIAK, M. REUS, A. G. MAQUEO CHEW, F. BUDA, E. J. BOEKEMA, D. A. BRYANT, A. R. HOLZWARTH, AND H. J. M. DE GROOT. Alternating syn-anti bacteriochlorophylls form concentric helical nanotubes in chlorosomes. *Proc. Natl. Acad. Sci. USA* **109**, 8525 (2009).
- [232] J. M. WOMICK, S. A. MILLER, AND A. M. MORAN. Probing the Dynamics of Intraband Electronic Coherences in Cylindrical Molecular Aggregates. *J. Phys. Chem. A* **113**, 6587 (2009).
- [233] J. M. WOMICK, S. A. MILLER, AND A. M. MORAN. Correlated Exciton Fluctuations in Cylindrical Molecular Aggregates. *J. Phys. Chem. B* **113**, 6630 (2009).
- [234] I. BUCHVAROV, Q. WANG, M. RAYTCHEV, A. TRIFONOV, AND T. FIEBIG. Electronic energy delocalization and dissipation in single- and double-stranded DNA. *Proc. Nat. Acad. Sci.* **104**, 4794 (2007).
- [235] A. V. RUBAN, R. BERERA, C. ILIOAIA, I. H. M. VAN STOKKUM, J. T. M. KENNIS, A. A. PASCAL, H. VAN AMERONGEN, B. ROBERT, P. HORTON, AND R. VAN GRONDELLE. Identification of a mechanism of photoprotective energy dissipation in higher plants. *Nature* **450**, 575 (2007).
- [236] C. DIDRAGA AND J. KNOESTER. Excitons in tubular molecular aggregates. *J. Lum.* **110**, 239 (2004).
- [237] N. S. GINSBERG, Y.-C. CHENG, AND G. R. FLEMING. Two-Dimensional Electronic Spectroscopy of Molecular Aggregates. *Acc. Chem. Res.* **42**, 1352 (2009).
- [238] Y.-C. CHENG AND G. R. FLEMING. Dynamics of Light Harvesting in Photosynthesis. *Annu. Rev. Phys. Chem.* **60**, 241 (2009).
- [239] E. L. READ, H. LEE, AND G. R. FLEMING. Photon echo studies of photosynthetic light harvesting. *Photosynth. Res.* **101**, 233 (2009).
- [240] N. W. ASHCROFT AND N. D. MERMIN. *Solid State Physics*. Brooks Cole (2005).
- [241] F. C. SPANO AND S. MUKAMEL. Excitons in confined geometries: Size scaling of nonlinear susceptibilities. *J. Chem. Phys.* **95**, 7526 (1991).
- [242] H. VON BERLEPSCH, S. KIRSTEIN, AND C. BÖTTCHER. Effect of alcohols on j-aggregation of a carbocyanine dye. *Langmuir* **18**, 7699 (2002).
- [243] Z. G. FETISOVA, A. M. FREIBERG, AND K. E. TIMPMANN. Long-range molecular order as an efficient strategy for light harvesting in photosynthesis. *Nature* **334**, 633 (1988).
- [244] J. SPERLING, A. NEMETH, J. HAUER, D. ABRAMAVICIUS, S. MUKAMEL, H. F. KAUFFMANN, AND F. MILOTA. Excitons and Disorder in Molecular Nanotubes: A 2D Electronic Spectroscopy Study and First Comparison to a Microscopic Model. *J. Phys. Chem. A* **114**, 8179 (2010).

-
- [245] E. L. READ, G. S. ENGEL, T. R. CALHOUN, T. MANČAL, T. K. AHN, R. E. BLANKENSHIP, AND G. R. FLEMING. Cross-peak-specific two-dimensional electronic spectroscopy. *Proc. Nat. Acad. Sci.* **104**, 14203 (2007).
- [246] E. L. READ, G. S. SCHLAU-COHEN, G. S. ENGEL, T. GEORGIU, M. Z. PAPIZ, AND G. R. FLEMING. Pigment Organization and Energy Level Structure in Light-Harvesting Complex 4: Insights from Two-Dimensional Electronic Spectroscopy. *J. Phys. Chem. B* **113**, 6495 (2009).
- [247] I. KUZNETSOVA, P. THOMAS, T. MEIER, T. ZHANG, X. LI, R. P. MIRIN, AND S. T. CUNDIFF. Signatures of many-particle correlations in two-dimensional Fourier-transform spectra of semiconductor nanostructures. *Solid State Commun.* **142**, 154 (2007).
- [248] A. D. BRISTOW, D. KARAIKAJ, X. DAI, R. P. MIRIN, AND S. T. CUNDIFF. Polarization dependence of semiconductor exciton and biexciton contributions to phase-resolved optical two-dimensional Fourier-transform spectra. *Phys. Rev. B* **79**, 161305 (2009).
- [249] T. ZHANG, I. KUZNETSOVA, T. MEIER, X. LI, R. P. MIRIN, P. THOMAS, AND S. T. CUNDIFF. Polarization-dependent optical 2D Fourier transform spectroscopy of semiconductors. *Proc. Nat. Acad. Sci.* **104**, 14227 (2007).
- [250] J. A. MYERS, K. L. M. LEWIS, P. F. TEKAVEC, AND J. P. OGILVIE. Two-color two-dimensional Fourier transform electronic spectroscopy with a pulse-shaper. *Opt. Exp.* **16**, 17420 (2008).
- [251] S.-H. SHIM AND M. T. ZANNI. How to turn your pump-probe instrument into a multi-dimensional spectrometer: 2D IR and Vis spectroscopies via pulse shaping. *Phys. Chem. Chem. Phys.* **11**, 748 (2009).
- [252] E. M. GRUMSTRUP, S.-H. SHIM, M. A. MONTGOMERY, N. H. DAMRAUER, AND M. T. ZANNI. Facile collection of two-dimensional electronic spectra using femtosecond pulse-shaping technology. *Opt. Exp.* **15**, 16681 (2007).
- [253] D. V. VORONINE, D. ABRAMAVICIUS, AND S. MUKAMEL. Manipulating multidimensional electronic spectra of excitons by polarization pulse shaping. *J. Chem. Phys.* **126**, 044508 (2007).
- [254] D. V. VORONINE, D. ABRAMAVICIUS, AND S. MUKAMEL. Coherent control of cross-peaks in chirality-induced two-dimensional optical signals of excitons. *J. Chem. Phys.* **125**, 224504 (2006).
- [255] J. BREDEBECK, J. HELBING, A. SIEG, T. SCHRADER, W. ZINTH, C. RENNER, R. BEHRENDT, L. MORODER, J. WACHTVEITL, AND P. HAMM. Picosecond conformational transition and equilibration of a cyclic peptide. *Proc. Nat. Acad. Sci.* **100**, 6452 (2003).
-

BIBLIOGRAPHY

- [256] C. KOLANO, J. HELBING, M. KOZINSKI, W. SANDER, AND P. HAMM. Watching hydrogen-bond dynamics in a β -turn by transient two-dimensional infrared spectroscopy. *Nature* **444**, 469 (2006).
- [257] P. HAMM. Three-dimensional-IR spectroscopy: Beyond the two-point frequency fluctuation correlation function. *J. Chem. Phys.* **124**, 124506 (2006).
- [258] F. DING AND M. ZANNI. Heterodyned 3D IR spectroscopy. *Chem. Phys.* **341**, 95 (2007).
- [259] S. GARRETT-ROE AND P. HAMM. Purely absorptive three-dimensional infrared spectroscopy. *J. Chem. Phys.* **130**, 164510 (2009).
- [260] D.B. TURNER, K.W. STONE, K. GUNDOGDU, AND K.A. NELSON. Three Dimensional Electronic Spectroscopy of Excitons in GaAs Quantum Wells. *J. Chem. Phys.* **131**, 144510 (2009).

List of Figures

1.1	Schematic of the two-dimensional methods S_I , S_{II} , and S_{III} .	5
1.2	1Q2D spectra of a homogeneously and an inhomogeneously broadened TLS	7
1.3	Effect of spectral diffusion on 1Q2D spectra	8
1.4	Manifestation of electronic couplings in 1Q2D spectra	9
1.5	Pathways of energy flow followed by 1Q2D-ES	9
1.6	Characterization of vibronic coherences in 1Q2D-ES	10
1.7	Signature of electronic coherences in 1Q2D spectra	10
1.8	Characterization of higher excited states by 2D spectroscopy	11
2.1	Feynman diagrams	15
3.1	Schematic of the complete setup	21
3.2	Design of the NOPA	23
3.3	Pulse compression	23
3.4	Setup of the first generation	25
3.5	ZAP-SPIDER traces	25
3.6	Setup of the second generation	26
3.7	Characteristics of the setup of the second generation	27
3.8	Flow jet	28
3.9	Determination of zero-points	29
3.10	Determination of stage calibration factors	30
3.11	Influence of stepsize on data evaluation	31
3.12	Error sources in the phasing procedure	33
4.1	Linear spectral properties of PERY	37
4.2	Quantum-chemistry calculations on PERY	39
4.3	Real and imaginary part 1Q2D spectra of PERY	41
4.4	Amplitude and phase part 1Q2D spectra of PERY	42
4.5	Oscillations in the 1Q2D spectral line-shapes of PERY	47
4.6	One-dimensional four-wave mixing signals of PERY	49
4.7	Simulated 1Q2D spectra of PERY	51
4.8	Components of the 1Q2D spectrum of a TLS	54
5.1	Linear spectral properties of Pinacyanol	59
5.2	Amplitude part 1Q2D spectra of Pinacyanol	63
5.3	Absorptive and dispersive part 1Q2D spectra of Pinacyanol	65
5.4	Quantum-chemical structures of Pinacyanol	66
5.5	ZINDO orbitals for Pinacyanol monomer	67
5.6	ZINDO orbitals for Pinacyanol dimer	68

LIST OF FIGURES

6.1	Linear spectral properties of C8O3	75
6.2	Schematic linear absorption of a double-wall cylinder	77
6.3	1Q2D electronic correlation spectra of C8O3	78
6.4	1Q2D electronic relaxation spectra of C8O3	80
6.5	Rephasing and non-rephasing real part spectra of C8O3	82
6.6	Level scheme for fitting 2D spectra of C8O3	89
6.7	Strategy for fitting of the 1Q2D spectra of C8O3	91
7.1	1Q2D spectra of Rhodamine 6G	98
7.2	2Q2D spectra of Rhodamine 6G	99
7.3	Potential energy surfaces	101
7.4	2Q2D spectra in the homogeneous limit	102
7.5	Simulated 2Q2D spectra of Rhodamine 6G	106
7.6	Simulated 1Q2D spectra of Rhodamine 6G	106
8.1	Linear absorption spectrum of C8S3	115
8.2	Absorptive part 1Q2D spectra of C8S3	123
8.3	Real part 2Q2D spectra of C8S3	125
8.4	Narrow line-shape simulations of 2Q2D spectra of C8S3	126

Zusammenfassung

Während des letzten Jahrzehntes haben multi-dimensionale ultraschnelle Spektroskopien großes Potential gezeigt, indem sie ein zunehmend breiteres experimentelles Fenster zur Struktur und den Dynamiken von atomaren und molekularen Systemen auf Femtosekunden- und Pikosekunden-Zeitskalen öffneten. Die Vielseitigkeit und Bedeutung von zwei-dimensionaler elektronischer Spektroskopie beruht auf dem Gewinn an zusätzlicher Information, die man durch Ausweitung der Spektren in zwei Frequenz-Dimensionen erhält. Wichtige experimentelle Einsichten wurden durch die Studie von Linienverbreiterungsmechanismen in Lösung, durch die Aufdeckung von elektronischen Kopplungen und Energietransferpfaden in natürlichen und synthetischen Lichtsammelkomplexen, die Untersuchung von elektronischen und vibronischen Kohärenzen und die Erforschung von Exziton-Exziton-Wechselwirkungen in Halbleitern gewonnen, um nur einige wenige Beispiele zu nennen. Eine Interpretation dieser reichhaltigen Quelle an Information wurde teilweise durch die enge Anbindung dieser experimentellen Errungenschaften an theoretische Bemühungen erreicht.

Die vorliegende Dissertation fasst Teile unserer Anstrengungen im Bereich der zwei-dimensionalen elektronischen Spektroskopie zusammen. Der Fortschritt verlief dabei parallel auf zwei Schienen: einerseits führten Verbesserungen in der Instrumentation zu einer breiteren Anwendbarkeit der Methode. Durch die Umsetzung eines kompakten, einfach einzurichtenden und passiv Phasen-stabilisierten Aufbaus zur Messung von zwei-dimensionalen elektronischen Spektren in drei verschiedenen Phasen-angepassten Geometrien wurde es möglich nicht nur Einzelquanten- sondern auch Doppelquanten-Kohärenzen zu studieren. Auf der anderen Seite wurden die existierenden Methoden angewandt um die elektronischen und vibronischen Dynamiken von molekularen Systemen unterschiedlicher Komplexität zu erforschen. Ein elektronisches Zwei-Level-System, dessen elektronischer Übergang an eine niederfrequente Schwingung gekoppelt ist, diente als Ausgangspunkt in unseren Untersuchungen. Das vibrationelle Wellenpaket, welches durch die Anregung mit einem Femtosekunden-Laserpuls erzeugt wird, manifestiert sich in oszillierenden Linienformen in zwei-dimensionalen Spektren. Das zu beobachtende Schwingungsmuster kann den gegenphasig verlaufenden Oszillationen in den Intensitäten der rephasierenden und nicht-rephasierenden Signalbeiträge zugeordnet werden. In einem nächsten Schritt wurden die Dynamiken der Linienformen eines Monomer-Dimer-Systems im Gleichgewicht untersucht. Es wurde gefunden, dass Exziton-Delokalisations-Effekte im Dimer die Zeitskala der spektralen Diffusion stark beeinflussen. Der Grad an Komplexität erreichte seinen Höhepunkt in der Untersuchung von Pfaden und Zeitskalen des Energietransfers in doppelwandigen zylindrischen J-Aggregaten. Die Dynamiken der Exzitonen in diesen molekularen Nanoröhrchen wurden mittels zeitlicher, energetischer und örtlicher Attribute charakterisiert. Zusätzlich wurde das Zweixziton-Band von C8S3-Aggregaten mittels Doppelquanten-Kohärenz zwei-dimensionaler elektronischer Spektroskopie erforscht, mit dem Ziel ein tieferes Verständnis der elektronischen Struktur und Dynamiken in dieser Klasse von Substanzen zu gewinnen.

Curriculum Vitae

PERSONAL DETAILS

Date of Birth	April 22, 1983
Place of Birth	Klagenfurt, Austria
Nationality	Austria
E-mail	alexandra.nemeth@univie.ac.at

EDUCATION

02/2010 - 03/2010	Research stay in the group of Prof. S. Mukamel at the Department of Chemistry, University of Irvine, California, USA
09/2009 - 10/2009	Research stay in the group of Prof. R. J. D. Miller at the Department of Chemistry, University of Toronto, Canada
04/2007 - 12/2010	Doctoral studies of natural sciences (chemistry) at the University of Vienna (research group: <i>Ultrafast Dynamics</i>)
03/2007	Diploma degree (passed with distinction)
02/2006 - 03/2007	Diploma thesis at the research group <i>Ultrafast Dynamics</i> , Department of Physical Chemistry, University of Vienna
08/2005 - 12/2005	Erasmus student at the Department of Chemical Physics, Lund University (Sweden)
10/2004	Intermediate degree (passed with distinction)
10/2001 - 03/2007	Undergraduate studies of chemistry at the University of Vienna
09/1993 - 07/2001	Grammar school in Klagenfurt
09/1989 - 07/1993	Elementary school in Klagenfurt

AWARDS

01/2009	Recipient of a DOC-fFORTE scholarship of the Austrian Academy of Sciences for a project entitled "Probing double-quantum coherences by two-dimensional electronic spectroscopy"
---------	---

List of Publications

Articles

- A. NEMETH, F. MILOTA, T. MANČAL, T. PULLERITS, J. SPERLING, J. HAUER, H. F. KAUFFMANN, AND N. CHRISTENSSON. Double-quantum two-dimensional electronic spectroscopy of a three-level system: Experiments and Simulations. *J. Chem. Phys.* **133**, 094505 (2010)
- J. SPERLING, A. NEMETH, J. HAUER, D. ABRAMAVICIUS, S. MUKAMEL, H. F. KAUFFMANN, AND F. MILOTA. Excitons and Disorder in Molecular Nanotubes: A 2D Electronic Spectroscopy Study and First Comparison to a Microscopic Model. *J. Phys. Chem. A* **114**, 8179 (2010)
- A. NEMETH, F. MILOTA, T. MANČAL, V. LUKEŠ, J. HAUER, H. F. KAUFFMANN, AND J. SPERLING. Vibrational wave packet induced oscillations in two-dimensional electronic spectra. I. Experiments. *J. Chem. Phys.* **132**, 184514 (2010)
- T. MANČAL, A. NEMETH, F. MILOTA, V. LUKEŠ, H. F. KAUFFMANN, AND J. SPERLING. Vibrational wave packet induced oscillations in two-dimensional electronic spectra. II. Theory. *J. Chem. Phys.* **132**, 184515 (2010)
- N. CHRISTENSSON, F. MILOTA, A. NEMETH, J. SPERLING, H. F. KAUFFMANN, T. PULLERITS, AND J. HAUER. Two-dimensional Electronic Spectroscopy of β -carotene. *J. Phys. Chem. B* **113**, 16409 (2009)
- A. NEMETH, J. SPERLING, J. HAUER, H. F. KAUFFMANN, AND F. MILOTA. Compact phase-stable design for single- and double-quantum two-dimensional electronic spectroscopy. *Opt. Lett.* **34**, 3301 (2009)
- F. MILOTA, J. SPERLING, A. NEMETH, T. MANČAL, AND H. F. KAUFFMANN. Two-dimensional electronic spectroscopy of molecular excitons. *Acc. Chem. Res.* **42**, 1364 (2009)
- F. MILOTA, J. SPERLING, A. NEMETH, D. ABRAMAVICIUS, S. MUKAMEL, AND H. F. KAUFFMANN. Excitonic couplings and interband energy transfer in a double-wall molecular aggregate imaged by coherent two-dimensional electronic spectroscopy. *J. Chem. Phys.* **131**, 054510 (2009)
- A. NEMETH, V. LUKEŠ, J. SPERLING, F. MILOTA, H. F. KAUFFMANN, AND T. MANČAL. Two-dimensional electronic spectra of an aggregating dye: simultaneous measurement of monomeric and dimeric line-shapes. *Phys. Chem. Chem. Phys.* **11**, 5986 (2009)
- A. NEMETH, F. MILOTA, J. SPERLING, H. F. KAUFFMANN, D. ABRAMAVICIUS, AND S. MUKAMEL. Tracing exciton dynamics in molecular nanotubes with 2D electronic spectroscopy. *Chem. Phys. Lett.* **469**, 130 (2009)

- F. MILOTA, J. SPERLING, A. NEMETH, AND H. F. KAUFFMANN. Two-Dimensional Electronic Photon Echoes of a Double Band J-Aggregate: Quantum Oscillatory Motion versus Exciton Relaxation. *Chem. Phys.* **357**, 45 (2009)
- A. NEMETH, F. MILOTA, T. MANČAL, V. LUKEŠ, H. F. KAUFFMANN, AND J. SPERLING. Vibronic modulation of lineshapes in two-dimensional electronic spectra. *Chem. Phys. Lett.* **459**, 94 (2008)
- J. SPERLING, A. NEMETH, P. BAUM, F. SANDA, E. RIEDLE, H. F. KAUFFMANN, S. MUKAMEL, AND F. MILOTA. Exciton Dynamics in a Disordered Conjugated Polymer: Three-Pulse Photon-Echo and Transient Grating Experiments. *Chem. Phys.* **349**, 244 (2008)

Book Contributions

- A. NEMETH, F. MILOTA, T. MANČAL, V. LUKEŠ, H. F. KAUFFMANN, AND J. SPERLING. Vibrational Beating in Two-Dimensional Electronic Spectra. *Ultrafast Phenomena XVI, Springer Series in Chemical Physics* **92** (2009)